UNIVERSITÄT PADERBORN
Die Universität der Informationsgesellschaft

FAKULTÄT FÜR
ELEKTROTECHNIK,
INFORMATIK UND
MATHEMATIK

Design and optimization of integrated optical antennas and LNOI waveguide structures

Von der Fakultät für Elektrotechnik, Informatik und Mathematik
der Universität Paderborn

zur Erlangung des akademischen Grades

Doktor der Ingenieurwissenschaften (Dr.-Ing.)

genehmigte Dissertation

von

M. Sc. Henna Farheen

Erster Gutachter:	Prof. Dr. Jens Förstner
Zweiter Gutachter:	Prof. Dr. J. Christoph Scheytt

Tag der mündlichen Prüfung: 23.04.2024

Paderborn 2024

Diss. EIM-E/377

Acknowledgement

During my time pursuing a Ph.D. at Paderborn University, I had the privilege to learn and grow in an environment filled with talented researchers. Especially the experience of working in the Theoretical Electrical Engineering Group gave me an indispensable chance to work collaboratively with a highly diverse and motivated group of scientists. I am grateful to the following individuals for their support and contributions to my thesis:

... My supervisor, Prof. Dr. Jens Förstner, for providing me with the opportunity and resources to carry out the work presented in this thesis. His supervision and constructive discussions were instrumental in achieving my goals.

... Prof. Dr. J. Christoph Scheytt, for his active collaboration and being the second examiner of my thesis.

... Dr. Viktor Myroshnychenko for being an incredible mentor providing endless support, with invaluable discussions and suggestions that have significantly contributed to this thesis.

... Dr. Manfred Hammer, for his tremendous support and motivation. His technical expertise and extensive experience contributed greatly to the final phase of this thesis.

... Prof. Dr. Stefan Linden and his group members, for the fruitful collaboration.

... My current and former group mates, for facilitating my work and helping me grow as a researcher.

... My family and friends, for providing me with the social and personal infrastructure I needed to thrive in this graduate environment.

Abstract

The design of integrated photonic devices with specific radiation characteristics is a multi-faceted problem. The ability to control the propagation of electromagnetic waves and their free-space radiation is a crucial task. This work employs full-wave numerical simulations to design and optimize various antennas and wave-guiding structures in the optical regime to achieve this.

The findings can be categorized into two parts. In the first part, the focus is on efficient radiation emission in specific directions. This is achieved by examining dielectric antennas and their phased array configurations. The antennas are made from low-loss materials such as hafnium dioxide, silicon, and tantalum pentoxide. These structures consist of a reflector and a director deposited on a glass substrate. An emitter, acting as an internal excitation source, is positioned in the feed gap between them. Antennas with rectangular-, tip-, and horn-shaped directors are explored, which control the shape of radiation patterns and guide light selectively. Additionally, optical phased arrays (OPAs) provide increased gain and directivity, small beamwidth, and more control over the main lobe direction. Large-scale 2-D silicon-based OPAs are realized for three different radiating elements that target distinctive objectives for their radiation characteristics. The OPA utilizes these antennas with balanced power and aligned phases to produce versatile radiation patterns and steer the beam into desired directions in the far-field.

In the second part, suppressing unwanted radiation in dielectric integrated optical waveguide channels is considered. For this purpose, the propagation of electromagnetic waves through lithium niobate rib waveguide structures on silicon dioxide platforms is investigated. We design and optimize integrated optical devices such as directional couplers, waveguide bends, and multi-mode interference couplers. The analysis provides an in-depth understanding required for fabricating platforms suitable for quantum optics applications.

Zusammenfassung

Der Entwurf integrierter photonischer Bauelemente mit spezifischen Strahlungseigenschaften ist ein vielschichtiges Problem. Die Fähigkeit, die Ausbreitung und die Abstrahlung von elektromagnetischen Wellen im freien Raum zu kontrollieren, ist ein entscheidendes Kriterium. In dieser Arbeit werden numerische Feldsimulationen eingesetzt, um verschiedene Antennen und wellenleitende Strukturen im optischen Bereich zu entwerfen und zu optimieren.

Die Ergebnisse lassen sich in zwei Teile gliedern. Im ersten Teil der Untersuchung liegt der Schwerpunkt auf der effizienten Abstrahlung in ausgewählte Richtungen. Dazu werden dielektrische Antennen und deren Phased-Array-Konfigurationen untersucht. Die Antennen werden aus verlustarmen Materialien wie Hafniumdioxid, Silizium und Tantalpentoxid hergestellt. Diese bestehen aus einem Reflektor und einem Direktor, die auf einem Glassubstrat aufgebracht sind. Ein Emitter, der als interne Anregungsquelle dient, befindet sich im Spalt zwischen den beiden. Dabei werden Antennen mit rechteckigen, stab- und hornförmigen Direktoren erforscht, die die Form der Strahlungsdiagramme kontrollieren und das Licht selektiv führen. Darüber hinaus bieten optische Phased Arrays (OPAs) eine höhere Verstärkung und Richtwirkung, eine geringe Strahlweite und eine verbesserte Kontrolle über die Richtung der Hauptkeule. Große 2D-OPAs auf Siliziumbasis werden für drei verschiedene Strahlelemente konstruiert, die hinsichtlich ihrer Strahlungseigenschaften unterschiedliche Anforderungen erfüllen. Der OPA nutzt diese Antennen mit ausbalancierter Leistung und angepasster Phase, um unterschiedliche Strahlungsdiagramme zu erzeugen und den Strahl im Fernfeld in die gewünschten Richtungen zu lenken.

Im zweiten Teil wird die Unterdrückung unerwünschter Strahlung in integrierten dielektrischen Lichtwellenleiterkanälen betrachtet. Dazu wird die Ausbreitung von elektromagnetischen Wellen durch Lithiumniobat-Rippenwellenleiterstrukturen auf Siliziumdioxid-Plattformen untersucht. Dabei werden integrierte optische Bauelemente wie Richtungskoppler, Wellenleiterkrümmer und Multimode-Interferenzkoppler entworfen und optimiert. Die Analyse liefert ein tiefgreifendes Verständnis für die Herstellung von Plattformen, die für quantenoptische Anwendungen geeignet sind.

Contents

Chapter 1

Introduction

Radiation is defined as the emission of energy into space or a medium of interest. This energy can be carried through particles or waves like electromagnetic or acoustic waves [1]. Controlling the propagation of radiated fields is of key interest in the field of optics [2]. Broadly, radiation can be classified as desired or undesired, tailored to the needs of a specific application. For example, wireless point-to-point communication requires highly directed emission between the transmitter and receiver without much loss [3]. On the other hand, a wireline communication system demands complete suppression of radiation outside the wire to transfer data efficiently [4]. Therefore, radiation control is essential in many real-time communication systems [5]. The former example employs devices like antennas, while the latter utilizes wave-guiding structures [6]. Studying electromagnetic propagation helps characterize and understand the limitations of these optical systems and facilitates radiation control through these devices [7]. In this work, we focus on dielectric media in which the material's refractive index influences wave propagation. However, the manipulation of light in the optical regime is limited by the narrow range of refractive indices available for these materials. An appropriate combination of materials and design methodologies produces topologies that can efficiently control wave propagation. This thesis considers different devices that are employed for this purpose.

First, we look into applications where the emission of radiation is desired. Transmitting antennas are devices that couple localized power into free propagating radiation in their surrounding medium [8, 9]. The reciprocal equivalent of such a system is the receiving antenna [10, 11]. In general, antennas emit radiation in the form of spherical waves that spread into free space. Sufficiently far away from these radiation sources, the energy is intercepted as approximate plane waves. This work primarily focuses on transmitting antennas in the optical regime. Typically, such antennas have been demonstrated using plasmonic or dielectric structures. Metallic nanoantennas, operating on the basis of surface plasmons, possess small size and resonant properties. However, these structures are accompanied by high ohmic losses due to absorption [12–17], making dielectric structures more attractive as they have low dissipative losses [18], reasonable bandwidths [19], and highly directional radiation patterns with near-unity radiation efficiency [20]. Especially, high-index dielectric antennas made of silicon, hafnium dioxide, germanium, or gallium phosphide have garnered significant attention [21–24]. Simultaneously, several hybrid metal-dielectric antennas have also shown promising results [25–27]. Ref. [28]

gives a broad overview of this developing area of research, along with its potential applications. In this thesis, we present broadband optical traveling-wave antennas made from low-loss dielectric materials. The antenna design considers two main objectives for its optimization: improving the antenna's directive nature and controlling the radiation pattern of such antennas. The optimized antennas exhibit ultra-high directivity, resulting from the interplay between the guided and leaky modes supported by the director. We successfully compare our numerical results to experimental measurements of the antennas that are fabricated using electron beam lithography. The results are in good agreement with one another. Our all-dielectric approach has led to the development of a new class of antennas that are highly suitable for application in the areas of optical communication and sensing with reduced cross-talk.

The use of multiple antennas aids in further improving the directive nature and overall gain of the system [29]. In the optical regime, they are called optical phased arrays, where manipulation of amplitude and phase of each antenna element is used for radiation control with the help of constructive and destructive interference [30]. Such systems tailor complex far-field radiation patterns and precisely control the radiation direction via beam steering [31]. Conventionally, the number of elements and the spacing between them control the shape of the emission pattern, angular resolution, beamwidth, and the periodicity of the grating lobes. Several array configurations implement 1-D OPAs that compactly assemble long and narrow radiators [32–34]. Unless these OPAs employ a highly precise tunable laser, such systems can steer the beam only in one direction [35]. On the other hand, beam steering in two directions can be achieved in 2-D OPAs with phase tuning at the operational wavelength. However, due to the large footprint of the radiating elements, this feature comes at the cost of a limited field of view (FOV), i.e., the grating-lobe-free region for beam steering [31,36,37]. This issue of limited beam steering range can be partially mitigated using a sparse array configuration [38] or can be circumvented by employing circularly symmetric array configurations, essentially producing a visible region with no grating lobes [39]. We numerically demonstrate large-scale 2-D silicon-based OPAs that are balanced in power and aligned in phase to produce suitable radiation patterns and steer the beam into desired directions in the far-field. Specifically, asymmetric horn antennas and circular grating antennas are investigated for increasing the upward radiating efficiency and the efficiency in the FOV, respectively. We also realize a circular OPA to address the limited beam steering range issue. These OPAs are anticipated to be attractive candidates for various applications like light detection and ranging (LiDAR), free-space communication, optical trapping, holographic and augmented-reality displays, optogenetic stimulation, and optic switches [40–47].

In contrast to the above, in the second part of this thesis, we consider areas that need efficient power transmission. These require field confinement in a guiding structure, suppressing radiation into the surrounding medium. For example, waveguides play a pivotal role in signal transmission, in particular, dielectric waveguides with a higher refractive index core than the surrounding cladding region. These structures guide electromagnetic waves being confined to the core region, by virtue of total internal reflection. Although silicon photonics has a well-established platform for integrated optics, lithium niobate (LN) has become a promising candidate due to its outstanding electro-optic properties and second-order nonlinear susceptibility [48–50]. LN-based integrated quantum photonics systems [51] have been adapted for two-photon absorption [52, 53] or non-linear interaction of waves to generate entangled photons [54–57]. In this work, X-cut lithium niobate on insulator (LNOI) rib waveguides are considered to design and optimize different optical components such as directional couplers,

waveguide bends, and multi-mode interference couplers that are excited by TE polarization. These components are fundamental elements needed on an integrated LN platform capable of light confinement at sub-wavelength scales [58]. These platforms offer dense integration of optical and electrical components for applications in microwave photonics and optical communication [59–62].

Structure of this thesis

The following content of this thesis is divided into six chapters. The theoretical background needed for this work is described in Chapter 2, capturing the fundamentals of antennas, antenna arrays, and optical waveguides. Starting with the Maxwell equations, we derive the relevant far-fields to characterize an antenna. Additionally, we look into different antenna types and array configurations, providing an overview of their principle of operation.

Chapter 3 briefly overviews the numerical methods and optimization techniques used in this work. In particular, we outline the finite integration technique utilized in CST Microwave Studio [63]. This tool is primarily employed in this work for electromagnetic simulations. Since a large portion of the work depends on optimization, we briefly look at the global and local optimizers used in the context of this work.

The results of this thesis can be broadly classified into three parts. Firstly, in Chapter 4, we introduce optical antennas that are rigorously investigated and optimized for $780\,\mathrm{nm}$ (emission wavelength of CdSeTe colloidal quantum dots). The proposed antennas are highly directive, a characteristic that strongly depends on the antenna geometry and material. Furthermore, we perform sensitivity analyses of these antennas, highlighting their robustness to fabrication imperfections.

Secondly, Chapter 5 focuses on optical phased arrays operating at the telecom wavelength of $1550\,\mathrm{nm}$ (C-band). The chapter describes radiating elements optimized to target objectives such as high upward efficiency and improved power efficiency in the FOV. We numerically demonstrate the integration of the optimized radiating elements in two distinct phased array systems and highlight their key advantages.

Finally, in Chapter 6, LNOI rib waveguides are investigated to design and optimize optical components. These waveguides combine the benefits of silicon and LN utilized in integrated quantum photonics. In particular, we characterize the optical properties of directional couplers, waveguide bends, and multi-mode interference couplers with the X-cut crystal orientation and excited with TE polarization.

Lastly, Chapter 7 summarizes this thesis and gives a brief outlook on closely related topics for future work.

The work done during the course of this thesis is conducted in cooperation with my colleagues in the Theoretical Electrical Engineering group at Paderborn University. The results presented in Chapter 4 were a collaboration with colleagues from the Department of Nanophotonics at Universität Bonn. The work on Chapter 6 was done in cooperation with colleagues from the System and Circuit Technology and Integrated Quantum Optics departments at Paderborn University.

Chapter 2

Theoretical background

This chapter delves into the essential concepts necessary for the theoretical background of this work. We start by discussing the Maxwell equations in Section 2.1, which serve as the foundation for electromagnetic simulations. In Section 2.2, we introduce antenna theory, summarizing the necessary quantities required for the characterization of classical antennas. Section 2.3 provides a brief overview of the operating principles of various linear antennas, while Section 2.4 looks into traveling-wave antennas that are the focus of Chapter 4 of this thesis. Finally, Section 2.5 explores the fundamentals and various configurations of antenna arrays, which lay the foundation for Chapter 5 of this thesis. The mathematical formulation of this chapter is based on [29, 64, 65], where more detailed information can be obtained.

2.1 Maxwell's equations

James Clerk Maxwell formulated the fundamental set of coupled partial differential equations called the Maxwell equations [66]. In combination with the Lorentz force and Newton's second law, these equations lay the foundation of classical electromagnetism, which describes the interaction of electromagnetic fields in the presence of charged particles [1]. The macroscopic Maxwell equations in the time domain are

$$\nabla \times \boldsymbol{E}(\boldsymbol{r},t) = -\frac{\partial}{\partial t}\boldsymbol{B}(\boldsymbol{r},t), \tag{2.1}$$

$$\nabla \times \boldsymbol{H}(\boldsymbol{r},t) = \frac{\partial}{\partial t}\boldsymbol{D}(\boldsymbol{r},t) + \boldsymbol{J}(\boldsymbol{r},t), \tag{2.2}$$

$$\nabla \cdot \boldsymbol{D}(\boldsymbol{r},t) = \rho(\boldsymbol{r},t), \tag{2.3}$$

$$\nabla \cdot \boldsymbol{B}(\boldsymbol{r},t) = 0, \tag{2.4}$$

where $\boldsymbol{E}$ is the electric field, $\boldsymbol{H}$ is the magnetic field, $\boldsymbol{D}$ is the electric flux density, $\boldsymbol{B}$ is the magnetic flux density, $\boldsymbol{J}$ is the current density and ρ is the charge density, defined at a point $\boldsymbol{r}$ in space at time t. These fields are related using the constitutive equations

$$\boldsymbol{D}(\boldsymbol{r},t) = \varepsilon_0 \boldsymbol{E}(\boldsymbol{r},t) + \boldsymbol{P}(\boldsymbol{r},t), \tag{2.5}$$

$$\boldsymbol{B}(\boldsymbol{r},t) = \mu_0 \boldsymbol{H}(\boldsymbol{r},t) + \boldsymbol{M}(\boldsymbol{r},t), \tag{2.6}$$

where ε_0 is the permittivity and μ_0 is the permeability in vacuum. Here, $\boldsymbol{P}$ and $\boldsymbol{M}$ are the polarization and magnetization, respectively, which describe the density of electric and magnetic dipole moments as

$$\boldsymbol{P}(\boldsymbol{r},t) = \varepsilon_0 \chi_e \boldsymbol{E}(\boldsymbol{r},t) \qquad \text{and} \qquad \boldsymbol{M}(\boldsymbol{r},t) = \mu_0 \chi_m \boldsymbol{H}(\boldsymbol{r},t), \tag{2.7}$$

where χ_e and χ_m are the electric and magnetic susceptibility, respectively. For a linear, isotropic, homogeneous material, the constitutive equations can be rewritten as,

$$\boldsymbol{D}(\boldsymbol{r},t) = \varepsilon \boldsymbol{E}(\boldsymbol{r},t) = \varepsilon_0 \varepsilon_r \boldsymbol{E}(\boldsymbol{r},t), \tag{2.8}$$

$$\boldsymbol{B}(\boldsymbol{r},t) = \mu \boldsymbol{H}(\boldsymbol{r},t) = \mu_0 \mu_r \boldsymbol{H}(\boldsymbol{r},t), \tag{2.9}$$

where ε and μ are the absolute permittivity and permeability, respectively, $\varepsilon_r = 1 + \chi_e$ is the relative permittivity, and $\mu_r = 1 + \chi_m$ is the relative permeability.

However, the linear proportionality $\boldsymbol{D} \propto \boldsymbol{E}$ and $\boldsymbol{B} \propto \boldsymbol{H}$ can only be approximated when ε_r and μ_r are real-valued and independent of frequency, which as per the Kramer-Kronig relation is valid only for a narrow range of frequencies.

One can obtain the stationary fields utilizing the harmonic time dependence of the electromagnetic fields, i.e., $\sim e^{j\omega t}$ as

$$\begin{pmatrix} \boldsymbol{E} \\ \boldsymbol{H} \end{pmatrix}(\boldsymbol{r},t) = \mathrm{Re}\left\{ \begin{pmatrix} \boldsymbol{E} \\ \boldsymbol{H} \end{pmatrix}(\boldsymbol{r}) e^{j\omega t} \right\}, \tag{2.10}$$

where ω is the angular frequency and $\boldsymbol{E}(\boldsymbol{r})$ and $\boldsymbol{H}(\boldsymbol{r})$ are the electric and magnetic fields in the frequency domain, respectively. The Maxwell equations in the frequency domain can be expressed as

$$\nabla \times \boldsymbol{E}(\boldsymbol{r}) = -j\omega \boldsymbol{B}(\boldsymbol{r}), \tag{2.11}$$

$$\nabla \times \boldsymbol{H}(\boldsymbol{r}) = j\omega \boldsymbol{D}(\boldsymbol{r}) + \boldsymbol{J}(\boldsymbol{r}), \tag{2.12}$$

$$\nabla \cdot \boldsymbol{D}(\boldsymbol{r}) = \rho(\boldsymbol{r}), \tag{2.13}$$

$$\nabla \cdot \boldsymbol{B}(\boldsymbol{r}) = 0. \tag{2.14}$$

One can also arrive at the wave equation for a linear, isotropic, non-magnetic material with no free charges, i.e., $\mu_r = 1$ and $\rho = 0$, by taking the curl of Eq. (2.11) and inserting Eq. (2.12),

$$\nabla \times (\nabla \times \boldsymbol{E}(\boldsymbol{r})) - k^2 \boldsymbol{E}(\boldsymbol{r}) = -j\omega\mu \boldsymbol{J}(\boldsymbol{r}). \tag{2.15}$$

The wave vector $\boldsymbol{k}$ pointing in the direction of propagation can be defined as,

$$|\boldsymbol{k}| =: k = \frac{\omega}{c_0}\sqrt{\varepsilon_r(\omega)} = \frac{\omega}{c_0} n(\omega) = k_0 n(\omega), \tag{2.16}$$

where k_0 is the vacuum wave number, c_0 is the speed of light in vacuum, and n is the refractive index of the medium. This equation that relates the wave number to the frequency is called the dispersion relation.

Similarly, the wave equation using the magnetic field can be obtained by taking the curl of Eq. (2.12) and inserting Eq. (2.11)

$$\varepsilon_r \nabla \times (\frac{1}{\varepsilon_r} \nabla \times \boldsymbol{H}(\boldsymbol{r})) - k^2 \boldsymbol{H}(\boldsymbol{r}) = 0. \tag{2.17}$$

2.2 Antennas for light

Traditionally, antennas are defined as a medium for transmitting or receiving radio waves [29]. Scaling down from the radio wave and microwave regime, the optical analog of such antennas is defined as a device that behaves like a converter between freely propagating optical radiation and localized energy [67]. One of the first antennas was constructed by Heinrich Hertz while he was verifying the electromagnetic theory proposed by Maxwell [68]. This was followed by a multitude of innovations giving rise to different types of antennas utilized for a wide range of applications [10, 28].

2.2.1 Antenna theory

Antenna theory is based on the Maxwell equations introduced in the section above. It is first important to understand how current and charge distribution can result in the radiation of electromagnetic waves. The following discussion is based on Ref. [64], where a more detailed insight can be found. For an antenna, say a wire antenna, with a current distribution localized in a defined space, electromagnetic fields are produced that propagate large distances from the location of the source. The radiation can be described more conveniently by utilizing electric (Φ) and magnetic ($\boldsymbol{A}$) potentials in place of $\boldsymbol{E}$ and $\boldsymbol{B}$ fields. Considering Gauss's law for magnetism in Eq. (2.4), the divergence-free magnetic flux $\boldsymbol{B}$ implies the existence of a vector potential $\boldsymbol{A}$, such that

$$\boldsymbol{B}(\boldsymbol{r},t) = \nabla \times \boldsymbol{A}(\boldsymbol{r},t). \tag{2.18}$$

Substituting Eq. (2.18) in Faraday's law (Eq. (2.1)),

$$\nabla \times \boldsymbol{E}(\boldsymbol{r},t) = -\nabla \times \frac{\partial}{\partial t}\boldsymbol{A}(\boldsymbol{r},t) \quad \Rightarrow \quad \nabla \times \left(\boldsymbol{E}(\boldsymbol{r},t) + \frac{\partial}{\partial t}\boldsymbol{A}(\boldsymbol{r},t)\right) = 0. \tag{2.19}$$

The curl-less quantity $\left(\boldsymbol{E} + \frac{\partial}{\partial t}\boldsymbol{A}\right)$ can be represented as the gradient of a scalar potential Φ as

$$\boldsymbol{E}(\boldsymbol{r},t) = -\nabla\Phi(\boldsymbol{r},t) - \frac{\partial}{\partial t}\boldsymbol{A}(\boldsymbol{r},t). \tag{2.20}$$

However, these potentials above are not uniquely defined, as they can always be varied by adding some constants. Therefore, using the following gauge transformation with a scalar function ψ, $\boldsymbol{A}$ and Φ can be transformed, keeping $\boldsymbol{E}$ and $\boldsymbol{B}$ invariant. This is called the gauge invariance of Maxwell's equations. The transformed potentials can be described by

$$\boldsymbol{A}'(\boldsymbol{r},t) = \boldsymbol{A}(\boldsymbol{r},t) + \nabla\psi(\boldsymbol{r},t), \tag{2.21}$$

$$\Phi'(\boldsymbol{r},t) = \Phi(\boldsymbol{r},t) - \frac{\partial}{\partial t}\psi(\boldsymbol{r},t). \tag{2.22}$$

However, in electromagnetism, for radiation problems, the Lorentz gauge is customarily used, which is defined by

$$\nabla \cdot \boldsymbol{A}(\boldsymbol{r},t) + \frac{1}{c^2}\frac{\partial}{\partial t}\Phi(\boldsymbol{r},t) = 0, \tag{2.23}$$

where $c = \frac{1}{\sqrt{\mu\varepsilon}}$ is the speed of light. Plugging Eq. (2.20) into Gauss's (Eq. (2.3)) and Ampere's (Eq. (2.2)) law, one arrives at

$$\nabla^2\Phi(\boldsymbol{r},t) + \frac{\partial}{\partial t}\left(\nabla\cdot\boldsymbol{A}(\boldsymbol{r},t)\right) = -\frac{\rho(\boldsymbol{r},t)}{\varepsilon}, \tag{2.24}$$

$$\left(\nabla^2 - \frac{1}{c^2}\frac{\partial^2}{\partial t^2}\right)\boldsymbol{A}(\boldsymbol{r},t) - \nabla\left(\nabla\cdot\boldsymbol{A}(\boldsymbol{r},t) + \frac{1}{c^2}\frac{\partial}{\partial t}\Phi(\boldsymbol{r},t)\right) = -\mu\boldsymbol{J}(\boldsymbol{r},t), \tag{2.25}$$

respectively. In conjunction with the Lorentz condition (Eq. (2.23)), Maxwell's equations in the potential form can also be expressed as equivalent wave equations.

$$\frac{1}{c^2}\frac{\partial^2}{\partial t^2}\Phi(\boldsymbol{r},t) - \nabla^2\Phi(\boldsymbol{r},t) = \frac{\rho(\boldsymbol{r},t)}{\varepsilon} \tag{2.26}$$

$$\frac{1}{c^2}\frac{\partial^2}{\partial t^2}\boldsymbol{A}(\boldsymbol{r},t) - \nabla^2\boldsymbol{A}(\boldsymbol{r},t) = \mu\boldsymbol{J}(\boldsymbol{r},t) \tag{2.27}$$

Here, ε and μ are constant in space (homogeneous media). It can be seen that ρ and $\boldsymbol{J}$ are the sources for the potentials Φ and $\boldsymbol{A}$, respectively. Therefore, when these source densities are known, the explicit causal solutions to these wave equations are the retarded potentials, which are defined as

$$\Phi(\boldsymbol{r},t) = \frac{1}{4\pi\varepsilon}\int_V \frac{\rho(\boldsymbol{r'},t_r)}{\mid \boldsymbol{r}-\boldsymbol{r'} \mid} d^3\boldsymbol{r'}, \tag{2.28}$$

$$\boldsymbol{A}(\boldsymbol{r},t) = \frac{\mu}{4\pi}\int_V \frac{\boldsymbol{J}(\boldsymbol{r'},t_r)}{\mid \boldsymbol{r}-\boldsymbol{r'} \mid} d^3\boldsymbol{r'}, \tag{2.29}$$

where $t_r = t - \dfrac{\mid \boldsymbol{r}-\boldsymbol{r'} \mid}{c}$ is the retarded time, $\boldsymbol{r}$ is the observation point in space, $\boldsymbol{r'}$ is the point in the zone of source density, t is the time, and the integration is performed over a localized volume V where ρ and $\boldsymbol{J}$ are non-zero.

Since we are generally interested in single frequencies, one can derive the phasor part of these retarded potentials by performing a Fourier transform on the potentials described above.

$$\Phi(\boldsymbol{r}) = \frac{1}{4\pi\varepsilon}\int_V \frac{\rho(\boldsymbol{r'})}{R} e^{-jkR} d^3\boldsymbol{r'} \tag{2.30}$$

$$\boldsymbol{A}(\boldsymbol{r}) = \frac{\mu}{4\pi}\int_V \frac{\boldsymbol{J}(\boldsymbol{r'})}{R} e^{-jkR} d^3\boldsymbol{r'} \tag{2.31}$$

Here, $R = \mid \boldsymbol{r}-\boldsymbol{r'} \mid$ and free-space wavenumber $k = \dfrac{\omega}{c} = \dfrac{2\pi}{\lambda}$, where λ is the wavelength. To calculate the fields far away from the source in the region referred to as the Fraunhofer zone, i.e., $r \gg r'$ and $r \gg \lambda$, the following far-field approximations are made using Taylor series expansion:

i) $\dfrac{1}{\mid \boldsymbol{r}-\boldsymbol{r'} \mid} \simeq \dfrac{1}{\mid \boldsymbol{r} \mid} = \dfrac{1}{r}$,

ii) $\mid \boldsymbol{r}-\boldsymbol{r'} \mid \simeq r - \boldsymbol{e}_r\cdot\boldsymbol{r'}$.

The far-field approximations of the retarded potentials can now be defined as

$$\Phi(\boldsymbol{r}) = \frac{e^{-jkr}}{4\pi\varepsilon r}\int_V \rho(\boldsymbol{r'})e^{j\boldsymbol{k}\cdot\boldsymbol{r'}}d^3\boldsymbol{r'}, \tag{2.32}$$

$$\boldsymbol{A}(\boldsymbol{r}) = \frac{\mu e^{-jkr}}{4\pi r}\int_V \boldsymbol{J}(\boldsymbol{r'})e^{j\boldsymbol{k}\cdot\boldsymbol{r'}}d^3\boldsymbol{r'}, \tag{2.33}$$

with the wavenumber vector $\boldsymbol{k} = k\boldsymbol{e}_r$. The angular dependence stems from the integral factors, which are essential in understanding the directional properties of the radiated fields. These integral factors are separated from the radial dependence and can be expressed using the charge form-factor $Q(\boldsymbol{k})$ and radiation vector $\boldsymbol{F}(\boldsymbol{k})$ as

$$Q(\boldsymbol{k}) = \int_V \rho(\boldsymbol{r'})e^{j\boldsymbol{k}\cdot\boldsymbol{r'}}d^3\boldsymbol{r'}, \tag{2.34}$$

$$\boldsymbol{F}(\boldsymbol{k}) = \int_V \boldsymbol{J}(\boldsymbol{r'})e^{j\boldsymbol{k}\cdot\boldsymbol{r'}}d^3\boldsymbol{r'}. \tag{2.35}$$

These integrals are the spatial Fourier transformation of the charge and current densities, which depend on $\boldsymbol{k}$ and $\boldsymbol{e}_r$, defined using angular coordinates θ (polar angle), and φ (azimuthal angle). Therefore, the angular dependence can be written using $Q(\theta,\varphi)$ and $\boldsymbol{F}(\theta,\varphi)$ and the radiation potentials can be defined as

$$\Phi(\boldsymbol{r}) = \frac{e^{-jkr}}{4\pi\varepsilon r}Q(\theta,\varphi), \tag{2.36}$$

$$\boldsymbol{A}(\boldsymbol{r}) = \frac{\mu e^{-jkr}}{4\pi r}\boldsymbol{F}(\theta,\varphi). \tag{2.37}$$

The $\boldsymbol{E}$ and $\boldsymbol{H}$ fields can now be calculated using Eq. (2.20) and Eq. (2.18), respectively, in conjunction with the Lorentz condition (Eq. (2.23)). The Fourier transformation replaces $\dfrac{\partial}{\partial t}$ with $j\omega$. Therefore,

$$\begin{aligned}\boldsymbol{E}(\boldsymbol{r}) &= -\nabla\Phi(\boldsymbol{r}) - j\omega\boldsymbol{A}(\boldsymbol{r}) = \frac{1}{j\omega\mu\varepsilon}\Big(\nabla(\nabla\cdot\boldsymbol{A}(\boldsymbol{r})) + k^2\boldsymbol{A}(\boldsymbol{r})\Big),\\ \boldsymbol{H}(\boldsymbol{r}) &= \frac{1}{\mu}\nabla\times\boldsymbol{A}(\boldsymbol{r}).\end{aligned} \tag{2.38}$$

However, using Eq. (2.27) in frequency domain, the $\boldsymbol{E}$ field from above can also be written as

$$\boldsymbol{E}(\boldsymbol{r}) = \frac{1}{j\omega\mu\varepsilon}\Big(\nabla\times\big(\nabla\times\boldsymbol{A}(\boldsymbol{r})\big) - \mu\boldsymbol{J}(\boldsymbol{r})\Big), \tag{2.39}$$

and in the source-free region, Eq. (2.39) can be expressed as

$$\boldsymbol{E}(\boldsymbol{r}) = \frac{1}{j\omega\mu\varepsilon}\nabla\times\big(\nabla\times\boldsymbol{A}(\boldsymbol{r})\big). \tag{2.40}$$

Computing $\nabla \times \boldsymbol{A}$ ignoring all terms that drop faster than $1/r$, the far-fields can be defined as

$$\boldsymbol{E}(\boldsymbol{r}) = -jk\eta \frac{e^{-jkr}}{4\pi r}(\boldsymbol{e}_r \times \boldsymbol{F}(\boldsymbol{r})) \times \boldsymbol{e}_r, \tag{2.41}$$

$$\boldsymbol{H}(\boldsymbol{r}) = -jk \frac{e^{-jkr}}{4\pi r}(\boldsymbol{e}_r \times \boldsymbol{F}(\boldsymbol{r})), \tag{2.42}$$

where $\eta = \dfrac{|\boldsymbol{E}|}{|\boldsymbol{H}|} = \sqrt{\mu/\varepsilon}$ is the wave impedance. Furthermore, the radiation vector can be decomposed in its radial and transversal components as

$$\boldsymbol{F}(\boldsymbol{r}) = \boldsymbol{e}_r(\boldsymbol{e}_r \cdot \boldsymbol{F}(\boldsymbol{r})) + (\boldsymbol{e}_r \times \boldsymbol{F}(\boldsymbol{r})) \times \boldsymbol{e}_r = \boldsymbol{e}_r F_r + \boldsymbol{F}_\perp(\boldsymbol{r}). \tag{2.43}$$

Resolving this in a spherical coordinate system reveals that only the angular components contribute to the transversal part of $\boldsymbol{F}$. Therefore, the fields can be represented using only the transversal components

$$\boldsymbol{E}(\boldsymbol{r}) = -jk\eta \frac{e^{-jkr}}{4\pi r}\boldsymbol{F}_\perp(\boldsymbol{r}), \tag{2.44}$$

$$\boldsymbol{H}(\boldsymbol{r}) = -jk \frac{e^{-jkr}}{4\pi r}(\boldsymbol{e}_r \times \boldsymbol{F}_\perp(\boldsymbol{r})). \tag{2.45}$$

2.2.2 Characteristics of an antenna

To characterize the performance of an antenna, it is necessary to comprehend the meaning of certain essential parameters. These are outlined below.

Radiation pattern

A radiation pattern or antenna pattern is a graphical representation of the antenna's radiation properties as a function of the spatial coordinates [69]. These radiation properties comprise the radiation intensity, power flux density, directivity, field strength, phase, or polarization [29]. Since these patterns are mostly determined in the far-field, they are represented using the directional coordinates, e.g., the spherical coordinate system for a sphere of radius r, polar angle θ, and azimuthal angle φ.

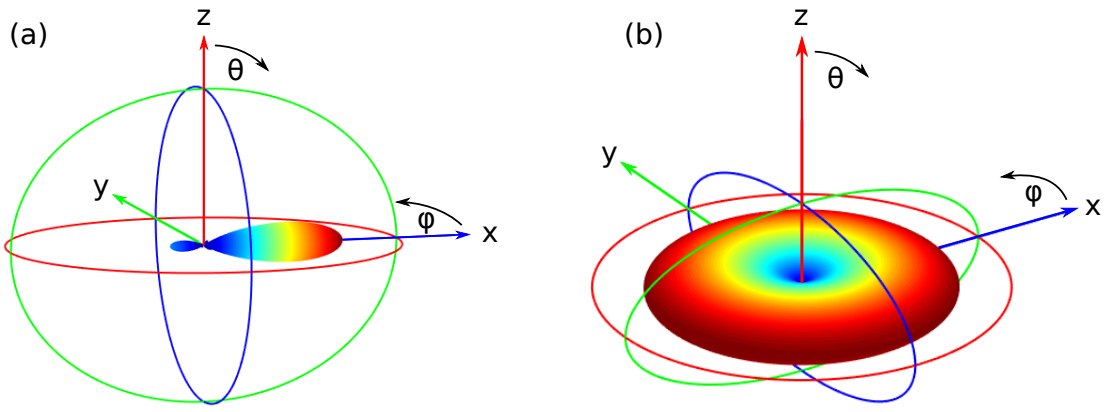

Figure 2.1: Types of radiation patterns in spherical coordinates. The three-dimensional radiation pattern of (a) a directional antenna and (b) an omnidirectional antenna.

Furthermore, there are different types of patterns. A pattern representing an isotropic radiator with equal radiation in all directions is called an isotropic pattern. Hypothetically, it represents a lossless antenna, which is used as the reference for defining the directionality of any antenna under investigation. However, such an antenna cannot be physically realized. On the other hand, a directional pattern has more radiation in some directions than the other directions. Therefore, they represent antennas that efficiently receive and radiate electromagnetic waves in a specific direction (see Figure 2.1a). A particular case for such an antenna is the omnidirectional antenna, as shown in the Figure 2.1b, representing the radiation pattern of a dipole emitter in a homogeneous environment. The pattern shows non-directionality in one plane ($\theta = 90°$) and directionality in the orthogonal plane ($\varphi = 0°$).

Radiation lobes

Radiation patterns are characterized by regions called radiation lobes, which are areas in the radiation pattern bounded by weak radiation intensity [29]. There are two types of radiation lobes: major and minor lobes. The major lobe points towards the maximum radiation, while the minor lobe is any lobe apart from the major lobe. When the minor lobe is in the same hemisphere as the major lobe, it is called a side lobe, and if there is more than one major lobe in the radiation pattern, they are called grating lobes. The side and grating lobes are undesired in a radiation pattern, representing radiation in unwanted directions. The ratio of power density in the side lobe to that of the major lobe is called the side lobe level (SLL). When the minor lobe is in the opposite hemisphere of the major lobe, it is called the back lobe. Furthermore, there are two common measurements used to determine the width of the main lobe, namely,

- Half-power beamwidth (HPBW): measures the angular spread of the beam between two points located at half the power of the peak of the main lobe,
- First-null beamwidth (FNBW): measures the angular spread of the beam between the first

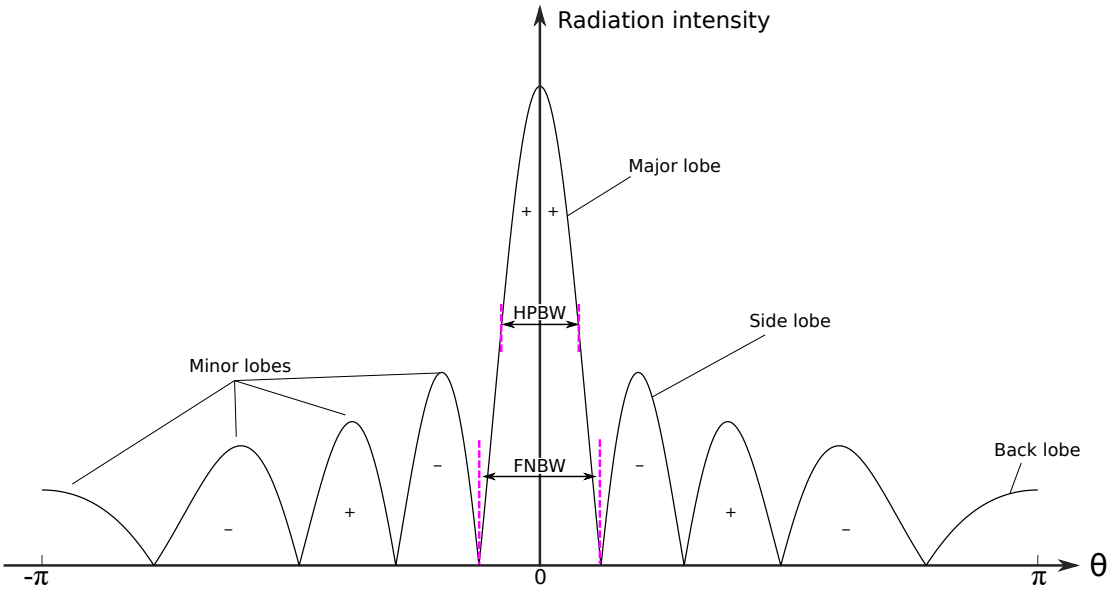

Figure 2.2: Characterization of different radiation lobes and beamwidths.

nulls of the pattern, i.e., the nulls of the main lobe.

Figure 2.2 displays an antenna pattern highlighting the above-described beamwidths and different lobes.

Directive gain and directivity

The term directive gain refers to the ratio of radiation intensity in a specific direction to the radiation intensity averaged over all directions. If the specific direction is the direction of maximum radiation (θ_{max}, φ_{max}), then the maximum directive gain is referred to as the directivity of an antenna. Mathematically, the radiation intensity U can be defined as the power that radiates from the antenna per unit solid angle [29].

$$U = r^2 P_{den}, \tag{2.46}$$

where r is the distance in the far-field and P_{den} is the power density given by the time-averaged Poynting vector,

$$P_{den}(\boldsymbol{r}) = \frac{1}{2}\Re\left(\boldsymbol{E}(\boldsymbol{r}) \times \boldsymbol{H}^*(\boldsymbol{r})\right). \tag{2.47}$$

Integration of the radiation intensity over the complete solid angle of 4π gives the total radiated power,

$$P_{rad} = \int_0^{2\pi} \int_0^{\pi} U(\theta, \varphi) \sin\theta d\theta d\varphi. \tag{2.48}$$

Further, dividing Eq. (2.48) by 4π gives the average radiation intensity, equivalent to the radiation intensity of an isotropic source U_0. Finally, the directive gain D can be defined as

$$D(\theta, \varphi) = \frac{U(\theta, \varphi)}{U_0} = \frac{4\pi U(\theta, \varphi)}{P_{rad}}, \tag{2.49}$$

and the dimensionless quantity, directivity D_{max} can be defined for the maximum radiation intensity U_{max} as

$$D_{max} = D = \frac{U_{max}}{U_0}. \tag{2.50}$$

This quantity can be used in measuring an antenna's ability to direct power in a given direction, thus highlighting its directional properties.

Front-to-back ratio

The front-to-back ratio is an important quantity that is instrumental in quantifying the directional performance of an antenna. It is defined as the ratio of maximum directive gain along the main lobe in the forward direction (θ_{fmax}, φ_{fmax}) to that in the opposite direction (θ_{bmax},$\varphi_{fmax} + 180°$),

$$F/B = \frac{D(\theta_{fmax}, \varphi_{fmax})}{D(\theta_{bmax}, \varphi_{fmax} + 180°)}. \tag{2.51}$$

Antenna gain and radiation efficiency

The antenna's gain can be defined as the ratio of the radiation intensity in a given direction to the input power of the antenna that would radiate isotropically [29]. Mathematically, for a lossless isotropic source, this can be written as

$$G(\theta, \varphi) = \frac{4\pi U(\theta, \varphi)}{P_{in}}. \tag{2.52}$$

However, it is customary to consider the losses of an antenna when calculating the gain G. This can be constituted by taking into account the radiation efficiency of the antenna η_{rad}, which accounts for the conduction and dielectric losses. Therefore, the total radiated power can be expressed using these losses as

$$P_{rad} = \eta_{rad} P_{in}, \tag{2.53}$$

where η_{rad} is the ratio of radiated power to the input power of the system, and it can also be used to relate the directivity and gain of the antenna by substituting Eq. (2.53) in Eq. (2.52)

$$G(\theta, \varphi) = \eta_{rad} \left[\frac{4\pi U(\theta, \varphi)}{P_{rad}} \right] = \eta_{rad} D(\theta, \varphi). \tag{2.54}$$

All of the definitions from above are used frequently in the scope of this work.

2.3 Linear antennas

As it has already been established in Eqs. (2.44)–(2.45), the transversal component $\boldsymbol{F}_{\perp}$ of the radiation vector $\boldsymbol{F}$ is used for determining the radiation pattern of an antenna. The radiation vector, in turn, is defined using the current density $\boldsymbol{J}$. To understand their working principle, we consider a linear antenna that consists of an infinitesimally thin wire of length l with a uniform current distribution $I(z)$ along l aligned to the z-axis, centered at the origin. An illustration of such an antenna can be seen in Figure 2.3.

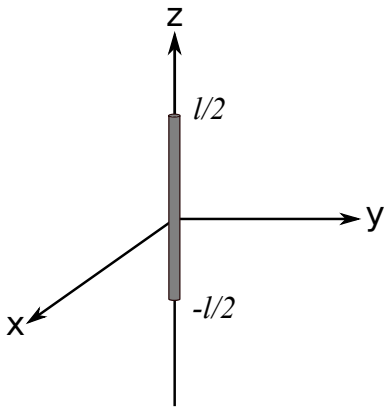

Figure 2.3: Schematic representation of a linear antenna of length l with current distribution along the z-axis.

The antenna possesses a current density of the form

$$\boldsymbol{J}(\boldsymbol{r}) = \begin{cases} I(z)\delta(x)\delta(y)\boldsymbol{e}_z & \text{for} \quad -l/2 \leq z \leq l/2, \\ 0 & \text{elsewhere.} \end{cases} \tag{2.55}$$

Depending on the current distributions, different antennas can be defined. For example:

$$I(z) = Il\delta(z) \qquad \text{Hertzian dipole,}$$
$$I(z) = I\sin(k(l/2 - |z|)) \qquad \text{Linear dipole.}$$

These antenna types are discussed in the following subsections.

2.3.1 Hertzian dipole

One of the simplest linear antennas is the Hertzian dipole, also known as the ideal dipole. Looking at Eq. (2.55), it is clear that the radiation vector in Eq. (2.37) would have only a z-component and for a current distribution of $I(z) = Il\delta(z)$ for a $l \ll \lambda$ and can be defined as

$$\boldsymbol{F}(\boldsymbol{r}) = F_z\boldsymbol{e}_z = \boldsymbol{e}_z \int Il\delta(x')\delta(y')\delta(z')e^{-j(k_x x' + k_y y' + k_z z')}dx'dy'dz'. \tag{2.56}$$

Resolving the wave vector $\boldsymbol{k}$ in a Cartesian coordinate system, the following components can be obtained:

$$k_x = k\cos\varphi\sin\theta \qquad k_y = k\sin\varphi\sin\theta \qquad k_z = k\cos\theta. \tag{2.57}$$

From above, it becomes clear that F_z only depends on θ. Therefore, using k_z from Eq. (2.57), while solving the integrals for x' and y' trivially and for z' over l, F_z from Eq. (2.56) can be written as

$$F_z(\theta) = \int_{-l/2}^{l/2} Il\delta(z')e^{-jkz'\cos\theta}dz' = Il. \tag{2.58}$$

Substituting Eq. (2.58) in Eq. (2.44), the electric far-field can be expressed using the transversal component of the radiation vector as

$$\boldsymbol{E}(r,\theta,\varphi) = -\frac{j\omega\mu}{4\pi}\frac{e^{-jkr}}{r}\int_{-l/2}^{l/2} Il\delta(z')\boldsymbol{e}_{z\perp}e^{-jkz'\cos\theta}dz'. \tag{2.59}$$

The transversal part of the radiation vector can be obtained by resolving $\boldsymbol{e}_z$ in the spherical coordinate system.

$$F_r = \boldsymbol{F}(\boldsymbol{r})\cdot\boldsymbol{e}_r = F_z\boldsymbol{e}_z\cdot\boldsymbol{e}_r = F_z\cos\theta \tag{2.60}$$
$$F_\theta = \boldsymbol{F}(\boldsymbol{r})\cdot\boldsymbol{e}_\theta = F_z\boldsymbol{e}_z\cdot\boldsymbol{e}_\theta = -F_z\sin\theta \tag{2.61}$$
$$F_\varphi = \boldsymbol{F}(\boldsymbol{r})\cdot\boldsymbol{e}_\varphi = F_z\boldsymbol{e}_z\cdot\boldsymbol{e}_\varphi = 0 \tag{2.62}$$

Therefore, the transversal component of the radiation vector only has a θ-component. Substituting that in Eq. (2.59), the final electric and magnetic far-fields can be obtained

$$\boldsymbol{E}(r,\theta,\varphi) = -\frac{j\omega\mu}{4\pi}\frac{e^{-jkr}}{r}\boldsymbol{e}_\theta F_\theta = j\frac{Il}{4\pi r}\eta k\sin(\theta)e^{-jkr}\boldsymbol{e}_\theta, \tag{2.63}$$

$$\boldsymbol{H}(r,\theta,\varphi) = -\frac{j\omega\mu}{4\pi\eta}\frac{e^{-jkr}}{r}\boldsymbol{e}_\varphi F_\theta = j\frac{Il}{4\pi r}k\sin(\theta)e^{-jkr}\boldsymbol{e}_\varphi. \tag{2.64}$$

Furthermore, it can be deduced from Eqs. (2.63)–(2.64) that the fields are omnidirectional, as they do not depend on the azimuthal angle φ (see Figure 2.4b). The radiation intensity can be calculated as

$$U(\theta) = \frac{\eta k^2}{32\pi^2} \mid Il \mid^2 \sin^2\theta. \tag{2.65}$$

Similarly, the directive gain can be obtained using Eq. (2.49)

$$D(\theta) = \frac{4\pi U(\theta)}{\frac{\eta k^2 \mid Il \mid^2}{12\pi}} = \frac{3}{2}\sin^2\theta, \tag{2.66}$$

where $\theta = 90°$ is the direction of maximum propagation, and no propagation takes place along the antenna element itself, i.e., $\theta = 0°$ (see Figure 2.4a). Such structures are commonly utilized as a point source, as they can mimic the behavior of quantum dots that are used in experiments for the purpose of excitation.

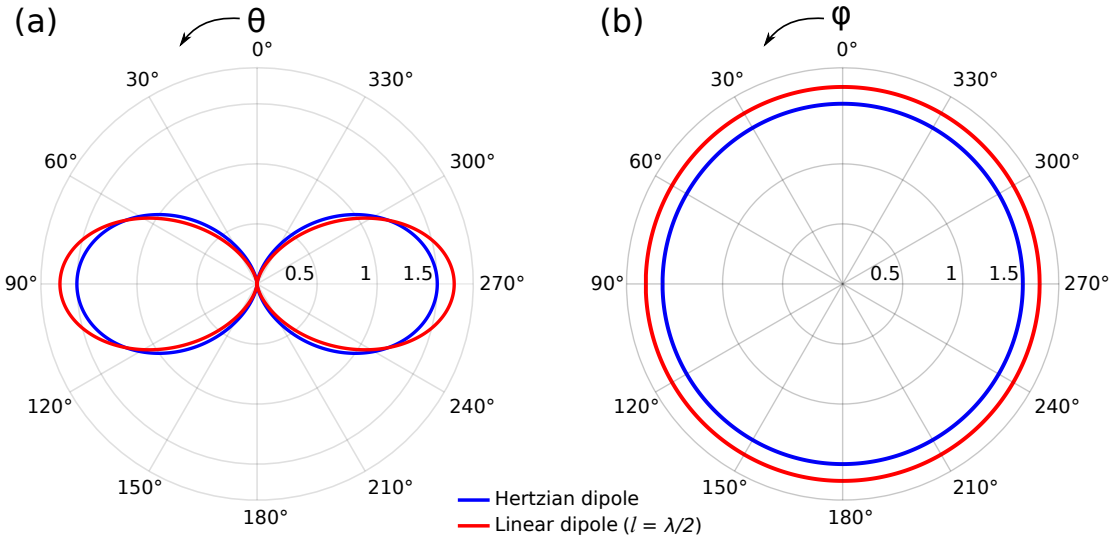

Figure 2.4: Radiation pattern of the Hertzian and linear dipoles as a function of the (a) polar angle θ and (b) azimuthal angle φ. The dipole antenna exhibits slightly higher directivity compared to the Hertzian dipole.

2.3.2 Linear dipole

Another commonly used linear antenna is the linear dipole with a sinusoidal current distribution of $I(z) = I\sin(k(l/2 - |z|))$, as shown in Figure 2.5. This antenna can be viewed as a

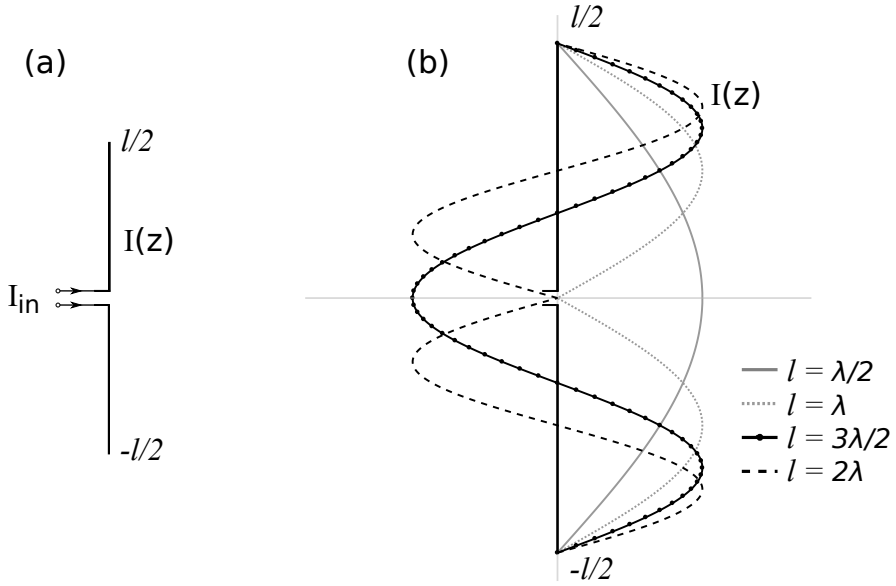

Figure 2.5: (a) Schematic representation of a dipole antenna. (b) Current distribution along the dipole antenna as a function of antenna length.

stack of multiple Hertzian dipoles along the z-axis. Therefore, following a similar workflow as Section 2.3.1, one can obtain the electric and magnetic far-fields by integrating the electric field of the Hertzian dipole over the length of the linear dipole as

$$\boldsymbol{E}(r,\theta,\varphi) = j\frac{I}{2\pi r}\eta k e^{-jkr} f(\theta)\boldsymbol{e}_\theta, \tag{2.67}$$

$$\boldsymbol{H}(r,\theta,\varphi) = j\frac{I}{2\pi r} k e^{-jkr} f(\theta)\boldsymbol{e}_\varphi, \tag{2.68}$$

where $f(\theta) = \dfrac{\cos\left(k\frac{l}{2}\cos(\theta)\right) - \cos\left(k\frac{l}{2}\right)}{\sin(\theta)}$ is the angular-dependent radiation pattern. The radiation pattern for such an antenna with a length of $\lambda/2$ is illustrated in Figure 2.4 along with the radiation pattern of a Hertzian dipole.

2.4 Traveling-wave antennas

The linear dipoles discussed above have a sinusoidal current distribution along the length of the antenna (for $l > 0.1\lambda$) but with a constant phase distribution. For long open-ended linear antennas, the current distribution is characterized by two waves of equal amplitude traveling with a 180° phase shift, which is induced by the reflection at the open end. Such antennas are called standing-wave or resonant antennas [29]. However, terminating the end of the antenna with a suitable impedance, such that the effect of reflection is minimized or eliminated, the current and voltage take the form of traveling waves in the same direction. These antennas are known as traveling-wave or non-resonant antennas [70]. Several structures can be classified as traveling-wave antennas. Starting from the concept of a slot on an infinite conducting plane and extending the analysis to apertures of any desired geometry, one can devise radiating elements

in the form of waveguide-fed slot radiators, open waveguide radiators, horn antennas, and so on. Thus, traveling-wave antennas offer a wide range of radiating elements suitable for applications such as good broadband operation, free space impedance matching, and improved gain [29]. Typically, these antennas can be broadly classified as slow wave or fast wave antennas depending on their phase velocity $v_p = \omega/k$, where ω is wave angular frequency and k is the wave number. Structures with $v_p/c < 1$ are termed as slow wave antennas, and the fast wave antenna possesses a phase velocity of $v_p > c$ [71]. The work in this thesis mainly focuses on the latter, also commonly known as leaky-wave antennas.

A leaky-wave antenna mainly comprises a waveguide with a leaking mechanism, such as a hollow metallic waveguide with a slit. The radiation from such an antenna results from the waves leaking over the length of the non-resonant guiding structure [72]. In the optical regime, dielectrics are preferred over metals due to the high ohmic losses that metals exhibit [12]. Since waveguides are the most vital component of leaky-wave antennas, it is necessary to recapitulate the working principle of a dielectric waveguide. Typically, it consists of a core surrounded by a cladding possessing a refractive index lower than that of the core. The total internal reflection of light causes its confinement in the core, resulting in wave propagation along the length of the core [73].

Consider a waveguide with a finite cross section in the xy-plane. The waveguide is assumed to be constant along the direction of propagation (z-axis), i.e., $\partial_z \varepsilon_r = 0$. The fields can be represented as

$$\begin{pmatrix} \mathbf{E} \\ \mathbf{H} \end{pmatrix} (x, y, z, \omega) = \begin{pmatrix} \mathbf{E}^p \\ \mathbf{H}^p \end{pmatrix} (x, y) \mathrm{e}^{j(\omega t - k_z z)}, \tag{2.69}$$

where $(\mathbf{E}^p, \mathbf{H}^p)^{\mathrm{T}}$ is the mode profile as a function of the transverse coordinates, and k_z is the propagation constant. For regions where $\boldsymbol{J} = 0$ and ε_r is constant, the wave equations can be defined using Eq. (2.69) in Eq. (2.15) and Eq. (2.17)

$$\begin{aligned} \left[\frac{\partial^2}{\partial x^2} + \frac{\partial^2}{\partial y^2} + (k_0^2 \varepsilon_r - k_z^2) \right] \mathbf{E}^p = 0, \\ \left[\frac{\partial^2}{\partial x^2} + \frac{\partial^2}{\partial y^2} + (k_0^2 \varepsilon_r - k_z^2) \right] \mathbf{H}^p = 0, \end{aligned} \tag{2.70}$$

which are a set of partial differential equations that can be solved with appropriate interface and boundary conditions, making it an eigenvalue problem such as

$$\mathsf{T}(k_z)\mathbf{V} = 0. \tag{2.71}$$

T is the system matrix that depends upon k_z and $\mathbf{V}$ denotes the vectorial profile or field. Solutions to this eigenvalue problem (2.71) are the modes this structure can support.

Using (2.69), one can obtain the transverse components, namely, E_x, E_y, H_x, and H_y utilizing the longitudinal electric and magnetic field components, i.e., E_z and H_z. Therefore, only 2-D partial differential equations must be solved for E_z and H_z.

$$\begin{aligned} \Delta_{\mathrm{T}} E_z + (k_0^2 \varepsilon_r - k_z^2) E_z = 0 \\ \Delta_{\mathrm{T}} H_z + (k_0^2 \varepsilon_r - k_z^2) H_z = 0 \end{aligned} \tag{2.72}$$

Other field components are directly derived by rewriting Maxwell's equations as

$$\begin{aligned} E_x &= \frac{-j}{k_0^2\varepsilon_r - k_z^2}(k_z\partial_x E_z + \omega\mu_0\partial_y H_z), \\ E_y &= \frac{-j}{k_0^2\varepsilon_r - k_z^2}(k_z\partial_y E_z - \omega\mu_0\partial_x H_z), \\ H_x &= \frac{-j}{k_0^2\varepsilon_r - k_z^2}(k_z\partial_x H_z - \omega\varepsilon_0\varepsilon_r\partial_y E_z), \\ H_y &= \frac{-j}{k_0^2\varepsilon_r - k_z^2}(k_z\partial_y H_z + \omega\varepsilon_0\varepsilon_r\partial_x E_z). \end{aligned} \tag{2.73}$$

Different types of modes can now be classified with respect to the longitudinal field components [74]:

- $H_z = 0$, $E_z \neq 0$: Transverse magnetic (TM) modes, where the magnetic field components are orthogonal to the direction of propagation.
- $E_z = 0$, $H_z \neq 0$: Transverse electric (TE) modes, where the electric field components are orthogonal to the direction of propagation.
- $E_z = H_z = 0$: Transverse electromagnetic (TEM) modes, where the electric and magnetic field components are orthogonal to the direction of propagation, which is only possible when $k_0^2\varepsilon_r - k_z^2 = 0$.
- $H_z \neq 0$, $E_z \neq 0$: Hybrid modes, where all the six field components are non-zero. Furthermore, depending on whether the electric or magnetic field component is dominant, they can be further classified as TM-like (HE) or TE-like (EH) modes.

Now, consider the dielectric waveguide represented in Figure 2.6 with the refractive index n_1 and surrounded by a homogeneous medium (n_s = n_2). The Helmholtz equation is expressed for

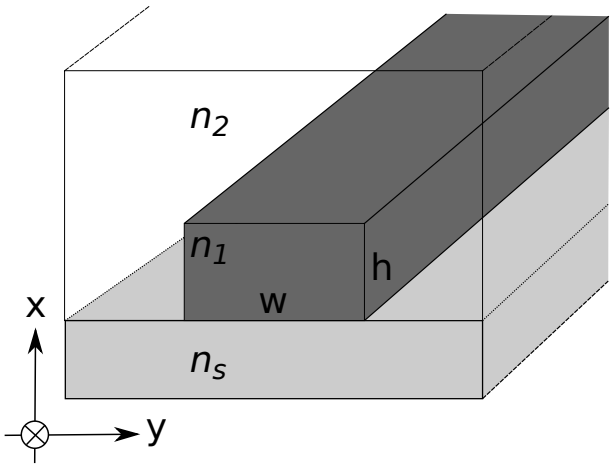

Figure 2.6: Schematic representation of a dielectric waveguide with refractive indices n_1, n_2, n_s, height h, width w, and direction of wave propagation along the z-axis.

both regions as

$$\begin{aligned} &\text{(Core)} \quad \left[\frac{\partial^2}{\partial x^2} + \frac{\partial^2}{\partial y^2} + (n_1^2 k_0^2 - k_z^2)\right] \mathbf{\Psi} = 0, \\ &\text{(Cladding)} \quad \left[\frac{\partial^2}{\partial x^2} + \frac{\partial^2}{\partial y^2} + (n_2^2 k_0^2 - k_z^2)\right] \mathbf{\Psi} = 0, \end{aligned} \tag{2.74}$$

where $\mathbf{\Psi}(x, y, z, \omega) = \mathbf{\Psi}(x, y)\mathrm{e}^{j(\omega t - k_z z)}$ is the solution to the problem described above. Such a dielectric waveguide supports a discrete finite set of modes that are distinguished by their polarization and propagation constant. Typically, a mode is expected to decay outside the core exponentially. Therefore, for the cladding expression, $n_2^2 k_0^2 - k_z^2$ should be negative, implying that the mode propagation constant k_z should be larger than the cladding wavenumber $n_2 k_0$. On the other hand, for the mode to be guided, the propagation constant should satisfy the condition $n_2 k_0 < k_z < n_1 k_0$.

To understand the leaking mechanism of a leaky-wave antenna, consider a substrate with refractive index $n_s \neq n_2$. The substrate in contact with the waveguide serves as a channel for leakage. This implies that when $k_z < n_s k_0$, the leaking wave couples to a radiating mode in the substrate, which behaves as the antenna aperture of the leaky-wave antenna [75]. This is analogous to a slit introduced in a metallic waveguide. In both these cases, the propagation of waveguide modes is significantly influenced. With respect to the surface normal of the waveguide, the direction of the main lobe θ_{ML} for such a system can be determined from

$$|\sin(\theta_{ML})| \approx k_z / k_s, \tag{2.75}$$

where $k_s = n_s k_0$ is the wavenumber of the substrate to which the antenna radiates. Furthermore, the radiation pattern depends on the modes excited in the waveguide (TE/TM/Hybrid). The waveguiding structure's radiation losses and finite length can account for the side lobes in the pattern.

2.4.1 Diffraction gratings

A set of periodic or aperiodic reflecting or transmitting elements characterized by the modulation of refractive index in the spatial domain are called diffraction gratings [76]. A monochromatic wave incident on such an arrangement undergoes diffraction, resulting in a finite set of diffracted waves that travel in discrete directions. Consider a reflection-type grating with a pitch d presented in Figure 2.7a, where a monochromatic wave with a wavelength of λ is incident on the grating at an angle α and is diffracted along a set of discrete angles β_m, where m is referred to as the diffraction order. Consequently, the wave diffracted from each groove along a specific direction is in phase with the diffracted waves generated from other grooves along the same direction, i.e., the waves constructively interfere.

Looking at Figure 2.7b, one can derive the differential path length between adjacent grooves as $d\sin\alpha + d\sin\beta$ for $\beta < 0$. For the crests and troughs of the waves to coincide, i.e., for constructive interference to occur, the differential path length has to be an integral multiple of the wavelength λ. This condition is known as the grating equation and is given by

$$m\lambda = d\sin\alpha + d\sin\beta. \tag{2.76}$$

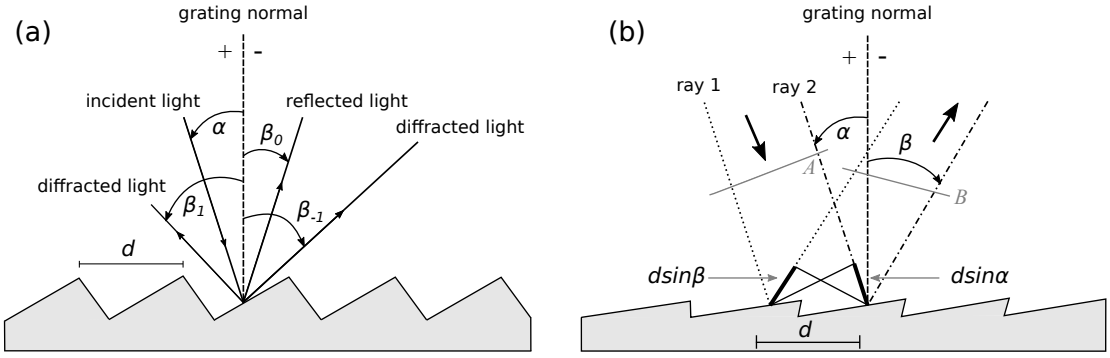

Figure 2.7: Schematic representation of (a) the working principle in diffraction gratings and (b) the geometrical path difference between light from adjacent grooves.

Clearly, the right-hand side of this expression cannot exceed the value of $2d$. Hence, the number of diffraction orders can be determined by the maximum integer value of m that satisfies the condition

$$|m\lambda/d| < 2. \tag{2.77}$$

Notably, waveguide-fed grating couplers and antennas rely on diffraction gratings to radiate the incident power along a desired direction. In such applications (given $\alpha = 90°$), it is sometimes desired to have near vertical emission, i.e., $\beta_0 = 0°$. Using the grating equation, it can be concluded that the second-order diffraction would reflect energy into the feeding waveguide ($\because \beta_2 = 90°$), which is an unwanted effect and results in loss of power. Therefore, most systems aiming for high efficiency employ gratings with a detuned grating pitch such that the emission angle is nearly broadside with no second-order diffraction. A possible way to circumvent the process of detuning is to use a varied grating pitch, i.e., a set of distinct grating pitches $\{d_1, d_2, ..., d_n\}$ that result in a constructive interference pattern along the broadside direction.

2.5 Antenna arrays

By using single linear antenna elements, we can regulate the radiation pattern in the θ-direction. However, to have control in the azimuthal plane, multiple antenna elements can be utilized in what is referred to as an antenna array [29]. These arrays can be arranged uniformly (linear or planar) or non-uniformly, and depending on the desired radiation characteristics, can be designed or synthesized in the appropriate configuration. Further details on this will be discussed in the following subsections.

2.5.1 Linear antenna arrays

The first array topology under investigation is a uniform linear array. A linear array is defined by a set of radiating elements placed along a line or a plane. The term uniform is introduced when the distance between each antenna is constant, commonly referred to as the pitch or inter-element spacing d. The analysis of uniform linear arrays begins with studying the influence of an antenna with a known radiation pattern placed near an identical antenna with an excitation of equal magnitude but with a phase shift. The results of this analysis are extended to an array topology with N such elements along a line, followed by a configuration with $N \times M$ elements in a plane.

2.5.1.1 Two-element array

Let us first consider an array with two elements, specifically linear dipole antennas, as described in Section 2.3.2. The antennas are placed along the x-axis with a separation of d between them. The antennas are driven by current $I\angle 0$ and $I\angle\alpha$, where α is the phase shift provided to the second antenna. The far-field of the array is evaluated at a point P, located at a distance r, as shown in the Figure 2.8.

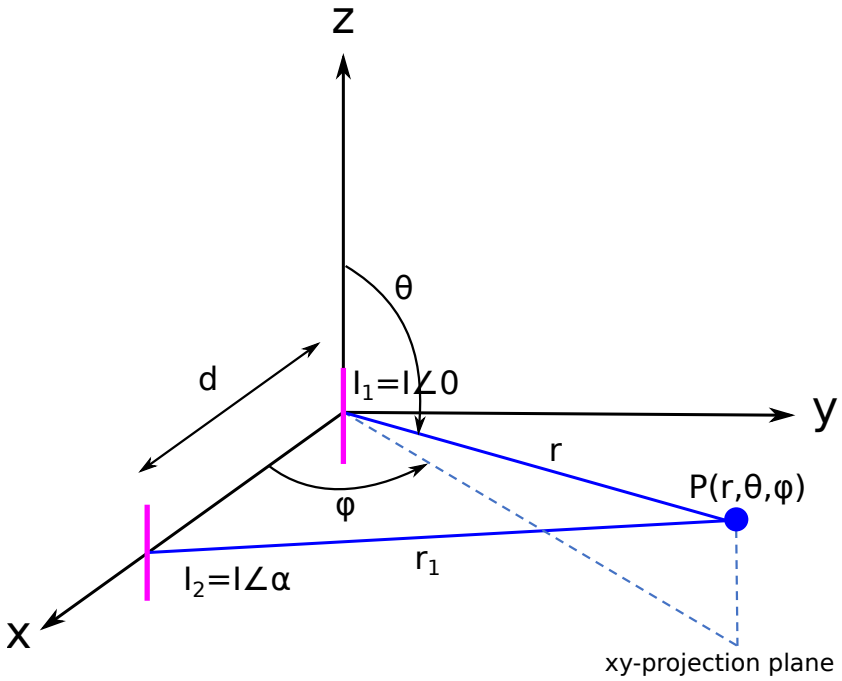

Figure 2.8: Schematic representation of an array with two dipole antennas along the x-axis.

In the far-field $r \parallel r_1$, implying that $r_1 \approx r - d\sin\theta\cos\varphi$. The electric far-field from antenna 1 can be defined as

$$\boldsymbol{E_1}(P) = j\eta\frac{I\angle 0}{2\pi r}f(\theta)e^{-jkr}\boldsymbol{e}_\theta, \tag{2.78}$$

where $f(\theta)$ is the angular-dependent radiation pattern of a linear dipole described before in Section 2.3.2. Similarly, for the second antenna, the electric far-field can be defined as

$$\boldsymbol{E_2}(P) = j\eta\frac{I\angle\alpha}{2\pi r_1}f(\theta)e^{-jkr_1}\boldsymbol{e}_\theta. \tag{2.79}$$

We can assume $r_1 \approx r$, with negligible error in the denominators. Therefore, the sum of the individual fields gives the total field with respect to both antennas at point P.

$$\boldsymbol{E}(P) = \boldsymbol{E_1}(P) + \boldsymbol{E_2}(P) = j\eta\frac{I}{2\pi r}f(\theta)\left(e^{-jkr} + e^{-jkr_1}e^{j\alpha}\right)\boldsymbol{e}_\theta \tag{2.80}$$

$$\boldsymbol{E}(P) = j\eta\frac{I}{2\pi r}f(\theta)\left(e^{-jkr} + e^{-jk(r-d\sin\theta\cos\varphi)}e^{j\alpha}\right)\boldsymbol{e}_\theta \tag{2.81}$$

$$\boldsymbol{E}(P) = j\eta\frac{I}{2\pi r}f(\theta)e^{-jkr}(1 + e^{jkd\sin\theta\cos\varphi}e^{j\alpha})\boldsymbol{e}_\theta \tag{2.82}$$

From the Eqs. (2.80)–(2.82), it is clear that the total field of the array is equivalent to the product of the field from a single antenna and a scalar factor known as the array factor, which is a function of θ and φ

$$\boldsymbol{E}(P) = j\eta\frac{I}{2\pi r}f(\theta)e^{-jkr}AF(\theta,\varphi)\boldsymbol{e}_\theta, \tag{2.83}$$

with

$$AF(\theta,\varphi) = (1 + e^{jkd\sin\theta\cos\varphi}e^{j\alpha}). \tag{2.84}$$

This is also referred to as the principle of pattern multiplication, whose general representation is illustrated in Figure 2.9.

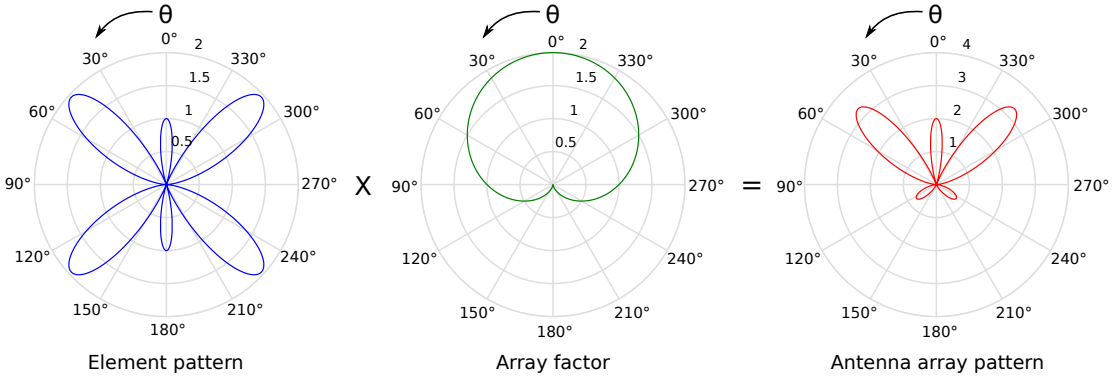

Figure 2.9: Illustration of the principle of pattern multiplication. The product of the patterns from a single antenna and the array factor produces the radiation pattern of the antenna array.

2.5.1.2 1-D arrays

The previous section shows how the array factor looks for a two-element array from Eq. (2.84). In the equation, the first element is the contribution of the element placed at the origin of the coordinate system, and the second term appears due to the second antenna placed at a distance d from the origin. The same can be deduced for a three- and four-element array, and the corresponding array factors can be expressed as

$$AF(\theta,\varphi) = (1 + e^{jkd\sin\theta\cos\varphi+j\alpha} + e^{jk2d\sin\theta\cos\varphi+j2\alpha}), \tag{2.85}$$

$$AF(\theta,\varphi) = (1 + e^{jkd\sin\theta\cos\varphi+j\alpha} + e^{jk2d\sin\theta\cos\varphi+j2\alpha} + e^{jk3d\sin\theta\cos\varphi+j3\alpha}). \tag{2.86}$$

Now consider an array of $(N+1)$-elements placed along the x-axis and separated by a distance d with a progressive phase shift of $nd\alpha$, where n represents the index of each array element. Figure 2.10 illustrates such a configuration, whose array factor can be expressed as

$$AF(\theta,\varphi) = \sum_{n=0}^{N} e^{jnd\alpha+jkn d\cos\psi}, \tag{2.87}$$

where $\cos\psi = \sin\theta\cos\varphi$. This expression can be evaluated as a standard geometric series

$$AF(\theta,\varphi) = \frac{1 - e^{j(N+1)(\alpha+k\cos\psi)d}}{1 - e^{j(\alpha+k\cos\psi)d}}, \tag{2.88}$$

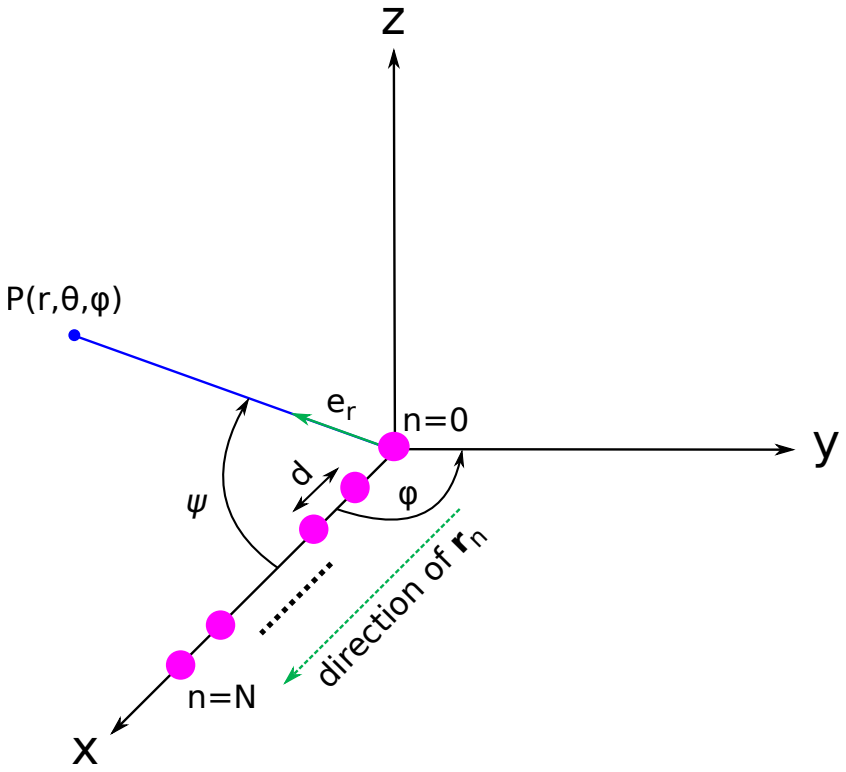

Figure 2.10: Schematic representation of a 1-D array of dipole antennas along the x-axis.

that can be deduced to

$$AF(\theta,\varphi) = e^{jN(\alpha+k\cos\psi)\frac{d}{2}}\left(\frac{e^{-j(N+1)(\alpha+k\cos\psi)\frac{d}{2}} - e^{j(N+1)(\alpha+k\cos\psi)\frac{d}{2}}}{e^{-j(\alpha+k\cos\psi)\frac{d}{2}} - e^{j(\alpha+k\cos\psi)\frac{d}{2}}}\right). \tag{2.89}$$

Therefore, the array factor can finally be written as

$$AF(\theta,\varphi) = e^{jN(\alpha+k\cos\psi)\frac{d}{2}}\left(\frac{\sin\left((N+1)(\alpha+k\cos\psi)\frac{d}{2}\right)}{\sin\left((\alpha+k\cos\psi)\frac{d}{2}\right)}\right). \tag{2.90}$$

Defining $u = kd\cos\psi$ and $u_0 = \alpha d$, we can express Eq. (2.90) as,

$$\mid AF(u) \mid = \left|\frac{\sin\left((N+1)\left(\frac{u+u_0}{2}\right)\right)}{\sin\left(\frac{u+u_0}{2}\right)}\right|. \tag{2.91}$$

To see the effect of the array factor $AF(u)$ on the final radiation pattern, we explore the influence of the number of elements constituting the array, the array's inter-element spacing (pitch), and the phase distribution along the array elements. For this analysis, we consider a linear array along the x-axis.

Figure 2.11 shows the influence of the number of elements in an array for an inter-element spacing of $\lambda/2$. As the number of elements in the array increases, the resulting main lobe is

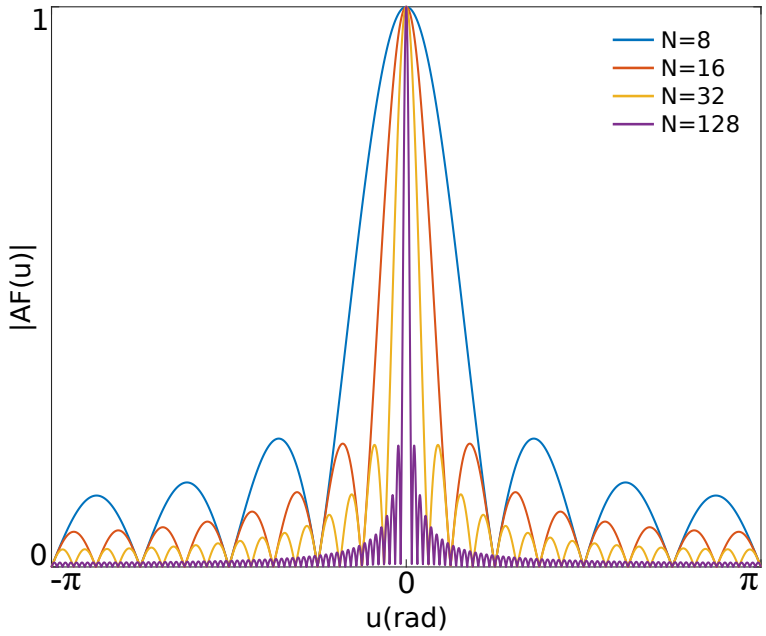

Figure 2.11: Illustration of the influence of the number of elements (N) constituting the array with an inter-element spacing of $\lambda/2$.

substantially narrowed with a higher number of side lobes. However, the side lobe level remains relatively constant for array configurations with elements $N \geq 8$ [29].

Figure 2.12 details the influence of the pitch on the far-field radiation pattern for an 8-element array along the x-axis. As it can be seen, when $d = \lambda/4$, the resultant radiation pattern illustrates a single broad main lobe in addition to two side lobes. Increasing the pitch to $\lambda/2$ narrows the main lobe with more side lobes. Interestingly, for inter-element spacing greater than $\lambda/2$, in addition to the main lobe narrowing and increased number of side lobes, the radiation patterns exhibit distinctive lobes with the same magnitude as the main lobe. These lobes are referred to as the grating lobes. This becomes evident from Figure 2.12c and d, which reveal two and four grating lobes for $d = \lambda$ and $d = 2\lambda$, respectively.

Note that no phase distribution was considered for the radiating elements to analyze the effect of pitch size and the number of elements in the array. However, considering the effect of having a progressive phase distribution among the array elements results in steering the main lobe to a desired direction [77]. Figure 2.13 demonstrates the principle of beam steering for the array with eight elements placed along the x-axis for which $\theta = 90°$. Figure 2.13a shows the radiation pattern for an array with $d = \lambda/2$ when no phase distribution is provided. Intuitively, the main lobe is along $\varphi = 90°$. Furthermore, Figure 2.13b and c demonstrate the steering of the beam by $+30°$ or $-30°$ from the previous case of $\varphi = 90°$, on providing the appropriate progressive phase shift. This concept is discussed further in Chapter 5.

Furthermore, for generalization, we can define the array factor independent of the array axis and coordinate system by considering a complex excitation of the form $w_n = |w_n|e^{j\phi_n}$ [65].

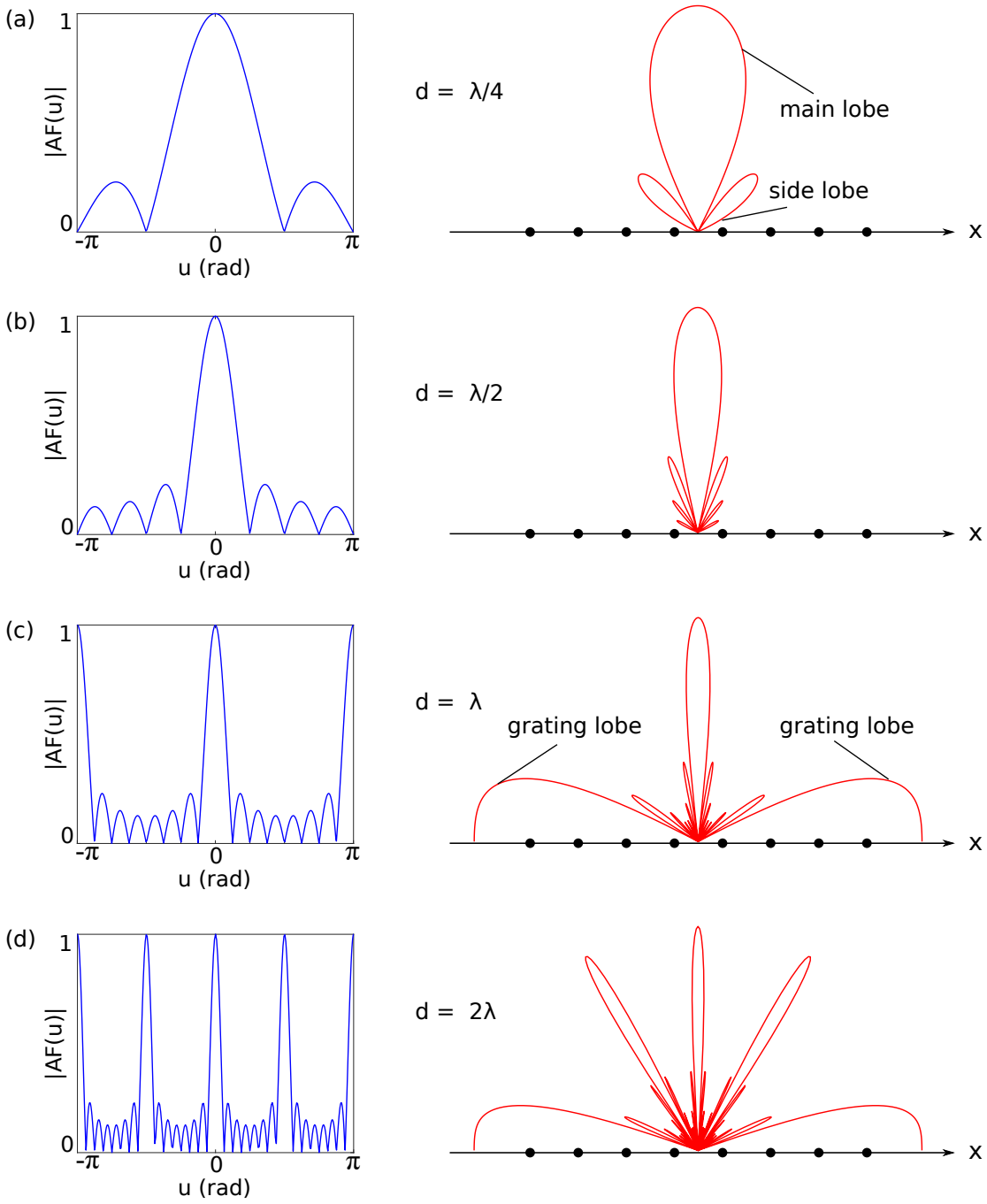

Figure 2.12: Illustration of the influence of inter-element spacing for a linear dipole array of 8 elements. $|\mathrm{AF(u)}|$ and far-field radiation patterns for an array with a pitch of (a) $d = \lambda/4$, (b) $d = \lambda/2$, (c) $d = \lambda$, and (d) $d = 2\lambda$.

Therefore, for an $(N+1)$-element uniform array, the array factor can be defined as

$$AF(\theta, \varphi) = \sum_{n=0}^{N} w_n e^{jk\boldsymbol{e}_r \cdot \boldsymbol{r}_n}, \tag{2.92}$$

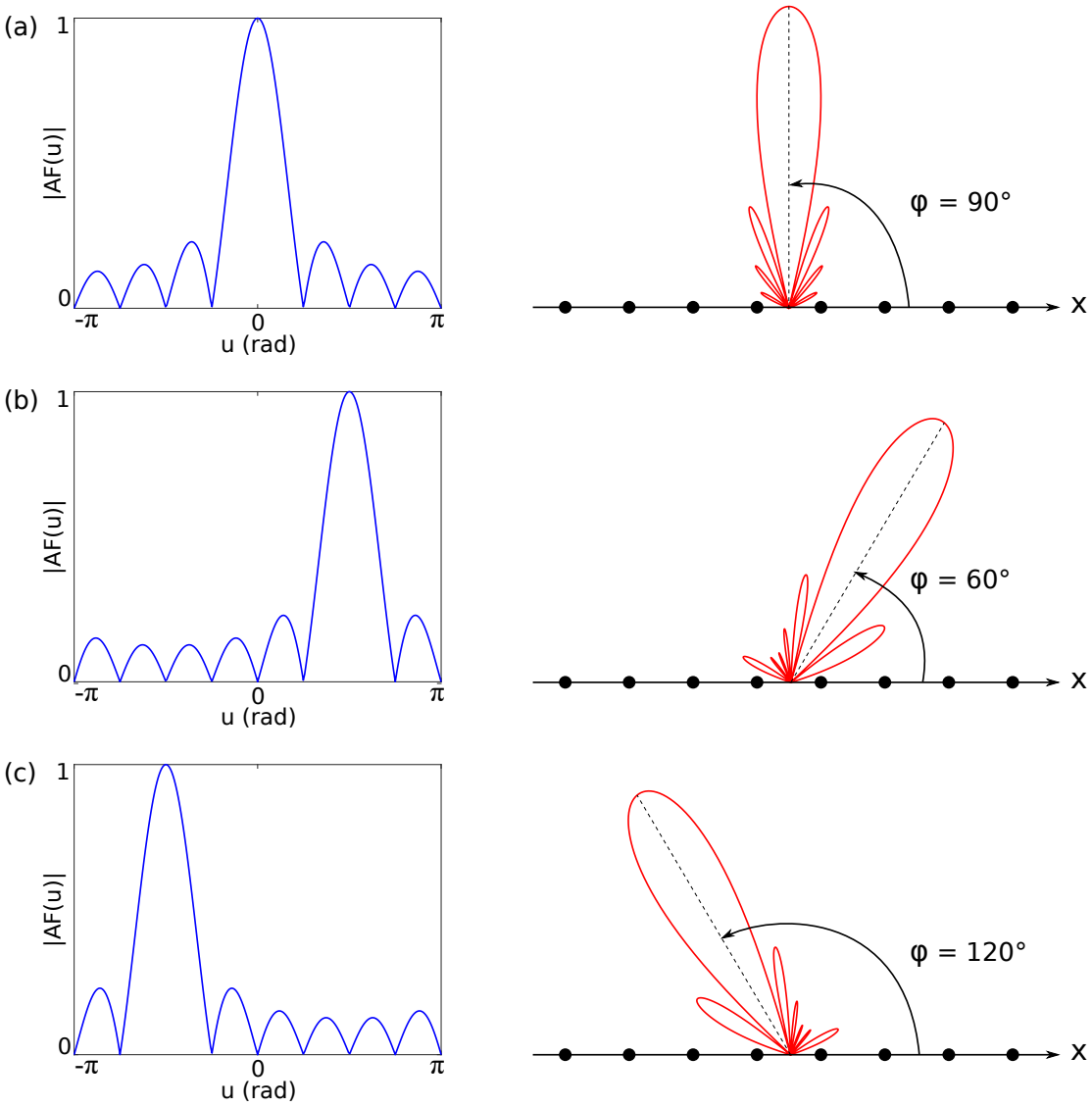

Figure 2.13: Demonstration of beam steering for a linear dipole array of 8 elements with an inter-element spacing of $\lambda/2$. $|\mathrm{AF(u)}|$ and far-field radiation patterns of the beam (a) not steered, (b) steered by $+30°$, and (c) steered by $-30°$.

where $\boldsymbol{e}_r$ is the unit vector in the direction of the point of interest, and $\boldsymbol{r}_n$ is the position vector for the n^{th} element of the array. For our 1-D array along the x-axis, $|w_n| = 1$, $\phi_n = nd\alpha$, $\boldsymbol{r}_n = nd\boldsymbol{e}_x$ and $\boldsymbol{e}_r \cdot \boldsymbol{r}_n = nd\cos\psi = nd\sin\theta\cos\varphi$.

2.5.1.3 2-D arrays

Consider a two-dimensional uniform array in the xz-plane with $(M+1)$-elements along the z-axis and $(N+1)$-elements along the x-axis, as shown in Figure 2.14. This system can be viewed as $(M+1)$ independent linear arrays, each having $(N+1)$ elements. From the previous section, we know the general form of the array factor for a uniform linear antenna array composed of

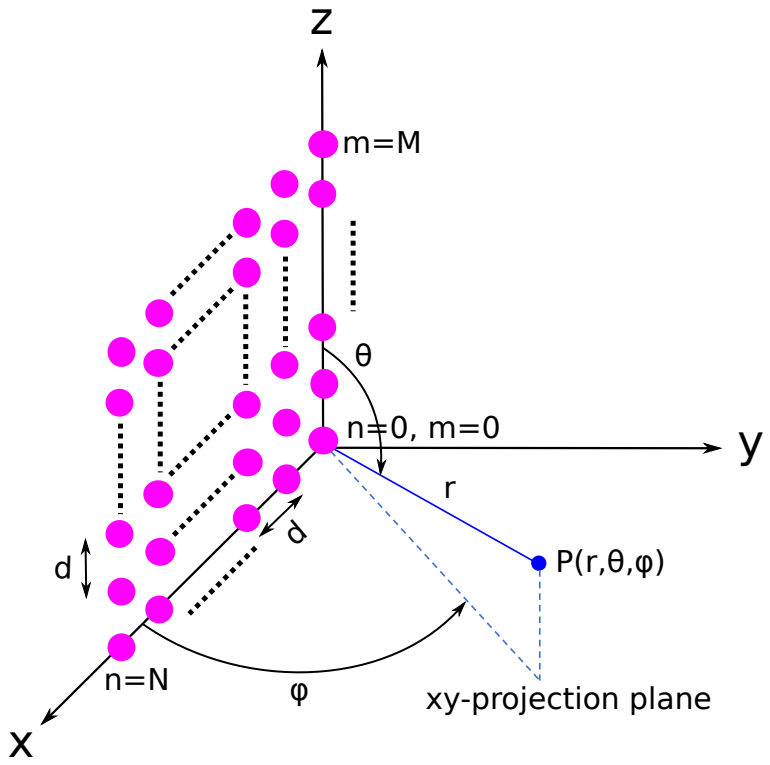

Figure 2.14: Schematic representation of a 2-D array of dipole antennas placed in the xz-plane.

$(N+1)$ elements (Eq. (2.92)). Hence, the principle of pattern multiplication can be applied to the $(M+1)$ linear arrays resulting in a generalized array factor of the form

$$AF(\theta,\varphi) = \sum_{m=0}^{M}\sum_{n=0}^{N} w_{m,n} e^{jk\boldsymbol{e}_r\cdot\boldsymbol{r}_n} e^{jk\boldsymbol{e}_r\cdot\boldsymbol{r}_m}. \tag{2.93}$$

In our problem, all elements are excited with a current of the same magnitude I_0, but with a progressive phase shift of integer multiples of α and β along the x-axis and z-axis, respectively. Additionally, $\boldsymbol{e}_r \cdot \boldsymbol{r}_n = nd\cos\psi = nd\sin\theta\cos\varphi$, with $n \in \{0,1,2,...N\}$ for the $(N+1)$-element array along the x-axis, and $\boldsymbol{e}_r \cdot \boldsymbol{r}_m = md\cos\theta$, with $m \in \{0,1,2,...M\}$ for the $(M+1)$-element array along the z-axis. The resulting expression for the magnitude of the array factor is

$$|AF(\theta,\varphi)| = \left|\frac{\sin\left((N+1)(\alpha+k\sin\theta\cos\varphi)\frac{d}{2}\right)}{\sin\left((\alpha+k\sin\theta\cos\varphi)\frac{d}{2}\right)}\right| \left|\frac{\sin\left((M+1)(\beta+k\cos\theta)\frac{d}{2}\right)}{\sin\left((\beta+k\cos\theta)\frac{d}{2}\right)}\right|. \tag{2.94}$$

Defining $u = kd\sin\theta\cos\varphi, u_0 = \alpha d, v = kd\cos\theta$ and $v_0 = \beta d$, we have

$$|AF(u,v)| = \left|\frac{\sin\left((N+1)\left(\frac{u+u_0}{2}\right)\right)}{\sin\left(\frac{u+u_0}{2}\right)}\right| \left|\frac{\sin\left((M+1)\left(\frac{v+v_0}{2}\right)\right)}{\sin\left(\frac{v+v_0}{2}\right)}\right|. \tag{2.95}$$

When $\alpha = \beta = 0$, the radiation is perpendicular to the plane of the array (broadside). Choosing suitable values of α and β allows one to steer the beam in any desired direction or generate complex far-field patterns. Such an array is called a phased or scanning array.

2.5.2 Circular antenna arrays

Consider a plane wave (Huygens source) impinging on a circular aperture [39], as shown in Figure 2.15a. For uniform apertures, the tangential fields over the aperture also known as the aperture electric and magnetic fields ($\boldsymbol{E}_a, \boldsymbol{H}_a$) are assumed to be constant. The two-dimensional Fourier transform of the aperture electric field is given by

$$\boldsymbol{f}(\theta,\varphi) = \int_A \boldsymbol{E}_a(\boldsymbol{r'})e^{j\boldsymbol{k}\cdot\boldsymbol{r'}}\,dS' = \boldsymbol{E}_a\int_A e^{j\boldsymbol{k}\cdot\boldsymbol{r'}}\,dS' = Af(\theta,\varphi)\boldsymbol{E}_a, \tag{2.96}$$

where A is the area of the aperture and $f(\theta,\varphi) = \frac{1}{A}\int_A e^{j\boldsymbol{k}\cdot\boldsymbol{r'}}\,dS'$ is the radiation pattern of the aperture and is determined by its geometry.

When working with a circular aperture of radius R, the radiation pattern of the aperture can be determined using the cylindrical coordinate system. It is important to note that for evaluating the integral, we can assume $\varphi = 0$, as $f(\theta,\varphi)$ is independent of φ due to the rotational symmetry in the cylindrical coordinates. Hence,

$$f(\theta) = \frac{1}{\pi R^2}\int_{\rho'=0}^{\rho'=R}\int_{\varphi'=0}^{\varphi'=2\pi} e^{jk\rho'\sin\theta\cos\varphi'}\,\rho'\,d\varphi'\,d\rho'. \tag{2.97}$$

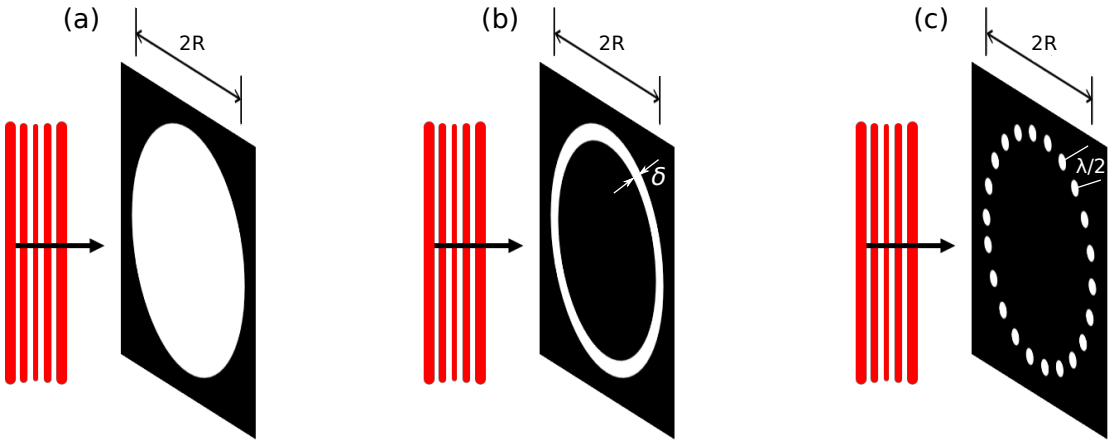

Figure 2.15: Illustration of a plane wave impinging on a (a) circular aperture, (b) ring aperture, and (c) discretized ring aperture.

We know that the zeroth-order Bessel function of the first kind can be defined by

$$J_0(k\rho' \sin\theta) = \frac{1}{2\pi} \int_{\varphi'=0}^{\varphi'=2\pi} e^{jk\rho' \sin\theta \cos\varphi'} \, d\varphi'. \tag{2.98}$$

Substituting Eq. (2.98) in Eq. (2.97), we get

$$\begin{aligned} f(\theta) &= \frac{2}{R^2} \int_{\rho'=0}^{\rho'=R} J_0(k\rho' \sin\theta) \rho' \, d\rho', \\ f(\theta) &= \frac{2}{R^2} \frac{RJ_1(kR\sin\theta)}{k\sin\theta} = \frac{2J_1(kR\sin\theta)}{kR\sin\theta}. \end{aligned} \tag{2.99}$$

Thus, the resulting pattern is a first-order Bessel function analogous to the sinc function, also known as the Airy pattern. The solid blue color line in Figure 2.16 represents $f(\theta, \varphi)$ derived for the circular aperture within the visible region of $-\frac{\pi}{2} \leq \theta \leq \frac{\pi}{2}$. Clearly, the radiation pattern has no grating lobes and an appreciably low side lobe level. Based on these observations, one can derive the radiation pattern of a thin annular ring of thickness δ shown in Figure 2.15b as [39]

$$|f_{ring}(\theta)| = |f_R(\theta) - f_{R-\delta}(\theta)| = 2J_0(kR\sin\theta), \tag{2.100}$$

where $f_R(\theta)$ and $f_{R-\delta}(\theta)$ are the radiation patterns of the circular apertures of radii R and $R - \delta$, respectively. The radiation pattern of such an annular ring is given by the red colored line in Figure 2.16. The side lobe level increases, but this configuration still offers the advantage of no grating lobes in the visible region. Interestingly, a discretized version of such an annular ring aperture realized using point source radiating elements produces a similar radiation profile.

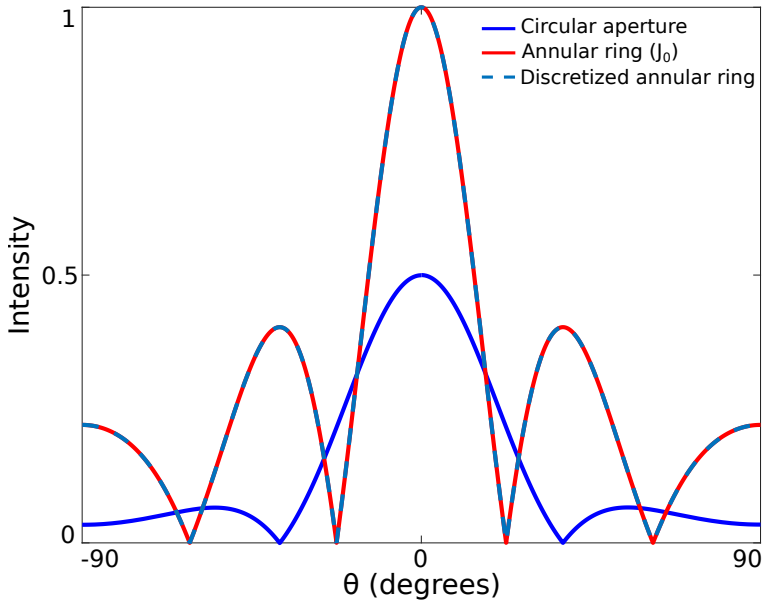

Figure 2.16: Radiation intensity as a function of polar angles for different circular apertures.

Such a setup has each radiating element separated by an arc length offset of $\lambda/2$, as proposed in Figure 2.15c. Therefore, placing radiators in a circular configuration to form an antenna array produces a single main beam and eliminates the presence of grating lobes in the far-field region. Before further investigating such arrays, let us derive the array factor for such an array configuration.

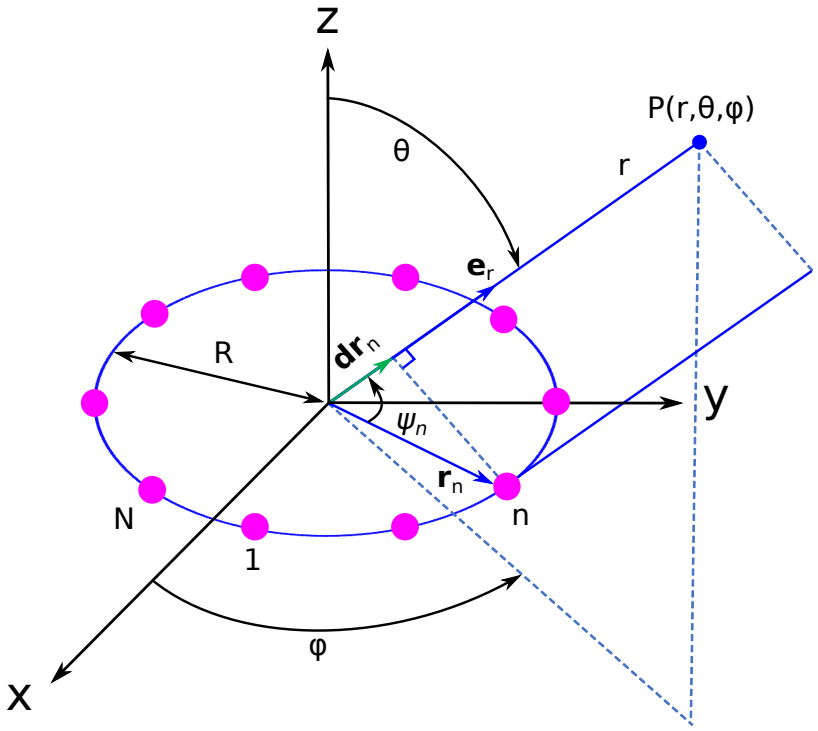

Figure 2.17: Schematic representation of a circular array with one ring of radiating elements.

Consider an N-element circular configuration of antennas in the xy-plane, as shown in Figure 2.17. The array consists of elements with a uniform angular spacing of $\Delta\varphi = 2\pi/N$ in a ring of radius R [29]. The unit vector in the Cartesian coordinate system takes the form

$$\boldsymbol{e}_r = \sin\theta\cos\varphi\boldsymbol{e}_x + \sin\theta\sin\varphi\boldsymbol{e}_y + \cos\theta\boldsymbol{e}_z. \tag{2.101}$$

For the xy-plane, $\theta = 90°$. Hence, the position vector of the n^{th}-element of the array is given by

$$\boldsymbol{r}_n = R\cos\varphi_n\boldsymbol{e}_x + R\sin\varphi_n\boldsymbol{e}_y, \tag{2.102}$$

with $\varphi_n = 2\pi n/N = n\Delta\varphi$, where $n = 1, 2, ...N$. To write the array factor of such an N-element circular array, we first calculate the differential distance $\boldsymbol{dr}_n$ as follows

$$\boldsymbol{dr}_n = (\boldsymbol{e}_r \cdot \boldsymbol{r}_n)\boldsymbol{e}_r = R\cos\psi_n\boldsymbol{e}_r. \tag{2.103}$$

Here,

$$\begin{aligned}\boldsymbol{e}_r \cdot \boldsymbol{r}_n &= (\sin\theta\cos\varphi\boldsymbol{e}_x + \sin\theta\sin\varphi\boldsymbol{e}_y + \cos\theta\boldsymbol{e}_z)\cdot(R\cos\varphi_n\boldsymbol{e}_x + R\sin\varphi_n\boldsymbol{e}_y)\\ &= R\sin\theta(\cos\varphi\cos\varphi_n + \sin\varphi\sin\varphi_n)\\ &= R\sin\theta\cos(\varphi - \varphi_n).\end{aligned} \tag{2.104}$$

Therefore,

$$\boldsymbol{dr}_n = R\sin\theta\cos(\varphi-\varphi_n)\boldsymbol{e}_r, \text{ where } n = 1, 2, ...N. \tag{2.105}$$

Thus, the array factor takes the form

$$AF(\theta,\varphi) = \sum_{n=1}^{N} w_n e^{jkR[\sin\theta\cos(\varphi-\varphi_n)]}. \tag{2.106}$$

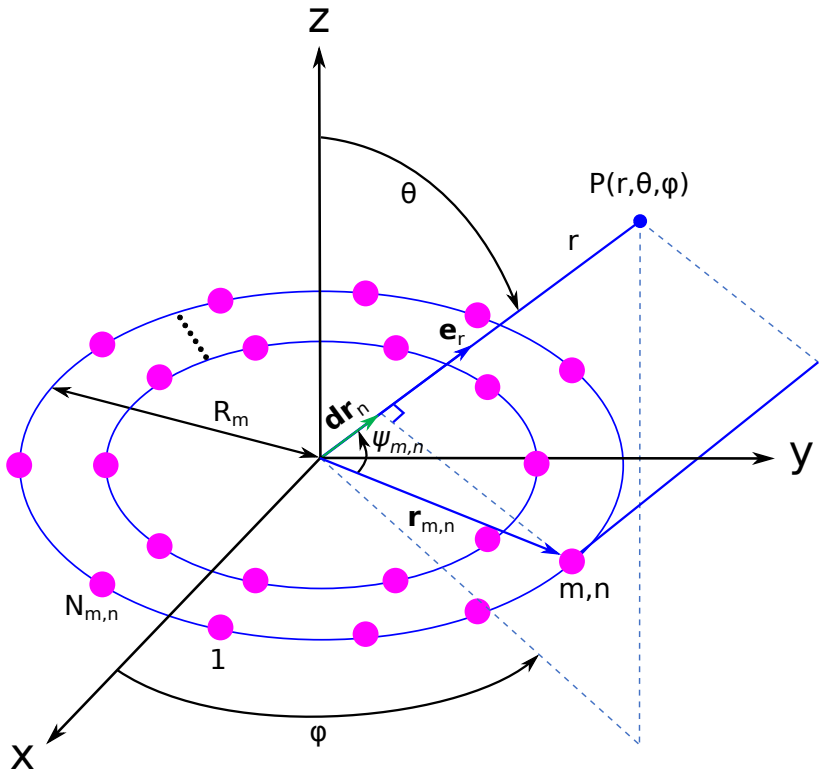

Figure 2.18: Schematic representation of a circular array with multiple rings of radiating elements.

Similarly, consider M concentric circular arrays with N_m elements in each ring, separated by a uniform arc length spacing, as shown in Figure 2.18. For $m \in \{1, 2, ...M\}$, the general form of the array factor can be defined as

$$AF(\theta,\varphi) = \sum_{m=1}^{M}\sum_{n=1}^{N_m} w_{m,n} e^{jkR_m[\sin\theta\cos(\varphi-\varphi_{m,n})-\sin\theta_0\cos(\varphi_0-\varphi_{m,n})]}, \tag{2.107}$$

where $w_{m,n}$ and $\varphi_{m,n} = 2\pi n/N_m$ are the electric field intensity and angular position of the n^{th}-element of the m^{th}-ring, respectively, R_m is the radius of the m^{th}-ring, and (θ_0, φ_0) represents the direction of the main lobe. For more details about such configurations, we refer the readers to Refs. [78, 79]. Overall, the concepts discussed in this chapter lay the foundation for understanding the results explained in this thesis.

Chapter 3

Numerical methods and optimization

Numerical modeling of various wave fields, from elastodynamics, acoustics, electromagnetics, etc., is used in different science disciplines, ranging from communications to medical diagnosis [80]. When it comes to classical electrodynamics, as discussed in Chapter 2, Maxwell's equations, in combination with the constitutive material equations, are used to derive the characteristics of electric and magnetic fields with suitable boundary conditions (BCs). Analytically, these equations can be explicitly solved for simple geometries. However, this becomes impossible for complex systems, making it imperative to solve these problems numerically. Numerical solutions to these problems can avoid the fabrication of several samples with experiments that produce geometries comprehending the simulated results. This helps to design sophisticated technologies with low cost and time.

Several popular techniques are already available that efficiently compute electromagnetic fields for practical applications, like the finite element method (FEM), finite difference time domain method (FDTD), boundary element method (BEM), finite integration technique (FIT), etc. The numerical results of this thesis are mainly produced using CST Microwave Studio [63], a commercial software package implementing the FIT, which Thomas Weiland first proposed in 1977 [81]. This makes it imperative for us to understand the underlying concepts to better analyze our results. This also helps identify computation-generated artifacts coming from the model under investigation and rectify them.

In this chapter, Section 3.1 discusses the fundamentals of the finite integration technique based on Refs. [82, 83]. Within FIT, we show the discretization of Maxwell's equations employed by this method, followed by the discretization of the constitutive material equations. We briefly look at the type of BCs utilized in this work. Furthermore, we explore the integration of transient fields and the numerical stability of FIT. In Section 3.2, we introduce the optimization theory, where we describe the problem to be optimized and the algorithms employed for this task during the course of this work.

3.1 Finite integration technique

Thomas Weiland utilizes the integral form of the Maxwell equations in the FIT, which are transformed into a system of linear algebraic equations called the Maxwell Grid Equations. Generally, based on the problem at hand, integration in the time domain needs to be performed,

or an eigenvalue problem for a linear system needs to be evaluated. Furthermore, the discrete solutions obtained from the method provide the analytical characteristics of the continuous solutions [84].

3.1.1 Discretization of Maxwell's equations

The complete set of Maxwell's equations can mathematically describe all macroscopic electromagnetic phenomena. The FIT uses the integral form of the Maxwell equations, which one can derive from the differential form, i.e., Eqs. (2.1)–(2.4)), using the Gauss's law and Stokes' theorem [1]. Therefore, for stationary matter, Maxwell's integral equations are

$$\oint_{\partial A} \boldsymbol{E}(\boldsymbol{r},t)\cdot d\boldsymbol{l} = -\frac{d}{dt}\int_A \boldsymbol{B}(\boldsymbol{r},t)\cdot d\boldsymbol{A}, \tag{3.1}$$

$$\oint_{\partial A} \boldsymbol{H}(\boldsymbol{r},t)\cdot d\boldsymbol{l} = \frac{d}{dt}\int_A \boldsymbol{D}(\boldsymbol{r},t)\cdot d\boldsymbol{A} + \int_A \boldsymbol{J}(\boldsymbol{r},t)\cdot d\boldsymbol{A}, \tag{3.2}$$

$$\oint_{\partial V} \boldsymbol{D}(\boldsymbol{r},t)\cdot d\boldsymbol{A} = \int_V \rho(\boldsymbol{r},t)dV, \tag{3.3}$$

$$\oint_{\partial V} \boldsymbol{B}(\boldsymbol{r},t)\cdot d\boldsymbol{A} = 0. \tag{3.4}$$

The FIT is based on the discrete reformulation of these integral equations Eqs. (3.1)–(3.4), making them suitable for simulating electromagnetic problems of complex structures on computers [83]. As the technique can be seen as the generalization of the FDTD method [85], similar to the Yee-Cube [86], in general, discretization of the Maxwell equations is done over an orthogonal grid doublet (G,$\widetilde{G}$). Figure 3.1a illustrates the primary grid G and the dual grid $\widetilde{G}$ is defined by taking the foci of all cells from the primary grid as the grid points for the mesh cells in the dual grid (see Figure 3.1b). Therefore, $\widetilde{G}$ is shifted in all directions by half the edge length of G. To begin with the discretization, the electromagnetic field problem needs to be limited to a bounded region in space, i.e., $\Omega \in \mathbb{R}^3$, comprising the region of interest. This is followed by the decomposition of Ω into a finite number of simplicial cells V_i, which yields the primary computational grid G.

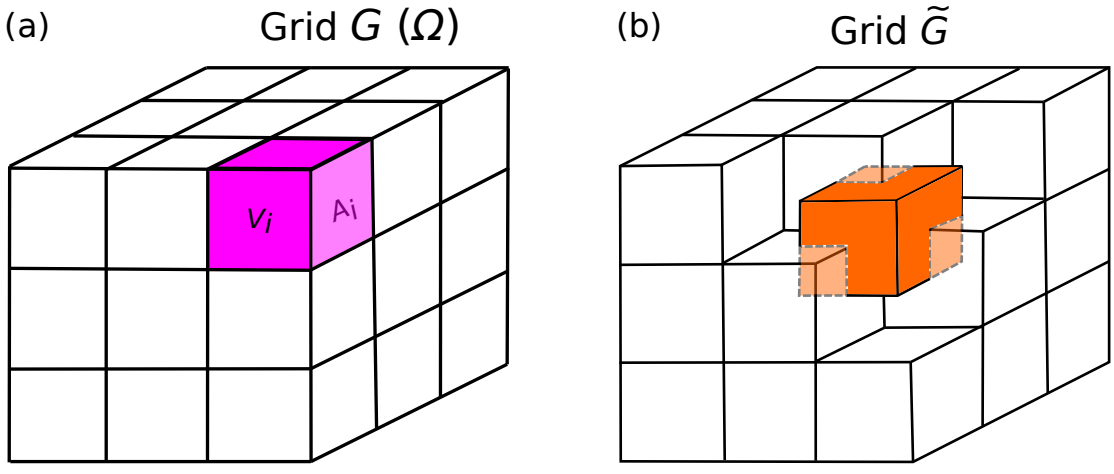

Figure 3.1: Schematic representation of the (a) primary grid G and (b) dual grid $\widetilde{G}$ (in orange) for V_i simplicial cells.

Every edge of the cell V_i possesses a direction, such that a directed graph can describe the union of these edges. Similarly, the facets of all polygons in the grid also possess a direction based on the right-hand rule. Assuming Ω has a brick shape, using the Cartesian coordinate system, G can be defined as

$$\begin{aligned} G := \{V_{i,j,k} \in \mathbb{R}^3 \mid V_{i,j,k} := [x_i, x_{i+1}] \times [y_j, y_{j+1}] \times [z_k, z_{k+1}], \\ i = 1, ..., I-1, j = 1, ..., J-1, k = 1, ..., K-1\}, \end{aligned} \tag{3.5}$$

where the coordinates i, j and k are used for numbering the nodes (x_i, y_j, z_k) along the x-, y- and z- axis, respectively. In total, M_p number of mesh points exist for M_c mesh cells, which are defined as

$$\begin{aligned} M_p &:= I \cdot J \cdot K, \\ M_c &:= (I-1) \cdot (J-1) \cdot (K-1). \end{aligned} \tag{3.6}$$

It is important to note here that the FIT is not limited to Cartesian meshes but can also support other variants of meshes, both structured and unstructured [87, 88]. Now, if we consider only one cell volume V_i of G, as shown in Figure 3.2a, the integral form of Faraday's law in Eq. (3.1) for the facet $A_z(i, j, k)$ (as highlighted by the dark gray region) can be written as

$$\widehat{e}_x(i,j,k) + \widehat{e}_y(i+1,j,k) - \widehat{e}_x(i,j+1,k) - \widehat{e}_y(i,j,k) = -\frac{d}{dt}\widehat{\widehat{b}}_z(i,j,k), \tag{3.7}$$

where $\widehat{e}_x(i,j,k) = \int_{(x_i,y_j,z_k)}^{(x_{i+1},y_j,z_k)} \boldsymbol{E} \cdot d\boldsymbol{l}$ is the electric voltage along one edge of $A_z(i,j,k)$ and $\widehat{\widehat{b}}_z(i,j,k) = \int_{A_z(i,j,k)} \boldsymbol{B} \cdot d\boldsymbol{A}$ is the magnetic flux through the facet $A_z(i,j,k)$. This approach can be applied to every facet of G, and the spatial discretization of the finite cell grid can be achieved.

Furthermore, $\widehat{e}(i,j,k)$ and $\widehat{\widehat{b}}(i,j,k)$ over the complete grid G are lexicographically ordered and assembled in column vectors such that the degrees of freedom occur in the x-, y- and

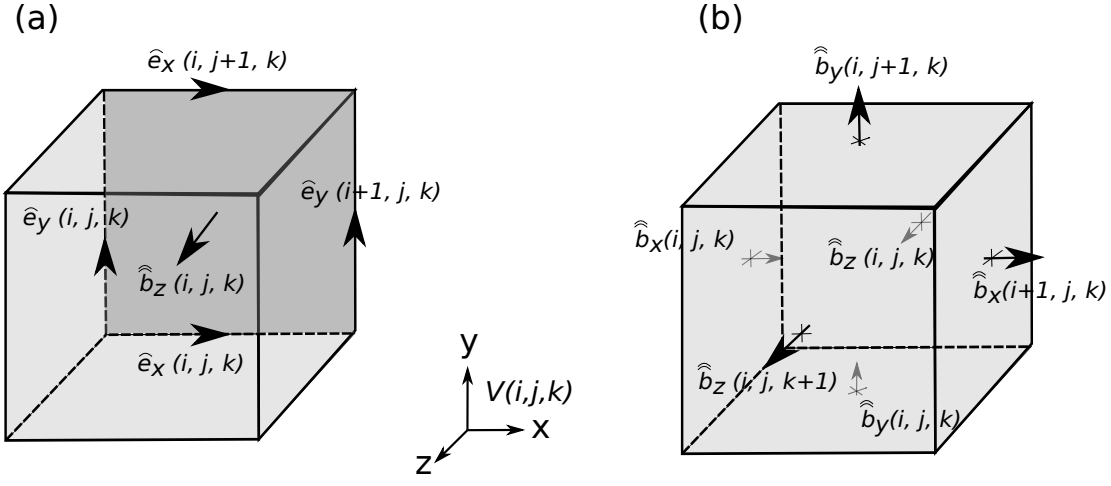

Figure 3.2: Illustration of the (a) magnetic flux $\widehat{\widehat{b}}$ through the facet $A_z(i,j,k)$ and the electric grid voltages $\widehat{e}$ along the edges, and (b) six magnetic facet fluxes for the cell $V_{i,j,k}$ in G.

z-direction, respectively.

$$\begin{aligned}\widehat{\boldsymbol{e}} &:= (\ \widehat{e}_{x,n}\ \mid\ \widehat{e}_{y,n}\ \mid\ \widehat{e}_{z,n}\ )^{\mathsf{T}}_{n=1,\dots,M_p} \in \mathbb{R}^{3M_p} \\ \widehat{\widehat{\boldsymbol{b}}} &:= (\ \widehat{\widehat{b}}_{x,n}\ \mid\ \widehat{\widehat{b}}_{y,n}\ \mid\ \widehat{\widehat{b}}_{z,n}\ )^{\mathsf{T}}_{n=1,\dots,M_p} \in \mathbb{R}^{3M_p}\end{aligned} \tag{3.8}$$

Eq. (3.7) can then be written collectively in the matrix form for the whole grid G as

$$\underbrace{\begin{pmatrix} & \cdots & \cdots & \cdots & & & \\ 1 & \cdots & 1 & \cdots & -1 & \cdots & -1 \\ & \cdots & \cdots & \cdots & & & \end{pmatrix}}_{\boldsymbol{C}:=} \underbrace{\begin{pmatrix} \widehat{e}_{n_1} \\ \vdots \\ \widehat{e}_{n_2} \\ \vdots \\ \widehat{e}_{n_3} \\ \vdots \\ \widehat{e}_{n_4} \end{pmatrix}}_{\widehat{e}} = -\frac{d}{dt} \underbrace{\begin{pmatrix} \vdots \\ \widehat{\widehat{b}}_{n} \\ \vdots \end{pmatrix}}_{\widehat{\widehat{b}}}, \tag{3.9}$$

where $\boldsymbol{C} \in \mathbb{R}^{3M_p \times 3M_p}$ is the discrete curl operator, which has the topological information of the orientation of the cell edges and their incidence relationships in G. Therefore, the matrix coefficients of $\boldsymbol{C}$ are $C_{i,j} \in \{-1, 0, 1\}$. Similarly, to derive the discrete divergence operator, Gauss's law for magnetism from Eq. (3.4) can be reformulated, for the cell V_i represented in Figure 3.2b as

$$\begin{aligned}-\widehat{\widehat{b}}_x(i,j,k) + \widehat{\widehat{b}}_x(i+1,j,k) - \widehat{\widehat{b}}_y(i,j,k) + \widehat{\widehat{b}}_y(i,j+1,k) \\ - \widehat{\widehat{b}}_z(i,j,k) + \widehat{\widehat{b}}_z(i,j,k+1) = 0.\end{aligned} \tag{3.10}$$

As it can be seen, Eq. (3.10) is an exact representation of Eq. (3.4) for the volume under consideration, and extending this again to the whole grid G, we get

$$\underbrace{\begin{pmatrix} & & & \cdots & \cdots & & & \\ . & -1 & 1 & -1 & 1 & -1 & 1 & . \\ & & & \cdots & \cdots & & & \end{pmatrix}}_{\boldsymbol{S}:=} \underbrace{\begin{pmatrix} \vdots \\ \widehat{\widehat{b}}_{n_1} \\ \widehat{\widehat{b}}_{n_2} \\ \widehat{\widehat{b}}_{n_3} \\ \widehat{\widehat{b}}_{n_4} \\ \widehat{\widehat{b}}_{n_5} \\ \widehat{\widehat{b}}_{n_6} \\ \vdots \end{pmatrix}}_{\widehat{\widehat{\boldsymbol{b}}}} = \mathbf{0}, \tag{3.11}$$

where $\boldsymbol{S} \in \mathbb{R}^{M_p \times 3M_p}$ is the discrete divergence matrix, which also holds the topological information like $\boldsymbol{C}$.

To discretize Eqs. (3.2)–(3.3), the dual grid $\widetilde{G}$ is considered, where the magnetic field and dielectric flux are assigned in the same way as the electric grid voltage and magnetic facet flux from G. Therefore, Ampere's law (Eq. (3.2)) can be discretized for a facet $\widetilde{A}_z(i,j,k)$ of a cell

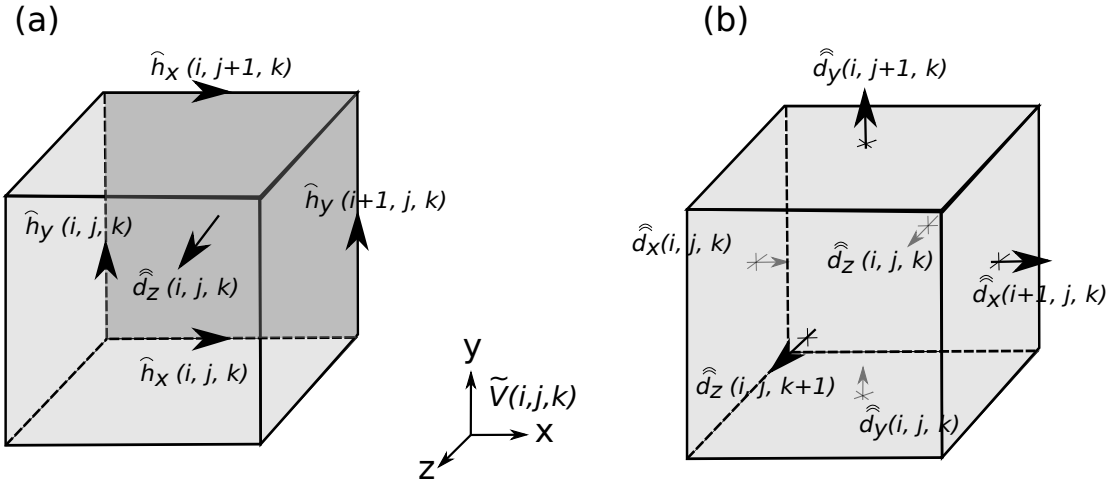

Figure 3.3: (a) A cell $\widetilde{V}_{i,j,k}$ highlighting the dielectric flux $\widehat{\widehat{d}}$ through the facet $\widetilde{A}_z(i,j,k)$ and the magnetic grid voltages $\widehat{h}$ along the edges of the cell. (b) Illustration of the six electric facet fluxes for the cell $\widetilde{V}_{i,j,k}$ in $\widetilde{G}$.

$\widetilde{V}(i,j,k)$ from the dual grid by adding the magnetic grid voltages to get the displacement and conductive currents from the facet under consideration shown in Figure 3.3a.

$$\begin{aligned}\widehat{h}_x(i,j,k) + \widehat{h}_y(i+1,j,k) - \widehat{h}_x(i,j+1,k) - \widehat{h}_y(i,j,k) \\ = \frac{d}{dt}\widehat{\widehat{d}}_z(i,j,k) + \widehat{\widehat{j}}_z(i,j,k)\end{aligned} \tag{3.12}$$

Similarly, Gauss's law (Eq. (3.3)) can be discretized for the cell of the grid $\widetilde{G}$ shown in Figure 3.3b as

$$\begin{aligned}-\widehat{\widehat{d}}_x(i,j,k) + \widehat{\widehat{d}}_x(i+1,j,k) - \widehat{\widehat{d}}_y(i,j,k) + \widehat{\widehat{d}}_y(i,j+1,k) \\ -\widehat{\widehat{d}}_z(i,j,k) + \widehat{\widehat{d}}_z(i,j,k+1) = q(i,j,k).\end{aligned} \tag{3.13}$$

Analogous to Eq. (3.9) and Eq. (3.11), these two new discretizations also result in dual discrete curl and divergence operators $\widetilde{\boldsymbol{C}}$ and $\widetilde{\boldsymbol{S}}$, respectively. Finally, for the grid pair $\{G, \widetilde{G}\}$, the Maxwell grid equations can be summarized as

$$\boldsymbol{C}\widehat{\boldsymbol{e}} = -\frac{d}{dt}\widehat{\widehat{\boldsymbol{b}}}, \tag{3.14}$$

$$\widetilde{\boldsymbol{C}}\widehat{\boldsymbol{h}} = \frac{d}{dt}\widehat{\widehat{\boldsymbol{d}}} + \widehat{\widehat{\boldsymbol{j}}}, \tag{3.15}$$

$$\widetilde{\boldsymbol{S}}\widehat{\widehat{\boldsymbol{d}}} = \boldsymbol{q}, \tag{3.16}$$

$$\boldsymbol{S}\widehat{\widehat{\boldsymbol{b}}} = \boldsymbol{0}. \tag{3.17}$$

3.1.2 Discretization of material equations

Typically, the FIT assumes that each discretized object is made of a piecewise linear, isotropic, and homogeneous material. This produces subdomains as large as the elementary volumes possessing constant material parameters (ε, μ, κ), which is accomplished using the staircase

approximation. To solve a problem, the grid equations discussed above require incorporating the material equations in a similar discrete form (Eqs. (2.8)–(2.9)). Figure 3.4 illustrates the primary area $A_x(i,j,k)$ intersecting with the grid flux $\widehat{\widehat{b}}_x(i,j,k)$ and the intersection of the dual edge $\widetilde{L}_x(i,j,k)$ with the grid voltage $\widehat{h}_x(i,j,k)$. For an inhomogeneous material, the point of intersection lies at the interface of the two materials with permeabilities μ_1 and μ_2, where the normal component of the magnetic flux density B_n is continuous at the interface. This is approximated as

$$\widehat{\widehat{b}}_x(i,j,k) = \iint_{A_x(i,j,k)} \boldsymbol{B} \cdot d\boldsymbol{A} = \iint_{A_x(i,j,k)} B_n(y,z)dydz \approx B_n A_x(i,j,k). \tag{3.18}$$

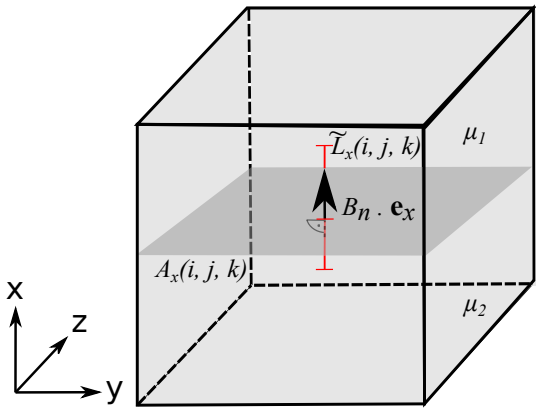

Figure 3.4: Primary surface $A_x(i,j,k)$ and dual edge $\widetilde{L}_x(i,j,k)$ used for the discretization of permeability.

When $\widetilde{L}_x(i,j,k)^{(1)}$ and $\widetilde{L}_x(i,j,k)^{(2)}$ are the dual edges for the material media with permeabilities μ_1 and μ_2, respectively, $\widehat{h}_x(i,j,k)$ can be expressed as

$$\begin{aligned}
\widehat{h}_x(i,j,k) &= \int_{\widetilde{L}_x(i,j,k)} \boldsymbol{H} \cdot d\boldsymbol{l} = \int_{\widetilde{L}_x(i,j,k)^{(1)}} B_n(x)/\mu_1 \, dx + \int_{\widetilde{L}_x(i,j,k)^{(2)}} B_n(x)/\mu_2 \, dx \\
&\approx B_n(\widetilde{L}_x(i,j,k)^{(1)})/\mu_1 + B_n(\widetilde{L}_x(i,j,k)^{(2)})/\mu_2 \\
&= B_n\Big(\widetilde{L}_x(i,j,k)^{(1)}/\mu_1 + \widetilde{L}_x(i,j,k)^{(2)})/\mu_2\Big) \\
&= B_n \overline{\mu^{-1}}(i,j,k)\widetilde{L}_x(i,j,k),
\end{aligned} \tag{3.19}$$

where the inverse permeability is averaged along the dual edge for a local effective material parameter, i.e., $\overline{\mu^{-1}}(i,j,k)$. Therefore, we can obtain $\widehat{\widehat{b}}_x$ as

$$\widehat{\widehat{b}}_x(i,j,k) \approx \underbrace{\frac{A_x(i,j,k)}{\widetilde{L}_x(i,j,k)\overline{\mu^{-1}}(i,j,k)}}_{M_\mu(i,j,k) :=} \widehat{h}_x(i,j,k), \tag{3.20}$$

where $M_\mu(i,j,k)$ is one entry of the diagonal magnetic material matrix $\boldsymbol{M}_\mu$.

Similarly, Figure 3.5 helps visualize the discretization of the permittivity, where the electric flux density D_n is sub-dividing the dual area into four parts of different materials. With this, $\widehat{\widehat{d}}_x$ can be approximated as

$$\begin{aligned}
\widehat{\widehat{d}}_x(i,j,k) &= \iint_{\widetilde{A}_x(i,j,k)} \boldsymbol{D}\cdot d\boldsymbol{A} = \iint_{\widetilde{A}_x(i,j,k)} D_n(y,z)dydz \\
&= \iint_{\widetilde{A}_x(i,j,k)^{(1)}} \varepsilon_1 E_n(y,z)dydz + \iint_{\widetilde{A}_x(i,j,k)^{(2)}} \varepsilon_2 E_n(y,z)dydz \\
&+ \iint_{\widetilde{A}_x(i,j,k)^{(3)}} \varepsilon_3 E_n(y,z)dydz + \iint_{\widetilde{A}_x(i,j,k)^{(4)}} \varepsilon_4 E_n(y,z)dydz \\
&\approx E_n\Big(\varepsilon_1\widetilde{A}_x(i,j,k)^{(1)} + \varepsilon_2\widetilde{A}_x(i,j,k)^{(2)} + \varepsilon_3\widetilde{A}_x(i,j,k)^{(3)} \\
&\quad + \varepsilon_4\widetilde{A}_x(i,j,k)^{(4)}\Big) \\
&= E_n\bar{\varepsilon}(i,j,k)\widetilde{A}_x(i,j,k),
\end{aligned} \tag{3.21}$$

where $\bar{\varepsilon}$ is the mean permittivity. We know that the electric grid voltage is expressed as

$$\widehat{e}_x(i,j,k) = \int_{L_x(i,j,k)} \boldsymbol{E}\cdot d\boldsymbol{l} = \int_{L_x(i,j,k)} E_n(x)dx \approx E_n L_x(i,j,k). \tag{3.22}$$

Therefore, the electric grid flux can be expressed using the electric grid voltages as

$$\widehat{\widehat{d}}_x(i,j,k) \approx \underbrace{\frac{\bar{\varepsilon}(i,j,k)\widetilde{A}_x(i,j,k)}{L_x(i,j,k)}}_{M_\varepsilon(i,j,k):=} \widehat{e}_x(i,j,k), \tag{3.23}$$

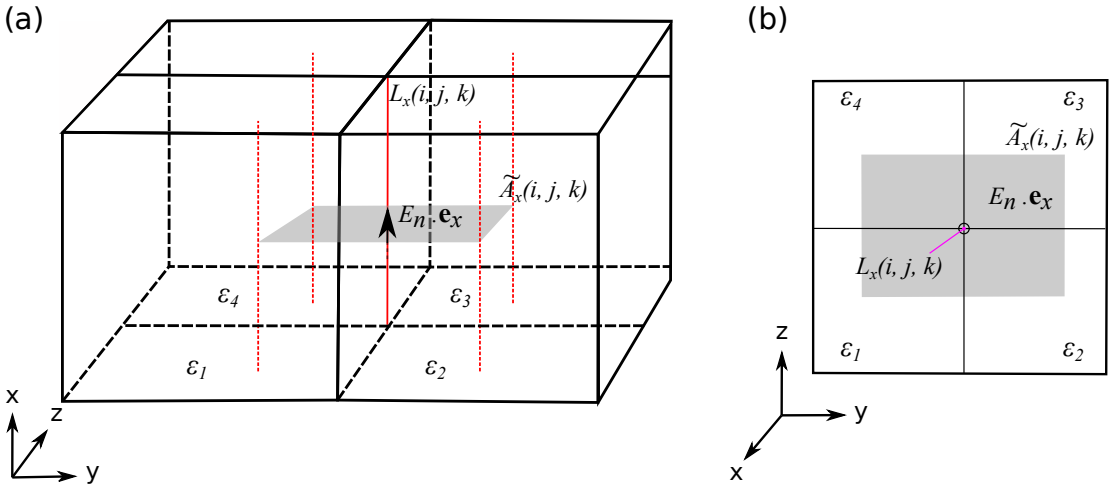

Figure 3.5: Discretization of the permittivity using a dual surface $\widetilde{A}_x(i,j,k)$ and primary edge $L_x(i,j,k)$.

where $M_\varepsilon(i,j,k)$ is one entry of the diagonal permittivity matrix $\boldsymbol{M}_\varepsilon$.

The discrete relationship between the grid current $\widehat{\widehat{j}}_x$ and electric voltage $\widehat{e}_x$ is obtained in a similar manner by utilizing the conductivity κ in place of ε

$$\widehat{\widehat{j}}_x(i,j,k) \approx \underbrace{\frac{\bar{\kappa}(i,j,k)\widetilde{A}_x(i,j,k)}{L_x(i,j,k)}}_{M_\kappa(i,j,k) :=} \widehat{e}_x(i,j,k), \tag{3.24}$$

where $M_\kappa(i,j,k)$ is one entry of the diagonal conductivity matrix $\boldsymbol{M}_\kappa$. Therefore, the discrete material equations can be collectively expressed as

$$\widehat{\widehat{\boldsymbol{d}}} = \boldsymbol{M}_\varepsilon \widehat{\boldsymbol{e}}, \tag{3.25}$$

$$\widehat{\widehat{\boldsymbol{b}}} = \boldsymbol{M}_\mu \widehat{\boldsymbol{h}}, \tag{3.26}$$

$$\widehat{\widehat{\boldsymbol{j}}} = \boldsymbol{M}_\kappa \widehat{\boldsymbol{e}}. \tag{3.27}$$

Furthermore, the material tensors for anisotropic materials can also be expressed in the diagonal form. This will be briefly discussed in Chapter 6.

3.1.3 Boundary conditions

Generally, a computer can deal with calculations of finite problems. This implies that the Maxwell equations must be solved over a finite domain. Therefore, for every problem, defining a relevant boundary condition (BC) for the realistic representation and simulation of the system under investigation becomes customary. Several BCs are available, for example, electric BC, magnetic BC, and periodic BC, but the most widely used BC in this work is the open BC. This BC implements a perfectly matched layer (PML) and extends the geometry in contact to virtual infinity using the PML. Electromagnetic waves can enter this boundary at a broad range of angles and frequencies, with almost no back reflections. The open BC is used to simulate all the optical antennas discussed in this work to characterize their optical properties in the far-field. More details on the PML implemented in FIT are discussed in [89, 90].

3.1.4 Integration of time

The discretized Maxwell's equations are still continuous in time, making it necessary to discretize the time dependence of the fields. This can be done using several methods. For high-frequency problems, where the wavelength of operation and dimensions of the structure of investigation are in the same range, the leapfrog scheme is efficiently employed for the FIT equations, analogous to the FDTD technique [85]. The leapfrog method employs a staggered grid for the discretization in time and the central difference scheme for the time derivatives appearing in Maxwell's equations.

To develop the leapfrog update equations, we begin by defining the central difference approximation of a time derivative as

$$\begin{aligned} f'(t_0 + (m+1/2)\Delta t) &= \frac{f(t_0 + (m+1)\Delta t) - f(t_0 + m\Delta t)}{\Delta t} + \mathcal{O}(\Delta t^2), \\ \Rightarrow f'^{(m+1/2)} &= \frac{f^{(m+1)} - f^{(m)}}{\Delta t} + \mathcal{O}(\Delta t^2), \end{aligned} \tag{3.28}$$

where m is the time-step index and Δt is the step size. The state variables for the FIT method are defined by

$$\widehat{\boldsymbol{h}}^{m} = \widehat{\boldsymbol{h}}(t_0 + m \cdot \Delta t) \qquad \text{and} \qquad \widehat{\boldsymbol{e}}^{m+1/2} = \widehat{\boldsymbol{e}}(t_0 + (m+1/2) \cdot \Delta t). \tag{3.29}$$

Using the central difference approximation, we have

$$\frac{d}{dt}\widehat{\boldsymbol{h}}^{m+1/2} \approx \frac{\widehat{\boldsymbol{h}}^{m+1} - \widehat{\boldsymbol{h}}^{m}}{\Delta t} \qquad \text{and} \qquad \frac{d}{dt}\widehat{\boldsymbol{e}}^{m+1} \approx \frac{\widehat{\boldsymbol{e}}^{m+3/2} - \widehat{\boldsymbol{e}}^{m+1/2}}{\Delta t}. \tag{3.30}$$

Substituting these differential quantities in the discretized curl equations (Eqs. (3.14)–(3.15)), we get

$$\begin{aligned} \boldsymbol{C}\widehat{\boldsymbol{e}}^{m+1/2} &= -\boldsymbol{M}_{\mu}\frac{d}{dt}\widehat{\boldsymbol{h}}^{m+1/2} \approx -\boldsymbol{M}_{\mu}\frac{\widehat{\boldsymbol{h}}^{m+1} - \widehat{\boldsymbol{h}}^{m}}{\Delta t}, \\ \widetilde{\boldsymbol{C}}\widehat{\boldsymbol{h}}^{m+1} &= \boldsymbol{M}_{\varepsilon}\frac{d}{dt}\widehat{\boldsymbol{e}}^{m+1} + \widehat{\widehat{\boldsymbol{j}}}^{m+1} \approx \boldsymbol{M}_{\varepsilon}\frac{\widehat{\boldsymbol{e}}^{m+3/2} - \widehat{\boldsymbol{e}}^{m+1/2}}{\Delta t} + \widehat{\widehat{\boldsymbol{j}}}^{m+1}. \end{aligned} \tag{3.31}$$

Therefore, the explicit recursive update equations obtained using the step size and the central difference approximated derivatives are

$$\begin{aligned} \widehat{\boldsymbol{h}}^{m+1} &= \widehat{\boldsymbol{h}}^{m} - \Delta t \cdot \boldsymbol{M}_{\mu}^{-1}\boldsymbol{C}\widehat{\boldsymbol{e}}^{m+1/2}, \\ \widehat{\boldsymbol{e}}^{m+3/2} &= \widehat{\boldsymbol{e}}^{m+1/2} + \Delta t \cdot \boldsymbol{M}_{\varepsilon}^{-1}(\widetilde{\boldsymbol{C}}\widehat{\boldsymbol{h}}^{m+1} - \widehat{\widehat{\boldsymbol{j}}}^{m+1}). \end{aligned} \tag{3.32}$$

Figure 3.6 provides a graphical representation of this update scheme.

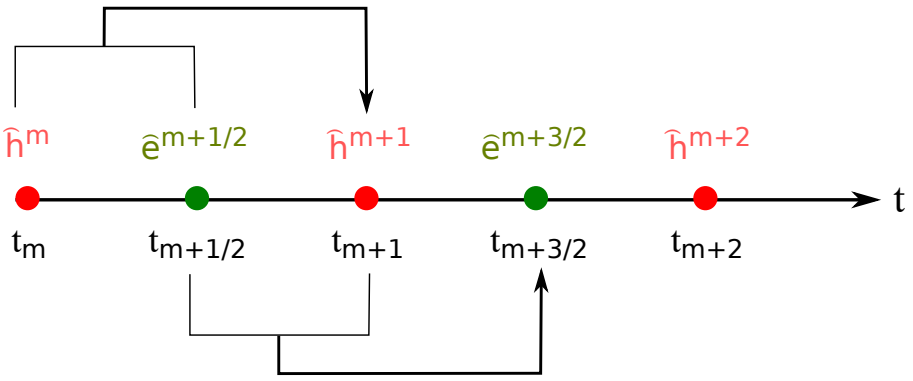

Figure 3.6: Schematic representation of the update scheme utilized by the leapfrog algorithm.

3.1.5 Numerical stability

Numerical stability is a key aspect of any time domain solver and depends on several problem-specific factors such as the boundary conditions, types of materials (lossy/dispersive), etc. Using the FDTD-based Courant stability criterion, one can define the maximum time step size in relation to the mesh size as [83]

$$\Delta t \leq \Delta t_{max} \approx \min_i \left\{ \varepsilon_i \mu_i \cdot \left(\frac{1}{\Delta x_i^2} + \frac{1}{\Delta y_i^2} + \frac{1}{\Delta z_i^2} \right)^{-1} \right\}^{1/2}. \tag{3.33}$$

For uniform, homogeneous grids, $\Delta x = \Delta y = \Delta z = \delta$, we get

$$\Delta t \leq \frac{1}{c}\frac{\delta}{\sqrt{3}}. \tag{3.34}$$

For the FIT approach, one can discuss stability independent of the discretization in time. For this purpose, we consider linear inhomogeneous differential equations of a lossless system ($\boldsymbol{M}_\kappa = \boldsymbol{0}$). This is summarized using the discretized curl equations as

$$\frac{d}{dt}\begin{bmatrix}\widehat{\boldsymbol{h}}\\ \widehat{\boldsymbol{e}}\end{bmatrix} = \begin{bmatrix}\boldsymbol{0} & -\boldsymbol{M}_\mu^{-1}\boldsymbol{C}\\ \boldsymbol{M}_\varepsilon^{-1}\widetilde{\boldsymbol{C}} & \boldsymbol{0}\end{bmatrix}\begin{bmatrix}\widehat{\boldsymbol{h}}\\ \widehat{\boldsymbol{e}}\end{bmatrix} + \begin{bmatrix}\boldsymbol{0}\\ -\boldsymbol{M}_\varepsilon^{-1}\widehat{\widehat{\boldsymbol{j}}}\end{bmatrix}. \tag{3.35}$$

With the aid of positive definite and symmetric matrices $\boldsymbol{M}_\mu^{1/2}$ and $\boldsymbol{M}_\varepsilon^{1/2}$, we transform the system to define a new state $\boldsymbol{x}$ and inhomogeneous term $\boldsymbol{b}$ as

$$\boldsymbol{x} = \begin{bmatrix}\widehat{\boldsymbol{h}}'\\ \widehat{\boldsymbol{e}}'\end{bmatrix} = \begin{bmatrix}\boldsymbol{M}_\mu^{1/2}\widehat{\boldsymbol{h}}\\ \boldsymbol{M}_\varepsilon^{1/2}\widehat{\boldsymbol{e}}\end{bmatrix} \qquad \text{and} \qquad \boldsymbol{b} = \begin{bmatrix}\boldsymbol{0}\\ -\boldsymbol{M}_\varepsilon^{-1/2}\widehat{\widehat{\boldsymbol{j}}}\end{bmatrix}. \tag{3.36}$$

The resulting state space takes the form

$$\frac{d}{dt}\boldsymbol{x} = \boldsymbol{A}\boldsymbol{x} + \boldsymbol{b}, \tag{3.37}$$

where $\boldsymbol{A}$ is the system matrix with the following state equations

$$\begin{aligned}\frac{d}{dt}\widehat{\boldsymbol{h}}' &= \boldsymbol{M}_\mu^{1/2}\frac{d}{dt}\widehat{\boldsymbol{h}} = \boldsymbol{M}_\mu^{1/2}\cdot(-\boldsymbol{M}_\mu^{-1}\boldsymbol{C}\widehat{\boldsymbol{e}}) = -\boldsymbol{M}_\mu^{-1/2}\boldsymbol{C}\boldsymbol{M}_\varepsilon^{-1/2}\widehat{\boldsymbol{e}}',\\ \frac{d}{dt}\widehat{\boldsymbol{e}}' &= \boldsymbol{M}_\varepsilon^{1/2}\frac{d}{dt}\widehat{\boldsymbol{e}} = \boldsymbol{M}_\varepsilon^{1/2}\boldsymbol{M}_\varepsilon^{-1}\widetilde{\boldsymbol{C}}\widehat{\boldsymbol{h}} - \boldsymbol{M}_\varepsilon^{1/2}\boldsymbol{M}_\varepsilon^{-1}\widehat{\widehat{\boldsymbol{j}}} = \boldsymbol{M}_\varepsilon^{-1/2}\widetilde{\boldsymbol{C}}\boldsymbol{M}_\mu^{-1/2}\widehat{\boldsymbol{h}}' - \boldsymbol{M}_\varepsilon^{-1/2}\widehat{\widehat{\boldsymbol{j}}}.\end{aligned} \tag{3.38}$$

The corresponding system matrix $\boldsymbol{A}$ retains a skew-symmetric nature and is given by

$$\boldsymbol{A} = \begin{bmatrix}\boldsymbol{0} & -\boldsymbol{M}_\mu^{-1/2}\boldsymbol{C}\boldsymbol{M}_\varepsilon^{-1/2}\\ \boldsymbol{M}_\varepsilon^{-1/2}\widetilde{\boldsymbol{C}}\boldsymbol{M}_\mu^{-1/2} & \boldsymbol{0}\end{bmatrix} = \begin{bmatrix}\boldsymbol{0} & \boldsymbol{A}_{12}\\ -\boldsymbol{A}_{12}^\mathsf{T} & \boldsymbol{0}\end{bmatrix}. \tag{3.39}$$

Using the characteristic equation $\det(\boldsymbol{A} - \lambda_{\boldsymbol{A},i}\boldsymbol{I}) = 0$, we find purely imaginary eigenvalues of the form $\lambda_{\boldsymbol{A},i} = \pm j\omega_i$ with real-valued frequencies ω_i. These eigenvalues will result in a pair of conjugate eigenvectors associated with undamped oscillating electromagnetic fields. This is plausible due to the absence of $\boldsymbol{M}_\kappa$ for lossless systems. Thus, we have established a concept for stability without considering time discretization, also viewed as spatial stability.

If the above state space description is discretized with a time step Δt using the approximate central difference scheme, we obtain a discrete-time state-space equation that includes the leapfrog scheme as follows [91]

$$\begin{bmatrix}\widehat{\boldsymbol{h}}'^{m+1}\\ \widehat{\boldsymbol{e}}'^{m+3/2}\end{bmatrix} = \underbrace{\begin{bmatrix}\boldsymbol{I} & \Delta t\boldsymbol{A}_{12}\\ -\Delta t\boldsymbol{A}_{12}^\mathsf{T} & \boldsymbol{I} + \Delta t^2\boldsymbol{A}_{12}^\mathsf{T}\boldsymbol{A}_{12}\end{bmatrix}}_{\boldsymbol{A}_d(\Delta t)}\begin{bmatrix}\widehat{\boldsymbol{h}}'^{m}\\ \widehat{\boldsymbol{e}}'^{m+1/2}\end{bmatrix} + \begin{bmatrix}\boldsymbol{0}\\ -\Delta t\boldsymbol{M}_\varepsilon^{-1/2}\widehat{\widehat{\boldsymbol{j}}}^{m+1}\end{bmatrix}, \tag{3.40}$$

where $\boldsymbol{A}_d(\Delta t)$ is the discrete-time system matrix. For this system, to ensure stability and satisfy energy conservation in the lossless system, all eigenvalues of the system must lie on the unit circle, i.e., $|\lambda_{\boldsymbol{A}_d,i}(\Delta t)| = 1$. If the system is spatially stable (with $\lambda_{\boldsymbol{A},i} = \pm j\omega_i$), the eigenvalues of the discrete-time system take the form [83]

$$\lambda_{\boldsymbol{A}_d,i}(\Delta t) = \frac{2 - (\Delta t\omega_i)^2}{2} \pm \sqrt{\frac{(2 - (\Delta t\omega_i)^2)^2}{4} - 1}. \tag{3.41}$$

Hence, the final stability condition that produces a more generalized Courant stability criterion is given by

$$|\lambda_{\boldsymbol{A}_d,i}(\Delta t)| = 1 \Rightarrow \Delta t \leq \frac{2}{\max_i |\omega_i|} \; \forall i. \tag{3.42}$$

Thus, an exact stability criterion defining the upper limit of the time step is obtained and can be extended to other methods, such as FDTD, when using a Cartesian grid.

3.2 Optimization theory

One of the definitions for optimization is "the process of finding the most effective or favorable value or condition" [92]. Today, most engineers prefer optimizing their designs' performance, as this would provide a better functioning system and a better understanding of the underlying physics. This section will give a short overview of the mathematical formulation of our optimization problem and the different optimization algorithms used in the scope of this work.

3.2.1 Mathematical formulation

The optimization process begins by first identifying an objective function that can quantitatively measure the performance of our system under investigation. This objective, in turn, depends on some system characteristics or variables, which may be constrained or unconstrained, and this process aims to find values for these variables that will optimize the objective. Once all the above-mentioned details are obtained, the modeling of the problem is complete, and one needs to recognize what kind of optimization algorithm fits best to their problem. This is a crucial factor that decides if the chosen algorithm can arrive at a solution quickly or slowly and, indeed, arrive at a solution for the given problem at all.

If we were to define this process mathematically, optimization targets minimizing or maximizing an objective function based on the constraints we define for the variables. Consider the following notations:

- $\boldsymbol{x}$ is the n-variables vector,
- g_i and h_j represent the constraint functions (scalar functions of $\boldsymbol{x}$),
- f is the objective we want to optimize as a function (scalar) of $\boldsymbol{x}$.

The optimization problem can be defined as

$$\min_{\boldsymbol{x}\in\mathbb{R}^n} f(\boldsymbol{x}) \qquad \text{subject to} \qquad \begin{array}{ll} g_i(\boldsymbol{x}) = 0, & i \in \mathcal{E} \\ h_j(\boldsymbol{x}) \leq 0, & j \in \mathcal{I}, \end{array} \tag{3.43}$$

where $\mathcal{E}$ and $\mathcal{I}$ are sets defining the indices for the equality and inequality constraints, respectively.

Similarly, maximization problems work identically, but we minimize the function $-f(\boldsymbol{x})$ instead. However, it is important to classify the problem based on the number of variables, the nature of the objective function, and the constraints applied to the variables. If all the constraints and the objective function are linear in nature with respect to $\boldsymbol{x}$, such a problem is called a linear programming problem. However, if either of the constraints or the objective function is non-linear, the problem can be termed a non-linear programming problem. Depending on the constraints, a problem can be further distinguished as a constrained or an unconstrained one. When $\mathcal{E} = \mathcal{I} = \emptyset$, we call it an unconstrained problem. For a constrained problem, these sets are not empty. However, in some cases, they can be reformulated as an unconstrained problem by introducing the constraints as penalties in the objective function [93].

In this work, we consider constrained optimization problems. Generally, these constraints could be linear by defining simple bounds like $a_i \leq x_i \leq b_i$ for $i = \{1, .., n\}$, or non-linear by describing complex relationships between the variables, or even convex. When a point $\boldsymbol{x}$ satisfies the bound, equality, and inequality constraints, it is considered a feasible point, and a set of all such points is referred to as a feasible region, Ω. This can be represented as

$$\Omega = \{\boldsymbol{x} \mid g_i(\boldsymbol{x}) = 0, i \in \mathcal{E}; \quad h_j(\boldsymbol{x}) \leq 0, j \in \mathcal{I}\}, \tag{3.44}$$

and the optimization problem can be defined as

$$\min_{\boldsymbol{x} \in \Omega} f(\boldsymbol{x}), \qquad \text{where} \quad f : \Omega \subset \mathbb{R}^n \to \mathbb{R}. \tag{3.45}$$

3.2.2 Algorithms used for optimization

There are two approaches to an optimization problem, i.e., finding a local solution or a global solution. Within local optimization, a local minimum is a point where the objective function is less than or equal to all the nearby feasible points (neighborhood $\mathcal{N}$). Therefore, $\boldsymbol{x}^*$ is a local solution if,

$$f(\boldsymbol{x}^*) \leq f(\boldsymbol{x}) \qquad \forall \boldsymbol{x} \in \mathcal{N} \cap \Omega.$$

Similarly, a point $\boldsymbol{x}^*$ is defined as a global solution if,

$$f(\boldsymbol{x}^*) \leq f(\boldsymbol{x}) \qquad \forall \boldsymbol{x} \in \Omega.$$

The framework of this thesis focuses on local and global optimizations, which are explained in the following subsections of this chapter. Generally, an optimization problem, especially a non-linear one, could possess multiple local minima. The minimum chosen depends upon the algorithm used to solve the problem and the initial point provided to it. Hence, finding a global minimum can be challenging at times. One can only be sure if the point located is a true global solution by providing some unique information about the objective function f. The algorithms utilized in the scope of this work aim to find the global optimum without any special information about the objective function. These algorithms are introduced in the following sections.

3.2.2.1 Particle swarm algorithm

Swarm intelligence has been defined as the collective foraging behavior of living beings [94]. All agents of a swarm communicate with one another to find their food using the fastest path and time. In 1995, Kennedy and Eberhart developed a stochastic optimization method, the particle swarm optimization (PSO), inspired by the nature of socially organized populations like fish schools, bird flocks, and animal herds [95]. Based on these social behavior simulation models, the algorithm uses a stochastically moving population of search points in the defined search space. The memory retains the so-called experience, which is the best position of every point. This experience is then used to influence the movement of the population towards global solutions by communicating it to the entire population. The convergence of the optimization algorithm is strongly influenced by the type of social networking used for communication.

To mathematically formulate this, let $\Omega \subset \mathbb{R}^n$ define the feasible search space of the optimization problem, and the objective can be defined as $f : \Omega \to Y \subseteq \mathbb{R}$ [96]. According to the nomenclature used in particle physics and social science models, the population can be referred to as a swarm, and each individual from the swarm is known as a particle. Therefore, we can define the swarm as a set of N particles or candidate solutions

$$S = \{\boldsymbol{s}_1, \boldsymbol{s}_2, \ldots, \boldsymbol{s}_N\}, \tag{3.46}$$

where each candidate solution is taken as a vector of real numbers,

$$\boldsymbol{s}_j = (s_{j1}, s_{j2}, \ldots, s_{jn})^\intercal \in \Omega, \qquad j = 1, 2, \ldots, N, \tag{3.47}$$

and N is defined by the user at the start of the optimization. Each particle holds a unique objective value, $f_j = f(\boldsymbol{x}_j) \in Y$, assuming that the objective function is available for each point in Ω. Within this search space Ω, the particles move iteratively by changing their position based on the velocity,

$$\boldsymbol{v}_j = (v_{j1}, v_{j2}, \ldots, v_{jn})^\intercal, \quad j = 1, 2, \ldots, N. \tag{3.48}$$

To enable particles to traverse the search space freely, their velocities are iteratively modified based on the memory of their best positions visited so far. This memory can be defined as,

$$P_s = \{\boldsymbol{p}_1, \boldsymbol{p}_2, \ldots, \boldsymbol{p}_N\}, \tag{3.49}$$

where the best position from each particle could be represented as,

$$\boldsymbol{p}_j = (p_{j1}, p_{j2}, \ldots, p_{jn})^\intercal \in \Omega, \quad j = 1, 2, \ldots, N. \tag{3.50}$$

For an iteration counter t, the current position and velocity for the j-th particle can be expressed as $\boldsymbol{s}_j(t)$ and $\boldsymbol{v}_j(t)$, respectively. The best position could be defined as

$$\boldsymbol{p}_j(t) = \arg\min_{\boldsymbol{s}_j(t)} f\left(\boldsymbol{s}_j(t)\right), \tag{3.51}$$

for a minimization problem. The algorithm estimates the global minimum using this information or experience as described in Eq. (3.50). Therefore, if * is the identifier pointing to the best position found so far, it can be defined as

$$\boldsymbol{p}^*(t) = \arg\min_{\boldsymbol{p}_j(t)} f\left(\boldsymbol{p}_j(t)\right). \tag{3.52}$$

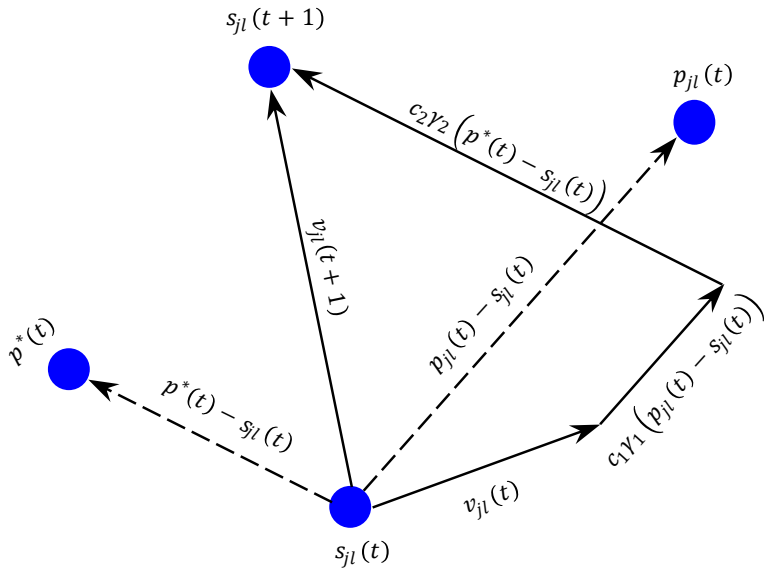

Figure 3.7: Illustration of the update mechanism utilized by the particle swarm optimizer.

Based on the social behavior simulations, the algorithm communicates this important information to the swarm. The following update equations then define the PSO

$$\boldsymbol{v}_{jl}(t+1) = \boldsymbol{v}_{jl}(t) + c_1\gamma_1\left(\boldsymbol{p}_{jl}(t) - \boldsymbol{s}_{jl}(t)\right) + c_2\gamma_2\left(\boldsymbol{p}^*(t) - \boldsymbol{s}_{jl}(t)\right), \tag{3.53}$$

$$\boldsymbol{s}_{jl}(t+1) = \boldsymbol{s}_{jl}(t) + \boldsymbol{v}_{jl}(t+1), \tag{3.54}$$

where $j = 1, 2, \ldots N$ and $l = 1, 2, \ldots, n$. Furthermore, γ_1 and γ_2 are the uniformly distributed random variables between $[0, 1]$, t is the counter for the iteration, and c_1 and c_2 are the weighting factors also known as the cognitive and social parameters, respectively. Figure 3.7 illustrates the update scheme for the PSO. In Eq. (3.53), $\boldsymbol{v}_{jl}$ provides an inertial movement of the particle depending on the previous position shift, which prevents the algorithm from being stuck around a local optimum. Hence, this term enables a global search, exploring different regions of Ω. On the other hand, the last two terms on the right-hand side of Eq. (3.53) facilitate a local search from each particle in the vicinity of $\boldsymbol{p}_{jl}$ and $\boldsymbol{p}^*$, which is the particle's own best position and the swarm's best position, respectively [97, 98]. Thus, PSO serves as a powerful optimization method for global maximization and minimization problems.

3.2.2.2 Trust region method

Trust region optimization (TRO) is highly efficient in solving non-linear optimization problems. The method begins by defining a region around the current best solution, where a model function m_k, usually a quadratic one, is trusted to adequately represent the objective function f. Simultaneously, a step is chosen to approximate the minimizer for this model function, which can be obtained by solving the following subproblem

$$\min_{\boldsymbol{p}\in\mathbb{R}^n} m_k(\boldsymbol{p}) = f_k + \boldsymbol{g}_k^\intercal \boldsymbol{p} + \frac{1}{2}\boldsymbol{p}^\intercal \boldsymbol{B}_k \boldsymbol{p} \qquad \text{s.t.} \|\boldsymbol{p}\| \leq \Delta_k, \tag{3.55}$$

where $\boldsymbol{B}_k$ is the hessian approximation, f_k is the objective function at the current iteration (k) and $\boldsymbol{g}_k$ is its gradient, the radius of the trust region $\Delta_k > 0$, and $\boldsymbol{p}_k^*$ is the minimizer for the model function defined in Eq. (3.55). The size of the trust region is updated in every iteration depending on the effectiveness of the chosen step, which can be decided based on the following equation

$$\rho_k = \frac{f(\boldsymbol{x}_k) - f(\boldsymbol{x}_k + \boldsymbol{p}_k)}{m_k(\mathbf{0}) - m_k(\boldsymbol{p}_k)}. \tag{3.56}$$

It is the ratio of the actual reduction in the original objective function f to the predicted reduction in f that is estimated by the model function. The values of ρ_k provide three possibilities for the size of the trust region:

1. If $\rho_k \approx 1$, it depicts a good agreement between m_k and f, implying that m_k is a good representative of f. Therefore, the size of the trust region can be increased, i.e., increasing Δ_k in the following iteration.
2. If ρ_k is positive but much smaller than 1, then we do not change the radius of the trust region.
3. If ρ_k is negative or close to zero, it implies that the m_k is an inadequate representative of f. This is only possible when $f(\boldsymbol{x}_k + \boldsymbol{p}_k)$ is greater than $f(\boldsymbol{x}_k)$, as the denominator of Eq. (3.56) is always non-negative [93]. Therefore, the size of the trust region is reduced by using a smaller Δ_k.

A convergence can be reached with each trust region that relies on the improvement from the previous iterations. Hence, this method aids in robust local optimization of a desired objective function.

Therefore, PSO in conjunction with the TRO, constitutes a hybrid optimization routine that is widely employed in the optimization of various optical structures in this thesis. This routine first establishes a global optimum with the particle swarm optimizer and then runs the local trust region optimizer to avoid being stuck with a local optimum.

Chapter 4

Highly directive antennas[1]

Over the last 20 years, optical antennas have become increasingly important for practical applications [11]. Among these, directional optical antennas have received significant attention from the photonics community because they can radiate electromagnetic energy in desired directions. Leaky-wave antennas, which allow power leakage along a non-resonant guiding structure through leaky modes, have shown excellent performance [102–115]. Additionally, highly directive emissions can also be achieved through the propagation of guided modes along these structures [99–101]. The interplay between leaky and guided modes in optical nanoantennas can lead to highly directive emissions, making them a promising technology for on-chip communication and sensing. Their ability to govern the directivity and angular distribution of optical radiation over a broad frequency range proves the potential of these antennas for robust wireless communication [116].

To achieve desirable functionality in nanoantennas, it is crucial to carefully design and optimize their structure geometry, size, and material. These factors significantly affect the electromagnetic response and functionality, allowing control over the number of modes excited, frequency, and angular radiation patterns. Different methods and strategies have been extensively used for this purpose, including classical gradient descent and swarm intelligence, genetic and evolutionary optimization strategies, inverse design and deep learning approaches, or their combinations [117–123].

In this chapter, we present antennas that are investigated with the goal of having a highly directive nature with the aid of guided modes. Section 4.1 discusses the characteristics of the excitation source utilized for this purpose, followed by a parametric study of different antenna design parameters to understand their influence on achieving directional emission. Furthermore, in Section 4.2, we explore different antenna designs and optimize them for improved performances. Three different antennas are explored together with the analysis of their optical characteristics.

[1] Section 4.1 is based on our publication [99] and Section 4.2 is based on publications [100, 101] of the candidate.

4.1 From leaky-wave to guided-wave antennas

To start our studies, we use a simple dielectric traveling-wave antenna made up of a reflector and a director which is deposited on a glass substrate with a refractive index of $n = 1.52$. The antenna is made of hafnium dioxide (HfO_2), which has a high refractive index ($n = 1.9$) and very low absorption loss at a wavelength of 780 nm. This wavelength is significant as it is the emission wavelength of the quantum dots employed in the experimental setup. Both the director and reflector are rectangular shaped, and their schematic representation is shown in Figure 4.1 with respect to the Cartesian coordinates. The antenna is modeled using seven design parameters highlighted in the schematic. These parameters include the antenna height (H), director length (DL), director width (DW), reflector length (RL), reflector width (RW), and distance of the field source from the director (DD) and the reflector (RD). The structure is oriented in the xy-plane with x-axis as its direction of wave propagation, also called the antenna axis ($\theta = 90°$), and the positive z-axis, also known as the optical axis ($\theta = 0°$), is normal to the substrate, pointing towards it. Between the reflector and the director is a feed gap, where the excitation source is placed. Before we can address our results, it is imperative for us to comprehensively analyze the features of the light source we require for our studies. For this purpose, full-wave numerical simulations are performed in the time domain utilizing the finite integration technique (FIT) employed in CST Microwave Studio [63].

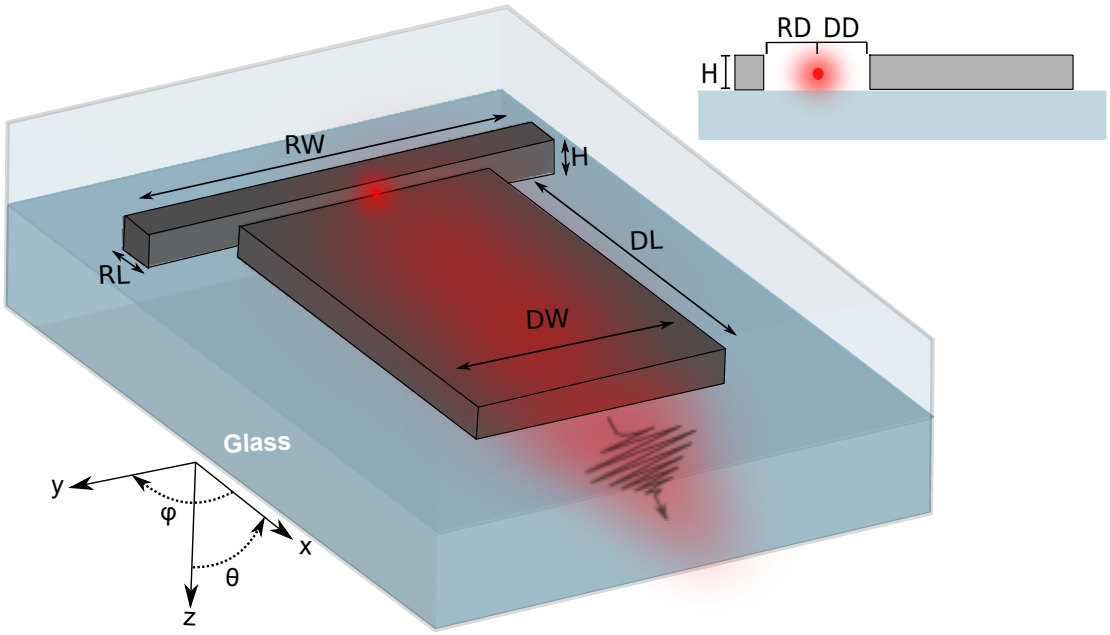

Figure 4.1: Schematic representation of the antenna under investigation highlighting its design parameters [100].

4.1.1 Analysis of the excitation source

In our studies, an Hertzian dipole (discussed in Section 2.3.1) with an emission wavelength of 780 nm is employed as the internal light source that is depicted by the solid red dot in Figure 4.1.

It can efficiently mimic the behavior of a quantum dot generally used in an experimental setup. To understand the coupling characteristics of a dipole emitter, we analyze the influence of the dipole orientation and its position displacement on the antenna's directive nature. The dipole emitter excites leaky and guided modes that direct the propagation towards the glass substrate. This is illustrated by the arrow in the red background of Figure 4.1. For this study, the reflector is chosen to have a length and width of 180 nm and 785 nm, respectively. Similarly, the director has a length and width of 2200 nm and 600 nm, respectively. The antenna has a height of 140 nm, and the reflector and director are separated by a feed gap of 260 nm, where the dipole is located. In the feed gap, the dipole is centrally placed along the symmetry plane of the antenna, 40 nm behind the director and 220 nm ahead of the reflector. This is an optimal position estimated by conducting a parameter sweep for various dipole positions. Furthermore, the emitter is placed 10 nm above the substrate, as the CdSeTe colloidal quantum dots used in the experiments normally have a diameter of 20 nm [100].

4.1.1.1 Effect of different dipole polarizations

Understanding how a dipole of different polarizations couples to the antenna is essential to approximate the random orientation of the quantum dots in the experimental setup. For this study, the dipole is centrally placed at the optimum position defined above. We then analyze the effect of having x-, y- and z-oriented dipoles. Figure 4.2 illustrates the calculated angular directive gain distributions of all three aforementioned orientations. As it can be seen, the strongest coupling is demonstrated by the highest intensity produced by the y-oriented dipole with its main lobe at $\theta = 66°$ and $\varphi = 0°$. On the other hand, the z-oriented dipole provides a weaker intensity, while the x-oriented dipole produces no appreciable far-field intensity. This implies that the y-oriented dipole offers the most relevant information needed for characterizing the emission of our antenna. Therefore, all the following work in this chapter uses a y-oriented dipole, which is also the TE polarization case.

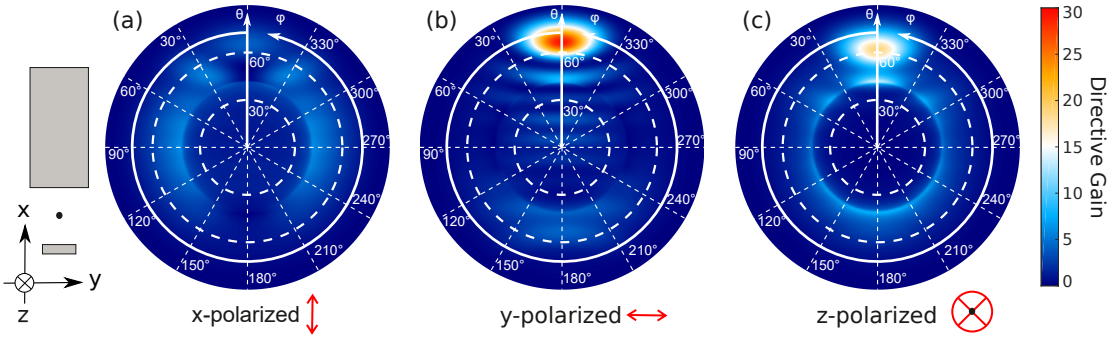

Figure 4.2: Calculated angular linear directive gain distributions for an (a) x-, (b) y-, and (c) z-polarized dipole coupled to the HfO_2 antenna.

4.1.1.2 Effect of dipole displacement

In an experimental setup, a few hundred quantum dots are usually placed in the feed gap area between the director and the reflector. It is instructive to study the impact of dipole displacement from its optimum position and observe how it affects the far-field emission pattern. Let us first

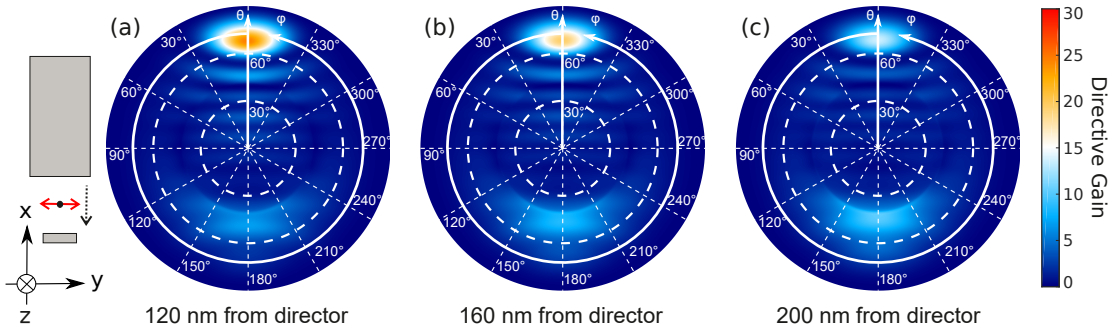

Figure 4.3: Calculated angular linear directive gain distributions for a dipole displaced along the x-axis. The direction of displacement is highlighted by the black dotted arrow and the distance of the dipole from the director is (a) 120 nm, (b) 160 nm, and (c) 200 nm. The red arrow represents the orientation of the dipole.

focus on the scenario where the y-oriented dipole is moved along the x-axis while keeping its y-position constant. In Figure 4.3, we can see the far-field emission pattern for the dipole located at 120 nm, 160 nm, and 200 nm from the director. As the distance between the dipole and the director grows, the main lobe intensity drops, with increased back reflection, as compared to

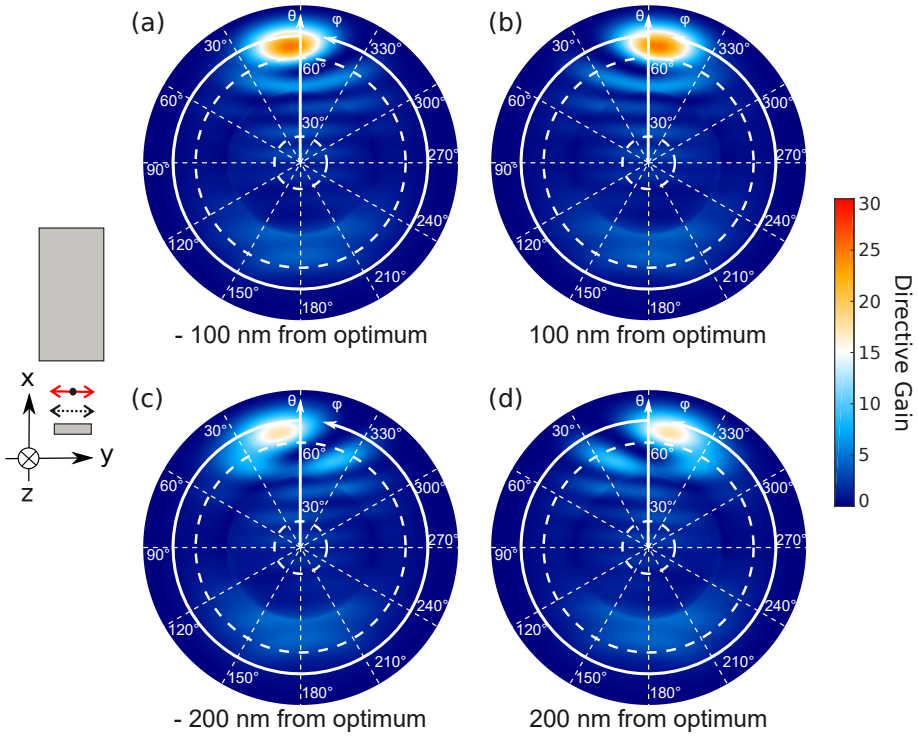

Figure 4.4: Calculated angular linear directive gain distributions for a dipole displaced along the y-axis by (a) -100 nm, (b) $+100$ nm, (c) -200 nm, and (d) $+200$ nm. The dipole displacement is highlighted by the black dotted arrow and the red arrow represents the orientation of the dipole.

Figure 4.2b (optimum case). This happens because the coupling efficiency of the dipole to the director decreases as the distance between them increases. As a result, the far-field emission pattern starts to resemble the radiation pattern of an uncoupled dipole.

Next, we study the influence of dipole displacement along the y-axis, keeping its x-position constant, which is 40 nm from the director. Figure 4.4 shows the angular emission patterns for the dipole that is displaced by -100 nm, $+100$ nm, -200 nm, and $+200$ nm, from the symmetry plane of the antenna, i.e., the optimal position with respect to the y-axis. We observe that all the configurations illustrate a change in the azimuthal position of the main lobe. Along the y-axis, displacing the dipole to -100 nm and -200 nm, the main lobe is shifted by $\Delta\varphi = +5°$ and $\Delta\varphi = +10°$, respectively. Similarly, for a displacement of $+100$ nm and $+200$ nm, $\Delta\varphi = -5°$ and $\Delta\varphi = -10°$, respectively. However, once again, the dipole coupling strength to the director reduces when the dipole moves farther away from its optimal central position, as demonstrated by the ± 200 nm offsets.

4.1.2 Analysis of the antenna geometry and material

In the next step, we want to understand the influence of the antenna geometry and material on its emission characteristics. For this purpose, we begin by analyzing the director's width and length and then we study antenna materials of different refractive indices. The numerical results are also validated with the experimental measurements.

4.1.2.1 Director width variation

For this analysis, we maintain the same reflector as for the case of the dipole study above, i.e., a length and width of $RL = 180$ nm and $RW = 785$ nm, respectively. The antenna has a height of $H = 140$ nm, and the dipole is positioned 40 nm behind the director and 220 nm in front of the reflector. Furthermore, the director is chosen to have a length of $DL = 2200$ nm, and its width is varied. Before we analyze the results, we must perform an eigenmode study to identify the guided modes supported by such a structure for varying widths. This is done using COMSOL Multiphysics that employs the FEM [124], which considers a 2-D cross-section of

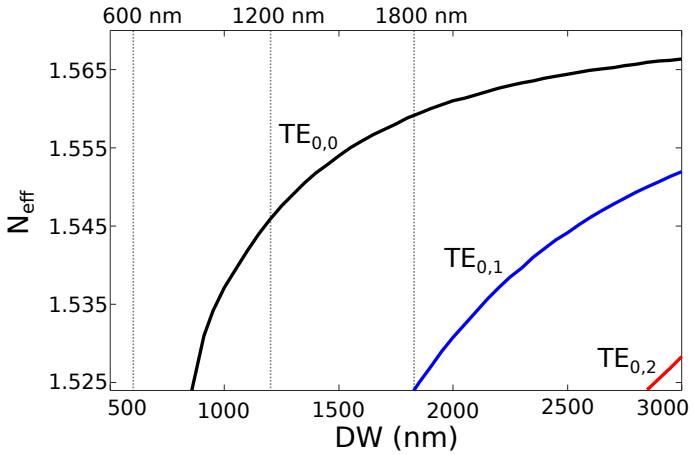

Figure 4.5: Calculated effective mode index N_{eff} as a function of the director width for the HfO_2 ridge waveguide. The antenna has a height of $H = 140$ nm.

the waveguide-like director possessing a transitional invariance along its propagation length. As a result, the effective mode indices (N_{eff}) of the guided modes as a function of the DW are shown in Figure 4.5. This plot shows that the first guided mode $\text{TE}_{0,0}$ is only excited when the width is $DW = 850\,\text{nm}$ or larger, and for smaller widths, only leaky modes are supported. The second guided mode $\text{TE}_{0,1}$ is only supported with structures of width $DW = 1800\,\text{nm}$ and above, and similarly, the higher-order modes are excited.

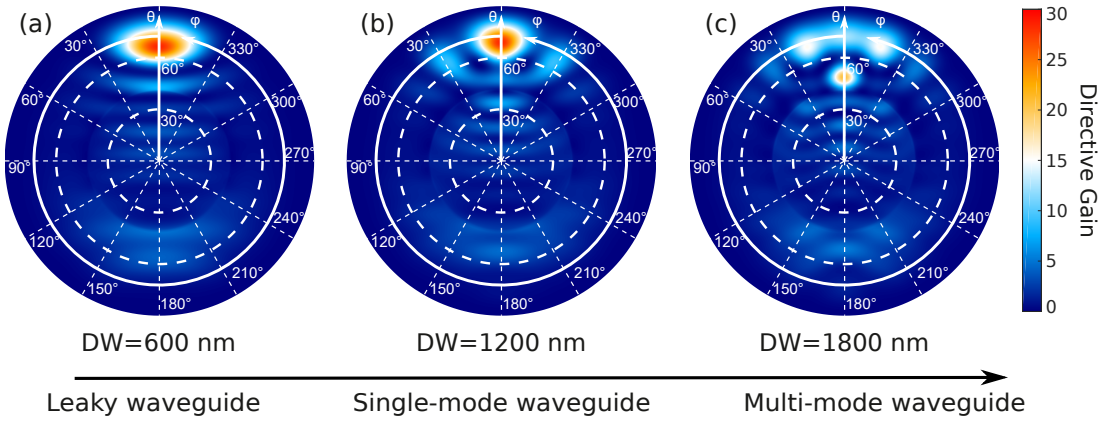

Figure 4.6: Calculated angular linear directive gain distributions of the HfO_2 antennas for a director width of (a) $DW = 600\,\text{nm}$, (b) $DW = 1200\,\text{nm}$, and (c) $DW = 1800\,\text{nm}$.

To see the effect of the aforementioned modes, we consider antennas with a $DW = 600\,\text{nm}$, $DW = 1200\,\text{nm}$, and $DW = 1800\,\text{nm}$, as demonstrated in Figure 4.6. In the first case, the structure behaves like a leaky-wave antenna since no guided mode is supported for a director width of 600 nm (as suggested by Figure 4.5). Therefore, the main lobe primarily results from the leaky-wave emission along the director [110], exhibiting a linear directivity of $D = 29.2$ along $\theta = 66°$ and $\varphi = 0°$. The second structure with a width of 1200 nm supports the first guided mode $\text{TE}_{0,0}$ and the leaky modes. Unlike the previous configuration, the guided $\text{TE}_{0,0}$ mode causes the majority of the emission to come from the director's end facet. At an angle of $\theta = 69°$ and $\varphi = 0°$, a directivity of $D = 28$ is observed. Finally, for the third configuration

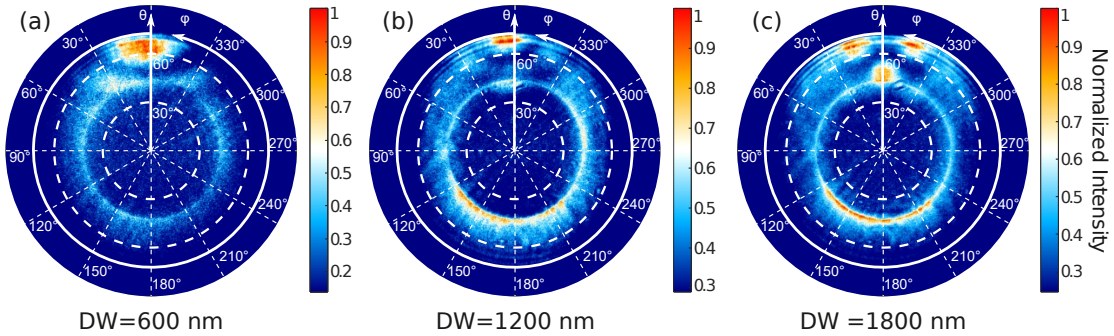

Figure 4.7: Measured angular far-field intensity distributions of the HfO_2 antennas for a director width of a) $DW = 600\,\text{nm}$, b) $DW = 1200\,\text{nm}$, and c) $DW = 1800\,\text{nm}$. The experimental numerical aperture is represented by the white circles at $\theta_{NA} = 72°$. The experimental intensities are normalized to their respective maxima [99].

with 1800 nm, the second guided mode $TE_{0,1}$ also becomes relevant together with the $TE_{0,0}$ and leaky modes, thus resulting in a multi-mode emission. This is also highlighted by the three hot spots of the emission pattern in the direction of the director (see Figure 4.6c). The main lobe points at $\theta = 49°$ and $\varphi = 0°$ with a directivity of $D = 21.3$. Therefore, increasing DW illustrates a transition from a leaky- to a single- and then to a multi-mode waveguide antenna with decreasing directivity.

To verify the numerical results from above, these antennas were fabricated employing a two-step electron-beam lithography process by our collaborating experimentalists [2]. Figure 4.7 shows the measured angular directive gain emission patterns for $DW = 600$ nm, $DW = 1200$ nm, and $DW = 1800$ nm. The experimental data is in good agreement with the main trends predicted by the numerical results. For $DW = 600$ nm, the emission pattern features its main lobe at approximately $\theta = 65°$ and $\varphi = 2°$. This shift in the azimuthal position can be explained by the dipole being displaced from its optimal central position in the experimental setup. Additionally, a ring-like feature at $\theta = 41.5°$ is observed, which can be attributed to the emission coming from the uncoupled quantum dots that mainly radiate at the critical angle between the air-glass interface [110]. For $DW = 1200$ nm, the main lobe shifts to a polar angle of approximately 69°, similar to the numerical results. Lastly, in good agreement with simulations, $DW = 1800$ nm demonstrates a multi-peak emission with its main lobe at $\approx 49°$. Therefore, it can be concluded that the prediction done by the numerical calculations is plausible.

4.1.2.2 Director length variation

Next, we study the director length's influence on the antenna's emission properties. To study the effect of having a guided mode in the structure, we consider a director cross-section that supports a single guided mode, i.e., a height of 180 nm and a width of 600 nm. The director length is then varied from 1400 nm to 3000 nm, implying that only the propagation length for the mode is varied, but the number of modes remains constant. Similar to the previous section, the reflector's dimensions, and the dipole's position remain the same.

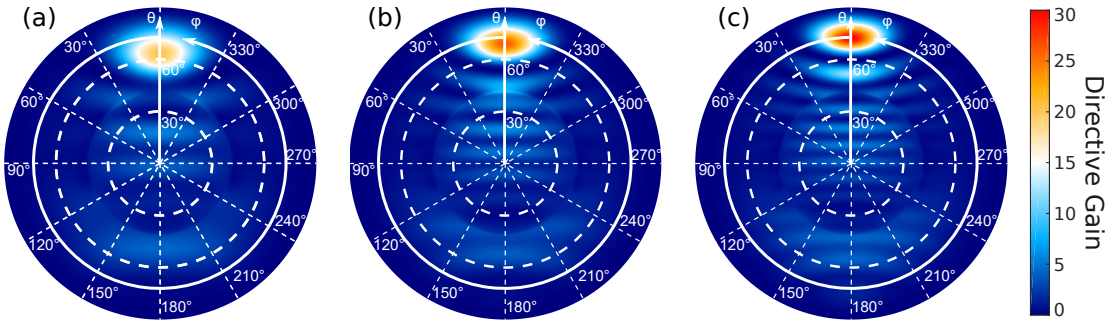

Figure 4.8: Calculated angular linear directive gain distributions of the HfO_2 antenna for a director length of a) $DL = 1400$ nm, b) $DL = 2200$ nm, and c) $DL = 3000$ nm.

[2] The antennas were fabricated and measured by colleagues from the department of Prof. Dr. Thomas Zentgraf at Paderborn University and Prof. Dr. Stefan Linden at Bonn University.

As it can be seen in Figure 4.8, with the increment of director length, the polar angle of the main lobe also increases from 63° to 69°, and finally to 72°. We already know, that the emission angle of an antenna is primarily influenced by the end facet diffraction and interference along the propagation direction. When the director is shorter, both these phenomena strongly affect the main lobe direction. But as the length of the director increases, the leakage radiation along the director becomes less relevant, as the leaky modes excited by the dipole quickly radiate into the substrate. Therefore, the end facet diffraction resulting from the propagation of the guided mode mainly characterizes the antenna emission pattern. In this regime, the direction of the main lobe remains almost constant with a maximum angle of $\theta_{max} = 80°$. This has been determined through numerical simulations for the director lengths up to 10000 nm (not shown here). Furthermore, the directivity increases with the director length, ranging from 20.9 to 25.4 and finally to 28.8 (see Figure 4.8). This also becomes evident from the increasing intensity of the main lobe. Along the $\varphi = 0°$ direction, the emission patterns show more side lobes with increasing director lengths. This can be attributed to the power that couples to the substrate's radiating modes. In this context, the director behaves as a finite-sized aperture, where the interference of the leakage radiation from different parts of the aperture results in the pattern of side lobes.

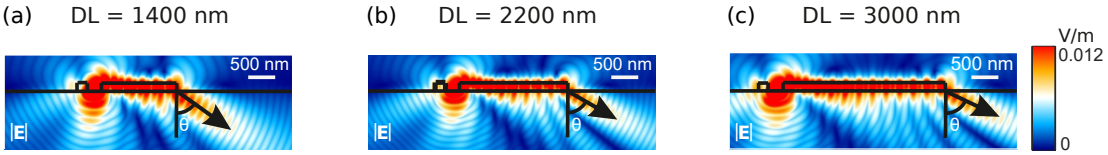

Figure 4.9: Calculated electric field distribution ($|\mathbf{E}|$) of the HfO_2 antenna in the xz-plane at $y = 0$ for a director length of a) $DL = 1400$ nm, b) $DL = 2200$ nm, and c) $DL = 3000$ nm.

To gain a better understanding of these antenna configurations, it's helpful to examine their near-field distribution. In Figure 4.9, we see that the shorter directors have higher leakage radiation, which decreases as the director length increases. This is because the number of guided modes stays the same, but the influence of the leaky modes decreases. Furthermore, the corresponding measured angular far-field intensity distributions are shown in Figure 4.10. In comparison to the

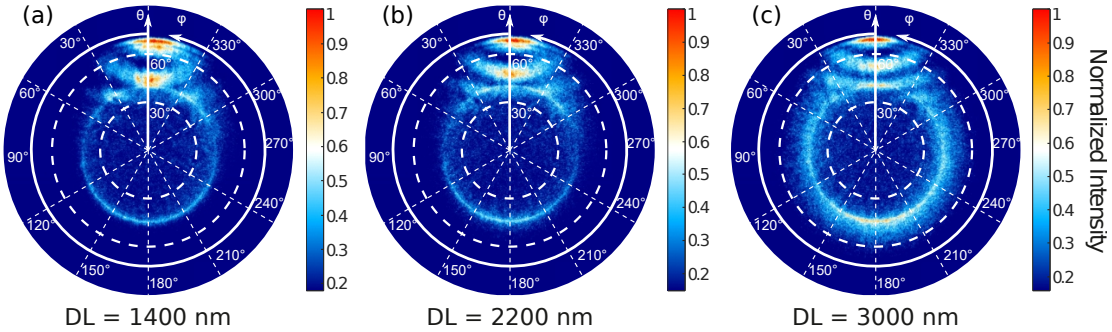

Figure 4.10: Measured far-field intensity distributions of the HfO_2 antenna for a director length of a) $DL = 1400$ nm, b) $DL = 2200$ nm, and c) $DL = 3000$ nm with a TE analyzer setting. The white circle at $\theta_{NA} = 72°$ in each pattern marks the numerical aperture of the experimental setup. These intensities are normalized to their respective maxima [99].

numerical calculation, these measurements do not show an evident increase in the polar angle of the main lobe as expected for the longer directors. This effect may occur because the objective lens has a finite collection angle, which implies that the main lobe of the longest antenna is not fully captured during the experiment. However, we still observe a series of side lobes along with the main lobe like the numerical results.

4.1.2.3 Material variation

As seen in Section 4.1.2.1, N_{eff} of the director plays a significant role in characterizing the emission of the antenna. To further investigate this point, we consider antennas made of three different materials, namely, hafnium dioxide (HfO_2), indium tin oxide (ITO), and titanium dioxide (TiO_2). However, all directors possess approximately the same real part of N_{eff}, i.e., $N_{\text{eff}}^{\text{HfO}_2} = 1.51 + 0.04i$ of the leaky HfO_2 antenna's director that had a width, height and length of 600 nm, 140 nm, and 2200 nm, respectively (discussed in Section 4.1.2.1). To accomplish ITO and TiO_2 directors of approximately the same effective mode index, suitable dimensions are found by fitting their corresponding electric field distribution inside the director as done in Ref. [125]. Calculations reveal that the ITO-director of width, height, and length of 900 nm, 110 nm, and 2200 nm, respectively, possesses an effective index of $N_{\text{eff}}^{\text{ITO}} = 1.51 + 0.06i$. Similarly, the TiO_2-director with the dimensions for width, height, and length of 800 nm, 40 nm, and 2200 nm, respectively, has an effective index of $N_{\text{eff}}^{\text{TiO}_2} = 1.50 + 0.05i$. Therefore, these dimensions were chosen for the directors, and the reflectors were kept the same as the HfO_2 an-

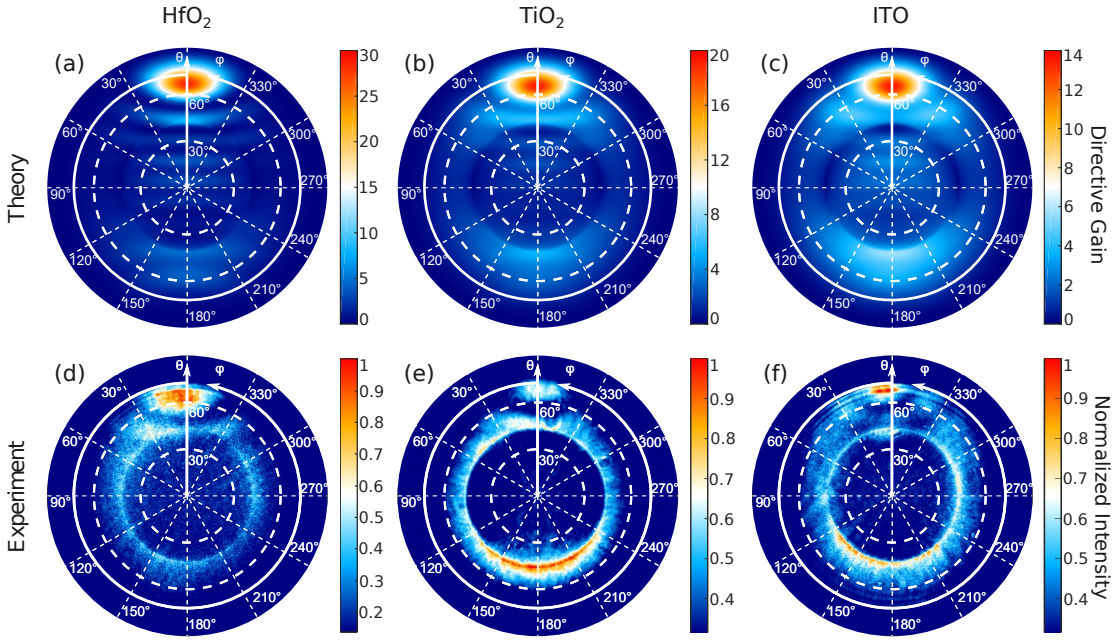

Figure 4.11: Calculated angular linear directive gain distributions of the a) HfO_2, b) TiO_2, and c) ITO antenna for TE polarization of the dipole. Measured angular far-field intensity distributions of the d) HfO_2, e) TiO_2, and f) ITO antenna obtained with the TE analyzer setting. These intensities are normalized to their respective maxima and the white circles at $\theta_{NA} = 72°$ indicate the numerical aperture of the experimental setup [99].

tenna, but their heights were maintained to be the same as their respective directors. Figure 4.11 shows the calculated and measured angular directive gain distributions for these antennas.

As seen in the theoretical calculations (Figure 4.11(a-c)), all three cases illustrate a pronounced main lobe at $\theta = 66^\circ$ and $\varphi = 0^\circ$. This implies that the main lobe angle for such antennas primarily results from the real part of N_{eff} [3]. On the other hand, the imaginary part of N_{eff} deals with attenuation, and, therefore, affects the antenna's directivity. The HfO_2 antenna, which has the lowest imaginary part of N_{eff}, has the largest directivity $D_{\text{HfO}_2} = 29.2$, followed by the TiO_2 antenna with $D_{\text{TiO}_2} = 19.4$, and the ITO antenna with $D_{\text{ITO}} = 13.6$. Interestingly, the difference in directivity is in good correspondence to the ratio of the power decay factor, $\exp\left(-2\text{Im}(N_{\text{eff}})2\pi L/\lambda\right)$ of the mode at the end facet after propagating a director length L (DL for our structure), which is approximately 24% for HfO_2-, 17% for TiO_2- and 12% for ITO-antenna. These results are corroborated with the experimental angular directive gain distributions shown in Figure 4.11(d-f). Similar to the numerical results, the experiments demonstrate a pronounced main lobe at $\theta \approx 66^\circ$. Furthermore, the uncoupled quantum dots demonstrate a ring-like feature in the emission pattern. This effect is more evident in the ITO- and TiO_2-antennas, implying that the antennas deposited by electron-beam evaporation (HfO_2) have superior quality in comparison to the structures fabricated by the sputtering process (ITO and TiO_2).

These numerical calculations and experimental measurements demonstrate that the effective refractive index of the director primarily determines the emission properties of such antennas. Therefore, we will investigate various antenna geometries and materials to achieve improved directive characteristics.

4.2 Optimization of the optical waveguide antennas

This section explores different antenna geometries suitable for producing highly directive radiation patterns. As discussed before, our antennas consist of a director and a reflector. We investigate different director types like rectangular-, horn-, and tip-shaped, while the reflector is always maintained to be rectangular. The same source is utilized, emitting at 780 nm with the strongest coupling to the antenna modes achieved using TE polarization. Apart from HfO_2, we also investigate other materials like silicon (Si) and tantalum pentoxide (Ta_2O_5) that can aid in achieving this goal.

CST Microwave Studio is utilized for performing full-wave numerical simulations in the time domain utilizing the FIT [63]. The work uses a hybrid optimization routine that employs PSO and TRO (refer Section 3.2.2). We optimize the directivity D of the antenna to produce highly directive structures. This cost function is given by

$$D = \max D(\theta, \varphi) = \frac{4\pi U(\theta, \varphi)}{\int_0^{2\pi} \int_0^{\pi} U(\theta, \varphi) \sin\theta d\theta d\varphi}, \tag{4.1}$$

where $U(\theta, \varphi)$ is the angular radiation intensity, θ is the polar angle, and φ is the azimuthal angle. The PSO employs a swarm with 30 particles to maximize the goal function, exploring the search space over 85 iterations. However, the iterative algorithm normally converged after $\sim$1000 evaluations. Furthermore, we extend the accuracy of the attained solution by feeding it to the local optimization routine (TRO), which also converged within $\sim$900 evaluations to the same results.

4.2.1 Optimization of rectangular antennas

In the first case, we optimize the same rectangular antenna, whose schematic representation is shown in Figure 4.1. We begin by identifying the seven geometric parameters that influence the optimization. These include the director length (DL), director width (DW), reflector length (RL), reflector width (RW), antenna height (H), distance of the field source from the director (DD) and the reflector (RD) (as defined in Section 4.1). These parameters are also highlighted in the schematic. These antennas are first investigated with HfO_2, followed by Si, and finally, Ta_2O_5 whose refractive indices are provided in Table 4.1.

Material	Refractive index (n)
HfO_2	1.9
Si	3.7+0.007i
Ta_2O_5	2.0978+0.0012487i

Table 4.1: List of refractive indices of different materials used in this investigation.

4.2.1.1 HfO_2 antennas

We begin with the directivity enhancement of the HfO_2 antennas. The optimization process produces a structure with design parameters summarized in the Table 4.2. Compared to the leaky-wave structure presented in Refs. [99, 110], the optimized antenna has a larger footprint.

Antenna Elements	Length (nm)	Width (nm)	Height (nm)	Separation (nm)
Director	DL = 3290	DW = 2000	H = 250	DD = 10
Reflector	RL = 330	RW = 3280	H = 250	RD = 160

Table 4.2: Design parameters of the optimized HfO_2 rectangular antenna obtained using a combination of PSO and TRO.

The calculated angular directive gain distribution of the optimized antenna is depicted in Figure 4.12. The tightly focused main lobe is directed into the substrate at an angle of $\theta = 41°$ and

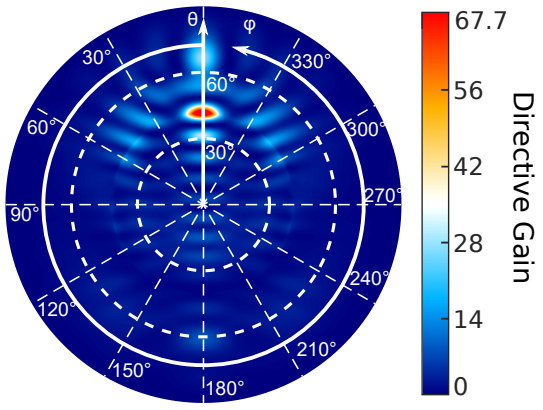

Figure 4.12: Calculated angular linear directive gain distribution of the optimized HfO_2 rectangular antenna exhibiting an in-plane directivity of $D = 67.7$ at $\theta = 41°$ and $\varphi = 0°$.

$\varphi = 0°$. A significantly improved linear directivity of 67.7 (18.3 dB) is demonstrated, in contrast to the 29.2 (14.65 dB) directed at $\theta = 66°$ by its leaky-wave counterpart [99]. This implies that the traveling guided modes govern the radiation characteristics of the optimized antenna. However, the emission pattern also possesses a weaker emission spot at $\theta \approx 68°$, most likely produced by the leaky modes. Thus, the highly directive nature of the structure is attributed to the contribution of both its leaky and guided modes.

To analyze the cause of the directive nature, we perform an eigenmode analysis to identify the guided modes supported by the director. The analysis reveals that the dipole excites seven guided modes in the waveguide-like director together with the leaky modes. These include three TE, two TM, and two hybrid modes with mode profiles, as shown in Figure 4.13c, highlighting the percentage of the input optical power they carry. The mode overlap integral with the aid of transverse components of the near-field calculates the power coupled to each orthogonal mode. Among the seven modes, $TE_{0,0}$ and $TE_{0,2}$ modes are strongly excited, with 27% and 14% of the input power coupled to them, respectively. This implies that these modes significantly influence the electromagnetic fields, thus governing the radiation pattern and improving the directivity. Other modes in the director are weakly excited with almost no power coupled to them, and the remaining power is found in the leaky modes, which also contributes to the radiation efficiency of the antenna. Furthermore, considering zero material losses in the antenna, the structure also exhibits a near-unity radiation efficiency that is highly desirable.

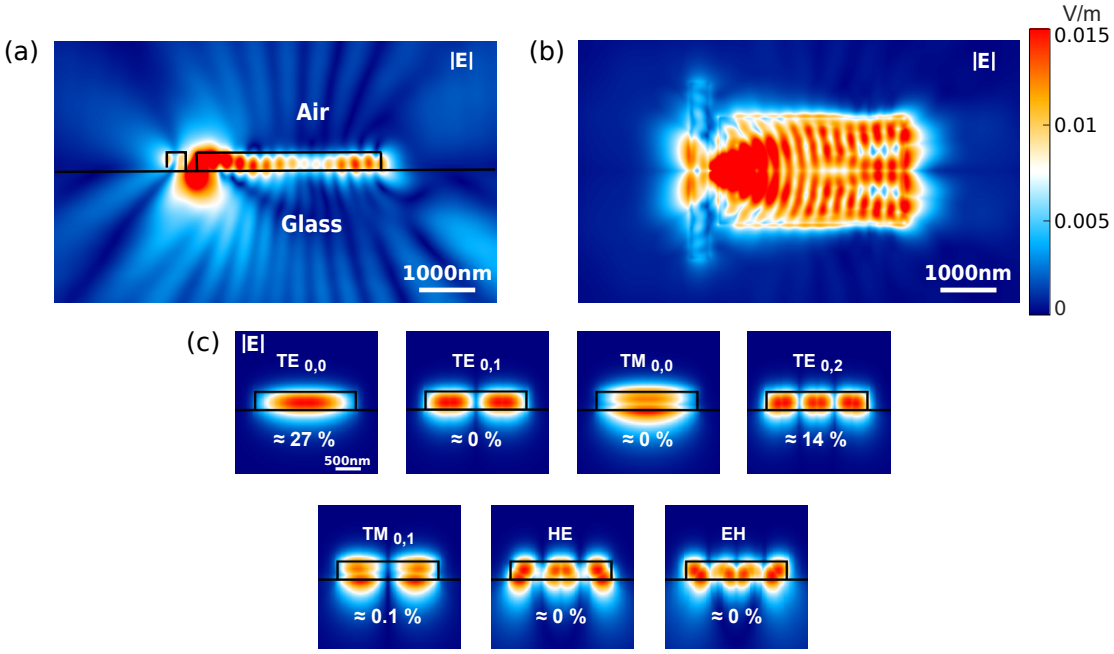

Figure 4.13: Calculated absolute electric field $|\mathbf{E}|$ (linear scale) of the optimized HfO_2 rectangular antenna in the (a) xz-plane at $y = 0$ and (b) xy-plane at $z = 0$, as produced by a y-oriented dipole emitter. (c) The absolute electric field intensity distribution of the first seven guided modes excited by dipole emitter in the optimized director featuring the amount of power coupled to them.

In Figure 4.13a and b, we can observe the electric near-field distribution along the structure. The antenna exhibits guided propagation along the director's length, with consecutive multi-mode interference effects. The strongest local electric field enhancement appears near the dipole, where the power couples into the modes of the director. The field weakens in the middle of the director due to destructive interference of the modes. It then strengthens again at the end facet of the director, attributing to the constructive interference of the modes. This demonstrates a constant interplay between the leaky and guided modes, resulting in the constructive and destructive interference of the electromagnetic fields.

We also perform a sensitivity analysis for each design parameter with respect to its directivity, thus giving an overview of the robustness of the optimized antenna. Figure 4.14 demonstrates directivity (blue curve) and the polar angle of the main lobe (gray curve) as a function of each design parameter. The optimum of each parameter is represented with the red dot, which together produces the directivity of 67.7 (18.3 dB). The directivity can be changed significantly by adjusting just a few design parameters. Figure 4.14a displays the directivity with the variation of the main lobe angle as a function of DL. The state of interference fringes formed by the dominant guided modes at the end facets of their corresponding directors constantly influences each configuration shown for this parameter. As DL increases, the influence of the leaky modes decreases, but the number of guided modes supported by the director remains the same. However, increasing DW and H leads to an increase in the number of guided modes excited by the dipole source. As seen in Figure 4.14b and c, both of these parameters have prominent resonant

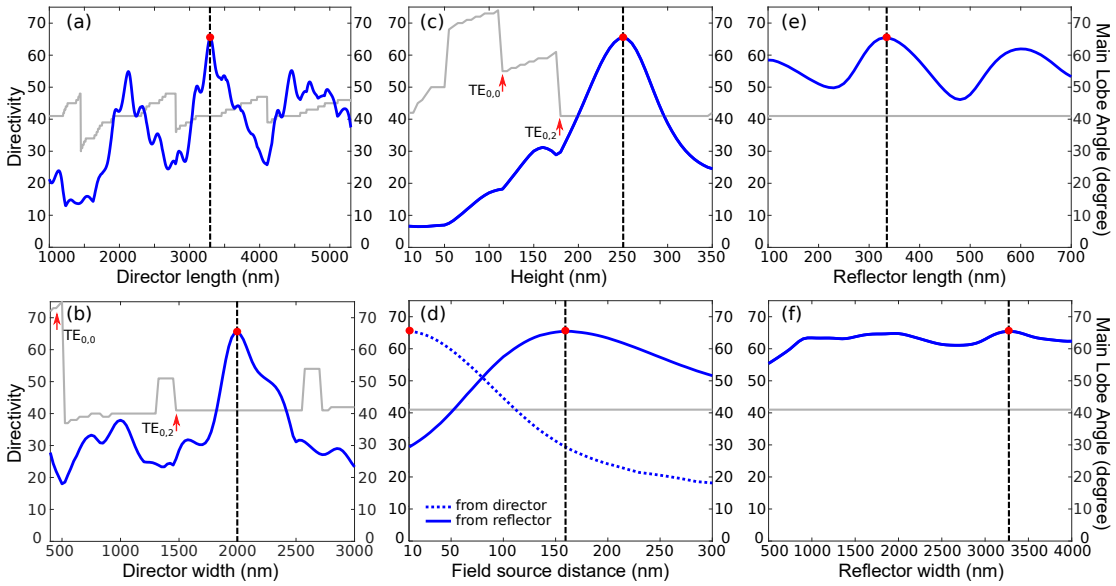

Figure 4.14: Results of the sensitivity analysis conducted on the seven considered parameters of the optimized HfO_2 rectangular antenna: (a) the director length (DL), (b) director width (DW), (c) antenna height (H), (d) distance of the field source from the director (DD) and the reflector (RD), (e) reflector length (RL), and (f) reflector width (RW). The red point and dashed line in each plot represent the optimized value of the respective parameter, as given in Table 4.2. The gray curves highlight the main lobe angle θ for the respective parameter configuration, and the red arrows depict the point from which the highlighted guided mode is supported.

peaks of directivity, which can be explained as a result of the specific state of interference from the increased number of guided modes. Strikingly, the emission angle is majorly influenced by the height of the antenna until the $TE_{0,2}$ mode is excited, beyond which the impact is negligible. Similar behavior is also observed in the case of DW. Interestingly, the optimum always occurs after the $TE_{0,2}$ mode is excited, as pointed out by the red arrows. This also displays the significance of the $TE_{0,0}$ and $TE_{0,2}$ modes in achieving the optimum. In contrast, the variation of the directivity is relatively smooth for increasing dipole source distances from the director and reflector (see Figure 4.14d). Notably, the directivity reduces for growing separation between the dipole source and the director. This can be associated with the decrement in the near-field coupling. On the other hand, the directivity is not substantially affected by variation of the reflector dimensions, as shown in Figure 4.14e and f. However, a Fabry-Pérot behavior is seen in the longer reflectors, and the reflector dimensions or the dipole position have no influence on the main lobe emission angle.

4.2.1.2 Si antennas

The rich linear and non-linear optical properties of silicon have resulted in its extensive use for photonic devices in the last decade [31, 126, 127]. Therefore, in this section, we study antennas made of Si on SiO_2 substrate. The large refractive index contrast between Si and SiO_2 can enhance the antenna's propagation characteristics, essential in achieving better directivity. The antenna has the same design parameters as in Figure 4.1. Using the same cost function, the hybrid optimization routine with PSO and TRO converges to the design parameters provided in Table 4.3.

Antenna Elements	Length (nm)	Width (nm)	Height (nm)	Separation (nm)
Director	DL = 7840	DW = 1545	H = 29	DD = 10
Reflector	RL = 380	RW = 720	H = 29	RD = 130

Table 4.3: Design parameters of the optimized Si rectangular antenna obtained using a combination of PSO and TRO.

This optimized structure preserves the superior directive nature of the HfO_2 rectangular antenna with a pronounced main lobe and slightly higher side lobe level (see Figure 4.15a). The structure exhibits a linear directivity of 74.8 (18.74 dB), which is higher than that from the HfO_2 antenna and has its main lobe directed at $\theta = 66°$ and $\varphi = 0°$. However, the director height is much smaller than the HfO_2 analog. This can be associated with the large refractive index contrast, which requires a smaller height to support modes with almost the same N_{eff} as the guided modes excited in the HfO_2 director [99]. The point source excites four guided modes, all being TE modes, and their mode profiles are shown in Figure 4.15b. Again, most of the power is coupled to the $TE_{0,0}$ (27%) and $TE_{0,2}$ mode (7%), showing their significance in achieving this highly directive pattern.

In Figure 4.15c, one sees the less-confined guided propagation of the modes in the director, which is mainly due to the small antenna height. However, the recurring constructive and destructive interference of these modes through the director is visible in Figure 4.15d. Notably, despite the material losses in Si, the antenna still illustrates a high radiation efficiency of almost

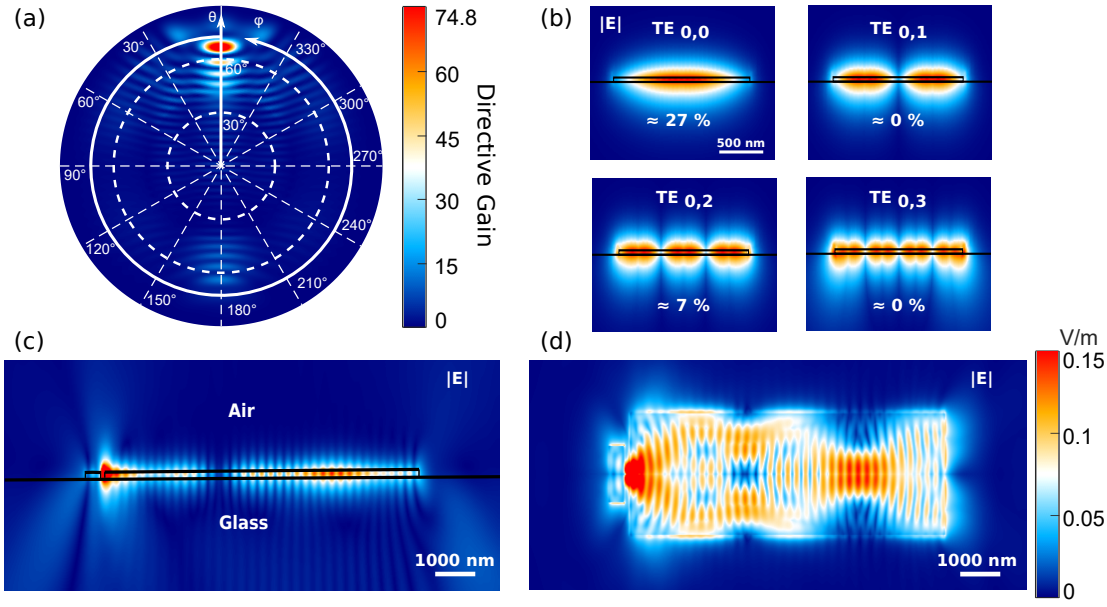

Figure 4.15: (a) Calculated angular linear directive gain distribution of the optimized Si rectangular antenna exhibiting an in-plane directivity of $D = 74.8$ at $\theta = 66°$ and $\varphi = 0°$. (b) The near-field intensity distribution of the four guided TE modes propagating in the director with the percentage of input power carried by them. (c,d) Calculated near-field distribution $|\mathbf{E}|$ of the optimized antenna in the (c) xz-plane at $y = 0$ and (d) xy-plane $z = 0$.

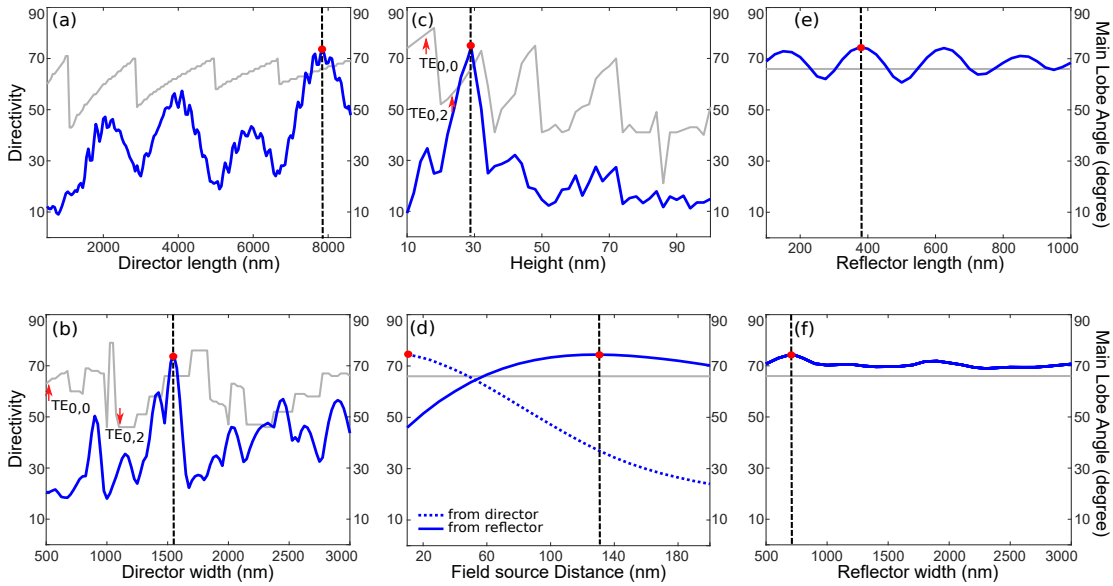

Figure 4.16: Sensitivity analysis of the seven considered parameters of the optimized Si rectangular antenna. The gray curves highlight the main lobe angle θ for the respective parameter configuration and the optimized values are marked with the red point and dashed line.

94%. Furthermore, the sensitivity analysis performed on the Si antenna has similar results like its HfO_2 counterpart. Figure 4.16 illustrates the results of the sensitivity analysis for each design parameter.

4.2.1.3 Ta_2O_5 antennas

As the next step, we validate the results obtained from the HfO_2 and Si antennas. For this purpose, the antennas were fabricated using a two-step electron beam lithography[3]. However, due to experimental difficulties, it was easier to fabricate the antennas using Ta_2O_5 rather than the other two materials as Ta_2O_5 could be more easily evaporated. Furthermore, Ta_2O_5 approximately has the same refractive index as HfO_2 and hence would illustrate similar optical properties like HfO_2 for validating our results. Additionally, at 780 nm, Ta_2O_5 possesses low losses making it a suitable material for our studies.

We perform the numerical optimization for the antenna composed of Ta_2O_5, again targeting improved directivity as the cost function for the hybrid optimization routine. The results for the design parameters from the optimization are presented in the Table 4.4.

Antenna Elements	Length (nm)	Width (nm)	Height (nm)	Separation (nm)
Director	DL = 5710	DW = 2730	H = 100	DD = 20
Reflector	RL = 395	RW = 860	H = 100	RD = 170

Table 4.4: Design parameters of the optimized Ta_2O_5 rectangular antenna obtained using a combination of PSO and TRO.

The scanning electron micrograph (SEM) of this fabricated optimized antenna is shown in Figure 4.17. The red box between the director and reflector represents the region where hundreds of QDs are deposited to serve as the excitation source.

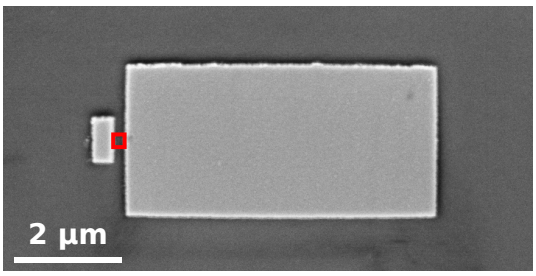

Figure 4.17: Scanning electron micrograph of the optimized Ta_2O_5 rectangular antenna. The red square marks the region where the QDs are deposited [101].

The eigenmode analysis reveals that the director supports three guided TE modes apart from the leaky modes. The guided propagation of these modes can be visualized in the near-field distribution of the optimized antenna shown in Figure 4.18a. The mode profiles featuring the percentage of input power carried by them are shown in Figure 4.18b. As predicted before, among the guided modes, the $TE_{0,0}$ and $TE_{0,2}$ modes carry the highest proportion of the input power, signifying their crucial role in governing the directional characteristics.

[3]The antennas were fabricated and measured by colleagues from the department of Prof. Dr. Thomas Zentgraf at Paderborn University and Prof. Dr. Stefan Linden at Bonn University.

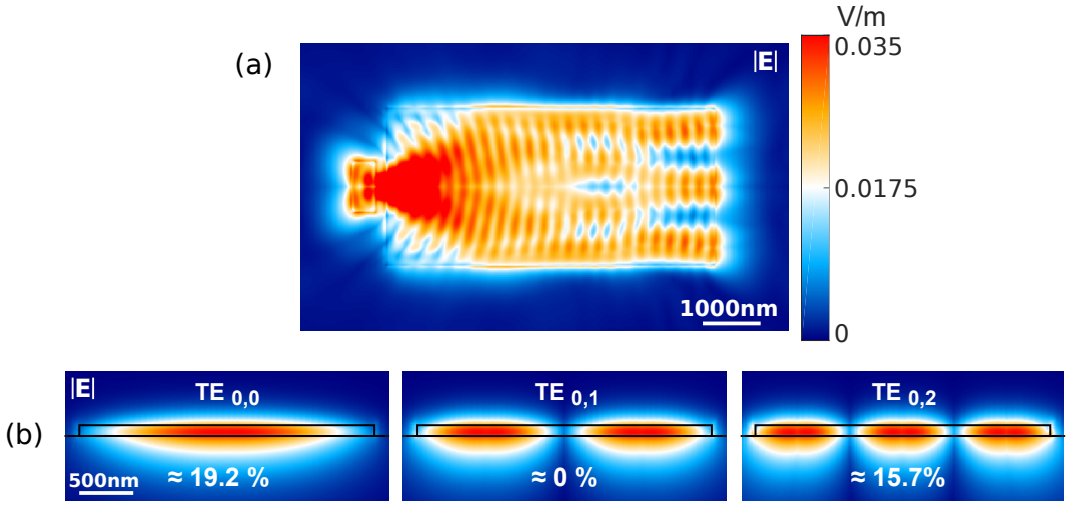

Figure 4.18: (a) Calculated near-field distribution ($|\mathbf{E}|$) of the optimized Ta_2O_5 rectangular antenna at $z = 50\,\text{nm}$ in the xy-plane. (b) Calculated electric field intensity distribution of the first three guided modes supported in the director with the percentage of input power carried by them.

The interference of these modes, mainly arising from the end facet of the director, results in a linear directivity of 63.1 (18 dB) with a main lobe angle of $\theta = 69°$ and $\varphi = 0°$. This is demonstrated by the calculated and measured angular directive gain distributions shown in Figure 4.19. Both the radiation patterns are in good qualitative agreement with one another, although some discrepancies are visible in the higher polar angles. This mainly comes from the fact that the numerical aperture of the experiment limits the highest collection angle to $\theta_{NA} = 79°$. Furthermore, the main lobe slightly deviates from the antenna axis ($\varphi = 0$), which

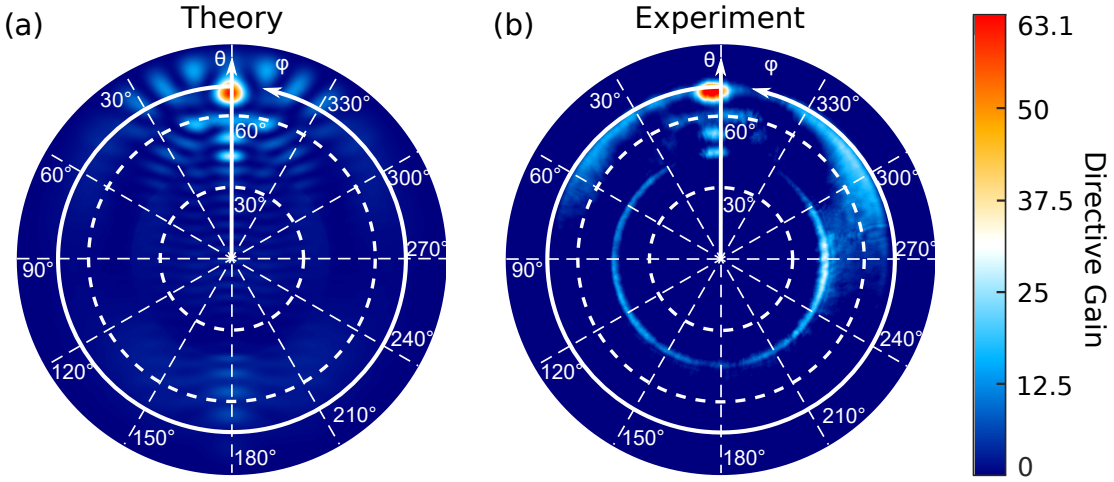

Figure 4.19: (a) Calculated angular linear directive gain distributions of the optimized Ta_2O_5 rectangular antenna exhibiting an in-plane directivity of $D = 63.1$ at $\theta = 69°$. (b) Measured far-field intensity distribution normalized to the theoretical maximum [101].

stems from the displacement of the cloud of quantum dots from the optimal position along the y-axis (as discussed in Section 4.1.1.2). Finally, the ring-like feature at $\theta = 41.5°$ comes from the uncoupled QDs that radiate power into the substrate at all azimuthal angles.

4.2.2 Optimization of horn antennas

To further improve the directivity, we explore different antenna geometries. One such geometry is that of a horn antenna. Conventionally, they are simple to construct and are non-resonant antennas with broadband operating capabilities. By varying the tapered design characteristics of the flared section, one can obtain excellent directional attributes for a wide range of frequencies [100]. Thus, the investigation of a dielectric equivalent of the horn antenna is sought in the following section.

4.2.2.1 HfO_2 and Si antennas

This section examines the characteristics of HfO_2 and Si horn antennas. These antennas have a rectangular reflector and a director that resembles an H-plane sectoral horn [29]. We utilize the same optimization setup and design parameters as for rectangular antennas, but we consider two more parameters to describe the flare section of the antenna: the horn length (HL) and the horn width (HW) at the flared end of the director. Figure 4.20 provides a schematic representation of the antenna highlighting its design parameters. Again the hybrid optimization routine is employed with the objective to maximize the directivity.

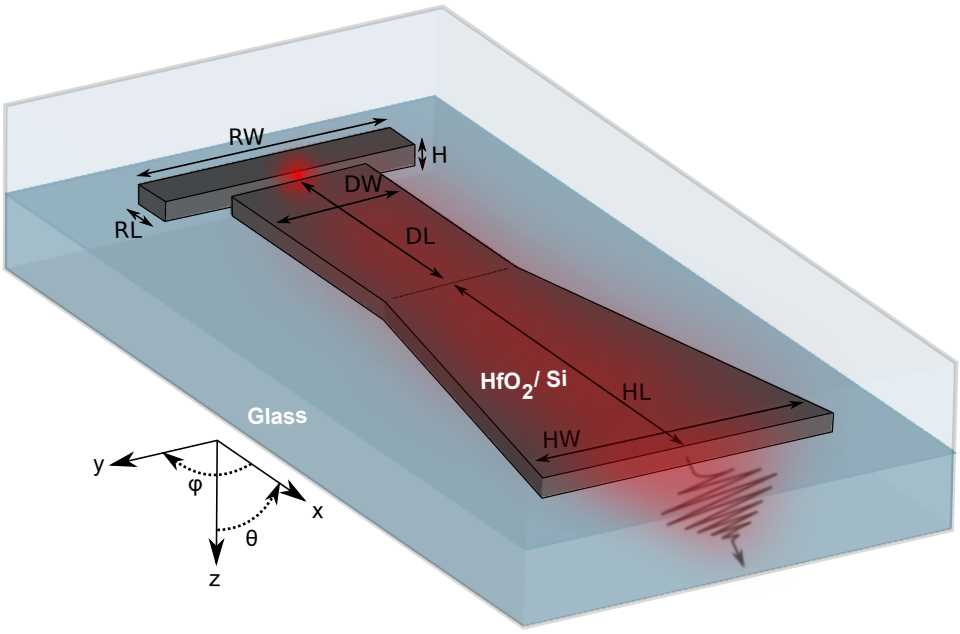

Figure 4.20: Schematic representation of the horn antenna, defined by nine design parameters: director length (DL), director width (DW), antenna height (H), horn length (HL), horn width (HW), reflector length (RL), reflector width (RW), and distance of the field source from the director (DD) and the reflector (RD). The red color depicts the power coupled to the guided and leaky modes that propagate through the director and radiate into the substrate.

The optimized values of the design parameters of the HfO_2 and Si horn antennas are presented in Table 4.5.

Design parameters	HfO_2 (nm)	Si (nm)
Horn length (HL)	5300	5920
Horn width (HW)	4085	4290
Director length (DL)	3500	4980
Director width (DW)	1935	1940
Antenna height (H)	255	40
Reflector length (RL)	595	890
Reflector width (RW)	3535	780
Director distance (DD)	30	10
Reflector distance (RD)	185	145

Table 4.5: Design parameters of the optimized HfO_2 and Si horn antennas obtained using a combination of PSO and TRO.

The optimized horn antennas are larger than their rectangular-shaped counterparts but boast a more concentrated emission pattern with higher directivity. This becomes evident from the angular linear directive gain distribution with a tightly focused pin-like main lobe at $\theta = 41°$ and $\theta = 49°$, possessing a directivity of 114 (20.56 dB) and 157 (21.95 dB) for the HfO_2 and Si horn antennas, respectively (Figure 4.21).

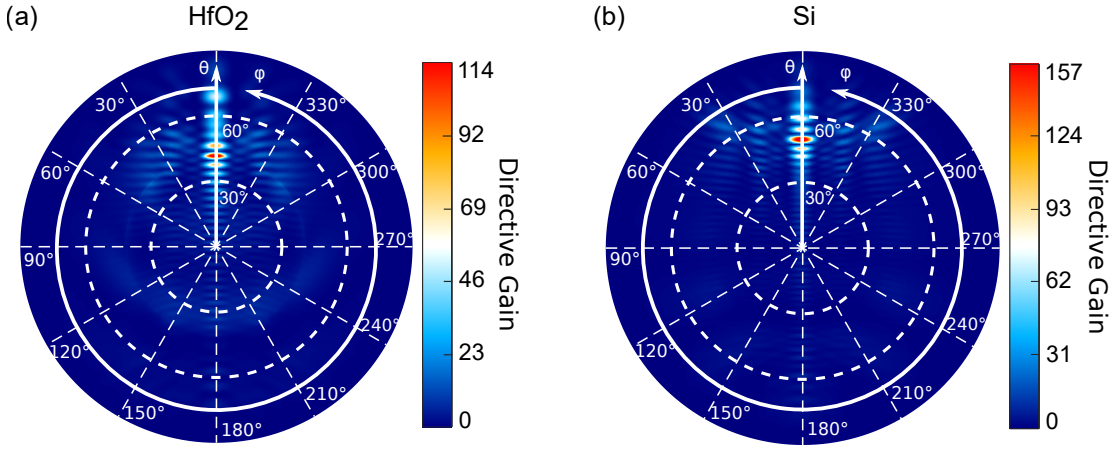

Figure 4.21: Calculated angular linear directive gain distribution of the optimized (a) HfO_2 and (b) Si horn antennas exhibiting an in-plane directivity of $D = 114$ at $\theta = 41°$ and $D = 157$ at $\theta = 49°$, respectively.

However, both structures possess slightly greater side lobe levels. This issue can be tackled with small variations in the horn section of the antenna, which strongly controls the radiation pattern. This feature is demonstrated in Figure 4.22, where the side lobe level (SLL) is plotted as a function of the HL and HW for the HfO_2 (blue curve) and Si (gray curve) antenna. The red dots in each plot represent the optimum configuration of both antennas. As it can be seen in Figure 4.22a, the SLL varies strongly with slight variations in HL for both antennas. However, changes in HW have a minimal influence on the SLL in the HfO_2 antenna but a more substantial

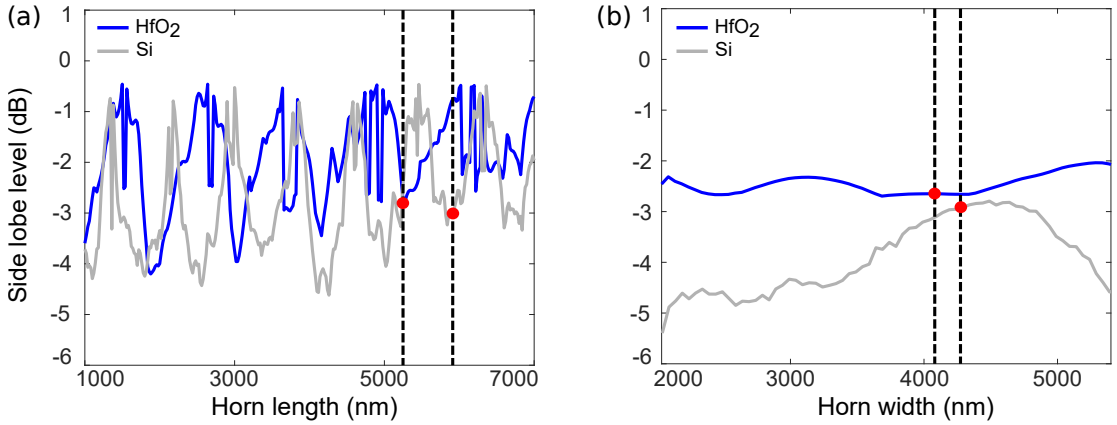

Figure 4.22: Side lobe level of the optimized HfO_2 (blue curves) and Si (gray curves) horn antenna as a function of its: (a) horn length and (b) horn width. Each plot features a red point and a dashed line that indicates the optimized value for that respective parameter.

effect in the Si antenna.

Notably, despite the different dimensions of the antennas, both the structures possess the same flare angle of $\approx 11^{\circ}$, implicating its vital importance in governing the radiation properties. Furthermore, the eigenmode analysis of the HfO_2 director indicates the presence of three TE and three TM modes in the rectangular section of the director. The Si antenna supports seven TE modes, but no TM modes due to its smaller height coming from a significant refractive index

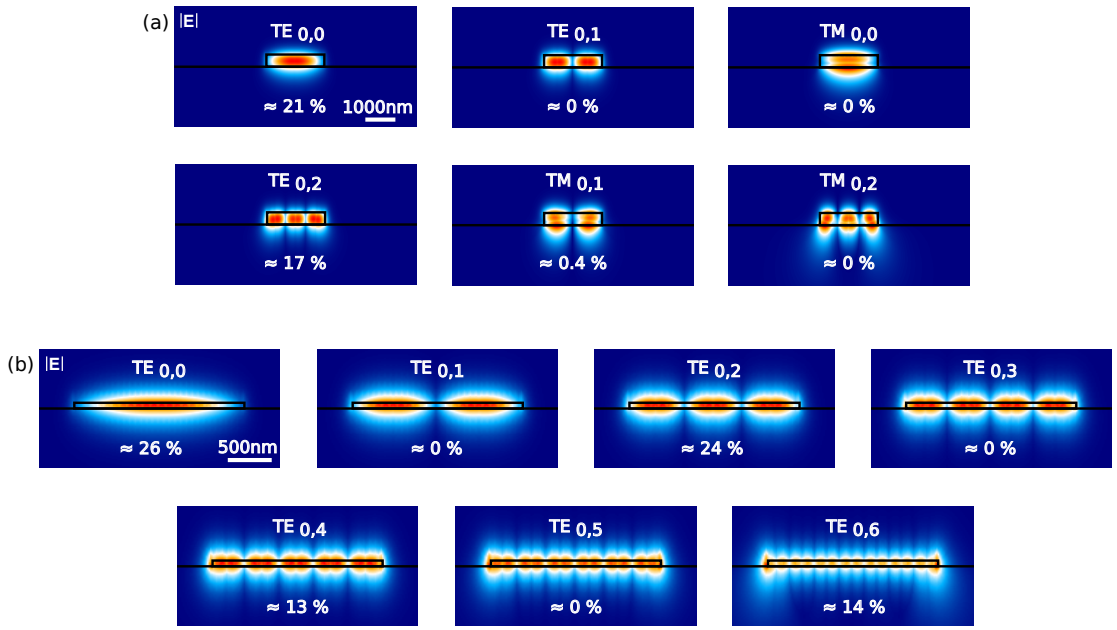

Figure 4.23: The electric field intensity distribution of the guided modes supported in the rectangular section of the optimized (a) HfO_2 and (b) Si director of the horn antenna. Each mode profile also highlights the percentage of input power carried by them.

contrast. These mode profiles from the rectangular section of both the antenna directors are illustrated in Figure 4.23, highlighting the amount of power coupled to them. Again, only the $TE_{0,0}$ and $TE_{0,2}$ modes carry most of the power in both the antennas and govern the radiation patterns. Interestingly, the Si antenna also supports the $TE_{0,4}$ and $TE_{0,6}$ modes, which have approximately 13% and 14% of the optical power coupled to them, respectively. The combination of these modes leads to the Si antenna's high directivity of 157 ($21.95\,\mathrm{dB}$). Furthermore, the flared section of both the directors supports other higher-order guided modes in addition to the ones excited in the rectangular section. But these higher-order modes carry negligible input power in them.

Figure 4.24 represents the simulated electric near-field distribution of both the antennas, highlighting how these modes interact with each other along the director. The fields emerging from both the horn antennas showcase similar radial patterns. Additionally, negligible back reflections to the flare section are observed, indicating the property of good impedance matching of these structures, which is an important feature of the horn antennas. It is noteworthy that the HfO_2 antenna has almost perfect radiation efficiency, while the Si antenna only has a radiation efficiency of 52% due to its extinction coefficient and larger antenna size.

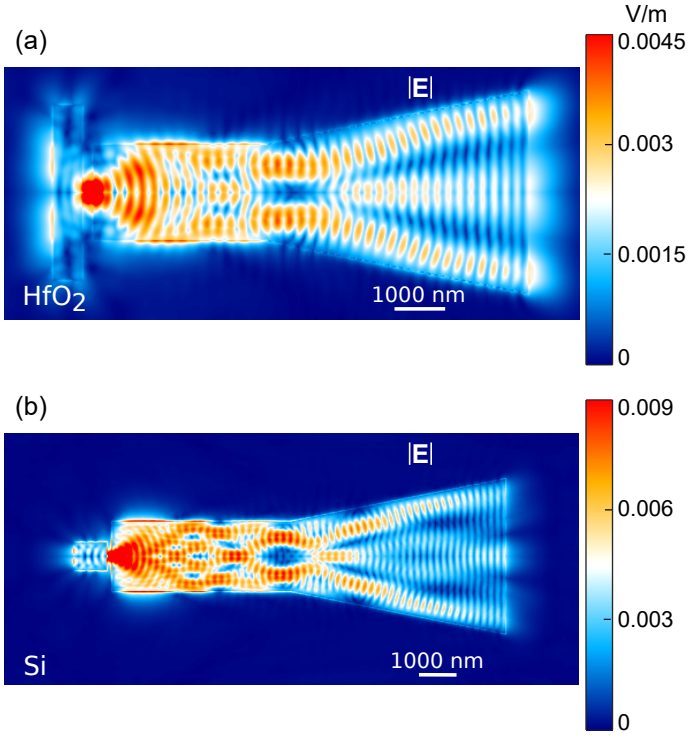

Figure 4.24: Calculated near-field distributions ($|\mathbf{E}|$) of the (a) HfO_2 and (b) Si optimized horn antennas at $z = 0$ in the xy-plane.

4.2.2.2 Ta_2O_5 antennas

To validate our numerical results from the horn antenna, we start with the optimization of a Ta_2O_5 horn antenna targeting similar attractive functionalities demonstrated by its HfO_2 and Si

counterparts. Using the same numerical setup and optimization routine, the optimized values of the nine design parameters from the optimization are provided in Table 4.6.

Design parameters (nm)
HL = 6400
HW = 4600
DL = 2855
DW = 1750
H = 210
RL = 770
RW = 2610
DD = 25
RD = 190

Table 4.6: Design parameters of the optimized Ta_2O_5 horn antenna obtained using a combination of PSO and TRO.

Figure 4.25 depicts the SEM of the fabricated horn antenna with the optimized parameters from above. To get an insight into the optical properties of the structure, we look at the electric near-field distribution shown in Figure 4.26a, which evidently showcases the interference of the modes excited in the director. The radial patterns emanating from the horn section of this antenna are comparable to those seen in the HfO_2 horn antenna. Additionally, it demonstrates outstanding impedance matching with minimal back reflections. The mode analysis reveals that the rectangular part of the director supports four TE and three TM modes, with the majority of the optical power being coupled to the $TE_{0,0}$ (26%) and $TE_{0,2}$ (19%) modes, like the other horn antennas considered above. Figure 4.26b showcases the mode profiles and the corresponding coupled power they carry. Furthermore, other higher-order modes are only minimally excited in the horn section of the director.

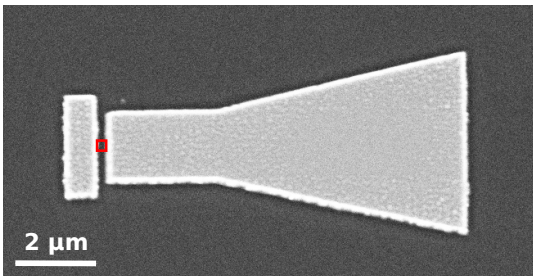

Figure 4.25: SEM of the Ta_2O_5 horn antenna. The red square represents the area where the QDs are deposited [101].

The antenna has a better linear directivity of 119 (20.75 dB) when compared to its rectangular counterpart. This is decisively proven by the ensuing directive gain distribution represented in Figure 4.27a. The needle-like main lobe has an in-plane propagation along $\theta = 41^\circ$ and $\varphi = 0^\circ$, in addition to a higher SLL, which also becomes visible in the far-field pattern represented by a series of concentrated spots along $\varphi = 0^\circ$. It is interesting to note that the optimized antenna exhibits far-field emission properties that are quantitatively similar to its HfO_2 counterpart, demonstrated in Figure 4.21a. These properties include directivity, main lobe angle, and side lobe level, as reported in Ref. [100]. Furthermore, the flare angle is $\approx 12^\circ$, almost the same as

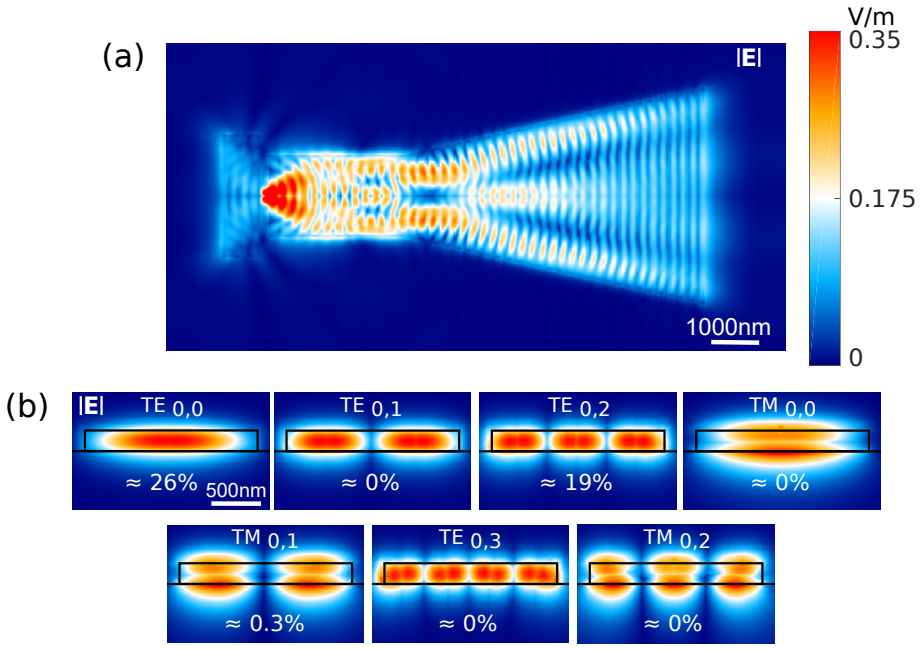

Figure 4.26: (a) The calculated near-field distributions ($|\mathbf{E}|$) of the optimized Ta_2O_5 horn antenna at $z = 50\,\text{nm}$ in the xy-plane. (c) Calculated electric field intensity distribution of the first seven guided modes supported by the director with the percentage of input power carried by them.

in the optimized HfO_2 antenna.

The experimentally measured far-field intensity distribution is depicted in Figure 4.27b. The

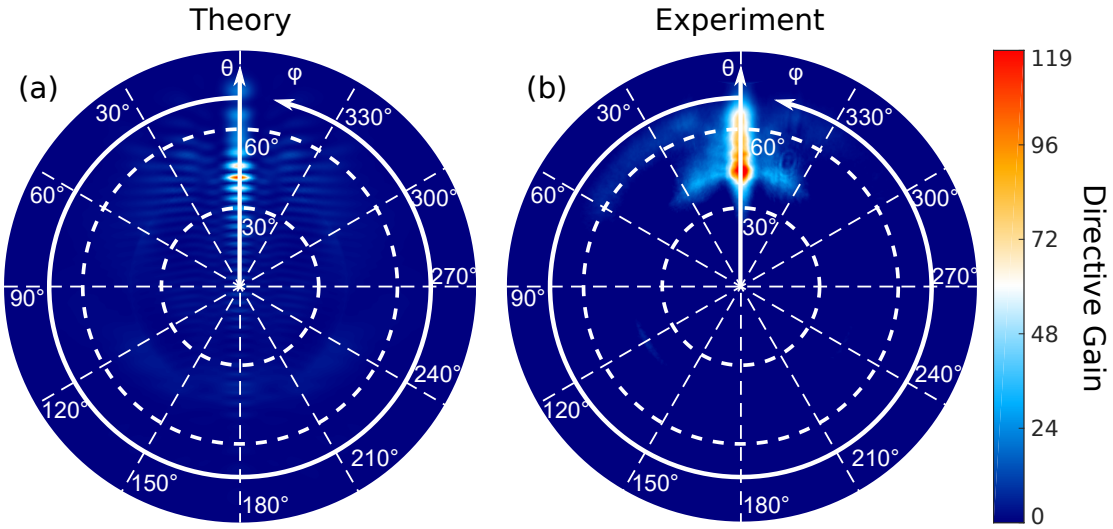

Figure 4.27: (a) Calculated angular linear directive gain distribution of the optimized Ta_2O_5 horn antenna exhibiting an in-plane directivity of $D = 119$ at $\theta = 41°$. (b) Measured far-field intensity distribution normalized to the theoretical maximum [101].

numerical results are consistent with the experimental findings, particularly in terms of the main lobe direction. Nevertheless, the main lobe and side lobes are not clearly separated in the polar direction due to the QDs' distribution around the optimal position, which results in a broadened emission pattern. The broadening effect is more noticeable here in comparison to the rectangular antenna due to the larger number of side lobes that are relatively smaller in size. Additionally, the final angular resolution of the optical setup and the QDs' emission wavelength distribution significantly affect the outcome.

4.2.3 Optimization of tip antennas

We utilize the inspiration from Yagi-Uda antennas and investigate the impact of changing the radiating end of the rectangular antenna [128–131], which is already optimized in Section 4.2.1.3. Our approach involves incorporating supplementary directors, which typically results in an improvement of the in-plane directivity of Yagi-Uda antennas. However, after adding a specific number of directors, the improvement in directivity is only marginal, while the structural size increases. For this reason, we decided to include five identical director components to the optimized rectangle antenna, whose parameters are mentioned in Table 4.4. Keeping the rectangular antenna constant, only the new additional structure is optimized with the same hybrid optimization routine with three new parameters defining it: the length (ADL), width (ADW), and the distance between the elements constructing this additional element (S). To simplify the fabrication process, all five additional directors were designed with the same height as the fundamental antenna section. Interestingly, the optimization results in a structure with all its additional directors attached to one another, i.e., $S = 0$. Thus, creating one tip element having a length $ADL = 4200\,\text{nm}$ and width $ADW = 400\,\text{nm}$. This tip element is attached to the fundamental rectangular antenna's director, as shown in the schematic representation in Figure 4.28a along with the SEM of the fabricated antenna in Figure 4.28b.

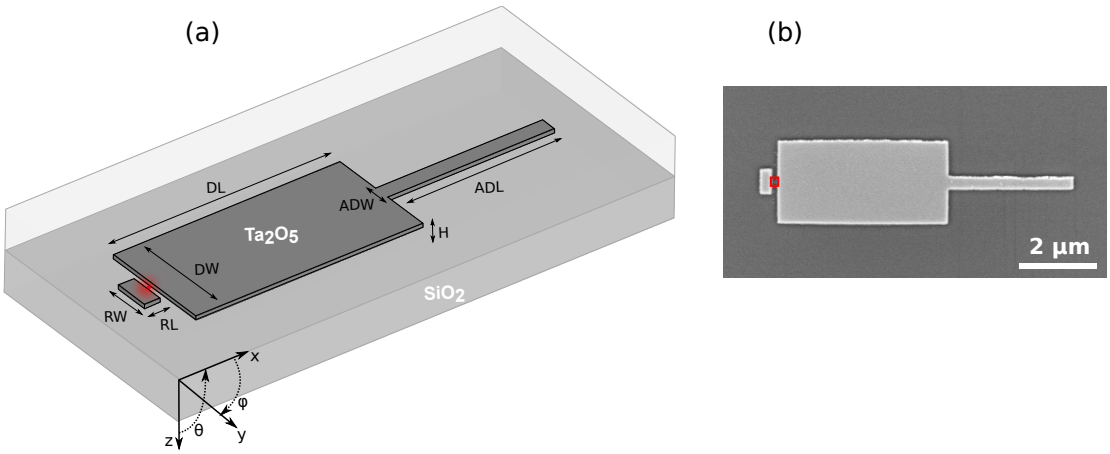

Figure 4.28: Schematic representation of the optimized Ta_2O_5 tip antenna, defined by the following design parameters: the director length (DL) and width (DW), additional tip director length (ADL) and width (ADW), reflector length (RL) and width (RW), antenna height (H), and distance of the field source from the director (DD) and the reflector (RD). (b) SEM of the optimized tip antenna where the red box points to the area where the QDs are deposited [101].

Design parameters (nm)
ADL = 4200
ADW = 400

Table 4.7: Design parameters of the optimized Ta_2O_5 tip antenna obtained using a combination of PSO and TRO.

From the simulated electric near-field distribution and the mode profiles of the excited modes, we can gain insight into the radiation properties of the antenna. Our analysis indicates that out of the three guided modes, the dipole emitter successfully couples to the $TE_{0,0}$ and $TE_{0,2}$ modes in the fundamental region of the antenna (refer to Figure 4.29b). These modes account for approximately 20% and 16% of the input optical power being coupled to them, respectively. However, the tip element of the antenna only supports leaky modes, which can also be observed in the evanescent propagation along the antenna's tip (Figure 4.29a). Therefore, the improved directivity of the tip antenna is based on the interplay between the guided and leaky modes.

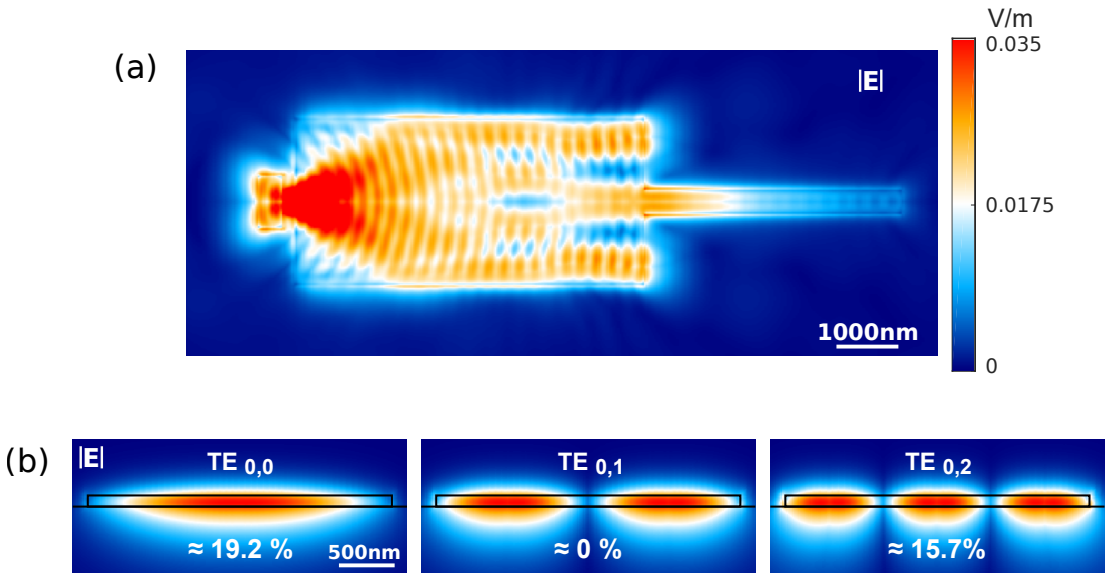

Figure 4.29: (a) The calculated near-field distribution ($|\mathbf{E}|$) of the optimized Ta_2O_5 tip antenna at $z = 50$ nm in the xy-plane. (b) Calculated electric field intensity distribution of the first three guided modes supported by the director together with the quantity of power coupled to them.

Figure 4.30a depicts the calculated far-field emission pattern of the optimized tip antenna that is significantly better than the fundamental rectangular antenna. It has a linear directivity of almost 96.5 (19.85 dB) and a lower SLL in the radiation pattern. The tip antenna also radiates with a similar main lobe angle of approximately $\theta = 70°$. The experimentally measured far-field results demonstrate excellent agreement with the simulated results, as seen in Figure 4.30b, in terms of directionality and SLL. The azimuthal angle of the main lobe is slightly shifted, similar to the rectangular antenna, due to the QDs being displaced from the optimal position.

Finally, by adding two more identical tip elements at the end of the primary rectangular section, the directivity of the tip antenna can be increased to the magnitude of the horn antenna

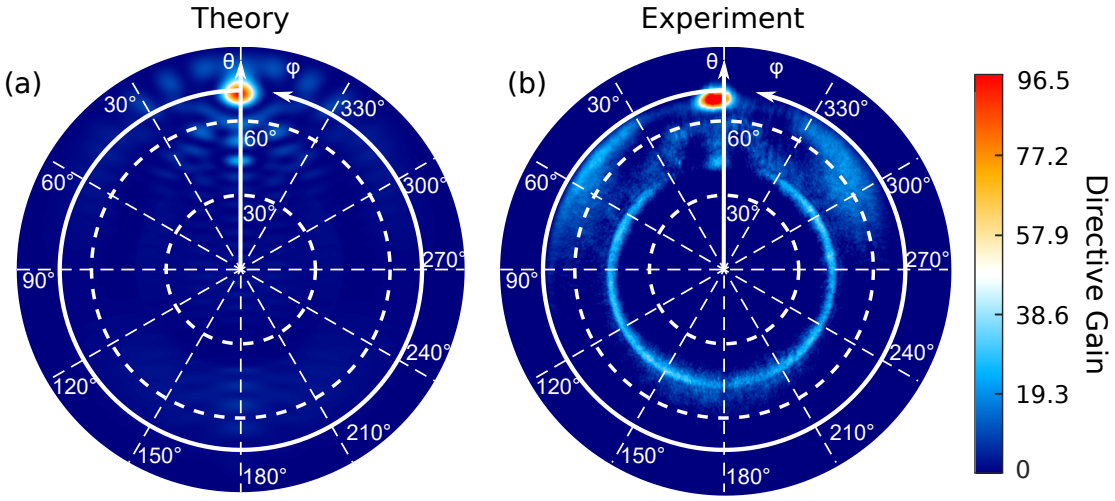

Figure 4.30: (a) Calculated angular linear directive gain distributions of the optimized Ta_2O_5 tip antenna exhibiting an in-plane directivity of $D = 96.5$ at $\theta = 70°$. (b) Measured far-field intensity distribution normalized to the theoretical maximum [101].

(discussed in Section 4.2.2.2). These two elements are added at the points where the other two hot spots are visible in the near-field plot of Figure 4.29a, i.e., on either side of the central hot spot. The near-field distribution of such an antenna can be seen in Figure 4.31. Our calculations demonstrate that such a fork-like structure consists of three channels for directed propagation and boasts a linear directivity of 110.

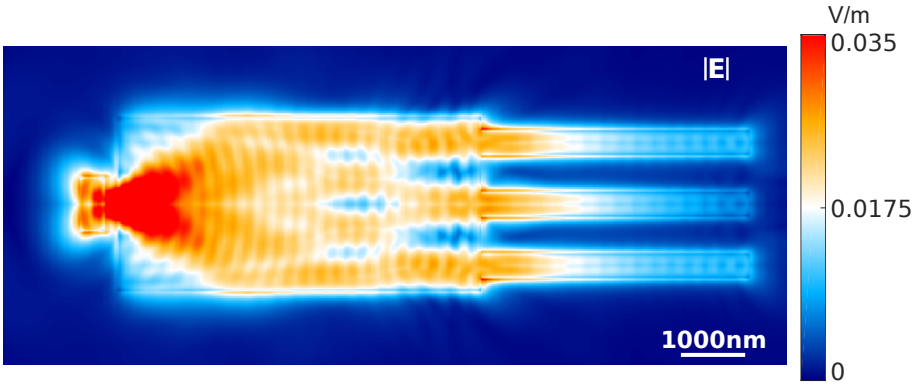

Figure 4.31: The calculated near-field distribution ($|\mathbf{E}|$) of the fork-like antenna at $z = 50\,\text{nm}$ in the xy-plane.

From the above analysis, it becomes clear that the tip element strongly influences the antenna's emission characteristics. For this purpose, we further perform a parametric study on the additional tip section to analyze the impact of each design parameter on its directive nature. Figure 4.32 displays the directivity (blue curves) and main lobe angle (gray curves) for varying tip length, tip width, and antenna height. The optimized value for these geometric parameters is highlighted using the red dots. On the one hand, it can be seen in Figure 4.32a that as the tip length increases, the directivity also increases and illustrates a smooth convergence to

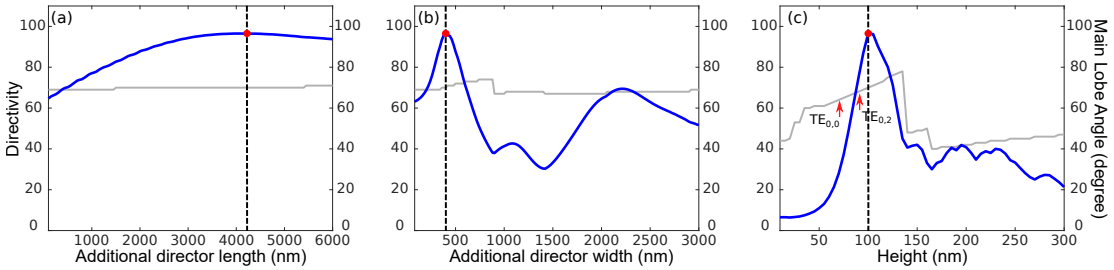

Figure 4.32: Sensitivity analysis for the design parameters defining the tip element of the optimized Ta_2O_5 tip antenna: (a) the additional director length (ADL) and (b) width (ADW), and (c) antenna height (H). In each plot, the red spot and dashed line indicate the optimized value of the corresponding parameter that results in a linear directivity of 96.5. The gray curves illustrate how the main lobe polar angle θ changes for each parameter configuration.

the optimum. On the other hand, resonant behavior is demonstrated by the tip width and the antenna height, which mainly comes from the variation in the number of modes supported by each of these configurations (see Figure 4.32b and c, respectively). Interestingly, the tip length and width do not influence the main lobe angle. However, it is actively governed by the antenna height, which is again attributed to the increasing number of modes excited by different antenna height configurations. With the increasing height, a smooth transition from a leaky-wave to a guided-wave structure takes place. This illustrates the possibility of tailoring the directivity and main lobe angle by manipulating the tip element and the antenna height.

4.2.4 Comparative study of all the investigated antennas

This section summarizes the vital radiation characteristics of all the antennas investigated in this work. For completeness, antennas made of Ta_2O_5 are compared here, as the tip antenna was realized only using Ta_2O_5. Figure 4.33a compares the forward directive gain for all antennas, where the blue, red, and green curves represent the rectangular, horn, and tip antenna, respectively. The gain is plotted as a function of the polar angle θ at $\varphi = 0$. The gray curve represents the same for a configuration without the antenna, consisting of only the dipole emitter on the substrate. It is evident that both the rectangular and tip antennas have their main lobes pointing in nearly the same direction, specifically at angles of $\theta = 69^\circ$ and 70°, respectively (represented by the black dashed lines). This is plausible, as both antennas possess the same height, i.e., $100\,\text{nm}$, and the antenna height has the strongest influence in controlling the main lobe direction (see Figure 4.32c). This also becomes evident with the horn antenna's main lobe pointing at $\theta = 41^\circ$ that comes from its significantly different height of $210\,\text{nm}$. Notably, all antennas display an in-plane directivity, as shown in the Figure 4.33b, where the main lobes from all the three antennas are aligned at $\varphi = 0^\circ$ for their respective polar angles θ. Additionally, the rectangular and tip antennas showcase a near-unity radiation efficiency, but due to the increased volume (height and width) of the material with an extinction coefficient, the horn antenna exhibits a radiation efficiency of 90%.

We compared the forward directivity of the antennas at different wavelengths in Figure 4.34 to observe their behavior across a broad spectrum. We noticed that all the antennas maintain a linear directivity of over 50 for a wide range of frequencies, approximately ~ 350 to $\sim 430\,\text{THz}$, indicating a broadband nature. In the plot, the black dashed line indicates the frequency of

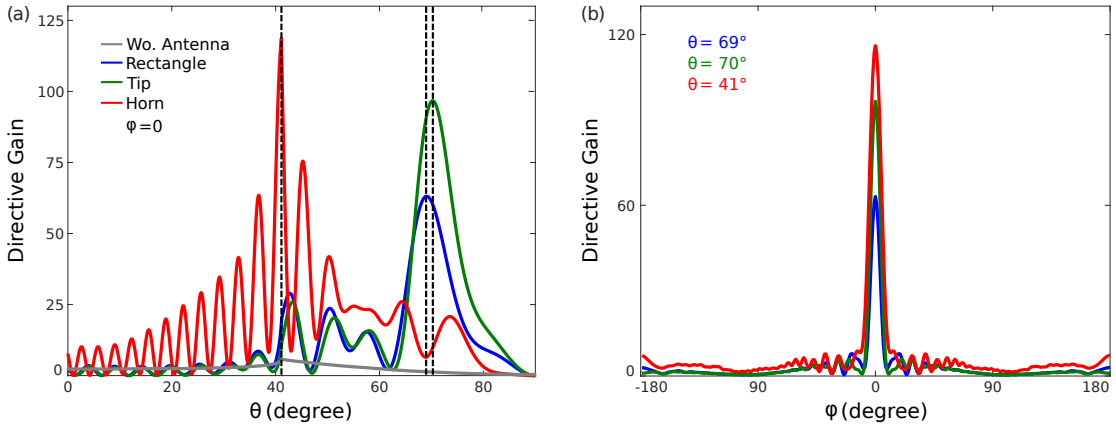

Figure 4.33: Calculated directive gain of the rectangular (blue curve), horn (red curve), and tip (green curve) antennas made of Ta_2O_5. The gray curve represents a dipole on the substrate without any antenna. The gain is plotted as a function of (a) polar angle θ at $\varphi = 0°$, with black dashed lines indicating the directions of the main lobe emission, and (b) azimuthal angle φ at each antenna's respective main lobe angle θ.

operation for our studies. While one may assume that the horn antenna would have the best performance in terms of bandwidth, the tip antenna exhibits a much broader bandwidth than the other two antennas. This can be attributed to the combined contribution of leaky and guided modes.

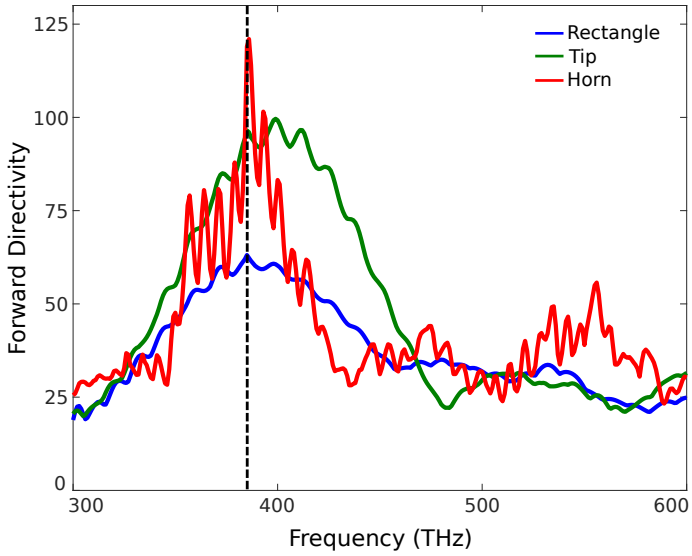

Figure 4.34: Forward directivity of the optimized Ta_2O_5 antennas as a function of frequency, showcasing their broadband nature. The black dashed line marks the frequency utilized in our study.

Furthermore, the Table 4.8 briefly overviews some additional radiation characteristics of these antennas and summarizes the important features from the comparison study. These characteristics include the directivity, front-to-back ratio (F/B), main lobe angle, angular width of the main

lobe, and side lobe level. In particular, the tip antenna presents the best front-to-back ratio and the lowest side lobe level. It also has a broad bandwidth and high directivity, making it the top choice for many applications.

Antenna type	Directivity	F/B	Main lobe	Angular width (-3 dB)	SLL
Without antenna	7 / 8.45 dB	0 dB	42°	21°	-9.8 dB
Rectangular	63.1 / 18 dB	9.14 dB	69°	8.8°	-3.4 dB
Horn	119 / 20.75 dB	11.3 dB	41°	1.8°	-2.1 dB
Tip	96.5 / 19.85 dB	11.57 dB	70°	8.5°	-5.8 dB

Table 4.8: Tabulated summary of the radiation characteristics of the optimized Ta_2O_5 antennas encompassing directivity, front-to-back ratio (F/B), main lobe angle, angular width at $-3\,\mathrm{dB}$, and side lobe level.

Overall, we can establish a design rule for the antennas described in this chapter under three aspects. Firstly, the in-coupling, which requires efficient coupling to the dominant TE modes in the waveguide-like director. Secondly, propagation of the field, which results from the beating of modes propagating through the director. Lastly, the out-coupling of the radiation, which is ensured by impedance matching at that interface. By adjusting the geometrical parameters of the antenna, these features can be addressed. This serves as a general guide for designing highly directive antennas of different dielectric materials in the optical regime. Furthermore, we believe that the directional capabilities of these antennas can be significantly enhanced with an array configuration. This topic will be explored in the following chapter.

Chapter 5

Optical phased arrays[1]

Antennas are vital components in integrated photonic systems, such as optical phased arrays (OPAs). These systems are commonly realized with silicon photonics, which is highly compatible with the complementary metal-oxide-semiconductor (CMOS) process, furnishing cost-effective commercial systems with high yields [132]. OPAs facilitate the dynamic control and manipulation of free-space light with a compact form factor in a non-mechanical manner. This is highly advantageous for incorporating a large number of antennas that facilitate the generation of desired far-field radiation patterns [31]. This chapter primarily focuses on planar OPAs that can be actively used for a wide range of applications, namely, light detection and ranging (LiDAR) [44–47], 3-D holography for augmented-reality displays [43], free-space optical communications [40, 41], optical switches [42], etc.

The investigation of 2-D OPAs has been the subject of many prior studies. In such OPAs, an ideal $\lambda/2$ spacing between the array elements is infeasible due to the inherently large size of the radiating elements. This results in undesirable grating lobes in uniform planar OPAs, which in turn limits the operational beam steering range (FOV) [36]. For example, Ref. [133] demonstrates an 8×8 transceiver array with an inter-element spacing of $33\,\mu$m. Apart from the large area the array occupies, it also has a drastically constrained FOV. This is majorly improved in Refs. [31,43], which demonstrate large-scale OPAS of 64×64 and 128×128 array configurations, having an inter-element spacing of $9\,\mu$m. These systems exhibit a significantly large gain and the possibility of synthesizing desired complex far-field patterns. However, the $9\,\mu$m pitch still limits the grating-lobe-free beam steering range to $\sim 6.8°$. On the other hand, Refs. [38, 134] produce smaller OPAs with a reduced pitch of $5.6\,\mu$m, which improves the array FOV. They also demonstrate the realization of a sparse OPA, where the radiating elements occupy an $N \times N$ grid in a non-uniform manner. Such an implementation displays relatively high gain, low SLL, and an increased number of resolvable spots. Furthermore, Ref. [39] demonstrates the complete elimination of grating lobes by using an annular ring aperture-based OPA, where the radiating elements are arranged in circles of increasing radii. These arrays possess a beam steering range that is no longer limited by the unit cell size but rather the individual radiator's 3- dB beamwidth.

In this chapter, Section 5.1 discusses the common architectures used in planar arrays. In Sec-

[1] This chapter is based on the publications [36, 37] of the candidate.

tion 5.2, we explore different radiating elements that are optimized to be employed in OPAs. Finally, in Section 5.3, we numerically demonstrate the characteristics of a large-scale rectangular array configuration utilizing the optimized radiating elements. Furthermore, we also briefly investigate the performance of circular arrays with these radiators.

5.1 Architecture of the optical phased arrays

An integrated OPA mainly comprises three main components. This includes, firstly, a network to efficiently distribute the optical power to every antenna of the array, generated from one coherent source. Secondly, a system for phase and amplitude modulation for each antenna. Finally, radiating elements, i.e., optical antennas that couple electromagnetic radiation to free space. This section briefly discusses the most common ways these three components are implemented.

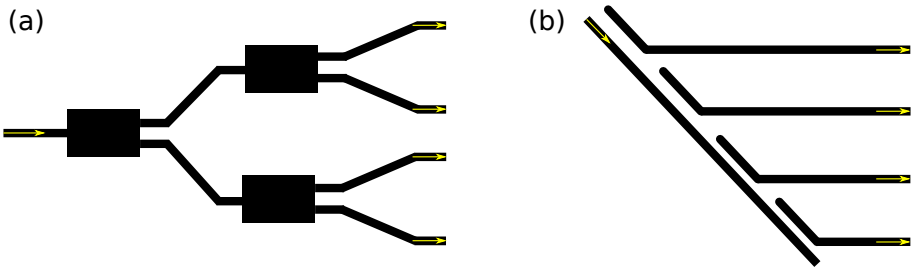

Figure 5.1: Common implementations of the light distribution techniques used in integrated OPAs. Schematic illustration of a (a) splitter tree and (b) cascaded configuration.

Power distribution is commonly done in two ways: 1) using a tree of multiple 1×2 splitters, like Y-splitters or multi-mode interference (MMI) splitters, or 2) using a cascaded system with a series of evanescent couplers that derive the pertinent power from a bus waveguide [135–137]. The representation of both these methods is illustrated in Figure 5.1a and b. While the 1-D arrays could use any of the above networks, 2-D arrays, on the other hand, generally need at least a one-dimensional cascaded power distribution to keep a small antenna pitch.

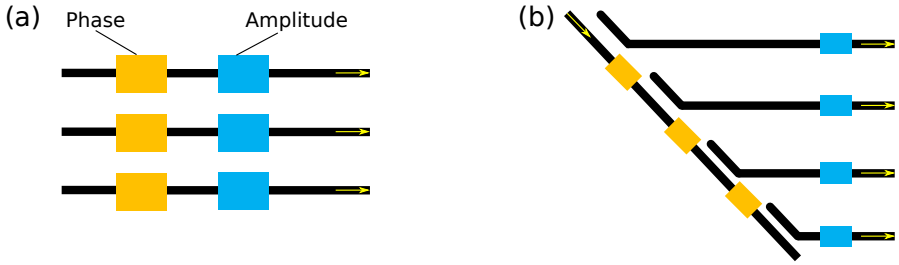

Figure 5.2: Common implementations of the phase tuning section used in integrated OPAs. (a) Individual modulators for phase tuning in each unit cell. (b) Phase shifters incorporated in the bus waveguides of the cascaded network.

Next, an efficient phase-tuning mechanism is needed for each antenna. Again, this is commonly implemented in two ways: directly incorporating the phase shifter with a tunability of 2π in each unit cell or using in-line phase shifters integrated into the bus waveguide of the cascaded power

distribution network. Schematics of both the implementations are shown in Figure 5.2a and b. Both methods provide independent control of these phase shifters, which proves instrumental in generating arbitrary radiation patterns. Furthermore, together with the phase shifters, additional amplitude modulators can also be implemented to control the amount of power reaching each antenna. These modulators do not necessarily need to be present after the power distribution system. Instead, the power distribution system can also be configured to deliver variable optical power to each antenna [138, 139].

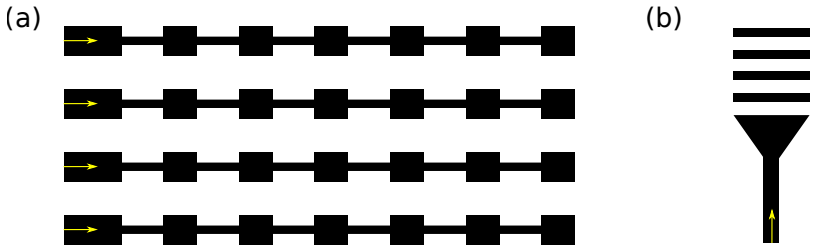

Figure 5.3: Common radiating elements used in integrated OPAs. Schematic illustration of (a) waveguide grating antennas and (b) desired compact optical antennas that can be employed in 1-D and 2-D OPAs, respectively.

Unlike the above two components, the third component, i.e., the optical antennas, is the most relevant to us, as these are the components we analyze in this thesis. Typically, the antennas employed are mostly grating-based structures. The 1-D phased arrays can employ long waveguide grating antennas, as illustrated in Figure 5.3a. However, 2-D phased arrays need to maintain a small pitch, which requires a more compact emitter (see Figure 5.3b). In the upcoming section, we visit different antenna types that can be employed in a 2-D phased array configuration.

5.2 Radiating elements for the optical phased arrays

Conventionally, non-plasmonic implementations of OPAs use well-established grating couplers as their basis for designing optical nanoantennas. Although highly efficient, conventional grating couplers are large, making them difficult to be directly integrated into OPAs. The most common way to address this issue is to scale down grating couplers to fit into the size constraints of an OPA unit cell. However, these scaled versions of the original device are less efficient and, even with optimization, can rarely produce desirable radiation efficiencies, considerable FOV, and well-focused radiation lobes [134]. Hence, designing and optimizing the radiating elements to address these issues is essential for having OPAs with improved radiation characteristics.

In an OPA configuration, the antennas are expected to possess a far-field emission pattern radiating upwards. Typically, this can be achieved by utilizing gratings, partial etches, or reflectors with a high refractive index contrast as a part of the radiating element. Such structures introduce a strong up-down asymmetry [134]. This section explores radiating elements optimized to target challenges like high upward radiation efficiency and improved intensity distribution in the FOV while maintaining a small main lobe angle. All the antennas are designed for an operational wavelength of $1.55\,\mu$m for efficient optical communication with low losses. These antennas are composed of Si ($n = 3.48$) surrounded by an environment of SiO_2 ($n = 1.45$) to

be employed in a 2-D phased array configuration, as proposed in Ref. [31]. The large refractive index contrast between the two materials facilitates a stronger light-matter interaction. The antennas have a height of $h_1 = 220\,\text{nm}$ and are fed by a waveguide with a width of $w = 400\,\text{nm}$. The results of this chapter are obtained utilizing full-wave numerical simulations performed in the frequency domain, employing the finite element method of CST Microwave Studio. Let us look at the different objectives for which the radiating elements were optimized.

5.2.1 Optimizing the upward radiation efficiency

This subsection addresses the challenge of radiating most of the received optical input power in the upward direction. The antennas are optimized to have high upward radiation efficiency that in the far-field can be defined as

$$\eta_{up} = \frac{\int_0^{2\pi} \int_0^{\pi/2} P_{rad}(\theta, \varphi) d\theta d\varphi}{P_{in}}, \tag{5.1}$$

where P_{rad} is the power radiating in the defined computation domain, P_{in} is the input optical power, θ is the polar angle, and φ is the azimuthal angle. Additionally, the optimization is constrained to find structures with broadside emission. Thus, the main lobe angle is limited to $|\theta_{max}| = 10°$. Furthermore, the optimization is performed keeping the technical specifications of the unit cell in mind to fit the optimized radiating element exactly in the same compact footprint of $9\,\mu\text{m} \times 9\,\mu\text{m}$, as the original design in Ref. [31]. Full-wave numerical simulations are performed in conjunction with a hybrid optimization routine that includes particle swarm optimization followed by the trust region method to ensure the likelihood of finding an approximate global optimum (described in Section 3.2.2). The PSO is implemented with a swarm size of 50 particles for 35 iterations, and the TRO considers 1000 evaluations. We propose two structures for the objective discussed above in the following part.

5.2.1.1 Asymmetric horn antenna

Section 4.2.2 already presented the key advantages of employing asymmetric dielectric horn antennas as the radiating elements with high directivity. Therefore, we explore the possibility of integrating this knowledge in the domain of optical phased antenna arrays operating in the C-band (1530-1565 nm) of communication. Here, we introduce a horn antenna with a small flare section, followed by four uniformly thick partial etches along the direction of propagation. Each grating is of a unique length GL_x that is separated by a unique offset OL_x. The schematic of the antenna highlighting all the design parameters used in the optimization is illustrated in Figure 5.4. Eleven parameters are used in the optimization, namely, flare length (FL), grating lengths ($GL_1 - GL_4$), offset lengths ($OL_1 - OL_4$), etch depth (h_2) defining the height of partial etching, and horn width (HW). The antenna is chosen to have only four gratings after analyzing the influence of the number of gratings employed in the antenna system, similar to the additional director study in Section 4.2.3. It is noted that there is no significant influence after four gratings and further addition of such gratings results in minimal increment in the performance that comes at the cost of increased antenna size. This is undesirable when aiming for a compact footprint for the antenna.

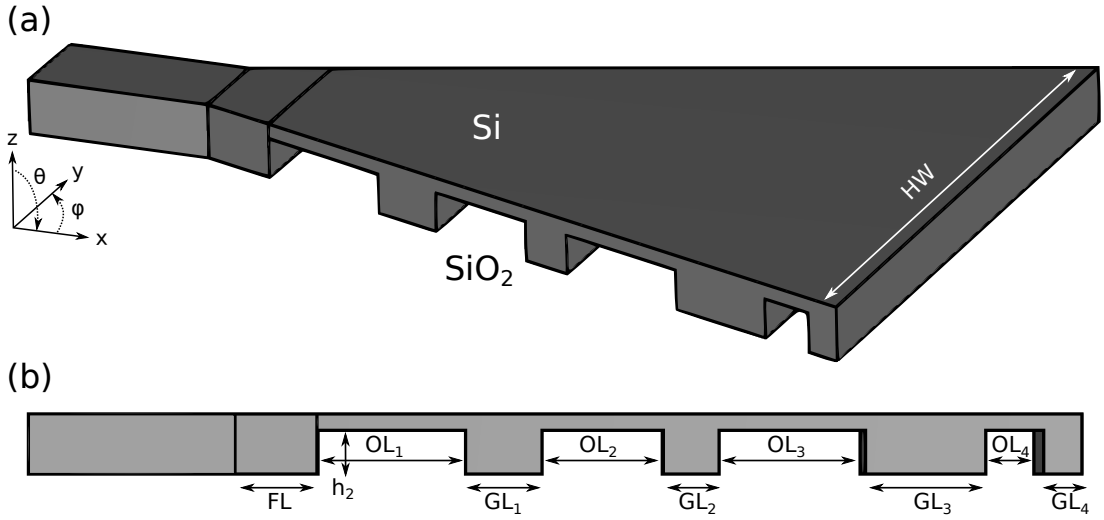

Figure 5.4: Schematic representation of the optimized asymmetric horn antenna viewed from two perspectives. (a) The top view highlights the horn width (HW), and (b) the side view highlights the etch depth (h_2) and the different parameters constituting the horn length, namely, flare length (FL), offset lengths (OL_x), and grating lengths (GL_x).

Design parameters	Dimensions (nm)
Flare length (FL)	300
Grating length (GL_1)	280
Grating length (GL_2)	200
Grating length (GL_3)	430
Grating length (GL_4)	135
Offset length (OL_1)	540
Offset length (OL_2)	440
Offset length (OL_3)	530
Offset length (OL_4)	210
Etch depth (h_2)	160
Horn width (HW)	2600

Table 5.1: Design parameters of the optimized asymmetric horn antenna obtained using a combination of PSO and TRO.

Using the constraints mentioned above, we begin with PSO, where the optimizer converged to its global optimum approximately after 20 iterations. This is followed by a TRO to avoid being stuck with a local optimum. The final optimum values of the design parameters are reported in Table 5.1 for which the antenna has a footprint of $3.06\,\mu\mathrm{m} \times 2.6\,\mu\mathrm{m}$. The near-field power distribution demonstrates that the structures can efficiently diffract more power to the upper hemisphere, as shown in Figure 5.5a. This results from utilizing the partial etch along the length of the horn section. This optimized structure exhibits a linear directivity of 16.5 with the main lobe directed at $\theta = 1^\circ$, possessing a SLL of $-6.8\,\mathrm{dB}$. This is illustrated in the angular linear directive gain distribution in Figure 5.5b.

To take a closer look at the antenna's performance, we analyze the optical response of the

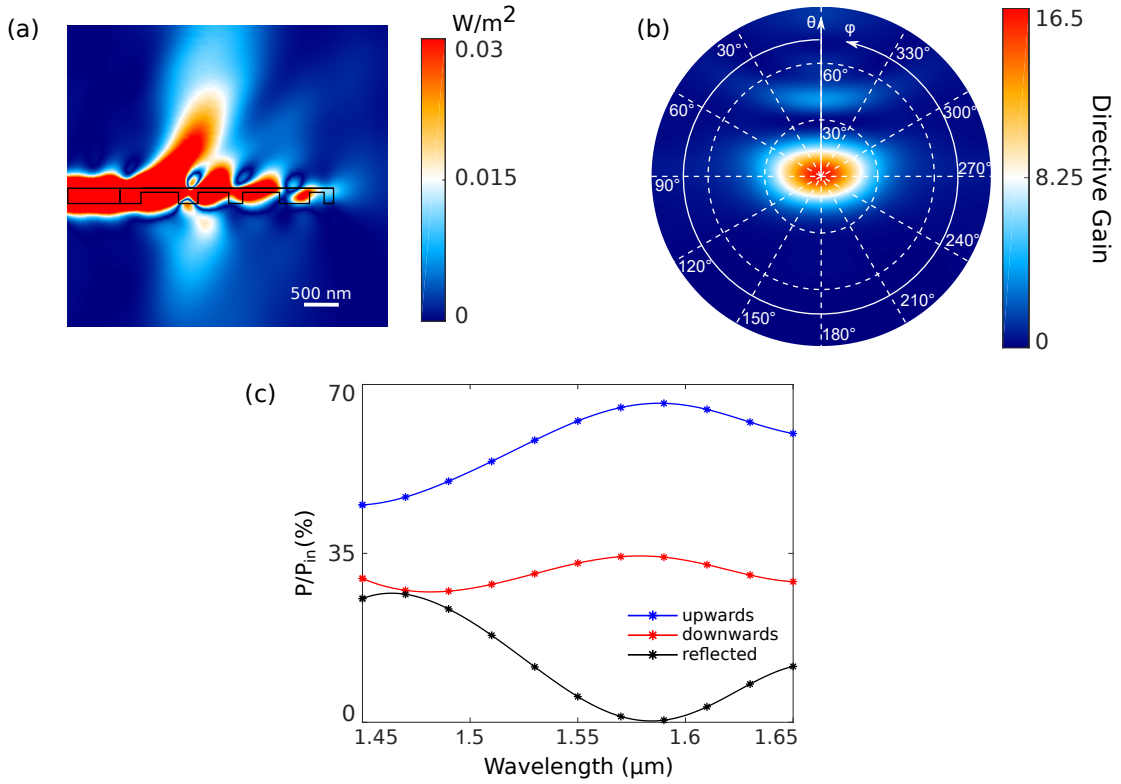

Figure 5.5: a) The calculated near-field power distribution (linear scale) of the optimized asymmetric horn antenna in the xz-plane at $y = 0\,\text{nm}$. (b) Calculated angular linear directive gain distribution of the antenna exhibiting a directivity of $D = 16.5$ at $\theta = 1°$ and $\varphi = 0°$. (c) Calculated optical radiation efficiencies of the optimized asymmetric horn antenna. The blue, red, and black curves represent the upward, downward, and reflected radiation efficiency, respectively.

optimized structure over a range of wavelengths. As seen in Figure 5.5c, the antenna maintains a good upward radiation efficiency of over 50% for the entire range of $1.45 - 1.65\,\mu$m (blue curve), boasting an efficiency of 64% at the design wavelength of $1.55\,\mu$m. Furthermore, the structure presents a downward radiation efficiency of 33% and a reflection efficiency of 3% at $1.55\,\mu$m. Although the downward efficiency is not actively fluctuating over the entire range (red curve), the reflection efficiency is tremendously low between $1.55 - 1.6\,\mu$m (black curve). Overall, the antenna showcases a desirable broadband nature for the entire range of wavelengths.

To further improve the upward radiation efficiency, we investigate the use of a high refractive index reflector in conjunction with the antenna. For this purpose, we consider a reflector made of Si with a thickness of H_{ref} that is placed at a distance Z_{ref} below the antenna and is X_{ref} longer from the end of the horn antenna, as shown in the Figure 5.6. In addition to the eleven parameters of the fundamental antenna, these three new design parameters are utilized in the same hybrid optimization process, and their optimized values are summarized in Table 5.2.

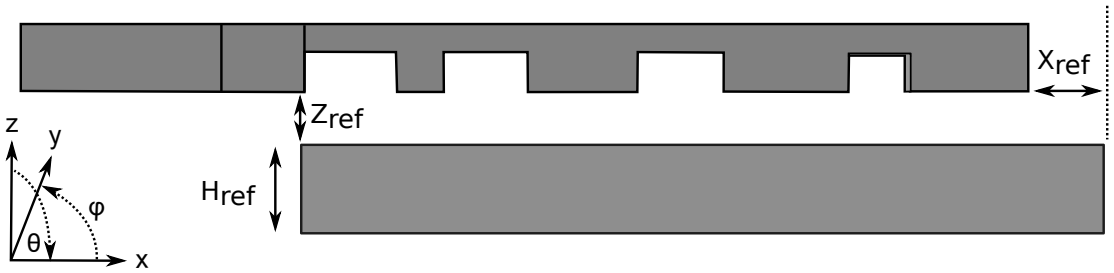

Figure 5.6: Schematic representation of the optimized asymmetric horn antenna with the reflector. The side view highlights the reflector height (H_{ref}) and its offsets from the antenna along the x- and z-axis, namely, X_{ref} and Z_{ref}.

Design parameters	Dimensions (nm)
Flare length (FL)	280
Grating length (GL_1)	150
Grating length (GL_2)	380
Grating length (GL_3)	430
Grating length (GL_4)	400
Offset length (OL_1)	370
Offset length (OL_2)	340
Offset length (OL_3)	350
Offset length (OL_4)	260
Etch depth (h_2)	140
Horn width (HW)	2600
Reflector thickness (H_{ref})	350
z-offset (Z_{ref})	200
x-offset (X_{ref})	300

Table 5.2: Design parameters of the optimized asymmetric horn antenna with the reflector obtained using a combination of PSO and TRO.

With the aid of the reflector, the optimized structure exhibits a much higher upward radiation efficiency with a nearly comparable footprint of $3.26\,\mu$m $\times$ $2.6\,\mu$m. These characteristics are highlighted in the near-field power distribution, demonstrating the upward radiation strengthening (see Figure 5.7a). In the far-field, the antenna has a directivity of 26.5 with the main lobe along $\theta = 4°$, as shown in Figure 5.7b. The antenna has a SLL of -5.2 dB. The improved directivity is manifested in the narrower main lobe compared to the fundamental antenna. Furthermore, Figure 5.7c demonstrates the broadband behavior of this antenna, where the red, blue, and black curves represent the downward, upward, and reflection radiation efficiency, respectively. Like the primary antenna, the new structure also maintains high performance over the entire wavelength range, with peak upward radiation efficiency of 83% at the design wavelength ($1.55\,\mu$m). Implicitly, the antenna produces a lower downward radiation efficiency of 16%, and less than 1% of the optical power is reflected back to the feeding waveguide. However, such reflectors come at the cost of increased fabrication complexity due to the need for multi-layer silicon photonics processing. Therefore, we consider an alternate design approach that can produce a comparable performance but with reduced fabrication efforts.

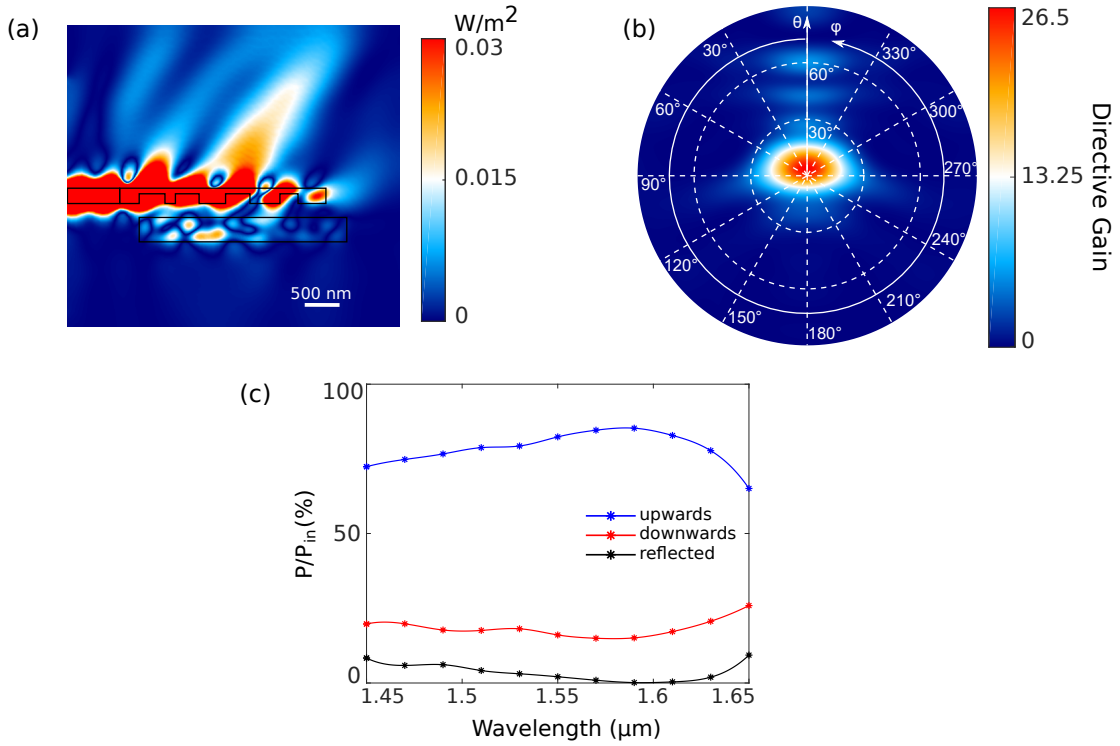

Figure 5.7: a) The calculated near-field power distribution (linear scale) of the optimized asymmetric horn antenna with the reflector in the xz-plane at $y = 0\,\text{nm}$. (b) Calculated angular linear directive gain distribution of the antenna exhibiting a directivity of $D = 26.5$ at $\theta = 4°$ and $\varphi = 0°$. (c) Calculated optical radiation efficiencies of the optimized asymmetric horn antenna with the reflector. The blue, red, and black curves represent the upward, downward, and reflected radiation efficiency, respectively.

5.2.1.2 Blazed grating antenna

To improve the up-down asymmetry, we consider blazed gratings in the following antenna. Such gratings are realized using L-shaped and U-shaped gratings that exhibit high diffraction efficiency. As dielectric horn antennas possess highly directive fields [99–101] and blazed gratings are suitable for near-vertical high radiation efficiency [140–143], we propose a compact blazed grating horn antenna, which is again optimized for an operational wavelength of $1.55\,\mu\text{m}$. The proposed antenna is a horn antenna composed of four gratings, where the first grating is a partially etched U-shaped trapezoidal grating, and the other three are L-shaped. As shown in the Figure 5.8, along the direction of propagation (x-axis), the different lengths are categorized as grating lengths (GL_x), offset lengths (OL_x), segment lengths (SL_x), and flare length (FL). Along with the horn width (HW), thirteen parameters are optimized, and the optimized values are shown in Table 5.3. The optimized structure has a compact footprint of $3.5\,\mu\text{m} \times 2\,\mu\text{m}$, where the height of the antenna is maintained at $h_1 = 220\,\text{nm}$ with a partial etch height of $h_2 = 110\,\text{nm}$, and the width of the feeding waveguide is $w = 400\,\text{nm}$.

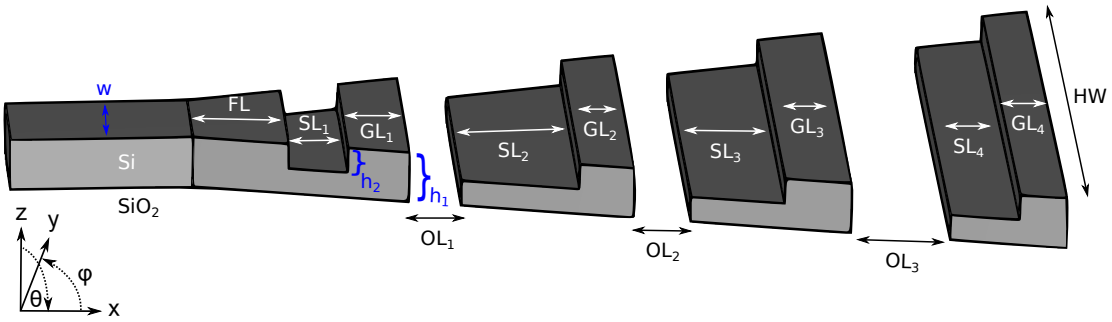

Figure 5.8: Schematic representation of the optimized blazed grating antenna, highlighting the parameters used in the optimization. The parameters in blue represent constant dimensions used in the numerical setup.

Design parameters	Dimensions (nm)
Flare length (FL)	390
Grating length (GL_1)	250
Grating length (GL_2)	220
Grating length (GL_3)	270
Grating length (GL_4)	190
Segment length (SL_1)	240
Segment length (SL_2)	480
Segment length (SL_3)	380
Segment length (SL_4)	280
Offset length (OL_1)	210
Offset length (OL_2)	230
Offset length (OL_3)	400
Horn width (HW)	2000

Table 5.3: Design parameters of the optimized blazed grating antenna obtained using a combination of PSO and TRO.

Figure 5.9a shows the near-field power distribution in the xz-plane at y =0. Along the length of the radiator, constructive interference is observed in the upper hemisphere due to the multilayer up-down asymmetries. Simultaneously, the lower hemisphere is dominated by destructive interference. The calculated angular far-field distribution in Figure 5.9b demonstrates a linear directivity of 22 centered at $\theta = 8°$, possessing a low SLL of -9.7 dB. As a function of the wavelength, the radiation efficiency emitting up and down is shown in Figure 5.9c. The upward radiation is higher for the shorter wavelengths and reduces rapidly for the longer wavelengths. This results in increased reflection to the waveguide, remarkably maintaining a low downward radiation efficiency for the full wavelength range. Thus, highlighting the efficiency of the antenna design in breaking the up-down symmetry while simultaneously preventing the increment of downward radiation. However, a sub-wavelength grating (SWG) design approach can lower the reflection efficiency over a wide range of wavelengths [142]. The antenna performs best at the design wavelength, exhibiting a high upward radiation efficiency of almost 78% and downward radiation efficiency of approximately 22%. This can be partly attributed to the U-shaped grating's partial etch, which creates a phase difference between the upward

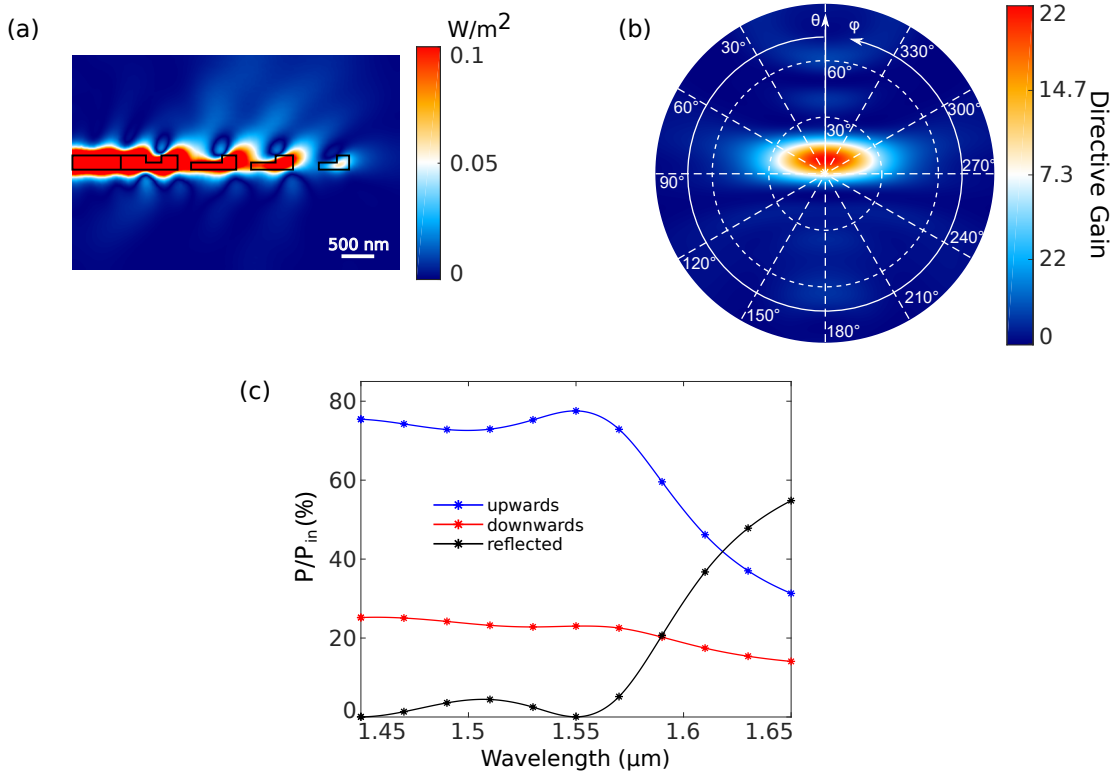

Figure 5.9: (a) Calculated near-field distribution of the power flow of the optimized blazed grating antenna in the xz-plane at $y = 0$. (b) Calculated angular linear directive gain distribution of the optimized antenna exhibiting a directivity of $D = 22$ at $\theta = 8°$ and $\varphi = 0°$. (c) Calculated optical radiation efficiencies of the optimized blazed grating antenna as a function of the wavelength.

and downward propagating radiation [31]. Furthermore, the aperiodic L-shaped trapezoidal diffraction gratings bolster the up-down asymmetry along the structure's length, reinforcing the constructive interference in the upward direction and destructive interference in the downward direction. This, in turn, reduces the in-plane propagation. The antenna has almost no power reflected back into the waveguide, thus making it highly efficient and desirable for OPAs.

5.2.2 Optimizing the field-of-view radiation efficiency

In this part, we target the improvement of radiation efficiency in the FOV to illuminate the whole FOV uniformly. For this purpose, the hybrid optimization routine optimizes the amount of power the radiating element directs into the OPA's FOV. The goal function is defined as

$$\eta_{FOV} = \frac{\int_0^{2\pi} \int_0^{FOV/2} P_{rad}(\theta, \varphi) d\theta d\varphi}{P_{in}}, \tag{5.2}$$

where P_{rad} is the power radiating in the defined computation domain, P_{in} is the input optical power, θ is the polar angle, and φ is the azimuthal angle. Using Bragg's law [144], for a $9\,\mu$m $\times$ $9\,\mu$m unit cell, the FOV can be approximated using

$$-\sin^{-1}\left(\frac{\lambda}{2d}\right) < \Delta FOV < \sin^{-1}\left(\frac{\lambda}{2d}\right), \tag{5.3}$$

which is approximately $6.8^\circ \times 6.8^\circ$ along the θ_x- and θ_y-axis, respectively, d is the size of the unit cell, and λ is the wavelength in the medium of propagation.

5.2.2.1 Circular grating antenna

To get a broader perspective, we look into antennas with circular gratings in this section, as we have already explored the benefits of using trapezoidal gratings. For this purpose, we use the circular grating antenna suggested in Ref. [31]. However, similar to the horn antenna in Section 5.2.1.1, we investigate two versions of the circular grating antenna, i.e., the antenna itself and the same antenna combined with a reflector. The fundamental antenna comprises an initial waveguide that feeds the optical power into the horn section consisting of a partial etch followed by five circular gratings with a variable pitch. The antenna is composed of Si and surrounded by a SiO_2 cladding. The schematic illustration of this antenna is shown in Figure 5.10, highlighting the twelve optimization parameters used. These design parameters are, namely, the angle (α), horn radii ($R_1 - R_3$), spacings ($S_1 - S_4$), and grating widths ($W_1 - W_4$). The parameters highlighted in blue represent the fixed parameters which are the excitation waveguide width $w = 400\,\text{nm}$, the full height of the antenna $h_1 = 220\,\text{nm}$, and the depth of the partial etch $h_2 = 110\,\text{nm}$. The optimization is carried out keeping the design specification of the unit cell in mind, and the resultant optimized value of the design parameters are shown in Table 5.4. The optimized structure has a compact footprint of $3.27\,\mu\text{m} \times 5.2\,\mu\text{m}$.

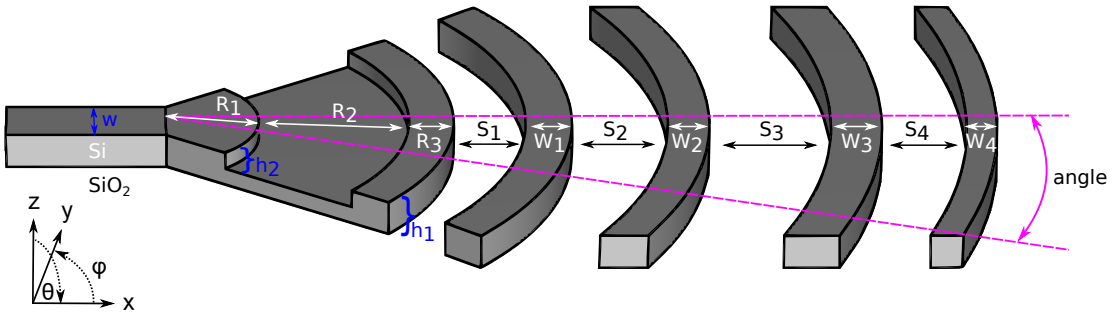

Figure 5.10: Schematic representation of the optimized circular grating antenna, highlighting the parameters used in the optimization. The parameters marked in blue represent the fixed constants used in the numerical setup.

Design parameters	Dimensions
Angle (α)	40°
Horn radius 1 (R_1)	585 nm
Horn radius 2 (R_2)	940 nm
Horn radius 3 (R_3)	280 nm
Grating width 1 (W_1)	290 nm
Grating width 2 (W_2)	260 nm
Grating width 3 (W_3)	320 nm
Grating width 4 (W_4)	190 nm
Spacing 1 (S_1)	450 nm
Spacing 2 (S_2)	600 nm
Spacing 3 (S_3)	760 nm
Spacing 4 (S_4)	530 nm

Table 5.4: Design parameters of the optimized circular grating antenna obtained using a combination of PSO and TRO.

Using a partial etch as seen in the schematic, an up-down asymmetry is introduced in the antenna to achieve higher upward radiation in comparison to the downward radiation with the aid of constructive-destructive interference [125, 145]. This also becomes apparent with the near-field power distribution of the antenna in Figure 5.11a, which highlights the power radiating upwards. At $1.55\,\mu$m, the antenna exhibits an upward efficiency of 51%, downward efficiency of 39%, and reflection efficiency of 10% back to the waveguide. Interestingly, almost 3.2% of the input optical power is radiated into the FOV, which is five times more than that from the reference antenna in Ref. [31]. Furthermore, the optimized structure exhibits a linear directivity of 54 with a perfect vertical emission at an angle of $\theta = 0°$ and $\varphi = 0°$, as shown in the calculated linear directive gain distribution in Figure 5.11b. The structure possesses a low SLL of -9.8 dB.

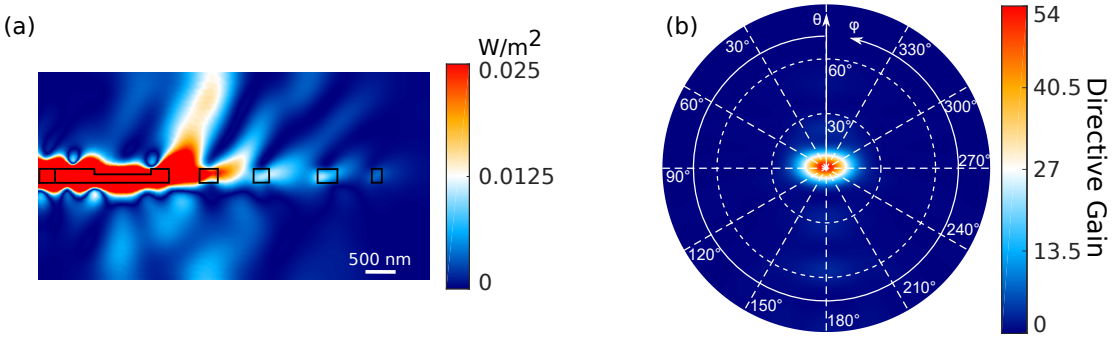

Figure 5.11: (a) Calculated near-field distribution of the power flow for the optimized circular grating antenna in the xz-plane at $y = 0$. (b) Calculated angular linear directive gain distribution of the optimized antenna exhibiting a directivity of $D = 54$ at $\theta = 0°$ and $\varphi = 0°$.

In the next step, aiming for higher upward efficiency, we add a reflector to the primary antenna. In contrast to the Section 5.2.1.1, this antenna system performs better when using a Bragg reflector consisting of two silicon mirrors, as opposed to the single-layer reflector that was previously used. These two mirrors having a thickness of $\lambda_{Si}/4$ are separated by a dis-

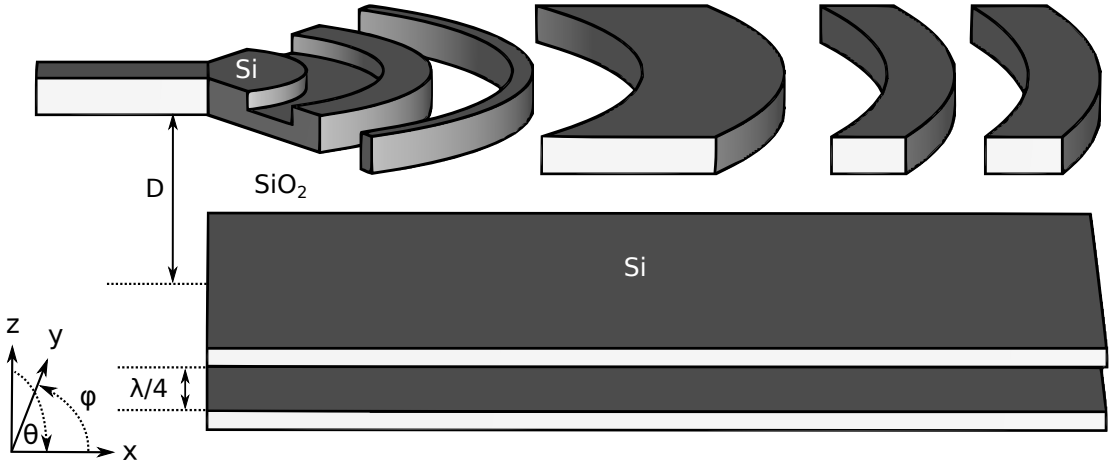

Figure 5.12: Schematic representation of the optimized circular grating antenna with the Bragg reflector, highlighting the parameter reflector distance (D) used in optimization.

tance of $\lambda_{SiO_2}/4$, where λ_{Si} and λ_{SiO_2} represent the wavelengths in Si and SiO_2, respectively. Figure 5.12 shows the schematic of this structure highlighting one new optimization parameter, the reflector distance D. This new parameter along with the twelve design parameters of the fundamental structure shown in Figure 5.10 are optimized. The optimized values are provided in Table 5.5 and the optimized antenna has a size of $3.3\,\mu$m $\times$ $5.2\,\mu$m, similar to the footprint of the optimized fundamental structure.

Design parameters	Dimensions
Angle (α)	60°
Horn radius 1 (R_1)	580 nm
Horn radius 2 (R_2)	450 nm
Horn radius 3 (R_3)	280 nm
Grating width 1 (W_1)	120 nm
Grating width 2 (W_2)	830 nm
Grating width 3 (W_3)	395 nm
Grating width 4 (W_4)	420 nm
Spacing 1 (S_1)	475 nm
Spacing 2 (S_2)	640 nm
Spacing 3 (S_3)	600 nm
Spacing 4 (S_4)	430 nm
Reflector distance (D)	1042 nm

Table 5.5: Design parameters of the optimized circular grating antenna with the Bragg reflector obtained using a combination of PSO and TRO.

The optimized antenna demonstrates a much better performance, which is also visible in the near-field power distribution (see Figure 5.13a). As it can be seen, more power is radiated in the upward direction, which can directly be attributed to the use of the Bragg reflector. This configuration exhibits an improved upward efficiency of 88%, a downward efficiency of 11%, and a reflection efficiency of 1%. In particular, 6.8% of the input optical power is directed into

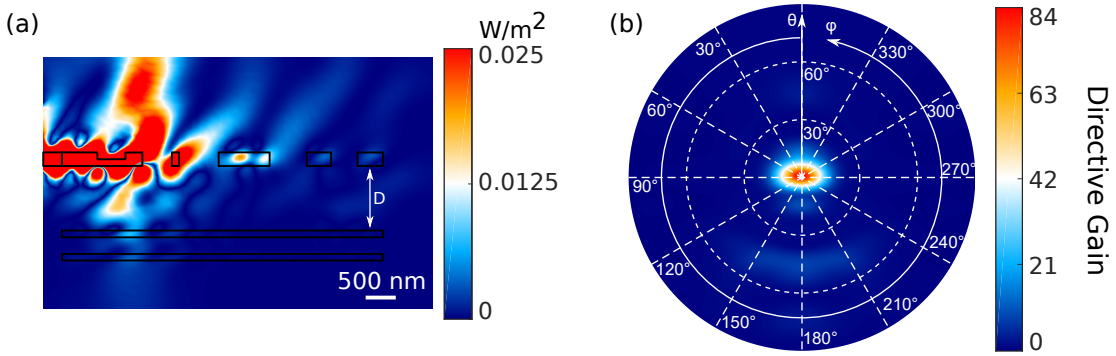

Figure 5.13: (a) Calculated near-field distribution of the power flow of the optimized circular grating antenna with the Bragg reflector in the xz-plane at $y = 0$. (b) Calculated angular linear directive gain distribution of the antenna exhibiting a directivity of $D = 84$ at $\theta = 1^\circ$ and $\varphi = 0^\circ$.

the FOV, which is essentially two times more than that of the fundamental structure and ten times more than the reference antenna. The calculated linear directive gain distribution also demonstrates an enhanced linear directivity of 84 with its main lobe along $\theta = 1^\circ$ and $\varphi = 0^\circ$ (see Figure 5.13b). This structure demonstrates a low SLL of -9.7 dB, which is comparable to the fundamental antenna.

To compare the performance of both the circular grating antennas with respect to the optimization goal function, Figure 5.14 plots the radiation efficiencies in the FOV for both the antennas as a function of the wavelength. The red and blue curves represent the antenna with and without the Bragg reflector, respectively. Additionally, the black curve illustrates the radiation efficiency in the FOV for the reference antenna from Ref. [31]. Compared to the reference antenna, our optimized antennas are more efficient in the FOV. In particular, at the design wavelength, the fundamental antenna concentrates almost five times more power in the FOV, and this improve-

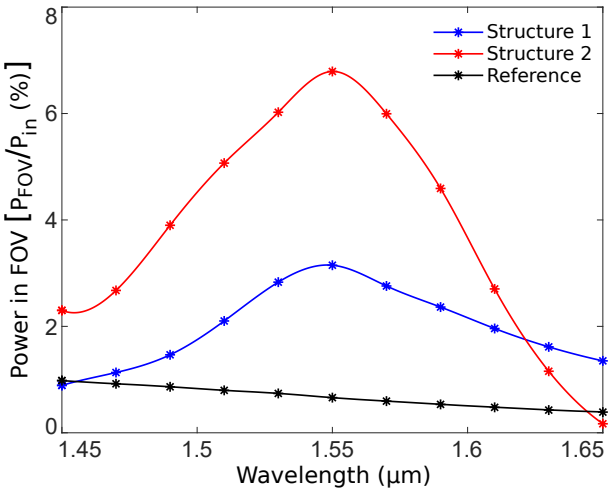

Figure 5.14: Calculated radiation efficiency in the FOV for both the optimized antennas along with the antenna presented in Ref. [31].

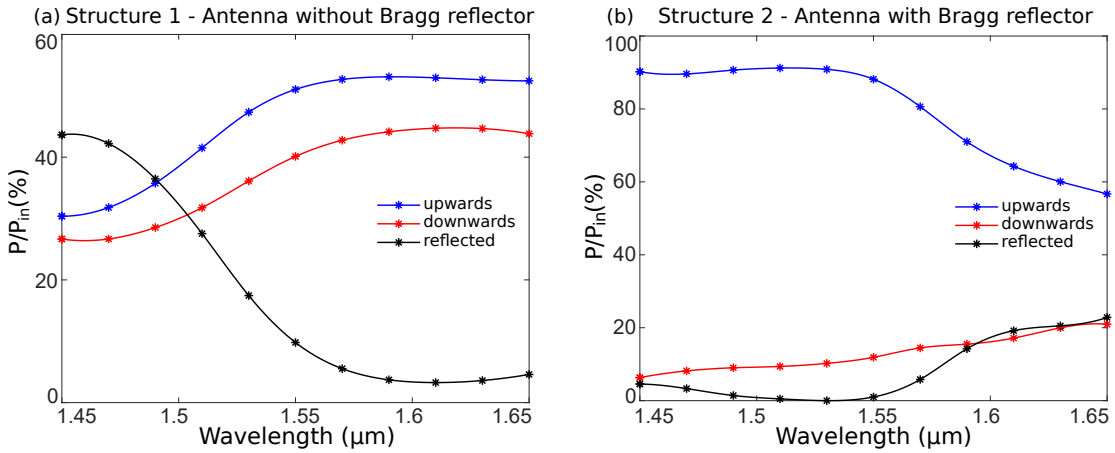

Figure 5.15: Calculated optical radiation efficiencies of the optimized circular grating antenna (a) without and (b) with the Bragg reflector.

ment becomes tenfold with the use of the Bragg reflector.

Interestingly, both the optimized antennas exhibit an enhanced optical response over a broad range of frequencies. Figure 5.15a and b, plot the calculated radiation efficiencies of both the circular gratings antennas investigated in this section as a function of the wavelength. The blue, red, and black curves represent the upward, downward, and reflected radiation efficiency, respectively. Remarkably, both antennas maintain high upward efficiency for a broad range of wavelengths, making them both broadband antennas. Especially, the reflector produces not just an increased upward efficiency but also a significantly reduced reflection efficiency, as depicted by the black curve in Figure 5.15b.

5.3 Optical phased array configurations

In this section, we utilize the radiating elements discussed previously in phased array systems, the theory of which has been introduced in Section 2.5. The electromagnetic far-field radiation of an OPA can be obtained using the far-field of a single antenna, i.e.,

$$\boldsymbol{E}_{array}(\theta,\varphi) = \boldsymbol{E}_{antenna}(\theta,\varphi)\, AF(\theta,\varphi), \tag{5.4}$$

where $\boldsymbol{E}_{array}(\theta,\varphi)$ is the far-field of the OPA, $\boldsymbol{E}_{antenna}(\theta,\varphi)$ is the far-field of a single antenna, $AF(\theta,\varphi)$ is the scalar function representing the array factor, θ is the polar, and φ is the azimuthal angle. All the radiating elements presented so far in the chapter are suitable to be employed in 2-D phased array configurations. For simplicity, all the phased array implementations will use the same antenna element, namely, the blazed grating antenna from Section 5.2.1.2.

5.3.1 Planar arrays

A planar phased array configuration has the antennas arranged in a matrix, as discussed in Section 2.5.1.3. In this case, each antenna is accompanied by a phase shifter and one can control the beam direction along two axes, namely, the θ_x- and θ_y-axis. However, this comes at the cost of having a large number of phase shifters in the system. In this section, we use the $9\,\mu$m $\times$ $9\,\mu$m unit cell, as in Ref. [31] that shows the large-scale implementation of a 64×64

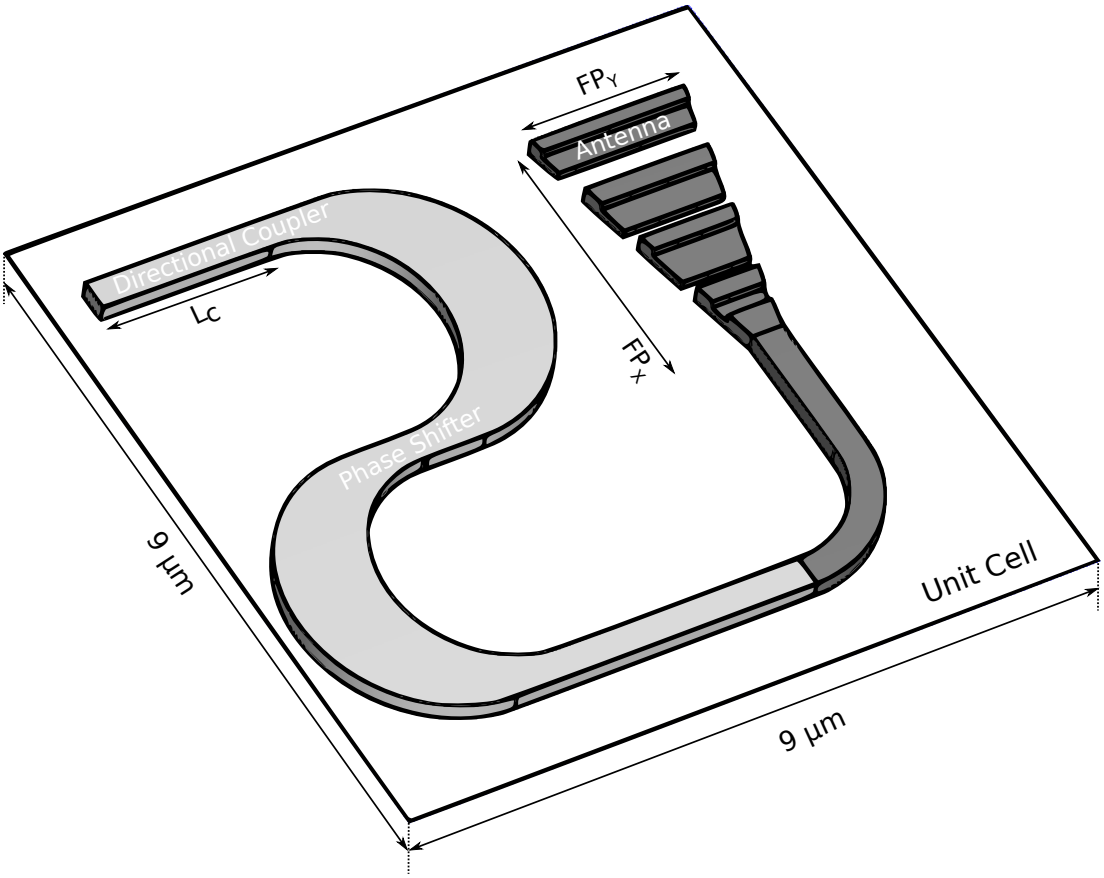

Figure 5.16: Schematic representation of the $9\,\mu$m $\times$ $9\,\mu$m unit cell, highlighting the three main components constituting the unit cell, namely, DC, PS, and the antenna. The dark gray region represents the unit cell element optimized and analyzed in this work. The parameters $\mathrm{FP_x}$ and $\mathrm{FP_y}$ represent the footprint of the antenna along the x- and y-axis, respectively.

array of such unit cells, with the possibility of controlling the phase input to each antenna element. The schematic representation of such a unit cell comprising the DC, PS, and dielectric antenna is illustrated in Figure 5.16. For such a $M \times N$ array of unit cells, the array factor can be defined using a Fourier transform ($\mathcal{F}$) as

$$AF(\theta, \varphi) = \sum_{m=1}^{M} \sum_{n=1}^{N} w_{mn} \cdot e^{j2\pi(x_m \cdot u + y_n \cdot v)} = \mathcal{F}(w_{mn}), \tag{5.5}$$

where $w_{mn} = |w_{mn}|e^{j\phi_{mn}}$ is the near-field from a single unit cell with an amplitude $|w_{mn}|$ and phase ϕ_{mn}, (x_m, y_n) are the coordinates of each antenna constituting the array, and the positions (u, v) in the far-field are defined as

$$(u, v) = \left(\frac{\sin\theta\cos\varphi}{\lambda}, \frac{\sin\theta\sin\varphi}{\lambda} \right), \tag{5.6}$$

with λ as the wavelength in the medium of propagation. These phased array systems can be efficiently utilized for pattern synthesis and beam steering. From Eq. (5.5), it becomes evident

that if one is aware of the desired far-field array factor $AF(\theta, \varphi)$, then the near-field emission w_{mn} can be obtained by performing a simple inverse Fourier transform of this target $AF(\theta, \varphi)$. The directional couplers and phase shifters can then attain the required near-field amplitude and distribute the necessary optical phase input to each antenna, respectively. However, as the section's name suggests, we demonstrate an OPA in which the far-field pattern is controlled only by the phase, and not the amplitude. For this reason, phased array optics and holography generally employ iterative computational methods like the Gerchberg-Saxton (GS) algorithm for arbitrary pattern generations [146]. Figure 5.17 illustrates the block diagram of a modified GS algorithm that is utilized in this work for generating desired patterns with uniform near-field emission [147].

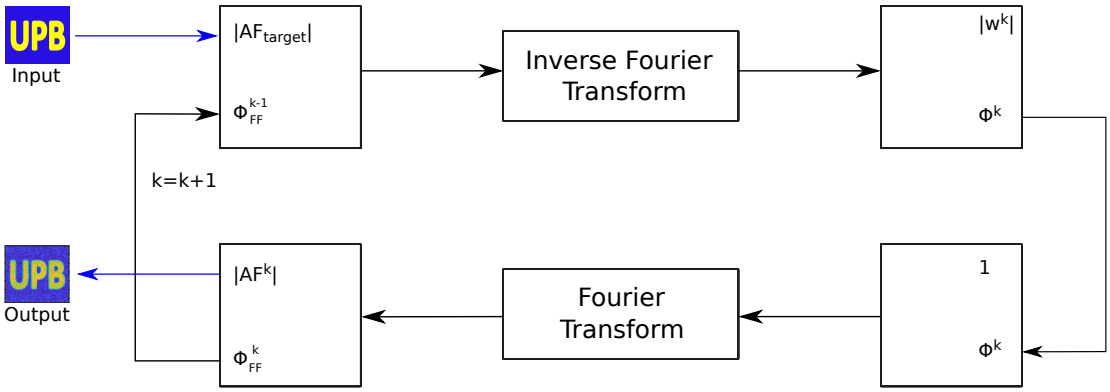

Figure 5.17: Illustration of the modified GS algorithm for the generation of a desired far-field pattern.

The algorithm begins by taking the inverse Fourier transform of the target far-field, which constitutes the desired amplitude $|AF_{target}|$ and an input phase distribution chosen by the user. Typically, the input phase distribution is either a random phase distribution or a uniform distribution of zeroes over the entire image [148]. Only the phase is retained from the resulting near-field emission, and the amplitude is set to unity. The Fourier transform of this near-field then yields the output array factor for that iteration. On similar lines, for the k^{th} iteration, the approximated array factor AF^k is formed using the target amplitude $|AF_{target}|$ and the phase distribution ϕ^{k-1} from the $(k-1)^{th}$ iteration, which is inverse Fourier transformed. The subsequent phase ϕ^k obtained from the near-field emission updates the output array factor AF^k through the Fourier transform. This method is repeated until the final output array factor $|AF^k|$ converges to target array factor $|AF_{target}|$. The algorithm aims to minimize the error in the iteratively computed far-field pattern versus its known target counterpart.

To demonstrate the application of the GS algorithm, let us consider the image with the initials of the Paderborn University "UPB" for the phased array synthesis. We first consider an ideal $\lambda/2$ inter-element spacing between each radiating element. For a 64×64 blazed-grating-antenna array with such an ideal spacing, the GS algorithm provides a phase distribution, as shown in Figure 5.18a, which produces the desired far-field pattern, as shown in Figure 5.18b with a uniform amplitude distribution. The image used for the pattern generation can be seen next to the far-field pattern. Nonetheless, we know that Ref. [31] uses an inter-element spacing of 9 μm. Such a large size of the unit cell produces grating lobes that are visible in the far-field pattern.

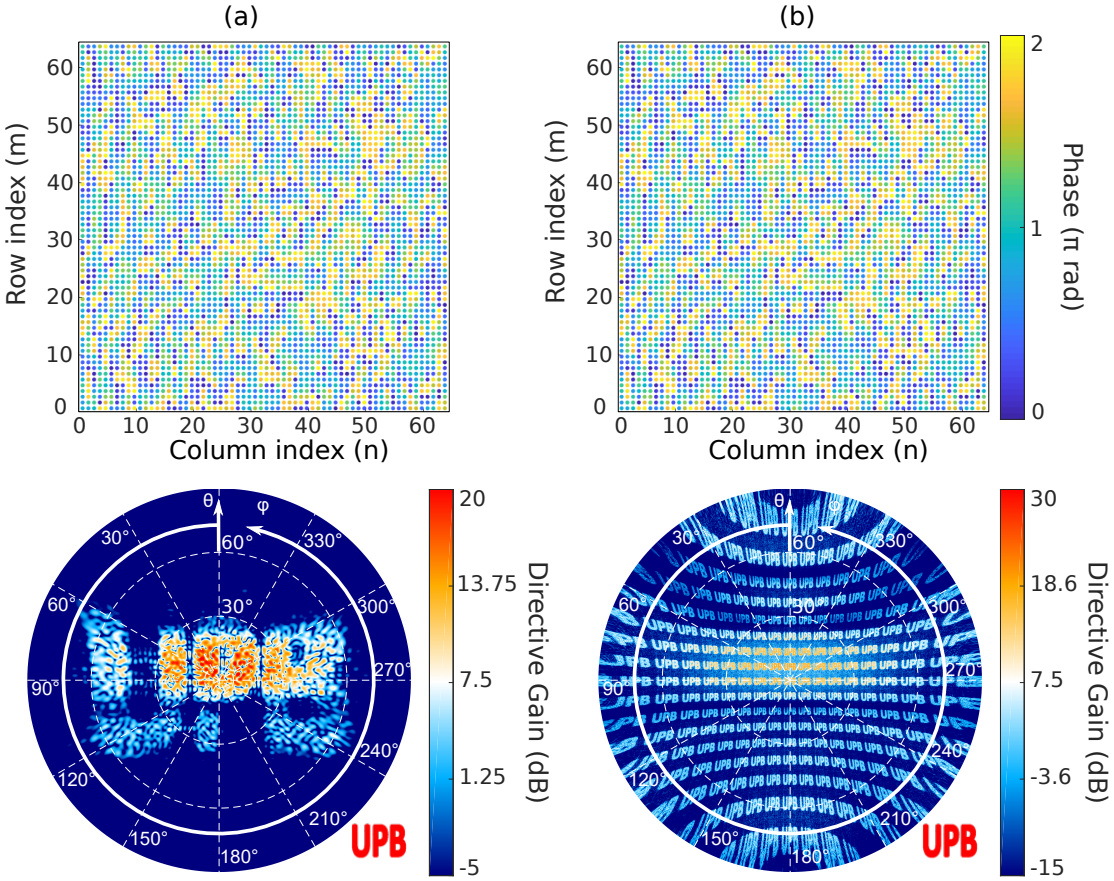

Figure 5.18: Phase and far-field distribution for generating the "UPB" initials by a 64×64 array with an inter-element spacing of (a) $\lambda/2$ and (b) $9\,\mu$m. The image used for the pattern generation is shown on the bottom right of the far-field patterns.

As per Eq. (2.77), such a unit cell would exhibit 16 interference orders in each direction, in addition to the main lobe. This phenomenon is also illustrated in the far-field pattern, which has 16 repetitions of "UPB" in each direction (Figure 5.18d).

Figure 5.19 illustrates a few more examples for pattern generation with an inter-element spacing of $9\,\mu$m in a 64×64 array configuration. For this purpose, the initials of the Department of Theoretical Electrical Engineering "TET" and the Paderborn University logo are considered, and their corresponding phase distribution and resultant far-field patterns can be seen in the left and right columns, respectively. The original images used for the process are displayed next to their respective far-field patterns.

Another possible application for these phased arrays is electronic beam steering, which can be done by controlling the phase distribution of the individual antennas. As mentioned earlier, a uniform input amplitude is maintained for all the radiating elements. To emphasize the visualization of the beam steering results, we consider an 8×8 array and analyze the results over a small region of the far-field, i.e., $\theta \leq 20°$. Fewer grating lobes are visible over a smaller region, and the phase inputs for the 8×8 array can be viewed easily compared to a 64×64

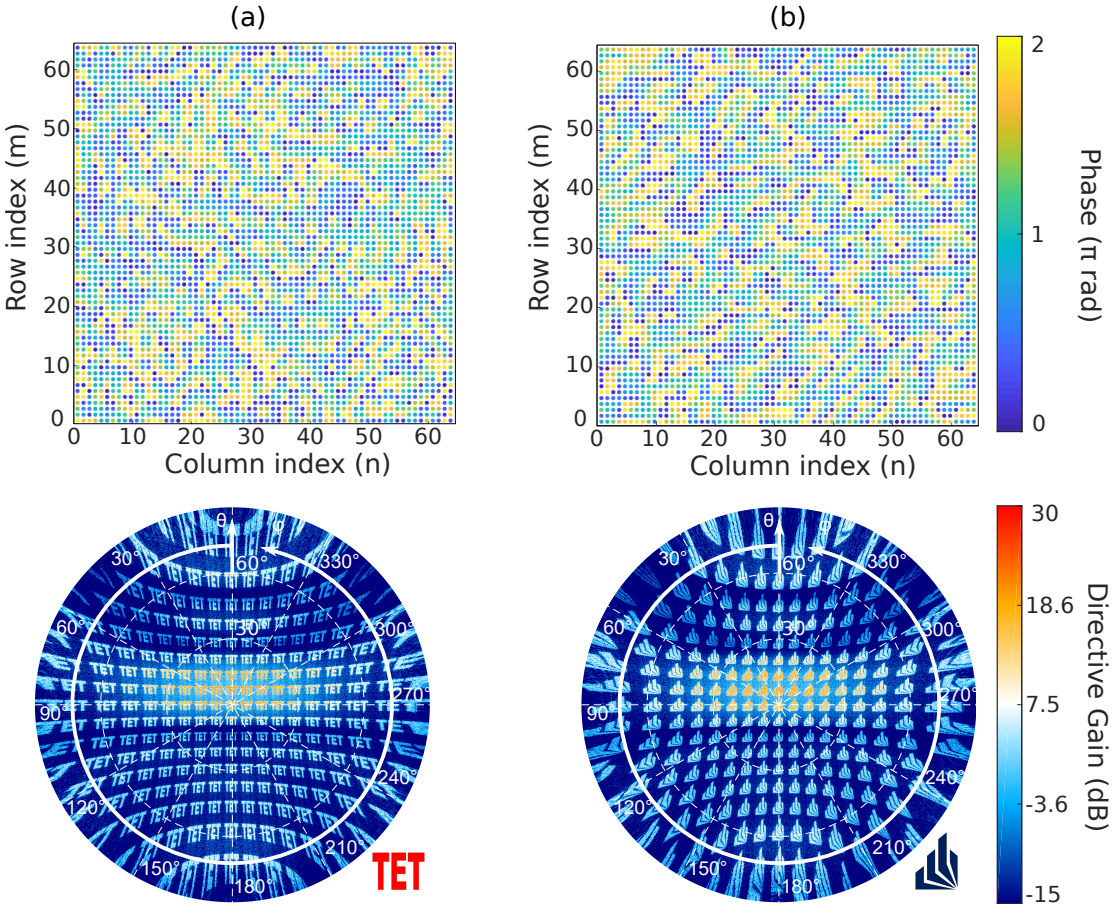

Figure 5.19: Phase and far-field distribution for a 64×64 array with unit cells sized $9\,\mu\text{m} \times 9\,\mu\text{m}$ to generate (a) the initials of the group Theoretical Electrical Engineering "TET" and (b) the Paderborn University logo. The images used for the pattern generation can be seen on the right of the far-field patterns.

array. With beam steering, the beam can be steered vertically, horizontally, or in any other direction. Additionally, the beam can be split into multiple beams while simultaneously steering it. Figure 5.20 shows the phase distribution and the corresponding far-field radiation pattern that illustrates the beam steering effect. For reference, Figure 5.20a shows the calculated angular far-field distribution for a zero phase distribution over all antennas with uniform input amplitude. All the far-field radiation patterns are normalized to this reference case. The beam can be steered vertically with a row-wise alternating phase distribution of zero and π to the array elements, as shown in Figure 5.20b. Such a phase shift causes the beam to move along the θ_x-axis, analogous to a 1-D beam steering case. The center of the beam is shifted by approximately $3.4°$, which is almost half of the angular separation between the main lobe and the first grating lobe. A column-wise alternating phase distribution of zero and π is provided to the array elements to steer the beam horizontally. This phase shift causes the beam to move along the θ_y-direction, as seen in Figure 5.20c. The beam can also be steered diagonally by using an alternating phase distribution of zero and π along both the row and column array elements,

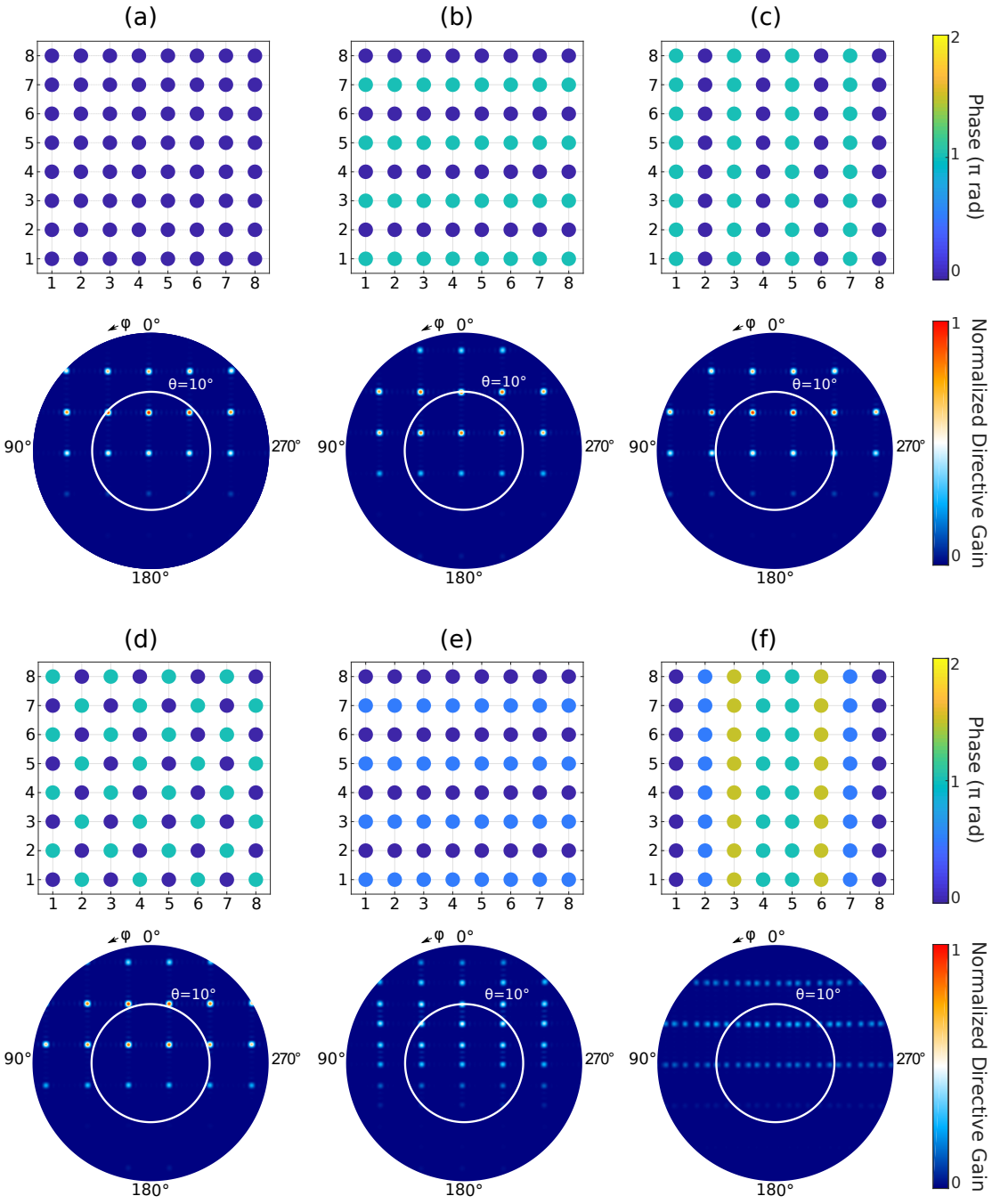

Figure 5.20: Demonstration of beam steering and beamforming with an 8×8 array configuration employing the blazed grating antenna. (a) Phase distribution and simulated linear far-field radiation pattern of a uniform phased array (zero phase distribution). (b-f) Phase distribution and the simulated linear far-field radiation pattern for the main lobe to be (b) shifted vertically, (c) shifted horizontally, (d) shifted diagonally, (e) split into two beams vertically, and (f) split into four beams horizontally.

essentially remaining constant along a diagonal and forming a symmetric phase matrix represented in Figure 5.20d, along with the far-field pattern demonstrating the diagonally steered beam. Furthermore, using a row-wise alternating phase distribution of zero and 90° causes the beam to split into two beams along the vertical direction, as shown in Figure 5.20e. Similarly, using a column-wise distribution as shown in Figure 5.20f splits the beam into four beams along the horizontal direction. The four beams nearly span over 7° from one end to the other.

It is evident from above that such large unit cells drastically limit the grating-lobe-free region over which the beam can be steered. Therefore, one way to circumvent this issue is to arrange the array elements in a circular fashion, where the unit cell size is no longer relevant. The following subsection briefly looks into these configurations.

5.3.2 Circular arrays

In Section 2.5.2, we already introduced the concept of a discretized annular aperture and an approximate realization of such an aperture using radiating elements. Such a configuration can also be extended to multiple concentric rings, thus creating a polar coordinate analog for the transition from linear to planar arrays. Note that the discussion in Section 2.5.2 focused on point source radiators having a radial offset of $\lambda/2$, with the outer radius of the aperture being λ. This subsection shows how our optimized radiating elements, specifically the blazed grating antenna from Section 5.2.1.2, can be utilized within such array configurations.

For the waveguide-fed phased array antennas presented so far, the dimensions of the antennas are always larger than λ, and there exists a minimum inter-element spacing to ensure depreciation in interference effects. Additionally, planar routing constraints also need to be met. Ref. [39] proposes a multi-annular-ring OPA considering the aforementioned constraints for

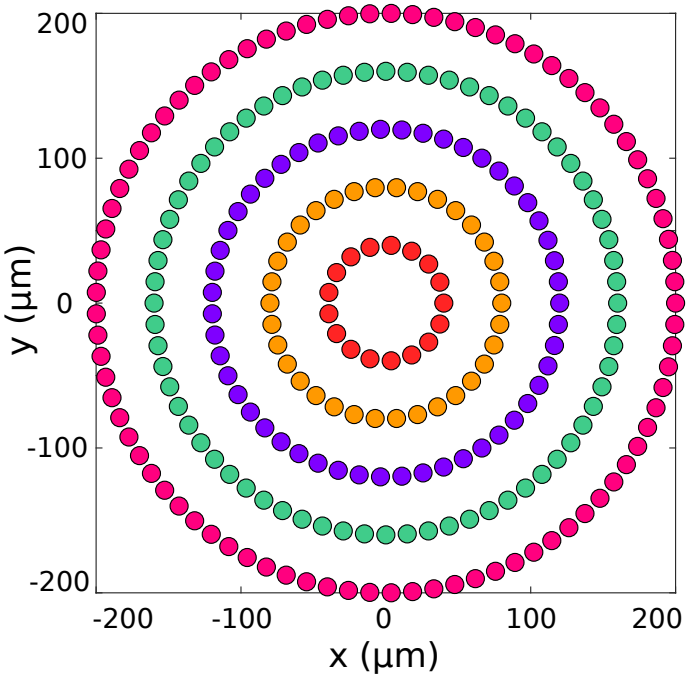

Figure 5.21: Arrangement of the antennas in a multi-annular-ring aperture optical phased array.

implementation in a standard photonics processing environment. The array comprises five concentric circular arrays with $N_m = mN_1$ number of elements in the m-th ring, where N_1 is the number of elements in the first ring. Similarly, the m-th ring has a radius of $R_m = mR_1$, where R_1 is the radius of the first ring. For the implementation, N_1 is chosen to be 17 and $R_1 = 40\,\mu$m. The relative positions of the radiating elements are as shown in Figure 5.21. The array configuration consists of 17, 34, 51, 68, and 85 elements in circles of radii 40, 80, 120, 160, and 200 μm, respectively. Although this realization deviates from the theoretically derived ideal array configuration described in Section 2.5.2, the following advantages are noted as the size of the array increases [39]:

- the half-power beamwidth (HPBW) decreases,
- the main beam's power is constant relative to the power in the side lobes,
- energy distribution in the side lobes is more uniform, i.e., reduced peak side lobe levels.

When the array is uniformly excited with no phase inputs, the resulting angular far-field radiation pattern is shown in Figure 5.22. As seen in the Figure 5.22a, no grating lobes exist in the entire visible region. To highlight the main beam, we take a look at the far-field within a smaller range of polar angles, i.e., $0^\circ \leq |\theta| \leq 10^\circ$, as illustrated in Figure 5.22b. The array configuration demonstrates a directivity of 35 dB, and the main beam is very narrow ($0.1^\circ \times 0.1^\circ$), maintaining a zeroth-order Bessel-like intensity distribution for an angular range of 2°, as demonstrated in [39]. Such a narrow beam is highly desirable in applications like LiDAR [44]. The logarithmic scale is used for the far-field patterns for better visualization.

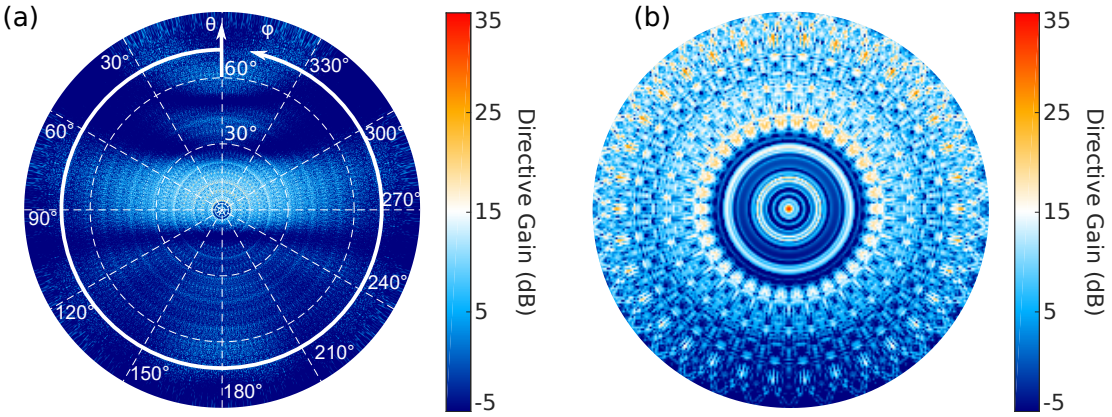

Figure 5.22: Simulated angular far-field radiation pattern for a circular array implemented with the blazed grating antenna for (a) $|\theta| \leq 90^\circ$ and (b) $|\theta| \leq 10^\circ$ in the logarithmic scale. A uniform amplitude with no phase inputs is provided to the antennas.

To make a comparison of this array configuration (255 elements) with its rectangular array equivalent, we simulate a 16×16 planar array (256 elements), where the unit cell has a size of $9\,\mu\text{m} \times 9\,\mu$m. The peak SLL for the circular array is -14 dB, which is lower compared to -13.1 dB from its planar array equivalent (see Figure 5.23). Additionally, this rectangular configuration exhibits undesirable grating lobes, which is clearly visible in Figure 5.23b that represents the far-field radiation pattern of this array over a smaller range of $|\theta| \leq 10^\circ$. Similar to the planar arrays, such radially configured antenna distributions can also steer the beam in

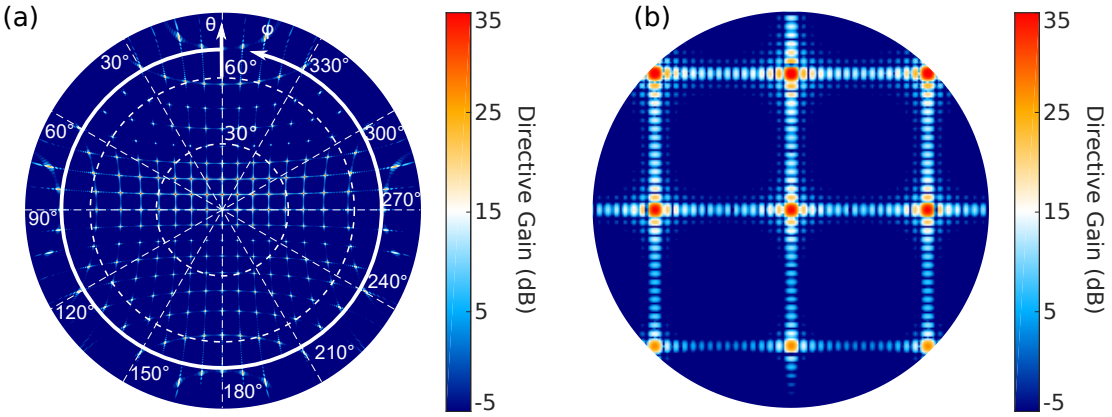

Figure 5.23: Simulated far-field radiation pattern for a 16×16 rectangular array implemented with the blazed grating antenna for (a) $|\theta| \leq 90°$ and (b) $|\theta| \leq 10°$. A uniform amplitude with no phase inputs is provided to the antennas.

a desired direction. Keeping a uniform amplitude distribution for all elements and varying the phase input, the beam can be steered along horizontal, vertical, and arbitrary directions with Figure 5.22 as a reference. In Figure 5.24, we demonstrate beam steering along the horizontal direction. Figure 5.24a and b illustrate the beam steered to $\theta = +10°$ and $\theta = -10°$, respectively. This horizontal axis is referred to as the θ_y-axis. For both the cases of $\theta = \pm 10°$, the main beam is steered along the desired direction and the directivity of the far-field emission drops from $35.3\,\text{dB}$ to $33.7\,\text{dB}$. However, all plots maintain a constant color scale to visualize these effects better. As with beam steering in any array configuration devoid of adaptive beamforming, the SLL increases to $-8.2\,\text{dB}$. If the beam is steered further toward the FOV limits of the radiator (HPBW), the side lobes become more pronounced, thus making the main beam and side lobes less distinguishable.

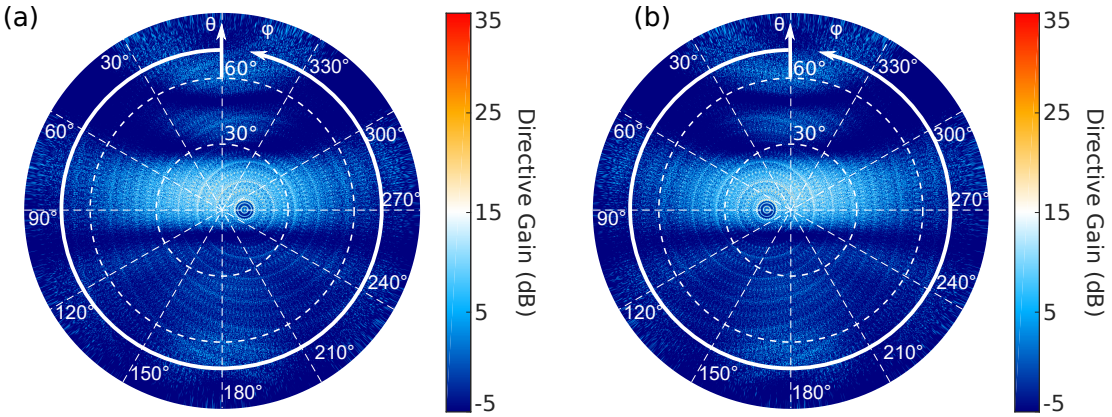

Figure 5.24: Simulated angular far-field radiation pattern for a circular array implemented with the blazed grating antenna steered to (a) $\theta = +10°$ and (b) $\theta = -10°$ along the θ_y-axis.

Similarly, the main beam can be steered to $\theta = +10°$ and $\theta = -10°$ along the vertical axis, which we call the θ_x-axis. This is demonstrated in the far-field distributions presented in Figure 5.25. When the beam is steered to $+10°$, the directivity is almost $36.1\,\text{dB}$. However, steering

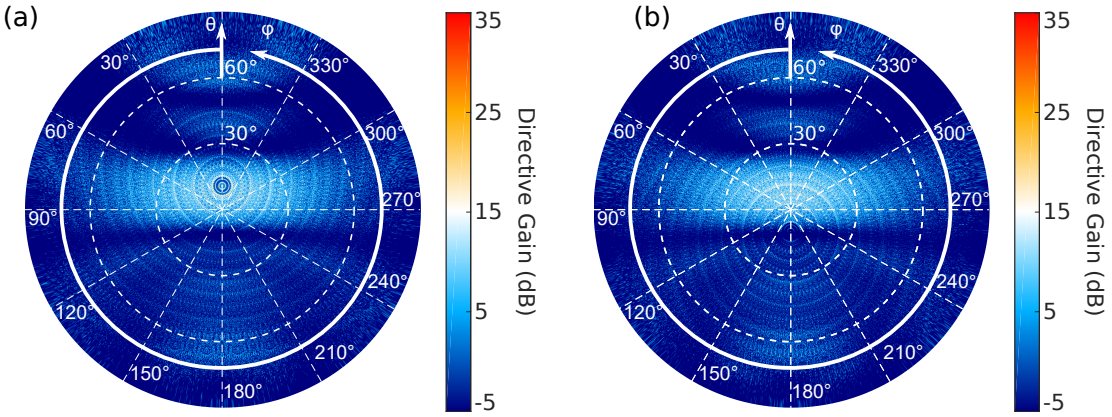

Figure 5.25: Simulated angular far-field radiation pattern for a circular array implemented with the blazed grating antenna steered to (a) $\theta = +10^\circ$ and (b) $\theta = -10^\circ$ along the θ_x-axis.

the beam to -10°, the directivity drops to 27.3 dB. This can be attributed to the far-field radiation pattern of the antenna, which has a lower power distribution in this region and its main lobe is directed along $\theta = 8^\circ$.

Furthermore, the far-field main lobe can be steered diagonally. Figure 5.26a and b demonstrate the beam steered to approximately $(\theta, \varphi) = (+14^\circ, 315^\circ)$ and $(\theta, \varphi) = (-14^\circ, 135^\circ)$, respectively. Like the two cases considered along the vertical axis, these cases also possess a directivity of approximately 36 dB and 27.1 dB for the diagonally up and down steering, respectively.

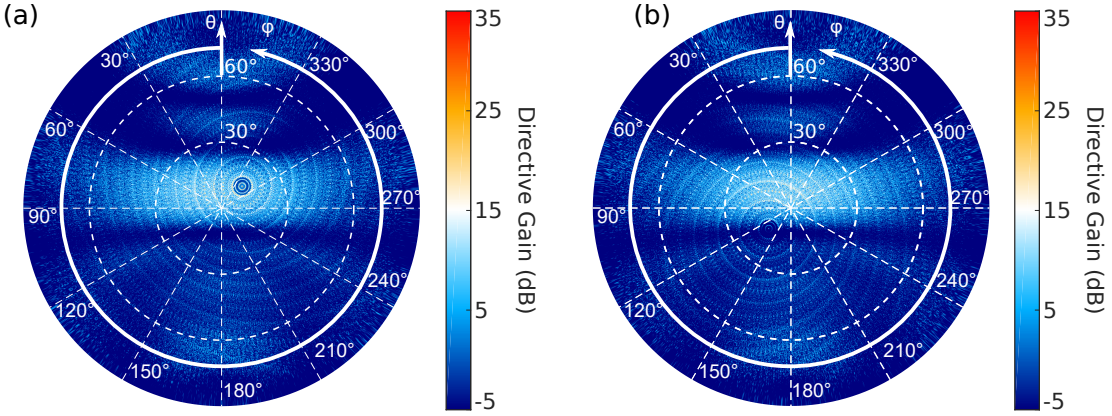

Figure 5.26: Simulated angular far-field radiation pattern for a circular array implemented with the blazed grating antenna steered diagonally (a) up and (b) down.

Overall, we explore different radiating elements that are optimized for unique objectives. We numerically demonstrate the realization of large-scale arrays utilizing the antennas presented in this chapter. Furthermore, we provide a detailed overview of how planar and circular arrays furnish platforms for implementing various optical systems that can benefit from the many advantages of phased arrays.

Chapter 6

LNOI waveguide structures

A lithium niobate (LN) crystal was first fabricated in 1928 [149], and its ferroelectric features were brought to light in 1949 [150]. Along the crystallographic Z-axis, the optical properties of such a crystal are rotationally symmetric, and the other two crystallographic X- and Y-axis are perpendicular to the Z-axis, forming an angle of 120°. Remarkable optical characteristics like high second-order optical non-linearity, strong electro-optic effect, large optical transparency window, and low material losses have made LN one of the most intensively researched materials for photonic applications [151]. Therefore, LN is a promising candidate for optical telecommunication devices.

Many areas of physics, be it classical or quantum, are commanded by non-linear processes which facilitate the complex manipulation of light [152–156]. Furthermore, realization of such processes in integrated waveguiding structures is essential in drawing quantum concepts into daily life [157]. The lack of crystal symmetry furnishes LN with several non-linear properties such as photoelasticity, piezoelectric effect, and, more importantly, ferroelectricity, which proves instrumental in periodically poling LN substrates needed for applications like frequency conversion, generation of photon pairs, parametric down-conversion, etc. [158–160]. Additionally, non-linear integrated waveguides are more advantageous than the bulk non-linear crystals, as they can be easily interfaced with fiber communication systems and attain strong field confinement over larger distances [57].

The evolution of the lithium-niobate-on-insulator (LNOI) technology in recent years has opened up new possibilities for integrated photonics with the implementation of tightly confined LN waveguides [161], with a high refractive index contrast between the waveguide core and the cladding region. These are realized by etching waveguide ribs in thin films with a high-refractive index bonded to a substrate with a lower refractive index. Such a configuration exhibits strong modal confinement, such that low bending radii and compact devices can be realized, thus making it an ideal platform for optical chip fabrication. LNOI-based waveguides combine the large second-order non-linear susceptibility of bulk LN with the design benefits of silicon photonics on the same platform to realize devices for various classical and quantum applications. Some of these applications are electro-optic and acousto-optic modulators, quantum photonic devices, and passive and active integrated photonic devices [162,163]. Refs. [161,164] give a good overview of the advances in this field, describing the novel systems developed with

this technology.

In this chapter, we present different LNOI rib waveguide optical components that are analyzed and optimized consisting of an anisotropic LN core layer over a SiO_2 substrate. These waveguides were investigated for the X-cut configuration for the TE polarization. Section 6.1 briefly reviews the anisotropy of LN. Then, in Section 6.2, we explore optical components: directional couplers, waveguide bends, and multi-mode interference couplers built using the LNOI rib waveguides.

6.1 Wave propagation in anisotropic media

In an isotropic medium, the electric dipole moment per unit volume is always parallel to the electric field. A scalar susceptibility, independent of the direction of the electric field, relates these quantities. However, this is not the case in anisotropic media, except for certain directions. Since an anisotropic crystal consists of a regular periodic array of atoms or molecules with a certain symmetry, the magnitude and direction of the induced polarization depend on the direction of the applied field [2]. For an anisotropic medium,

$$\begin{aligned} \mathbf{D}(\boldsymbol{r}) &= \varepsilon_0 \mathbf{E}(\boldsymbol{r}) + \mathbf{P}(\boldsymbol{r}), \\ \mathbf{P}(\boldsymbol{r}) &= \varepsilon_0 \hat{\chi}(\boldsymbol{r}) \mathbf{E}(\boldsymbol{r}), \end{aligned} \tag{6.1}$$

where $\hat{\chi}$ comprises nine components $\chi_{i,j}$ that together constitute the electric susceptibility tensor. The magnitude of these coefficients is determined by the orientation of the anisotropic crystal with respect to the x-, y-, and z-axes. These can be chosen such that the off-diagonal elements of the susceptibility tensor are zero, thus defining the principal dielectric axis of the crystal. Then we can rewrite $\mathbf{P}(\boldsymbol{r})$ from Eq. (6.1) with respect to the Cartesian coordinate system as

$$\begin{aligned} P_x &= \varepsilon_0 \chi_{11} E_x, \\ P_y &= \varepsilon_0 \chi_{22} E_y, \\ P_z &= \varepsilon_0 \chi_{33} E_z, \end{aligned} \tag{6.2}$$

where the elements of the dielectric permittivity tensor can be related to that of the susceptibility tensor,

$$\varepsilon_{ij} = \varepsilon_0 (1 + \chi_{ij}). \tag{6.3}$$

For the principal coordinate system, the dielectric tensor can be defined as

$$\hat{\varepsilon}(\boldsymbol{r}) = \begin{bmatrix} \varepsilon_x & 0 & 0 \\ 0 & \varepsilon_y & 0 \\ 0 & 0 & \varepsilon_z \end{bmatrix} = \varepsilon_0 \begin{bmatrix} n_x^2 & 0 & 0 \\ 0 & n_y^2 & 0 \\ 0 & 0 & n_z^2 \end{bmatrix}. \tag{6.4}$$

From the above discussion, if we consider a plane wave propagating through such a medium, it is evident that the polarization state can vary as it propagates through the crystal. As the phase velocity depends on the propagation direction and polarization state, two eigenwaves with eigen phase velocities and polarization directions exist for a given propagation direction. Wave with a polarization parallel to one of these directions has an invariant polarization state while propagating through the anisotropic medium. Such materials exhibit optical rotation, conical refraction, and double refraction [2]. Furthermore, anisotropic materials with non-linear responses are widely employed for phase-matched second-harmonic generation [165].

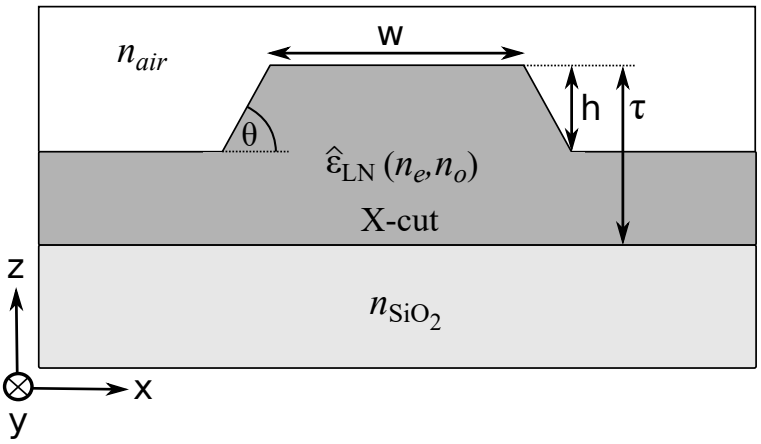

Figure 6.1: Schematic representation of the cross-section of a LNOI rib waveguide with a width w, etch depth h, film-height τ, and a side-wall angle of θ. Beneath the LN waveguide is the SiO_2 layer, serving as a buffer layer between the substrate and the waveguide. The coordinate system for the LN rib waveguide is also highlighted on the left, where the extra-ordinary refractive index (n_e) is along x-axis, and the ordinary refractive index (n_o) is along the y- and z-axis.

6.2 Investigated optical components

Optical components are indispensable parts of a photonic integrated circuit (PIC). Especially couplers like polarization splitters [166], multiplexers [167], and wavelength filters with bent couplers [168] are necessary for the enhanced functionality of PICs for optical communication. The work in this thesis focuses on optical components based on LNOI rib waveguides, whose schematic representation is illustrated in Figure 6.1.

In particular, we only investigate the X-cut LN. The coordinate system used in the investigation is highlighted in the figure. The optical axis of the anisotropic LN crystal is along the x-direction, and the structure is assumed to be uniform along the direction of propagation, which in this case is the y-axis. The waveguide is defined by its width w, film-height τ, etch depth h, and a sidewall angle θ. At the wavelength of operation of 775 nm, the refractive indices of bulk LN and SiO_2 used in the investigation are presented in the Table 6.1. These values were provided by the experimentalists of the Integrated Quantum Optics group at Paderborn University.

Material	Refractive index
SiO_2 (n_{SiO_2})	1.45
LN (n_e)	2.1783
LN (n_o)	2.2584

Table 6.1: Values of the refractive indices for bulk LN and SiO_2 used at the operational wavelength of 775 nm. The X-cut LN employs n_e along the x-axis and n_o along the other two axes.

Furthermore, based on the constraints provided by the experimentalists for the fabrication, we concentrate our analysis on thin film LN with a thickness of $\tau = 600$ nm for two specific

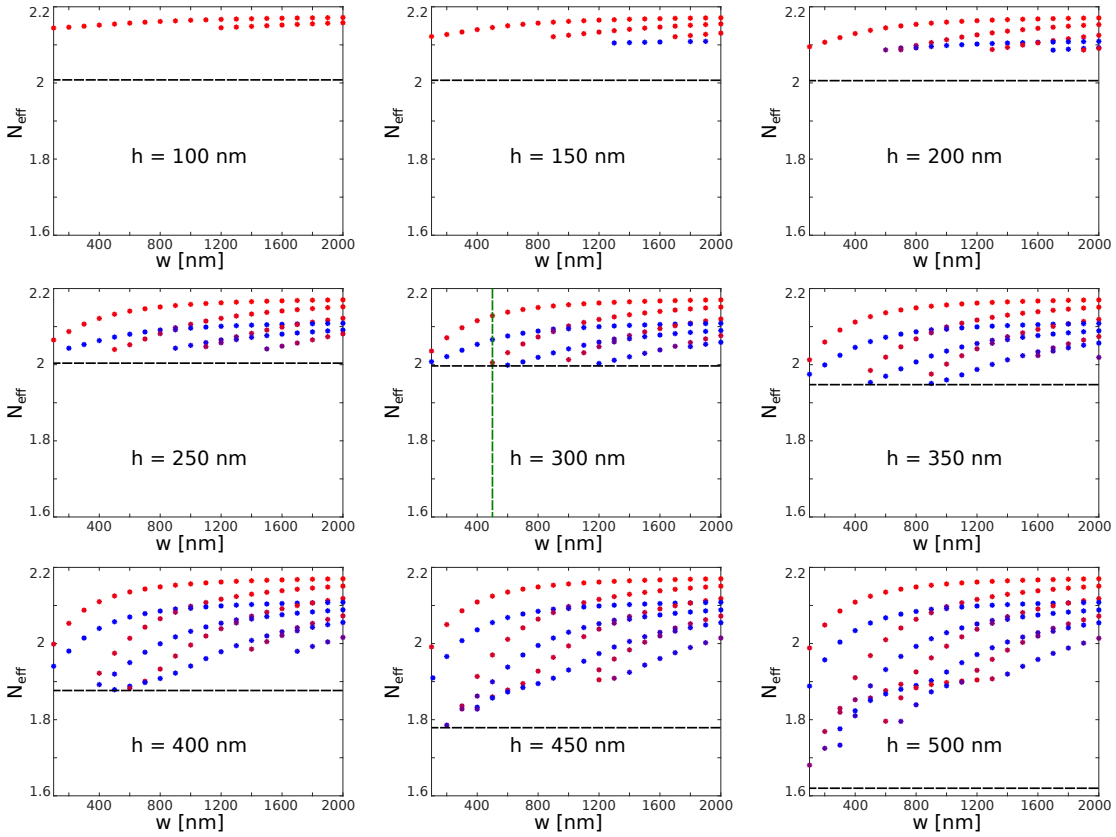

Figure 6.2: Effective mode indices of the guided modes supported in LNOI rib waveguides with a film thickness of $\tau = 600\,\text{nm}$ and a side-wall angle of $\theta = 70°$. The waveguide width (w) ranges from $100 - 2000\,\text{nm}$ and etch depths (h) between $100 - 500\,\text{nm}$ at an operational wavelength of $775\,\text{nm}$. The red and blue dots in the plots represent the TM-like and TE-like modes, respectively. The green dashed line indicates the configuration chosen for further investigations and is referred to as Structure 1.

side-wall angles, i.e., $\theta = 70°$ and $\theta = 60°$.

We perform an eigenmode analysis for varying waveguide widths and etch depths to identify the different modes these configurations support. This is done with the finite element method utilizing the mode analysis solver employed in COMSOL Multiphysics [124]. For $\tau = 600\,\text{nm}$ and $\theta = 70°$, limiting our search to the first eight guided modes, Figure 6.2 shows the effective indices (N_{eff}) of the guided modes as a function of the w for different h. The blue and red dots represent the TE-like and TM-like modes, respectively. The black dashed line represents the N_{eff} of the fundamental mode supported in the slab waveguide configuration on either side of the rib. This value signifies the lower limit for the N_{eff} a guided mode can have in the rib waveguide. Furthermore, the modal analysis exhibits two essential features. On the one hand, we can see the hybridization of modes. At these points, the TE and TM modes are so close to each other that they possess field components of the same order. On the other hand, we can also see the cross-over of modes, where the curves representing the TE and TM modes cross each other. This phenomenon is commonly observed in bent anisotropic waveguides, where the

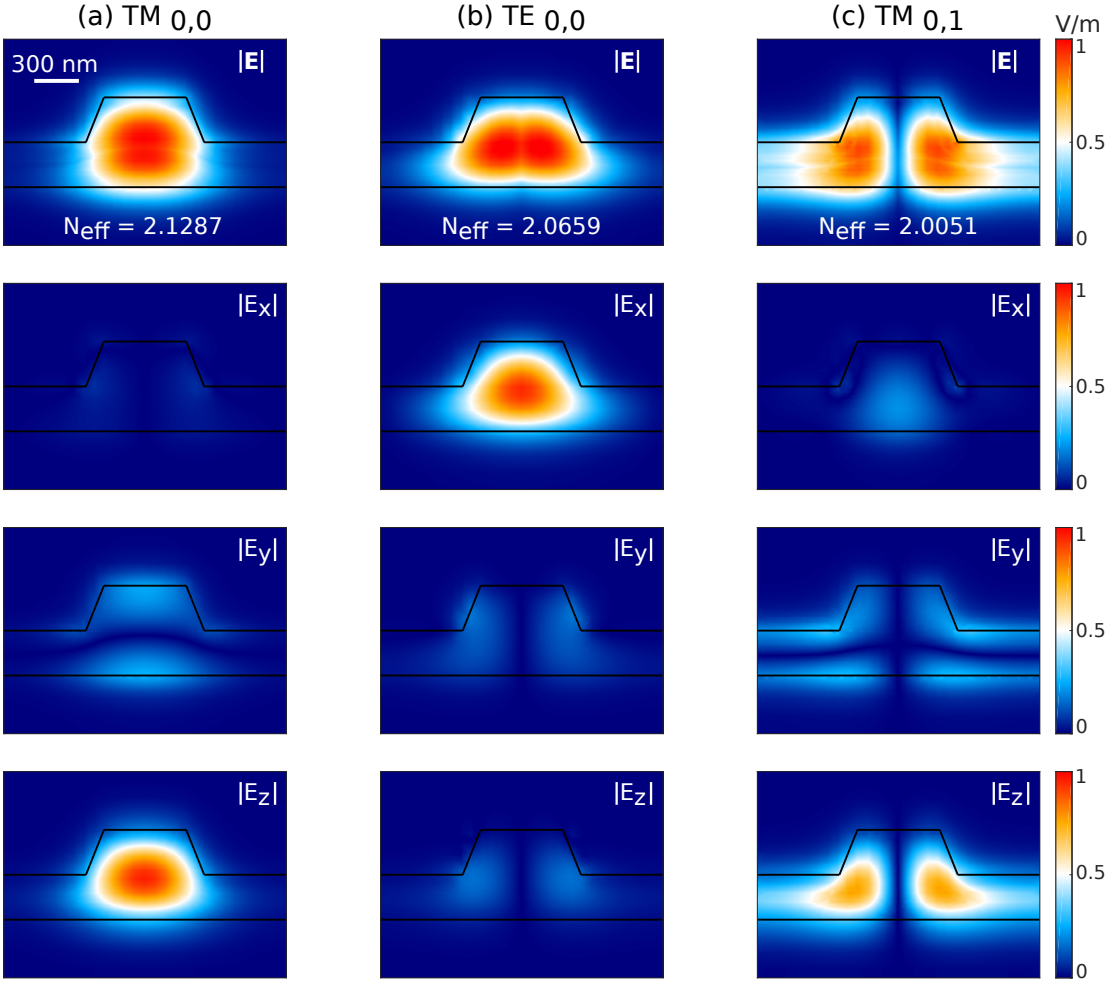

Figure 6.3: Mode profiles of the guided modes supported by the Structure 1 rib waveguide at a wavelength of 775 nm. The absolute electric field intensity distribution of the (a) $TM_{0,0}$, (b) $TE_{0,0}$, and (c) $TM_{0,1}$ modes along with their E_x, E_y, and E_z field components.

crystal orientation changes along the direction of propagation.

Although one expects the TE mode to be the fundamental mode, the figure shows that the TM mode is the fundamental mode. This can be attributed to the higher refractive index n_o being aligned to the vertical axis (z-axis), which has a more substantial influence on the TM modes, unlike the TE modes, which are affected by n_e that is aligned along the horizontal axis. Thus, the anisotropy plays a vital role in determining the fundamental mode. Therefore, the shallow depths only support TM modes, while the TE modes become apparent as the etch depth increases. Intuitively, the waveguides become multi-modal at larger widths and etch depths, supporting several higher-order TE and TM modes. The green line highlights the exact configuration that we choose for further analysis ($w = 500\,\text{nm}$, $h = 300\,\text{nm}$), as suggested by the experimentalists. We refer to this configuration as Structure 1, which shows the presence of two TM and one TE mode, and the fundamental mode is the TM mode.

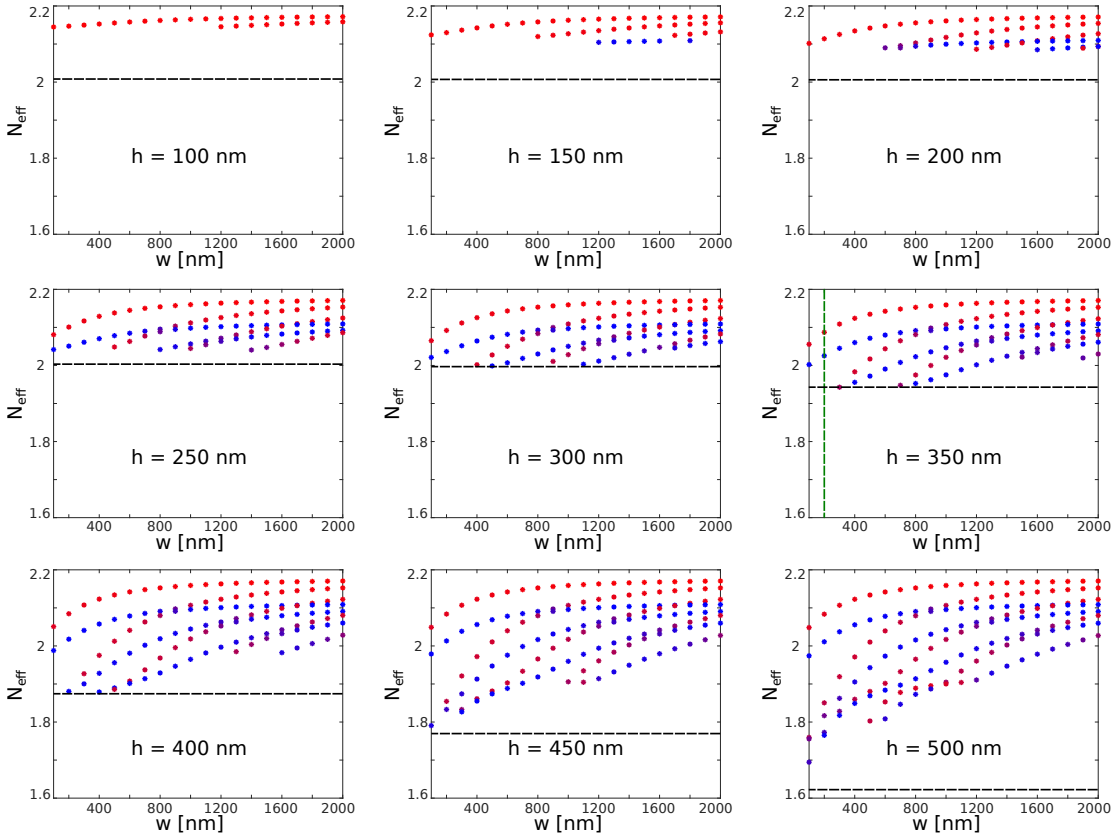

Figure 6.4: Effective mode indices of the guided modes supported in LNOI rib waveguides with a film thickness of $\tau = 600\,\text{nm}$ and a side-wall angle of $\theta = 60°$. The waveguide width (w) ranges from $100 - 2000\,\text{nm}$ and etch depths (h) between $100 - 500\,\text{nm}$ at an operational wavelength of $775\,\text{nm}$. The red and blue dots in the plots represent the TM-like and TE-like modes, respectively. The green dashed line indicates the configuration chosen for further investigations and is referred to as Structure 2.

Figure 6.3 shows the calculated electric field intensity distribution of the three guided modes supported in Structure 1, highlighting their respective effective mode index. Figure 6.3a (first column from left) represents the absolute electric field distribution of the $\text{TM}_{0,0}$ mode, followed by the illustration of its three electrical field components. The mode shows a strong vertical field component (E_z), making it a TM-like mode. Figure 6.3b (middle column) represents the $\text{TE}_{0,0}$ mode, which has a strong horizontal field component (E_x). Finally, Figure 6.3c (first column from the right) represents the $\text{TM}_{0,1}$ mode with a strong vertical component. All the mode profiles are normalized to the maximum of the fundamental mode, the $\text{TM}_{0,0}$ mode.

Similarly, the eigenmode analysis for waveguide configurations with $\tau = 600\,\text{nm}$ and $\theta = 60°$ are shown in Figure 6.4. A similar trend is observed in the eigenmode analysis conducted for $\theta = 70°$, where the smaller etch depths mainly support the TM modes, and the TE modes become apparent for larger widths and etch depths. The green line indicates the second geometry configuration used in the further investigations, referred to as Structure 2. In particular, the structure supports one TE and one TM mode, where the fundamental mode is again the

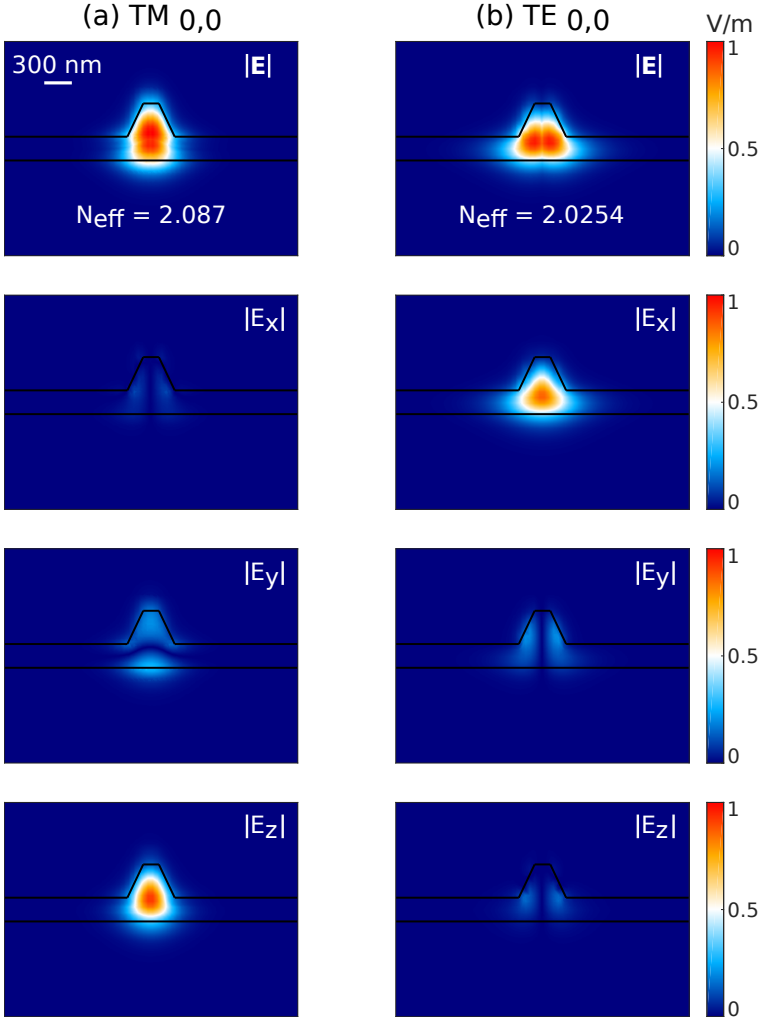

Figure 6.5: Mode profiles of the guided modes supported by the Structure 2 rib waveguide at a wavelength of 775 nm. The absolute electric field intensity distribution of the (a) $TM_{0,0}$ and (b) $TE_{0,0}$ modes along with their E_x, E_y, and E_z field components.

TM mode. Figure 6.5a and b show the calculated electric field intensity distribution of the two guided modes supported in Structure 2, namely, $TM_{0,0}$ and $TE_{0,0}$, along with their respective effective mode index. Again, the TM mode shows a strong vertical component, and the TE mode has a strong horizontal component. The plots are normalized to the maximum of the fundamental TM mode. The design parameters for the two rib waveguide geometries used in further investigations are summarized in the Table 6.2.

Structure 1	Structure 2
$w = 500\,\text{nm}$	$w = 200\,\text{nm}$
$h = 300\,\text{nm}$	$h = 350\,\text{nm}$
$\theta = 70°$	$\theta = 60°$

Table 6.2: Parameters of the two rib waveguide geometries.

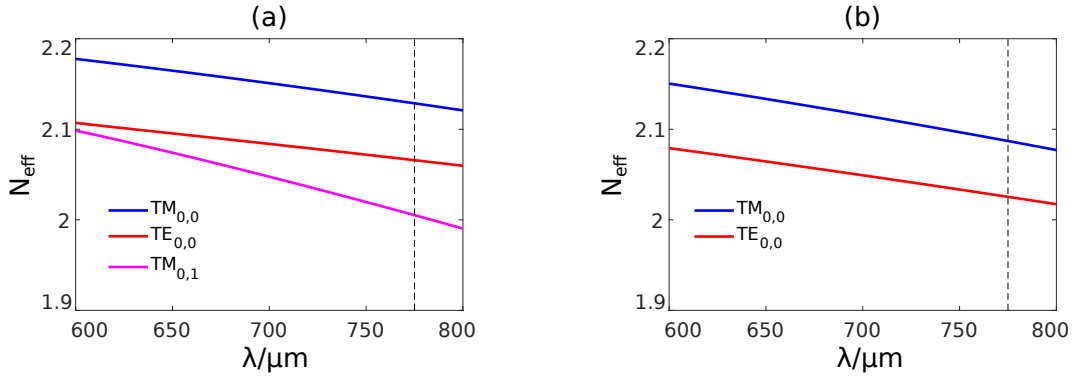

Figure 6.6: The effective mode index (N_{eff}) as a function of the vacuum wavelength for guided modes supported in (a) Structure 1 and (b) Structure 2 rib waveguides. The black dashed line indicates the wavelength used for further simulations.

Furthermore, Figure 6.6a and b show the effective indices N_{eff} of the guided modes as a function of the wavelength for Structure 1 and Structure 2, respectively. The black dashed line marks the wavelength of investigation, i.e., 775 nm. As can be seen, both structures support guided modes with an effective index that reduces with the increase in the operational wavelength.

Waveguides provide the fundamental infrastructure for integrated optics. Based on desired applications, it is possible to realize more complex systems with these components. In this thesis, three optical components are investigated that are built using the geometry parameters discussed above (Structure 1 and Structure 2). The following sections display our work on directional couplers, waveguide bends, and multi-mode interference couplers, vital components in integrated optics.

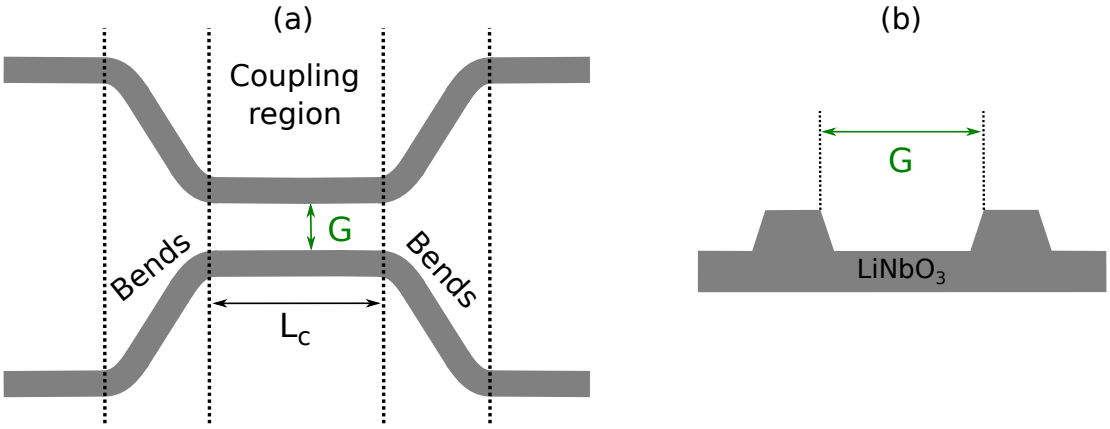

Figure 6.7: (a) Schematic representation of the top view of a directional coupler with a gap G between the parallel waveguides in the coupling region. (b) Illustration of the coupling region to highlight the gap G.

6.2.1 Directional couplers

In integrated optics, one of the vital components is the directional coupler (DC), which is capable of coupling light between adjacent waveguides. As discussed in Chapter 5, DCs have been widely employed in the distribution and splitting of optical signals due to their ease of design, and structural simplicity. Further, DCs can also be utilized for building more advanced structures like resonators, polarization splitters, interferometers, multiplexers, wavelength filters, etc. [166–169]. The following section briefly overviews the features of such devices.

Typically, a DC comprises two identical waveguides placed next to each other, as shown in Figure 6.7a. Initially, these waveguides are well separated, followed by the bending of these waveguides to bring them close together, where the coupling can take place [170]. Then again, the waveguides are separated using the bends. In the coupling region, the evanescent field from the first waveguide overlaps with the second waveguide core, and this coupling is strongly dependent on the gap G between them. The coupled mode theory explains this effect, which considers the coupling as a perturbation caused by the adjacent waveguide [171, 172].

If both waveguides are treated as a single system, the wave equations reveal that such a system comprises two system modes: symmetric and anti-symmetric. Consider a system with two identical Structure 1 rib waveguides that are separated by a gap G (like Figure 6.7b). We choose $G = 1\,\mu$m, as it is the smallest gap that the experimentalists could fabricate. On launching one of the waveguides with the $TE_{0,0}$ mode results in an excitation of the symmetric and anti-symmetric mode of the composite system, with effective indices $N_{\text{eff,s}} = 2.0661$ and $N_{\text{eff,a}} = 2.0656$, respectively. These mode profiles are illustrated in Figure 6.8a. The different effective mode indices indicate that both these modes have different propagation constants and propagate at different velocities. Therefore, for such a system, the coupling length L_c at which

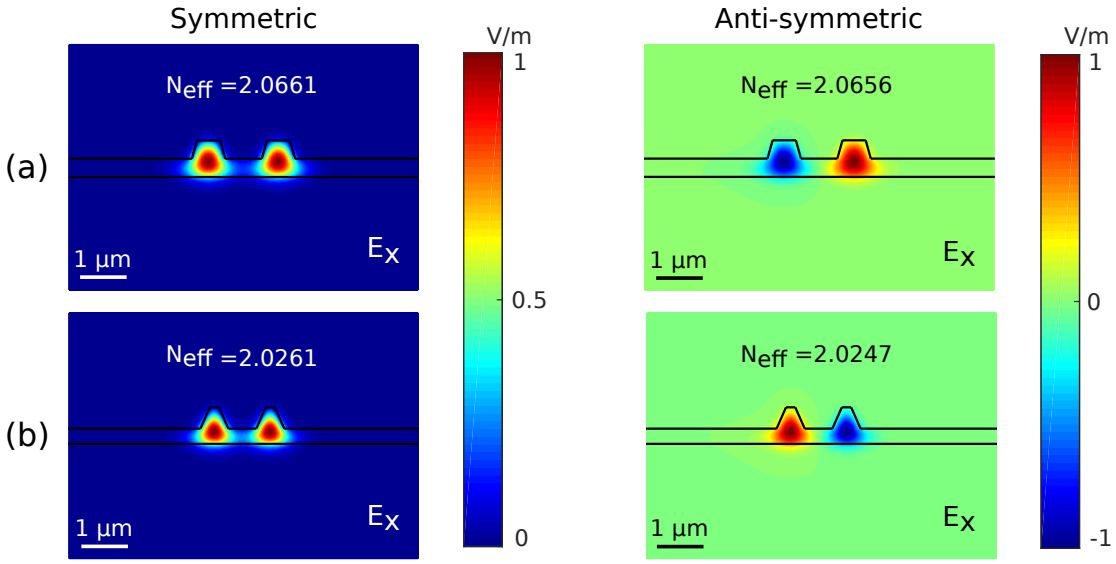

Figure 6.8: Symmetric (left column) and anti-symmetric (right column) mode profiles for the DC constructed with (a) Structure 1 and (b) Structure 2 rib waveguides, respectively. The mode profiles are represented with the E_x-component, which is the dominant TE-component of the field.

the complete power is transferred from one waveguide to the other can be given by

$$L_c = \frac{\lambda}{2 \cdot |N_{\text{eff,s}} - N_{\text{eff,a}}|}, \tag{6.5}$$

where λ is the wavelength of operation. For a pair of straight waveguides, the incoupled power sinusoidally oscillates between the two waveguides with a period of L_c, which for this system is approximately 775 μm.

Similarly, considering a gap of $G = 1\,\mu$m between two Structure 2 rib waveguides, we obtain a coupling length of approximately 276 μm. Figure 6.8b illustrates the symmetric and anti-symmetric mode excited by the $\text{TE}_{0,0}$ mode launched in one of the waveguides. It is evident from Eq. (6.5) that having a larger difference in the effective indices of the two system modes results in shorter L_c. Therefore, this system with Structure 2 rib waveguides possesses a shorter L_c.

6.2.2 Waveguide bends

Another important component in the integrated photonic circuitry is the waveguide bends. These bends can generally result in losses [173]. Nevertheless, they are the fundamental building blocks in integrated optics. Therefore, a precise analysis of their optical properties and bending losses becomes necessary. In this section, we look into different bend configurations with respect to Structure 1 and Structure 2 rib waveguides.

6.2.2.1 90°-bends

We begin with investigating 90° bends, equivalent to a quarter of a circle, as demonstrated in Figure 6.9a. Typically, the structures can support both TE- and TM-polarization, but we use the $\text{TE}_{0,0}$ mode for exciting the bend (as for the DCs) and observe how the mode propagates through

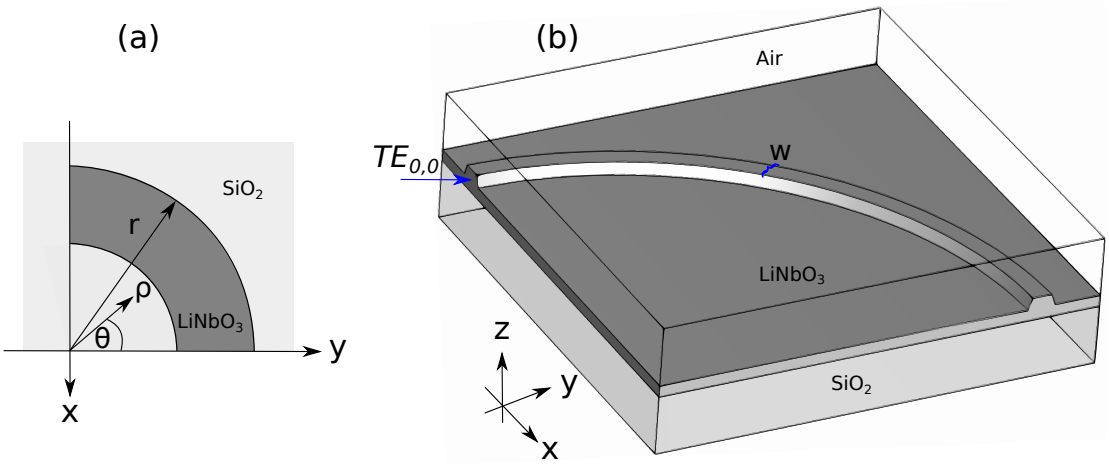

Figure 6.9: A 90°-bent LN rib waveguide on a SiO_2 substrate. (a) Top view and (b) 3-D schematic of the waveguide regularly bent around the z-axis with a radius of curvature r for wave propagation along the θ-direction. The waveguide is excited with the $\text{TE}_{0,0}$ mode, and the wave propagation faces a permittivity tensor with off-diagonal elements along the bend.

the bend. The waveguide is uniformly bent around the z-axis with a radius of curvature r. Its 3-D schematic representation is illustrated in Figure 6.9b. We are interested in waves that propagate in the θ-direction at an angle θ with a mode profile that is confined along the ρ-direction, i.e., the radial direction. Due to the anisotropy, the mode propagating through the waveguide in the θ-direction is dealing with a permittivity tensor consisting of off-diagonal elements, unlike the crystal-axis-aligned straight waveguides, which face a diagonal permittivity. Furthermore,

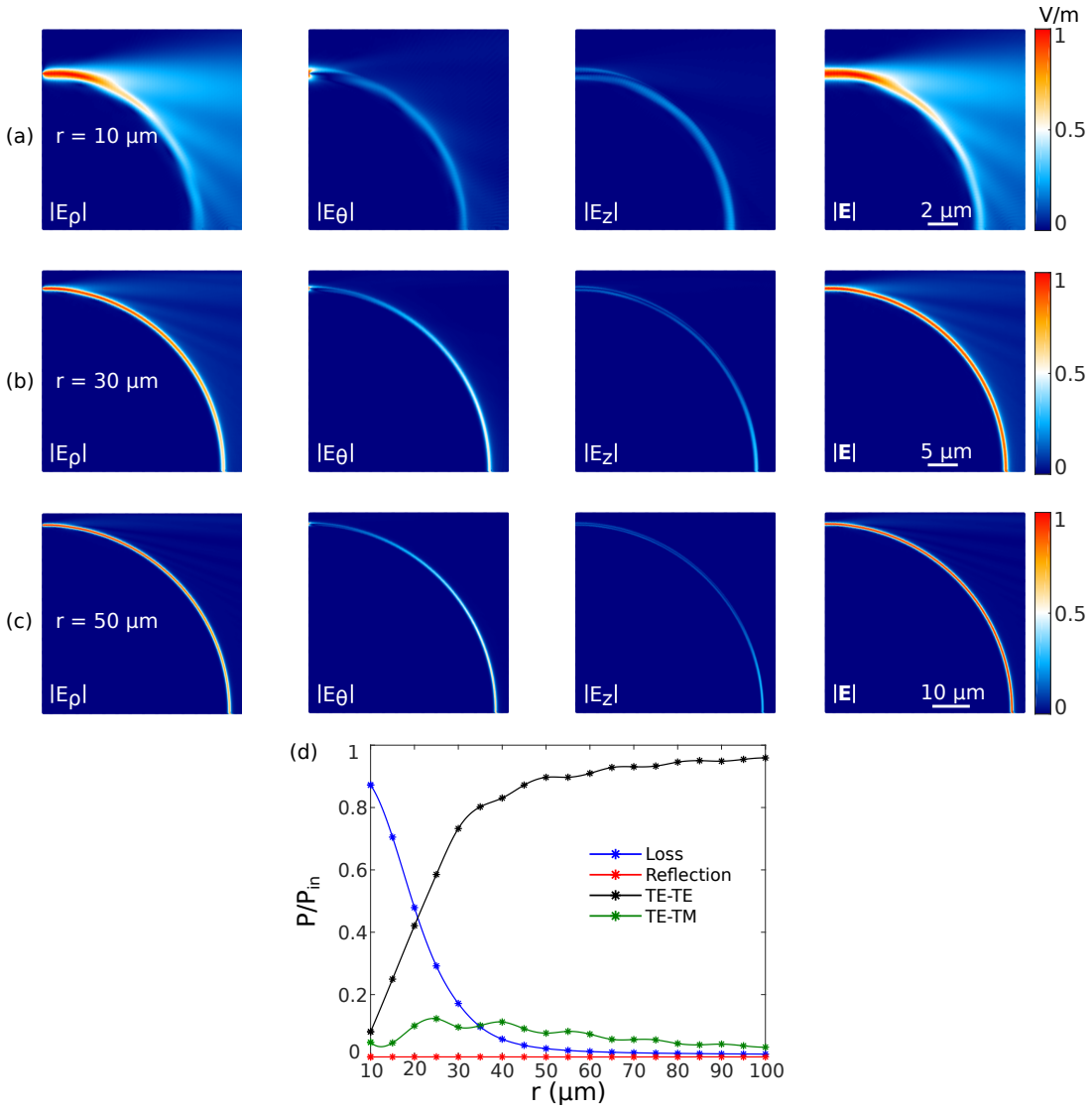

Figure 6.10: Absolute electric fields in the xy-plane at $z = 250\,\text{nm}$ for the 90°-bent Structure 1 rib waveguides with a curvature radius of (a) $r = 10\,\mu\text{m}$, (b) $r = 30\,\mu\text{m}$, and (c) $r = 50\,\mu\text{m}$. The waveguides are excited with the $\text{TE}_{0,0}$ mode. The radial component E_ρ, angular component E_θ, vertical component E_z, and the full absolute electric field $|\boldsymbol{E}|$ are represented column-wise for each radius, starting from the left side. The fields are normalized to their respective full absolute electric field. (d) Power efficiency for the 90°-bent Structure 1 rib waveguide as a function of the bend radius.

the change in crystal orientation results in a mode cross-over between the fundamental TE- and TM-mode at the output waveguide with respect to the input waveguide. As per the dispersion relation, the incoming waveguide orientation supports a TM-polarized fundamental mode, while the fundamental mode of the outgoing waveguide orientation is TE-polarized.

It is important to get a clear picture of how the modes propagate through these bends and

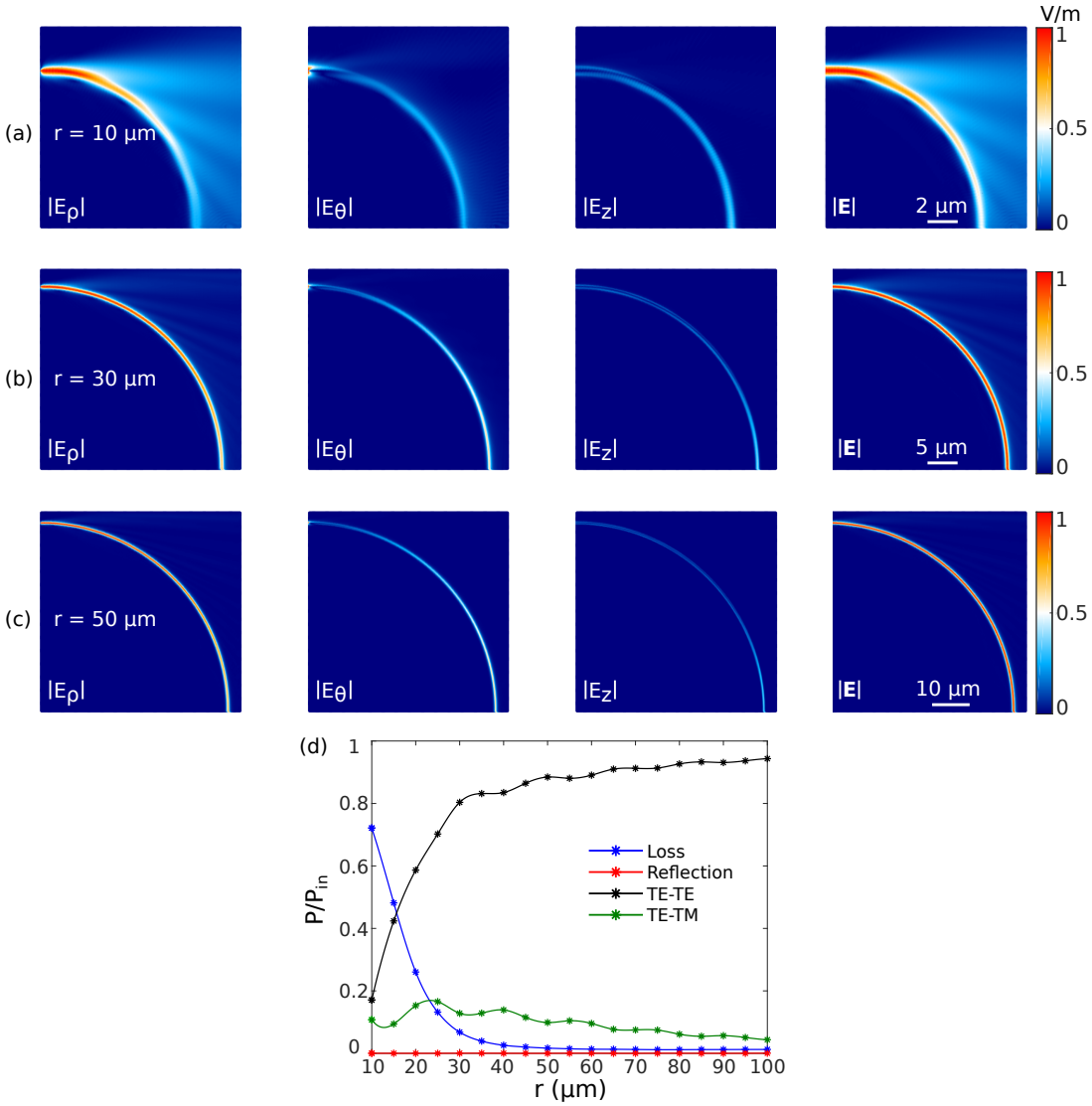

Figure 6.11: Absolute electric fields in the xy-plane at $z = 200\,\text{nm}$ for the 90°-bent Structure 2 rib waveguides with a curvature radius of (a) $r = 10\,\mu\text{m}$, (b) $r = 30\,\mu\text{m}$, and (c) $r = 50\,\mu\text{m}$. The waveguides are excited with the $\text{TE}_{0,0}$ mode. The radial component E_ρ, angular component E_θ, vertical component E_z, and full absolute electric field $|\boldsymbol{E}|$ are represented column-wise for each radius, starting from the left side. The fields are normalized to their respective full absolute electric field. (d) Power efficiency for the 90°-bent Structure 2 rib waveguide as a function of the bend radius.

decay with respect to the radial arguments or what influence different bend radii have on their propagation. Intuitively, one expects the waveguides with smaller radii to exhibit higher losses than the larger radii due to the sharper bends in the smaller structures. Therefore, the loss mainly comes from the waveguide's power radiating as it bends along the curvature. Additionally, a part of the input optical power is also coupled to the other polarization due to the bending, i.e., the TM polarization, resulting in a polarization conversion that is estimated at the output end of the waveguide. We first investigate the bends with respect to the Structure 1 rib waveguides. Starting from the left column, Figure 6.10a shows the absolute radial-, angular- and vertical-components of the electric field for a bent Structure 1 rib waveguide of radius $r = 10\,\mu$m. These fields are normalized to the absolute electric field of the same structure shown in the fourth column. The radial component demonstrates the strongest field, which can be attributed to the $TE_{0,0}$ mode coupled to this waveguide, having a strong horizontal component. On the other hand, from the vertical component of the field E_z, it becomes evident that a part of the TE polarization couples to the TM polarization along the propagation direction, demonstrating the effect of polarization conversion.

Similarly, Figure 6.10b and c illustrate the fields for the larger radii, i.e., $r = 30\,\mu$m and $r = 50\,\mu$m. As seen in the fourth column, more power is transmitted to the end of the waveguide bend as the radius increases. This is manifested in the brighter red part of the field confined within the waveguide and the lesser white part of the fields radiating away from the bend. Figure 6.10d shows the power efficiencies for such Structure 1 rib waveguides for a bend radius ranging from $10-100\,\mu$m. The amount of power carried forward by the TE mode is depicted by the black curve, and the green curve represents the amount of power coupled from the TE mode to the TM mode. The red curve shows the reflection efficiency, and the blue curve depicts the bending losses given by the power leaving the waveguide core region. As the radius increases, the bending losses decrease and are less than 1% at $r = 100\,\mu$m. Meanwhile, polarization conversion drops but remains as high as 3% at $r = 100\,\mu$m.

Furthermore, we do a similar investigation with Structure 2 rib waveguides. These waveguides also demonstrate a similar response, as shown in Figure 6.11. However, the smaller radii, for example, $r = 10\,\mu$m, exhibit lower losses than the Structure 1 waveguides, as more power is coupled to the TE polarization.

6.2.2.2 S-bends

In the next step, we look into other bend configurations. We investigate the more sophisticated S-bends, as shown in Figure 6.12. These bends have a cosine dependence and are defined using two parameters, L and P, which are the horizontal and vertical separation between the incoming and outgoing waveguide. Such structures can be used for establishing a connection between waveguides at position (L, P). The x-position of the waveguide core center for such a bend can be defined as

$$p(y) = P\cos\left(\frac{\pi}{2L}y\right)^2, \tag{6.6}$$

where y ranges between $0-L$. Such a configuration presents the same crystal orientation at the incoming and outgoing waveguide. Therefore, the modes at the input and output are identical. Again, this evaluation is done for both, Structure 1 and Structure 2 waveguide bends. The $TE_{0,0}$

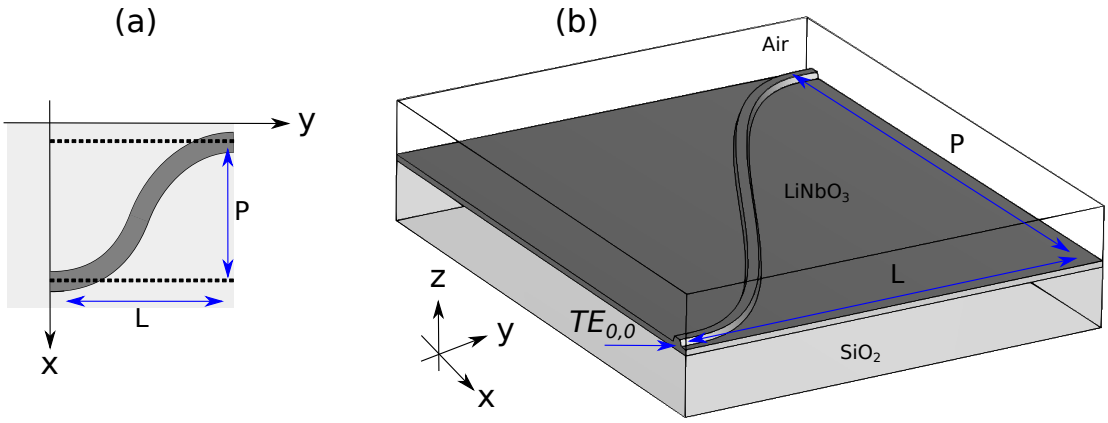

Figure 6.12: An S-bent LN rib waveguide on a SiO_2 substrate. (a) Top view and (b) 3-D schematic of the structure, where the input and output of the waveguide are horizontally and vertically separated by a distance of L and P, respectively. The waveguide is excited by the $TE_{0,0}$ mode, as demonstrated on the input side.

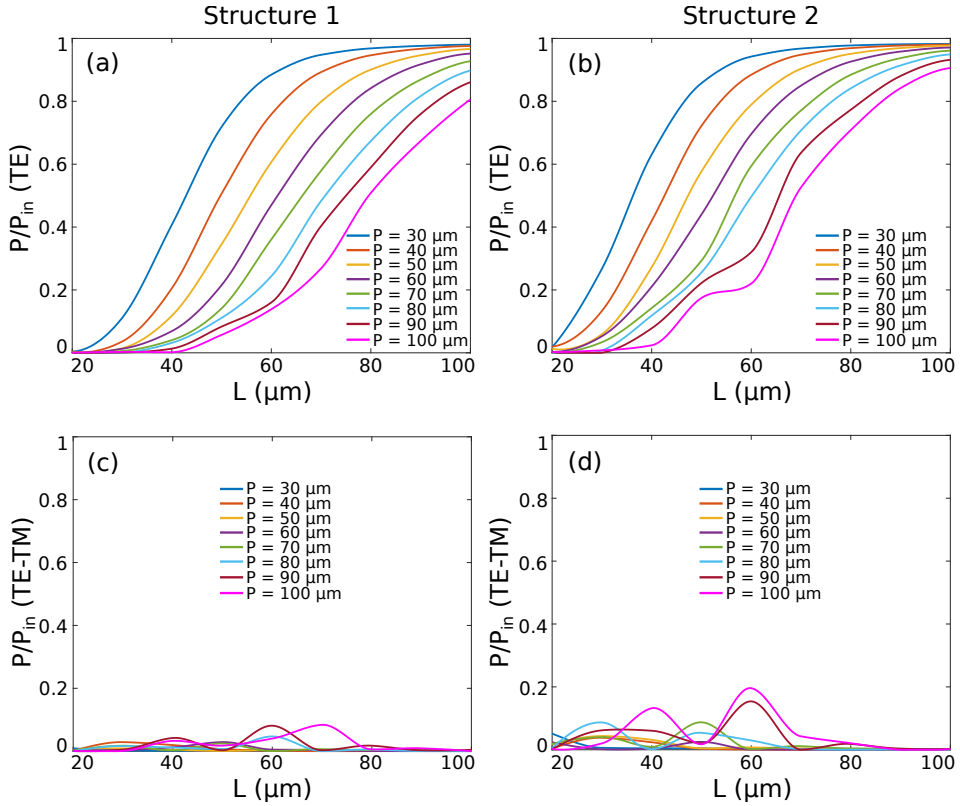

Figure 6.13: Power efficiency for the S-bent (a,c) Structure 1 and (b,d) Structure 2 rib waveguide, as a function of the horizontal separation L for different values of the vertical separation P. The waveguides are excited with the $TE_{0,0}$ mode, and the amount of power carried forward by the same TE mode (upper row) and coupled to the $TM_{0,0}$ mode (lower row) is depicted.

mode is launched at the input, and we analyze the amount of power carried forward by the same TE mode and the amount of power coupled to the $TM_{0,0}$ mode.

Figure 6.13a and b represent the power carried by the $TE_{0,0}$ mode as a function of L ranging from $20 - 100\,\mu$m for P ranging from $30 - 100\,\mu$m for Structure 1 and Structure 2 rib waveguides, respectively. As can be seen, different combinations of these two parameters provide more than 90% transmissions with the TE mode. Furthermore, Figure 6.13c and d represent the polarization conversion in Structure 1 and Structure 2 rib waveguides, respectively. The smaller configurations of the Structure 1 S-bent waveguides present a conversion of under 1%. On the other hand, the larger configurations of Structure 2 S-bent waveguides exhibit very low polarization conversion, along with some smaller configurations, for example, a combination of $L = 30\,\mu$m and $P = 30\,\mu$m has less than 1% of power coupled to the TM mode. Therefore, these bends can prove beneficial when integrated into photonic circuitry. Furthermore, one can also investigate other bend configurations based on their requirements.

6.2.3 Multi-mode interference couplers

Other popular structures are the MMI-based devices as they are easy to fabricate and incorporate in intricate PICs like Mach-Zehnder modulators and switches, ring lasers, phase diversity

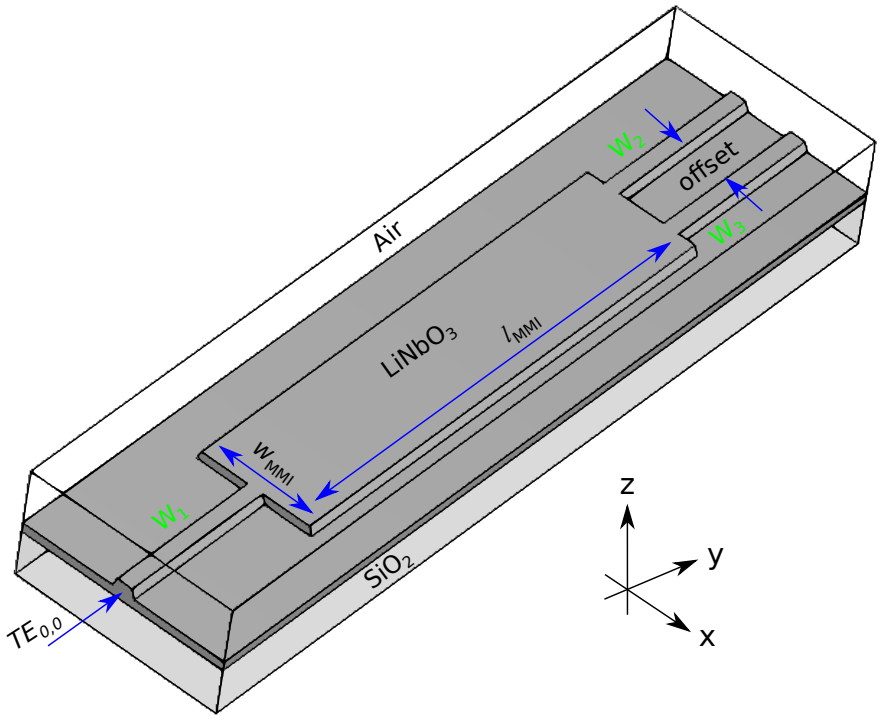

Figure 6.14: Schematic representation of the 3-D multi-mode interference coupler constructed with LN rib waveguides on a SiO_2 substrate. The incoming and outgoing waveguides are identical, and the central coupler has a length and width of l_{MMI} and w_{MMI}, respectively. The outgoing waveguides are separated by a distance of offset. The system is excited by the $TE_{0,0}$ mode, as demonstrated at the incoming waveguide.

networks, coherent receivers, etc. [174]. An MMI coupler is a device consisting of incoming and outgoing waveguides for coupling the light in and out of the coupler between these waveguides. Essentially, the MMI coupler is a broad optical waveguide. As such, it spreads the in-coupled light over many guided modes and exploits the particularities of their interference pattern [175–177]. This optical power is then split or combined at the output desirably. In this work, we look at 1×2 MMI couplers, which should ideally achieve an equal 50-50 power split at the output. This implies that the power would enter through one path with wave propagation along y-axis and leave through two paths [178], as represented by the schematic in Figure 6.14. When an MMI coupler is excited, the incident wave is decomposed into the eigenmodes, each possessing a unique propagation constant, allowing them to propagate independently with different velocities. This results in an interference pattern that changes along the MMI coupler length. Therefore, a suitable combination of the length l_{MMI} and width w_{MMI} of the coupling segment needs to be determined that leads to a splitting ratio close to 50-50, keeping in mind the complex nature of light affected by the optical losses, reflection, and interference from the multiple modes.

We begin with the optimization of an MMI coupler with identical incoming and outgoing Structure 1 rib waveguides. The incoming waveguide is launched with a $\mathrm{TE}_{0,0}$ mode, which connects to the broader coupler waveguide of length l_{MMI} and width w_{MMI}. The entire structure has the etch depth of $h = 300\,\mathrm{nm}$ on the LN thin film. The outgoing waveguides are separated by a distance of offset, measured between the two waveguides as shown in the schematic (Figure 6.14). In total, three design parameters were optimized, namely, l_{MMI}, w_{MMI}, and offset, using the hybrid optimization routine of PSO and TRO (as discussed in Section 3.2.2). The objective of the optimization routine is to achieve 50% power flow in one of the outgoing waveguides, in our case W_2, by targeting the $\mathrm{S}_{2,1}$ parameter. Assuming that the offset is sufficiently large such that the waves in the outgoing waveguides do not interact, due to the symmetry in the system, achieving 50% power in waveguide W_2 would automatically result in the remaining 50% of the optical power to be transmitted to waveguide W_3. Similarly, the MMI coupler is also optimized with the Structure 2 rib waveguides, where the entire structure has an etch depth of $h = 350\,\mathrm{nm}$ on the LN thin film. The design parameters of both the optimized MMI couplers are presented in Table 6.3.

Design parameters	Structure 1	Structure 2
l_{MMI}	$23\,\mu$m	$26.8\,\mu$m
w_{MMI}	$3.6\,\mu$m	$3.88\,\mu$m
offset	$1.49\,\mu$m	$1.94\,\mu$m

Table 6.3: Optimized values of the design parameters for the MMI coupler with Structure 1 and Structure 2 rib waveguides.

Figure 6.15a shows the absolute electric field of the optimized MMI coupler with Structure 1 rib waveguides in the xy-plane at $z = 250\,\mathrm{nm}$ from the bottom of the thin film. The structure exhibits a transmission of 42% in both the outgoing waveguides, with almost no reflection back to the incoming waveguide. The remaining power is lost to the non-guided scattered waves, mainly at the interface between the broad coupling waveguide and the outgoing waveguides. However, one can mitigate this issue using adiabatic tapering waveguides, which can achieve

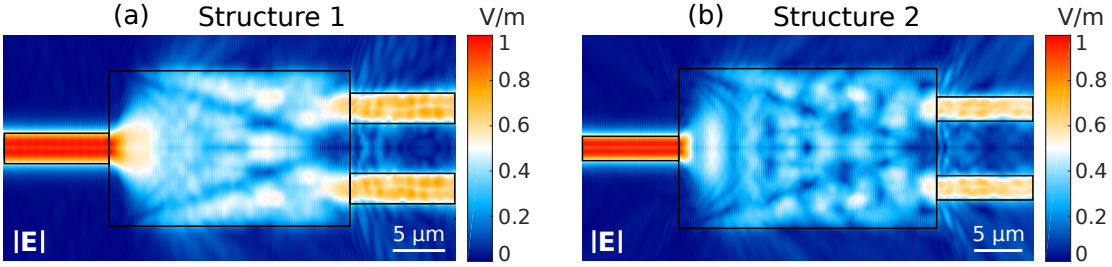

Figure 6.15: Absolute electric fields in the xy-plane for the MMI coupler with incoming and outgoing rib waveguides of (a) Structure 1 at $z = 250\,\text{nm}$ and (b) Structure 2 at $z = 200\,\text{nm}$. The waveguides are excited with the $\text{TE}_{0,0}$ mode.

better impedance matching at this interface and have a higher transmission in both outgoing waveguides. Figure 6.15b demonstrates the absolute electric field for the optimized MMI coupler with Structure 2 rib waveguides in the xy-plane at $z = 200\,\text{nm}$ from the bottom of the thin film. This configuration achieves approximately 40% power transmission in both the outgoing waveguides with almost no reflection to the incoming waveguide. However, the scattering losses are slightly higher than in the previous configuration, which can be attributed to the narrow geometry of the rib waveguides.

Overall, we present an overview of specific LNOI waveguides and certain optical components based on them as parts of integrated photonic circuits. It should be noted that we only consider systems with X-cut and y-propagating configurations. Other structures may exist that have even better performance. Furthermore, we systematically explore and compare different waveguide bends with respect to their power loss and polarization conversion. Lastly, we optimize and analyze MMI couplers based on these LNOI waveguides.

Chapter 7

Summary

This work explores the design and optimization of various antenna types to have efficient control over their radiation patterns. We begin with the target of directivity enhancement for nanoantennas in the optical regime, specifically in the near-infrared range (780 nm). This is followed by analyzing the use of nanoantennas in phased array systems. Again, different antenna geometries are proposed and optimized to tailor radiation characteristics in efficient optical phased array systems, particularly for the telecom wavelength ($1.55\,\mu$m). Furthermore, the thesis analyzes various optical components for LNOI-based integrated optical circuits. In particular, we investigate anisotropic crystal geometries suitable for integrated quantum photonic applications at a wavelength of 775 nm. The results obtained in this work can be discussed in three subsequent parts:

Highly directive antennas:

We investigate highly directional dielectric traveling-wave antennas composed of two dielectric building blocks, i.e., the reflector and director, with dipole emitters as the internal light source. We analyze the design parameters constituting the antenna geometry and their influence on the complex interplay between the leaky and guided modes supported in the waveguide-like director. This allows us to characterize the directive nature of these optical waveguide antennas. The experimental and numerical calculations show that the emission properties of the antennas are mainly affected by the effective mode index of the director. This opens up opportunities to explore different director types and materials for constructing these antennas. It is also established that the strongest coupling is achieved with the TE-polarization of the dipole (y-oriented dipole). Together these results give us room to improve the antennas' directivity by using different optimization algorithms.

We successfully optimize the directivity of three traveling-wave antennas for broadband use. The three antennas investigated are rectangular-, tip-, and horn-antenna, placed over a glass substrate with dipole emitters used as the internal excitation source. Numerically, we investigate these antennas composed of HfO_2, Si, and Ta_2O_5 while experimentally, they are validated using Ta_2O_5. Our antennas demonstrate highly directional characteristics, especially the horn antennas are more directive than the other two types, exhibiting linear directivity as high as 157 (21.95 dB). However, this comes at the cost of a larger footprint and higher side lobe levels.

The directionality is primarily due to two dominant TE modes that couple strongly to the dipole emitter in addition to the leaky modes. These guided modes dominate the far-field emission pattern and govern the direction of the main lobe emission. Therefore, the antennas offer an opportunity to tailor the directivity and main lobe angle of the far-field radiation pattern. On the other hand, these antennas are not only ultra-directional but also highly efficient and have a wide operating frequency range, especially the tip antenna. A comprehensive analysis of the antennas' modes, radiation patterns, parametric influences, and bandwidths highlights their robust nature to fabrication imperfections, as indicated by the sensitivity analysis of the design parameters. The numerical simulations are in good agreement with the experimental results obtained from the fabricated samples. Although these antennas have a larger footprint, their feasibility for sample production indicates that they can be efficiently used in practical applications such as integrated optical devices, on-chip communication, beam shaping, and wireless communication. Finally, we anticipate that the directional properties of these antennas can be further enhanced by utilizing them in an array design.

Optical phased arrays:

The efficient operation of an optical phased array demands a radiation element characterized by high performance and a compact footprint. Therefore, we look into three distinct Si antennas designed and optimized to target different cost functions. The first objective of interest is increasing the total emitted power in the upward direction. For this purpose, we consider two types of asymmetric dielectric horn antennas. The first geometry introduces a vertical asymmetry in the form of two-level gratings with unique grating pitches, where the variable pitch provides more control variables in the optimization process for improving the upward radiation with a near-broadside emission profile. The second geometry introduces a heterogeneous grating configuration consisting of a U-shaped grating in combination with L-shaped gratings, resulting in a compact horn-shaped blazed grating antenna. Both these optimized antennas are capable of high upward efficiency of the magnitude of 63% and 78% with the radiation directed along 1° and 8°, respectively. The second objective of interest is to direct more power into the field of view of size $6.8^\circ \times 6.8^\circ$. For this purpose, a circular grating antenna with a variable grating pitch in conjunction with a partial etch is considered. The optimized antenna demonstrates an upward efficiency of 51% and can concentrate 3.2% of the optical power into the field of view.

Furthermore, exploiting the benefits of multi-layer silicon photonics, we investigate the design and optimization of reflector geometries to further improve the upward efficiency and power in the field of view. Using a single reflector, the asymmetric horn antenna can efficiently radiate almost 83% of the input optical power upward, maintaining a near-broadside emission along 4°. On the other hand, using a two-layer Bragg reflector with the circular grating antenna improves the upward radiation efficiency to approximately 88% with 6.8% of the optical power being directed into the field of view. We demonstrate that the proposed antennas are suitable for large-scale 2-D OPAs capable of pattern synthesis, beam steering, and beamforming. Additionally, these antennas are employed in architectures that increase the grating-lobe-free beam steering range using the large HPBW of the radiating element. We anticipate that our robust, optimized antennas can be easily fabricated and utilized to enhance the performance of OPAs in different applications such as LiDARs, holography, imaging, optogenetic stimulation, augmented-reality displays, and various communication systems.

LNOI waveguide structures:

Finally, we systematically investigate different optical components based on LNOI rib waveguides that can be essentially utilized in integrated quantum photonic circuits. We focus on X-cut LNOI waveguides with an anisotropic LN core layer over a silicon dioxide substrate, and this system is excited with the TE mode. We begin with a broad eigenmode analysis for different heights and widths of the rib waveguide. Based on the results, the experimentalists chose two geometries for further investigation. Waveguides with these two geometries are applied for designing directional couplers, waveguide bends, and multi-mode interference couplers, whose optical properties are then individually characterized. For the directional couplers, the symmetric and anti-symmetric modes are characterized to estimate the coupling length at which a complete power transfer between the two rib waveguides can be attained. Another critical aspect that is investigated is the bends in such waveguides. Two types of bends are studied, namely, the 90°-bends and S-bends, and the losses introduced due to their bent curvature are analyzed. In general, sharper bends result in higher losses of the input optical power. Furthermore, bends in these LNOI rib waveguides also result in polarization conversion, even for structures with a bend radius as high as $100\,\mu$m. The parametric study conducted on these bends helps identify different design configurations to mitigate these issues of high bending losses or polarization conversion in such structures. Lastly, we optimize and characterize the 1×2 multi-mode interference couplers, practical devices in integrated optics. The optimized multi-mode interference couplers demonstrate symmetrical power transmission of up to 42% in both outgoing waveguides. Devices of these types are considered for application in the field of integrated photonic quantum systems.

List of Figures

List of Tables

Acronyms

Acronym	Meaning
BC	Boundary condition
CMOS	Complementary metal-oxide semiconductor
FDTD	Finite difference time domain
FEM	Finite element method
FIT	Finite integration technique
PML	Perfectly matched layer
PSO	Particle swarm optimization
TRO	Trust region optimization
TEM	Transverse electromagnetic
TE	Transverse electric
TM	Transverse magnetic
SEM	Scanning electron micrograph
GS	Gerchberg-Saxton
OPA	Optical phased array
FOV	Field of view
LN	Lithium niobate
LNOI	Lithium niobate on insulator
MMI	Multi-mode interference
DC	Directional coupler
HPBW	Half power beam width
SLL	Side lobe level

Symbols

Symbol	Meaning
$\mathbf{E}$	Electric field
$\mathbf{H}$	Magnetic field
$\mathbf{D}$	Electric displacement
$\mathbf{B}$	Magnetic flux density
$\mathbf{J}$	Current density
$\mathbf{P}$	Polarization
$\mathbf{M}$	Magnetization
t	Time
ω	Angular frequency
k_0	Vacuum wavenumber
c_0	Speed of light
λ_0	Vacuum wavelength
ε_0	Vacuum permittivity
μ_0	Vacuum permeability
χ	Susceptibility
ε_r	Relative permittivity
μ_r	Relative permeability
$\mathbf{S}$	Poynting vector
N_{eff}	Effective refractive index
D	Directivity
(x, y, z)	Cartesian coordinates
(ρ, θ, z)	Cylindrical coordinates
(r, θ, φ)	Spherical coordinates
k_x, k_y, k_z	Wavenumbers in x-, y-, z-direction

List of publications [1]

The following journal articles and conference proceedings accompanied the work of this thesis:

Journal articles:

1. H. Farheen, A. Strauch, J. C. Scheytt, V. Myroshnychenko, and J. Förstner. Optimized, highly efficient silicon antennas for optical phased arrays. *Photonics and Nanostructures-Fundamentals and Applications* 58:101207, 2024.

2. H. Farheen, S. Joshi, J. C. Scheytt, V. Myroshnychenko, and J. Förstner. An efficient compact blazed grating antenna for optical phased arrays. *arXiv:2306.02795 [physics.optics]*, 2023.

3. H. Farheen, L. Yan, V. Quiring, C. Eigner, T. Zentgraf, S. Linden, J. Förstner, and V. Myroshnychenko. Broadband optical Ta_2O_5 antennas for directional emission of light. *Opt. Express* 30(11):19288-19299, 2022.

4. H. Farheen, T. Leuteritz, S. Linden, V. Myroshnychenko, and J. Förstner. Optimization of optical waveguide antennas for directive emission of light. *J. Opt. Soc. Am. B* 39(1):83–91, 2022.

5. T. Leuteritz, H. Farheen, S. Qiao, F. Spreyer, C. Schlickriede, T. Zentgraf, V. Myroshnychenko, J. Förstner, and S. Linden. Dielectric travelling wave antennas for directional light emission. *Opt. Express* 29(10):14694–14704, 2021.

6. M. Hammer, H. Farheen, and J. Förstner. How to suppress radiative losses in high-contrast integrated Bragg gratings. *J. Opt. Soc. Am. B* 40(4):862–873, 2023.

7. V. Myroshnychenko, P. M. M. Jose, H. Farheen, S. Ejaz, C. Brosseau, and J. Förstner. From Swiss-Cheese to discrete ferroelectric composites: Assessing the ferroelectric butterfly shape in polarization loops. *Physica Scripta* 99.4:045952, 2024.

8. S. Alhaddad, Y. Grynko, H. Farheen, and J. Förstner. Numerical analysis of the coherent mechanism producing negative polarization at backscattering from systems of absorbing particles. *Opt. Lett.* 47(1):58–61, 2022.

[1] List updated last on 31.05.2024.

Conference contributions:

1. H. Farheen, S. Joshi, J. C. Scheytt, V. Myroshnychenko, and J. Förstner. Increasing the upward radiation efficiency of optical phased arrays using asymmetric silicon horn antennas in *IEEE Photonics Conference, IPC 2023*, Orlando, United States of America, Proceedings, 2023.

2. H. Farheen, A. Strauch, J. C. Scheytt, V. Myroshnychenko, and J. Förstner. Optimized silicon antennas for optical phased arrays in *SPIE Photonics West 2023, OPTO 2023*, San Francisco, United States of America, Proceedings, 2023.

3. H. Farheen, L. Yan, T. Leuteritz, S. Qiao, F. Spreyer, C. Schlickriede, V. Quiring, C. Eigner, C. Silberhorn, T. Zentgraf, S. Linden, V. Myroshnychenko, and J. Förstner. Tailoring the directive nature of optical waveguide antennas in *SPIE Photonics West 2023, OPTO 2023*, San Francisco, United States of America, Proceedings, 2023.

4. H. Farheen, L. Yan, T. Leuteritz, S. Qiao, F. Spreyer, C. Schlickriede, V. Quiring, C. Eigner, T. Zentgraf, S. Linden, J. Förstner, and V. Myroshnychenko. Enhancing directivity in optical waveguide antennas in *DPG (Spring) Meetings 2022*, Regensburg, Germany, Proceedings, 2022.

5. H. Farheen, L. Yan, T. Leuteritz, S. Qiao, F. Spreyer, C. Schlickriede, V. Quiring, C. Eigner, T. Zentgraf, S. Linden, J. Förstner, and V. Myroshnychenko. Design and optimization of broadband optical antennas in *12th International Conference on Metamaterials, Photonic Crystals and Plasmonics, META 2022*, Torremolinos, Spain, Proceedings, 2022.

6. H. Farheen, L. Yan, T. Leuteritz, S. Qiao, F. Spreyer, C. Schlickriede, V. Quiring, C. Eigner, T. Zentgraf, S. Linden, J. Förstner, and V. Myroshnychenko. Engineering highly directive optical waveguide antennas in *8th International Conference on Antennas and Electromagnetic Systems, AES 2022*, Marrakesh, Morocco, Proceedings, 2022.

7. H. Farheen, A. Hildebrandt, V. Myroshnychenko, M. Peter, C. Schlickriede, K. Gharib, T. Zentgraf, S. Linden, and J. Förstner. Optical waveguide antennas for directive emission of light in *9th International Conference on Surface Plasmon Photonics, SPP9*, Copenhagen, Denmark, Proceedings, 2019.

8. H. Farheen, T. Leuteritz, V. Myroshnychenko, M. Peter, C. Schlickriede, K. Gharib, T. Zentgraf, S. Linden, and J. Förstner. Optical waveguide antennas for directive emission of light: Optimized for high directivity in *8th Doctoral Conference on Optics, DoKDoK 2019*, Eisenach, Germany, Proceedings, 2019.

9. H. Farheen, A. Hildebrandt, V. Myroshnychenko, M. Peter, C. Schlickriede, K. Gharib, T. Zentgraf, S. Linden, and J. Förstner. Optical waveguide antennas for directive emission of light: A parametric study in *7th Doctoral Conference on Optics, DoKDoK 2018*, Friedrichroda, Germany, Proceedings, 2018.

10. A. Strauch, H. Farheen, V. Myroshnychenko, and J. Förstner. Optimization of silicon nanoantenna for optical phased arrays in *PhotonIcs and Electromagnetics Research Symposium, PIERS 2023*, Prague, Czech Republic, Proceedings, 2023.

11. M. Hammer, H. Farheen, and J. Förstner. Lossless operation of high-contrast integrated

optical waveguide gratings in *XXIX International Workshop on Optical Wave & Waveguide Theory and Numerical Modelling, OWTNM 2023*, Marseille, France, Proceedings, 2023.

12. A. Strauch, H. Farheen, V. Myroshnychenko, and J. Förstner. Optimization of silicon nanoantenna for optical phased arrays in *14th Annual Meeting Photonic Devices, AMPD 2023*, Berlin, Germany, Proceedings, 2023.

13. L. Yan, H. Farheen, F. Spreyer, C. Schlickriede, V. Myroshnychenko, T. Zentgraf, J. Förstner, and S. Linden. Directional emission from dielectric multi-mode interference antennas in *8th International Topical Meeting on Nanophotonics and Metamaterials, NANOMETA 2022*, Seefeld, Austria, Proceedings, 2022.

14. A. Strauch, H. Farheen, V. Myroshnychenko, and J. Förstner. Optimization of silicon nanoantenna for optical phased arrays in *DPG (Spring) Meetings 2022*, Regensburg, Germany, Proceedings, 2022.

15. A. Strauch, H. Farheen, V. Myroshnychenko, and J. Förstner. Optimization of silicon nanoantenna for optical phased arrays in *10th Doctoral Conference on Optics, DoKDoK 2022*, Arnstadt, Germany, Proceedings, 2022.

16. T. Leuteritz, M. Peter, S. Linden, C. Schlickriede, F. Spreyer, T. Zentgraf, H. Farheen, J. Förstner. Directional emission from dielectric antennas: A parametric study in *DPG (Spring) Meetings 2018*, Berlin, Germany, Proceedings, 2018.

Bibliography

[1] John David Jackson. *Classical electrodynamics*. American Association of Physics Teachers, 1999.

[2] Amnon Yariv and Pochi Yeh. *Optical Waves in Crystals: Propagation and Control of Laser Radiation*. John Wiley and Sons, Inc., New York, NY, 1983.

[3] Constantine A Balanis. *Modern Antenna Handbook*. John Wiley & Sons, 2011.

[4] Manfred Hammer, Henna Farheen, and Jens Förstner. How to suppress radiative losses in high-contrast integrated Bragg gratings. *JOSA B*, 40(4):862–873, 2023.

[5] Masataka Nakazawa, Kazuro Kikuchi, and Tetsuya Miyazaki. *High spectral density optical communication technologies*, volume 6. Springer Science & Business Media, 2010.

[6] Robert G Hunsperger. *Integrated optics: Theory and technology*. Springer Science & Business Media, 2009.

[7] Chong Sheng, Hui Liu, Shining Zhu, and Dentcho A Genov. Active control of electromagnetic radiation through an enhanced thermo-optic effect. *Scientific Reports*, 5(1):8835, 2015.

[8] Palash Bharadwaj, Bradley Deutsch, and Lukas Novotny. Optical antennas. *Advances in Optics and Photonics*, 1(3):438–483, 2009.

[9] TH Taminiau, FD Stefani, Franciscus B Segerink, and NF Van Hulst. Optical antennas direct single-molecule emission. *Nature Photonics*, 2(4):234–237, 2008.

[10] Lukas Novotny and Niek Van Hulst. Antennas for light. *Nature Photonics*, 5(2):83–90, 2011.

[11] Aleksandr E Krasnok, Ivan S Maksymov, Andrei I Denisyuk, Pavel Alexandrovich Belov, Andrei E Miroshnichenko, Constantin R Simovski, and Yu S Kivshar. Optical nanoantennas. *Physics-Uspekhi*, 56(6):539, 2013.

[12] Vincenzo Giannini, Antonio I Fernández-Domínguez, Susannah C Heck, and Stefan A Maier. Plasmonic nanoantennas: Fundamentals and their use in controlling the radiative properties of nanoemitters. *Chemical Reviews*, 111(6):3888–3912, 2011.

[13] Naomi J Halas, Surbhi Lal, Wei-Shun Chang, Stephan Link, and Peter Nordlander. Plasmons in strongly coupled metallic nanostructures. *Chemical Reviews*, 111(6):3913–3961, 2011.

[14] Thang B Hoang, Gleb M Akselrod, Christos Argyropoulos, Jiani Huang, David R Smith, and Maiken H Mikkelsen. Ultrafast spontaneous emission source using plasmonic nanoantennas. *Nature Communications*, 6(1):1–7, 2015.

[15] Stephen Sanders and Alejandro Manjavacas. Nanoantennas with balanced gain and loss. *Nanophotonics*, 9(2):473–480, 2020.

[16] A Yu Nikitin, F Guinea, FJ Garcia-Vidal, and Luis Martin-Moreno. Fields radiated by a nanoemitter in a graphene sheet. *Physical Review B*, 84(19):195446, 2011.

[17] Peter Muhlschlegel, H-J Eisler, Olivier JF Martin, Bert Hecht, and DW Pohl. Resonant optical antennas. *Science*, 308(5728):1607–1609, 2005.

[18] Arseniy I Kuznetsov, Andrey E Miroshnichenko, Mark L Brongersma, Yuri S Kivshar, and Boris Luk'yanchuk. Optically resonant dielectric nanostructures. *Science*, 354(6314), 2016.

[19] Rajesh K Mongia and Prakash Bhartia. Dielectric resonator antennas - A review and general design relations for resonant frequency and bandwidth. *International Journal of Microwave and Millimeter-Wave Computer-Aided Engineering*, 4(3):230–247, 1994.

[20] Alexander E Krasnok, Andrey E Miroshnichenko, Pavel A Belov, and Yuri S Kivshar. All-dielectric optical nanoantennas. *Optics Express*, 20(18):20599–20604, 2012.

[21] AI Barreda, JM Saiz, F González, F Moreno, and P Albella. Recent advances in high refractive index dielectric nanoantennas: Basics and applications. *AIP Advances*, 9(4):040701, 2019.

[22] Basudeb Sain, Cedrik Meier, and Thomas Zentgraf. Nonlinear optics in all-dielectric nanoantennas and metasurfaces: A review. *Advanced Photonics*, 1(2):024002, 2019.

[23] Javier Cambiasso, Gustavo Grinblat, Yi Li, Aliaksandra Rakovich, Emiliano Cortés, and Stefan A Maier. Bridging the gap between dielectric nanophotonics and the visible regime with effectively lossless gallium phosphide antennas. *Nano Letters*, 17(2):1219–1225, 2017.

[24] Sébastien Bidault, Mathieu Mivelle, and Nicolas Bonod. Dielectric nanoantennas to manipulate solid-state light emission. *Journal of Applied Physics*, 126(9):094104, 2019.

[25] Sergii Morozov, Michele Gaio, Stefan A Maier, and Riccardo Sapienza. Metal-dielectric parabolic antenna for directing single photons. *Nano Letters*, 18(5):3060–3065, 2018.

[26] Nitzan Livneh, Moshe G Harats, Daniel Istrati, Hagai S Eisenberg, and Ronen Rapaport. Highly directional room-temperature single photon device. *Nano Letters*, 16(4):2527–2532, 2016.

[27] Evgenia Rusak, Isabelle Staude, Manuel Decker, Jürgen Sautter, Andrey E Miroshnichenko, David A Powell, Dragomir N Neshev, and Yuri S Kivshar. Hybrid nanoan-

tennas for directional emission enhancement. *Applied Physics Letters*, 105(22):221109, 2014.

[28] Paolo Biagioni, Jer-Shing Huang, and Bert Hecht. Nanoantennas for visible and infrared radiation. *Reports on Progress in Physics*, 75(2):024402, 2012.

[29] Constantine A Balanis. *Antenna theory: Analysis and design*. John Wiley & Sons, 2015.

[30] Farshid Ashtiani and Firooz Aflatouni. N $\times$ N optical phased array with 2N phase shifters. *Optics Express*, 27(19):27183–27190, 2019.

[31] Jie Sun, Erman Timurdogan, Ami Yaacobi, Zhan Su, Ehsan Shah Hosseini, David B Cole, and Michael R Watts. Large-scale silicon photonic circuits for optical phased arrays. *IEEE Journal of Selected Topics in Quantum Electronics*, 20(4):264–278, 2013.

[32] Behrooz Abiri, Reza Fatemi, and Ali Hajimiri. A 1-D heterodyne lens-free optical phased array camera with reference phase shifting. *IEEE Photonics Journal*, 10(5):1–12, 2018.

[33] Michael R Kossey, Charbel Rizk, and Amy C Foster. End-fire silicon optical phased array with half-wavelength spacing. *APL Photonics*, 3(1):011301, 2018.

[34] Christopher V Poulton, Matthew J Byrd, Manan Raval, Zhan Su, Nanxi Li, Erman Timurdogan, Douglas Coolbaugh, Diedrik Vermeulen, and Michael R Watts. Large-scale silicon nitride nanophotonic phased arrays at infrared and visible wavelengths. *Optics Letters*, 42(1):21–24, 2017.

[35] Aroutin Khachaturian, Reza Fatemi, and Ali Hajimiri. Achieving full grating-lobe-free field of view with low-complexity co-prime photonic beamforming transceivers. *Photonics Research*, 10(5):A66–A73, 2022.

[36] Henna Farheen, Andreas Strauch, J Christoph Scheytt, Viktor Myroshnychenko, and Jens Förstner. Increasing the field-of-view radiation efficiency of optical phased antenna arrays. *arXiv preprint arXiv:2303.18107*, 2023.

[37] Henna Farheen, Suraj Joshi, J Christoph Scheytt, Viktor Myroshnychenko, and Jens Förstner. An efficient compact blazed grating antenna for optical phased arrays. *arXiv preprint arXiv:2306.02795*, 2023.

[38] Reza Fatemi, Aroutin Khachaturian, and Ali Hajimiri. A nonuniform sparse 2-D large-FOV optical phased array with a low-power PWM drive. *IEEE Journal of Solid-State Circuits*, 54(5):1200–1215, 2019.

[39] Aroutin Khachaturian, Reza Fatemi, Artsroun Darbinian, and Ali Hajimiri. Discretization of annular-ring diffraction pattern for large-scale photonics beamforming. *Photonics Research*, 10(5):1177–1186, 2022.

[40] William S Rabinovich, Peter G Goetz, Marcel Pruessner, Rita Mahon, Mike S Ferraro, Doe Park, Erin Fleet, and Michael J DePrenger. Free space optical communication link using a silicon photonic optical phased array. In *Free-Space Laser Communication and Atmospheric Propagation XXVII*, volume 9354, page 93540B. International Society for Optics and Photonics, 2015.

[41] Wolfgang M Neubert, Klaus H Kudielka, Walter R Leeb, and Arpad L Scholtz. Experimental demonstration of an optical phased array antenna for laser space communications. *Applied Optics*, 33(18):3820–3830, 1994.

[42] Pierre-Alexandre Blanche, Lloyd LaComb, Youmin Wang, and Ming C Wu. Diffraction-based optical switching with MEMS. *Applied Sciences*, 7(4):411, 2017.

[43] Jerry Zhou, Jie Sun, Ami Yaacobi, Christopher V Poulton, and Michael R Watts. Design of 3D hologram emitting optical phased arrays. In *Integrated Photonics Research, Silicon and Nanophotonics*, pages IT4A–7. Optical Society of America, 2015.

[44] Christopher Vincent Poulton, Matthew J Byrd, Peter Russo, Erman Timurdogan, Murshed Khandaker, Diedrik Vermeulen, and Michael R Watts. Long-range LiDAR and free-space data communication with high-performance optical phased arrays. *IEEE Journal of Selected Topics in Quantum Electronics*, 25(5):1–8, 2019.

[45] Jesse Levinson, Jake Askeland, Jan Becker, Jennifer Dolson, David Held, Soeren Kammel, J Zico Kolter, Dirk Langer, Oliver Pink, Vaughan Pratt, et al. Towards fully autonomous driving: Systems and algorithms. In *2011 IEEE Intelligent Vehicles Symposium (IV)*, pages 163–168. IEEE, 2011.

[46] Christopher V Poulton, Ami Yaacobi, David B Cole, Matthew J Byrd, Manan Raval, Diedrik Vermeulen, and Michael R Watts. Coherent solid-state LiDAR with silicon photonic optical phased arrays. *Optics Letters*, 42(20):4091–4094, 2017.

[47] Pavan Bhargava, Taehwan Kim, Christopher V Poulton, Jelena Notaros, Ami Yaacobi, Erman Timurdogan, Christopher Baiocco, Nicholas Fahrenkopf, Seth Kruger, Tat Ngai, et al. Fully integrated coherent LiDAR in 3D-integrated silicon photonics/65nm CMOS. In *2019 Symposium on VLSI Circuits*, pages C262–C263. IEEE, 2019.

[48] R. W. Boyd. *Nonlinear Optics, Third Edition*. Academic Press, Inc., USA, 3rd edition, 2008.

[49] Wolfgang Sohler, Hui Hu, Raimund Ricken, Viktor Quiring, Christoph Vannahme, Harald Herrmann, Daniel Büchter, Selim Reza, Werner Grundkötter, Sergey Orlov, et al. Integrated optical devices in lithium niobate. *Optics and Photonics News*, 19(1):24–31, 2008.

[50] Jing Wang, Haoru Yang, Nina Xiong, Muyan Zhang, Na Qian, Sicheng Yi, Shaofu Xu, and Weiwen Zou. Toward photonic-electronic convergence based on heterogeneous platform of merging lithium niobate into silicon. *JOSA B*, 40(6):1573–1590, 2023.

[51] Jianwei Wang, Fabio Sciarrino, Anthony Laing, and Mark G Thompson. Integrated photonic quantum technologies. *Nature Photonics*, 14(5):273–284, 2020.

[52] Jan Philipp Höpker, Varun B Verma, Maximilian Protte, Raimund Ricken, Viktor Quiring, Christof Eigner, Lena Ebers, Manfred Hammer, Jens Förstner, Christine Silberhorn, et al. Integrated superconducting nanowire single-photon detectors on titanium in-diffused lithium niobate waveguides. *Journal of Physics: Photonics*, 3(3):034022, 2021.

[53] Jan Philipp Höpker, Moritz Bartnick, Evan Meyer-Scott, Frederik Thiele, Stephan Krapick, Nicola Montaut, Matteo Santandrea, Harald Herrmann, Sebastian Lengeling, Raimund Ricken, et al. Towards integrated superconducting detectors on lithium niobate waveguides. *arXiv:1708.06232 [physics.ins-det]*, 2017.

[54] Guang-Tai Xue, Yun-Fei Niu, Xiaoyue Liu, Jia-Chen Duan, Wenjun Chen, Ying Pan, Kunpeng Jia, Xiaohan Wang, Hua-Ying Liu, Yong Zhang, et al. Ultrabright multiplexed energy-time-entangled photon generation from lithium niobate on insulator chip. *Physical Review Applied*, 15(6):064059, 2021.

[55] Jia-Chen Duan, Ji-Ning Zhang, Yin-Jun Zhu, Chang-Wei Sun, Yi-Chen Liu, Ping Xu, Zhenda Xie, Yan-Xiao Gong, and Shi-Ning Zhu. Generation of narrowband counter-propagating polarization-entangled photon pairs based on thin-film lithium niobate on insulator. *JOSA B*, 37(7):2139–2145, 2020.

[56] PR Sharapova, KH Luo, H Herrmann, M Reichelt, T Meier, and Ch Silberhorn. Toolbox for the design of $LiNbO_3$-based passive and active integrated quantum circuits. *New Journal of Physics*, 19(12):123009, 2017.

[57] Nicola Montaut, Linda Sansoni, Evan Meyer-Scott, Raimund Ricken, Viktor Quiring, Harald Herrmann, and Christine Silberhorn. High-efficiency plug-and-play source of heralded single photons. *Physical Review Applied*, 8(2):024021, 2017.

[58] Mian Zhang, Cheng Wang, Rebecca Cheng, Amirhassan Shams-Ansari, and Marko Lončar. Monolithic ultra-high-Q lithium niobate microring resonator. *Optica*, 4(12):1536–1537, 2017.

[59] Rui Luo, Haowei Jiang, Steven Rogers, Hanxiao Liang, Yang He, and Qiang Lin. On-chip second-harmonic generation and broadband parametric down-conversion in a lithium niobate microresonator. *Optics Express*, 25(20):24531–24539, 2017.

[60] Jie Wang, Fang Bo, Shuai Wan, Wuxia Li, Feng Gao, Junjie Li, Guoquan Zhang, and Jingjun Xu. High-Q lithium niobate microdisk resonators on a chip for efficient electro-optic modulation. *Optics Express*, 23(18):23072–23078, 2015.

[61] Li Chen, Qiang Xu, Michael G Wood, and Ronald M Reano. Hybrid silicon and lithium niobate electro-optical ring modulator. *Optica*, 1(2):112–118, 2014.

[62] Ashutosh Rao, Aniket Patil, Jeff Chiles, Marcin Malinowski, Spencer Novak, Kathleen Richardson, Payam Rabiei, and Sasan Fathpour. Heterogeneous microring and mach-zehnder modulators based on lithium niobate and chalcogenide glasses on silicon. *Optics Express*, 23(17):22746–22752, 2015.

[63] Dassault Systémes, "CST Studio Suite," https://www.cst.com.

[64] Sophocles J Orfanidis. *Electromagnetic waves and antennas*. Rutgers University New Brunswick, NJ, 2002.

[65] Robert E Collin and Francis J Zucker. *Antenna theory, part 1*. McGraw Hill, 1969.

[66] James Clerk Maxwell. VIII. A dynamical theory of the electromagnetic field. *Philosophical Transactions of the Royal Society of London*, (155):459–512, 1865.

[67] Alberto G Curto, Giorgio Volpe, Tim H Taminiau, Mark P Kreuzer, Romain Quidant, and Niek F van Hulst. Unidirectional emission of a quantum dot coupled to a nanoantenna. *Science*, 329(5994):930–933, 2010.

[68] Jed Z Buchwald. *The creation of scientific effects: Heinrich Hertz and electric waves*. University of Chicago Press, 1994.

[69] Warren L Stutzman and Gary A Thiele. *Antenna theory and design*. John Wiley & Sons, 2012.

[70] R Elliott. *Traveling Wave Antennas*. McGraw-Hill, 1965.

[71] Adrian Sutinjo, Michal Okoniewski, and Ronald H Johnston. Radiation from fast and slow traveling waves. *IEEE Antennas and Propagation Magazine*, 50(4):175–181, 2008.

[72] John L Volakis. *Antenna engineering handbook*. McGraw-Hill Education, 2007.

[73] Bahaa EA Saleh and Malvin Carl Teich. *Fundamentals of photonics*. John Wiley & Sons, 2019.

[74] Katsunari Okamoto. *Fundamentals of Optical Waveguides*. Academic Press, SanDiego, 2000.

[75] Manuel Peter. *Active plasmonic and dielectric nanoantennas*. PhD thesis, Universitäts- und Landesbibliothek Bonn, 2017.

[76] Christopher Palmer. Diffraction grating handbook. MKS Instruments. *Inc.: New York, NY, USA*, 2020.

[77] Robert C Hansen. *Phased array antennas*. John Wiley & Sons, 2009.

[78] Panayiotis Ioannides and Constantine A Balanis. Uniform circular arrays for smart antennas. *IEEE Antennas and Propagation Magazine*, 47(4):192–206, 2005.

[79] Panayiotis Ioannides and Constantine A Balanis. Mutual coupling in adaptive circular arrays. In *IEEE Antennas and Propagation Society Symposium, 2004.*, volume 1, pages 403–406. IEEE, 2004.

[80] René Marklein. *The finite integration technique as a general tool to compute acoustic, electromagnetic, elastodynamic, and coupled wave fields*. IEEE Press and John Wiley and Sons, New York, NY, USA, 2002.

[81] Thomas Weiland. A discretization model for the solution of Maxwell's equations for six-component fields. *Archiv Elektronik und Uebertragungstechnik*, 31:116–120, 1977.

[82] Markus Clemens and Thomas Weiland. Discrete electromagnetism with the finite integration technique. *Progress In Electromagnetics Research*, 32:65–87, 2001.

[83] Carsten Carstensen. *Computational Electromagnetics: Proceedings of the GAMM Workshop on Computational Electromagnetics, Kiel, Germany, January 26-28, 2001*, volume 28. Springer Science & Business Media, 2003.

[84] Ursula Van Rienen. *Numerical methods in computational electrodynamics: Linear systems in practical applications*, volume 12. Springer Science & Business Media, 2001.

[85] Allen Taflove, Susan C Hagness, and Melinda Piket-May. Computational electromagnetics: The finite-difference time-domain method. *The Electrical Engineering Handbook*, 3, 2005.

[86] Kane Yee. Numerical solution of initial boundary value problems involving Maxwell's equations in isotropic media. *IEEE Transactions on Antennas and Propagation*, 14(3):302–307, 1966.

[87] Ursula van Rienen and Thomas Weiland. Triangular discretization method for the evaluation of RF-fields in cylindrically symmetric cavities. *IEEE Transactions on Magnetics*, 21(6):2317–2320, 1985.

[88] R Schuhmann and T Weiland. A stable interpolation technique for FDTD on non-orthogonal grids. *International Journal of Numerical Modelling: Electronic Networks, Devices and Fields*, 11(6):299–306, 1998.

[89] FL Teixeira and WC Chew. Complex space approach to perfectly matched layers: A review and some new developments. *International Journal of Numerical Modelling: Electronic Networks, Devices and Fields*, 13(5):441–455, 2000.

[90] Li Zhao and Andreas C Cangellaris. GT-PML: Generalized theory of perfectly matched layers and its application to the reflectionless truncation of finite-difference time-domain grids. *IEEE Transactions on Microwave Theory and Techniques*, 44(12):2555–2563, 1996.

[91] R Schuhmann and T Weiland. Conservation of discrete energy and related laws in the finite integration. *Journal of Electromagnetic Waves and Applications*, 15(4):477–478, 2001.

[92] Shawna D Lockhart and Cindy M Johnson. *Engineering design communication: Conveying design through graphics*. Addison-Wesley, 2000.

[93] Jorge Nocedal and Stephen Wright. *Numerical optimization*. Springer Science & Business Media, 2006.

[94] Pakize Erdogmus. Introductory chapter: Swarm intelligence and particle swarm optimization. *Particle Swarm Optimization with Applications*, page 1, 2018.

[95] James Kennedy and Russell Eberhart. Particle swarm optimization. In *Proceedings of ICNN'95-International Conference on Neural Networks*, volume 4, pages 1942–1948. IEEE, 1995.

[96] Konstantinos E Parsopoulos and Michael N Vrahatis. *Particle swarm optimization and intelligence: Advances and applications*. IGI global, 2010.

[97] Riemann Ruiz-Cruz, Edgar N Sanchez, Fernando Ornelas-Tellez, Alexander G Loukianov, and Ronald G Harley. Particle swarm optimization for discrete-time inverse optimal control of a doubly fed induction generator. *IEEE Transactions on Cybernetics*, 43(6):1698–1709, 2012.

[98] Alex Lazinica. *Particle swarm optimization*. BoD–Books on Demand, 2009.

[99] Till Leuteritz, Henna Farheen, Siqi Qiao, Florian Spreyer, Christian Schlickriede, Thomas Zentgraf, Viktor Myroshnychenko, Jens Förstner, and Stefan Linden. Dielectric travelling wave antennas for directional light emission. *Optics Express*, 29(10):14694–14704, 2021.

[100] Henna Farheen, Till Leuteritz, Stefan Linden, Viktor Myroshnychenko, and Jens Förstner. Optimization of optical waveguide antennas for directive emission of light. *JOSA B*, 39(1):83–91, 2022.

[101] Henna Farheen, Lok-Yee Yan, Viktor Quiring, Christof Eigner, Thomas Zentgraf, Stefan Linden, Jens Förstner, and Viktor Myroshnychenko. Broadband optical Ta_2O_5 antennas for directional emission of light. *Optics Express*, 30(11):19288–19299, 2022.

[102] William W Hansen. Radiating electromagnetic waveguide, June 25 1946. US Patent 2,402,622.

[103] Thomas A Milligan. *Modern antenna design*. John Wiley & Sons, 2005.

[104] Arthur A Oliner, David R Jackson, and JL Volakis. Leaky-wave antennas. *Antenna Engineering Handbook*, 4:12, 2007.

[105] Jonathan Hu and Curtis R Menyuk. Understanding leaky modes: Slab waveguide revisited. *Advances in Optics and Photonics*, 1(1):58–106, 2009.

[106] Song-Tsuen Peng and Arthur A Oliner. Guidance and leakage properties of a class of open dielectric waveguides: Part I-Mathematical formulations. *IEEE Transactions on Microwave Theory and Techniques*, 29(9):843–855, 1981.

[107] AA Oliner, Song-Tsuen Peng, Ting-Ih Hsu, and A Sanchez. Guidance and leakage properties of a class of open dielectric waveguides: Part II-New physical effects. *IEEE Transactions on Microwave Theory and Techniques*, 29(9):855–869, 1981.

[108] Lluis Torner, Fernando Canal, and Jordi Hernandez-Marco. Leaky modes in multilayer uniaxial optical waveguides. *Applied Optics*, 29(18):2805–2814, 1990.

[109] T Tamir and Foon Kou. Varieties of leaky waves and their excitation along multilayered structures. *IEEE Journal of Quantum Electronics*, 22(4):544–551, 1986.

[110] Manuel Peter, Andre Hildebrandt, Christian Schlickriede, Kimia Gharib, Thomas Zentgraf, Jens Förstner, and Stefan Linden. Directional emission from dielectric leaky-wave nanoantennas. *Nano Letters*, 17(7):4178–4183, 2017.

[111] David R Jackson, Christophe Caloz, and Tatsuo Itoh. Leaky-wave antennas. *Proceedings of the IEEE*, 100(7):2194–2206, 2012.

[112] Mowafak K Mohsen, MS M Isa, AAM Isa, MSIM Zin, S Saat, Z Zakaria, IM Ibrahim, M Abu, A Ahmad, and MK Abdulhameed. The fundamental of leaky wave antenna. *Journal of Telecommunication, Electronic and Computer Engineering (JTEC)*, 10(1):119–127, 2018.

[113] David R Jackson. Recent advances in leaky-wave antennas. In *2013 International Symposium on Electromagnetic Theory*, pages 9–12. IEEE, 2013.

[114] DR Jackson, J Chen, R Qiang, F Capolino, and AA Oliner. The role of leaky plasmon waves in the directive beaming of light through a subwavelength aperture. *Optics Express*, 16(26):21271–21281, 2008.

[115] Qi Song, Salvatore Campione, Ozdal Boyraz, and Filippo Capolino. Silicon-based optical leaky wave antenna with narrow beam radiation. *Optics Express*, 19(9):8735–8749, 2011.

[116] Leila Yousefi and Amy C Foster. Waveguide-fed optical hybrid plasmonic patch nanoantenna. *Optics Express*, 20(16):18326–18335, 2012.

[117] Sean Molesky, Zin Lin, Alexander Y Piggott, Weiliang Jin, Jelena Vucković, and Alejandro W Rodriguez. Inverse design in nanophotonics. *Nature Photonics*, 12(11):659–670, 2018.

[118] Wei Ma, Zhaocheng Liu, Zhaxylyk A Kudyshev, Alexandra Boltasseva, Wenshan Cai, and Yongmin Liu. Deep learning for the design of photonic structures. *Nature Photonics*, pages 1–14, 2020.

[119] Jiaqi Jiang, Mingkun Chen, and Jonathan A Fan. Deep neural networks for the evaluation and design of photonic devices. *Nature Reviews Materials*, pages 1–22, 2020.

[120] Peter R Wiecha, Clément Majorel, Christian Girard, Aurélien Cuche, Vincent Paillard, Otto L Muskens, and Arnaud Arbouet. Design of plasmonic directional antennas via evolutionary optimization. *Optics Express*, 27(20):29069–29081, 2019.

[121] Thorsten Feichtner, Oleg Selig, Markus Kiunke, and Bert Hecht. Evolutionary optimization of optical antennas. *Physical Review Letters*, 109(12):127701, 2012.

[122] Edgar Briones, Riemann Ruiz-Cruz, Joel Briones, Natalia Gonzalez, Jorge Simon, Mayela Arreola, and Gregorio Alvarez-Alvarez. Particle swarm optimization of nanoantenna-based infrared detectors. *Optics Express*, 26(22):28484–28496, 2018.

[123] Jacob Robinson, Seelig Sinton, and Yahya Rahmat-Samii. Particle swarm, genetic algorithm, and their hybrids: Optimization of a profiled corrugated horn antenna. In *IEEE Antennas and Propagation Society International Symposium (IEEE Cat. No. 02CH37313)*, volume 1, pages 314–317. IEEE, 2002.

[124] COMSOL Multiphysics GmbH, Göttingen, Germany. https://www.comsol.de.

[125] Günther Roelkens, Dries Van Thourhout, and Roel Baets. High efficiency silicon-on-insulator grating coupler based on a poly-silicon overlay. *Optics Express*, 14(24):11622–11630, 2006.

[126] Isabelle Staude and Jörg Schilling. Metamaterial-inspired silicon nanophotonics. *Nature Photonics*, 11(5):274–284, 2017.

[127] Yuri Kivshar. All-dielectric meta-optics and non-linear nanophotonics. *National Science Review*, 5(2):144–158, 2018.

[128] Sergio Lechago, Carlos García-Meca, Amadeu Griol, Miroslavna Kovylina, Laurent Bellieres, and Javier Martí. All-silicon on-chip optical nanoantennas as efficient interfaces for plasmonic devices. *ACS Photonics*, 6(5):1094–1099, 2019.

[129] Jinfa Ho, Yuan Hsing Fu, Zhaogang Dong, Ramón Paniagua-Dominguez, Eleen HH Koay, Ye Feng Yu, Vytautas Valuckas, Arseniy I Kuznetsov, and Joel KW Yang. Highly directive hybrid metal-dielectric Yagi-uda nanoantennas. *ACS Nano*, 12(8):8616–8624, 2018.

[130] René Kullock, Maximilian Ochs, Philipp Grimm, Monika Emmerling, and Bert Hecht. Electrically-driven Yagi-uda antennas for light. *Nature Communications*, 11(1):1–7, 2020.

[131] Terukazu Kosako, Yutaka Kadoya, and Holger F Hofmann. Directional control of light by a nano-optical Yagi-uda antenna. *Nature Photonics*, 4(5):312–315, 2010.

[132] SungWon Chung, Hooman Abediasl, and Hossein Hashemi. A monolithically integrated large-scale optical phased array in silicon-on-insulator CMOS. *IEEE Journal of Solid-State Circuits*, 53(1):275–296, 2017.

[133] Hooman Abediasl and Hossein Hashemi. Monolithic optical phased-array transceiver in a standard SOI CMOS process. *Optics Express*, 23(5):6509–6519, 2015.

[134] Reza Fatemi, Parham P Khial, Aroutin Khachaturian, and Ali Hajimiri. Breaking FOV-aperture trade-off with multi-mode nano-photonic antennas. *IEEE Journal of Selected Topics in Quantum Electronics*, 27(1):1–14, 2020.

[135] Ami Yaacobi, Jie Sun, Michele Moresco, Gerald Leake, Douglas Coolbaugh, and Michael R Watts. Integrated phased array for wide-angle beam steering. *Optics Letters*, 39(15):4575–4578, 2014.

[136] JC Hulme, JK Doylend, MJR Heck, JD Peters, ML Davenport, JT Bovington, LA Coldren, and JE Bowers. Fully integrated hybrid silicon two dimensional beam scanner. *Optics Express*, 23(5):5861–5874, 2015.

[137] Christopher V Poulton, Ami Yaacobi, Zhan Su, Matthew J Byrd, and Michael R Watts. Optical phased array with small spot size, high steering range and grouped cascaded phase shifters. In *Integrated Photonics Research, Silicon and Nanophotonics*, pages IW1B–2. Optica Publishing Group, 2016.

[138] Josué J López, Scott A Skirlo, Dave Kharas, Jamison Sloan, Jeffrey Herd, Paul Juodawlkis, Marin Soljačić, and Cheryl Sorace-Agaskar. Planar-lens enabled beam steering for chip-scale LiDAR. In *2018 Conference on Lasers and Electro-Optics (CLEO)*, pages 1–2. IEEE, 2018.

[139] Aseema Mohanty, Qian Li, Mohammad Amin Tadayon, Gaurang R Bhatt, Euijae Shim, Xingchen Ji, Jaime Cardenas, Steven A Miller, Adam Kepecs, and Michal Lipson. An active visible nanophotonics platform for sub-millisecond deep brain neural stimulation. In *CLEO: Applications and Technology*, pages ATh3Q–1. Optica Publishing Group, 2018.

[140] Qiankun Liu, Daniel Benedikovic, Tom Smy, Ahmad Atieh, Pavel Cheben, and Winnie N Ye. Circular optical phased arrays with radial nano-antennas. *Nanomaterials*, 12(11):1938, 2022.

[141] Arash Kazemian, Pengdi Wang, Yating Zhuang, and Yasha Yi. Optimization of the silicon-based aperiodic optical phased array antenna. *Optics Letters*, 46(4):801–804, 2021.

[142] Daniel Benedikovič, Qiankun Liu, Alejandro Sánchez-Postigo, Ahmad Atieh, Tom Smy, Pavel Cheben, and Winnie N Ye. Circular optical phased array with large steering range and high resolution. *Sensors*, 22(16):6135, 2022.

[143] Daniele Melati, Mohsen Kamandar Dezfouli, Yuri Grinberg, Jens H Schmid, Ross Cheriton, Siegfried Janz, Pavel Cheben, and Dan-Xia Xu. Design of compact and efficient silicon photonic micro antennas with perfectly vertical emission. *IEEE Journal of Selected Topics in Quantum Electronics*, 27(1):1–10, 2020.

[144] Henry Gwyn Jeffreys Moseley. XCIII. The high-frequency spectra of the elements. *The London, Edinburgh, and Dublin Philosophical Magazine and Journal of Science*, 26(156):1024–1034, 1913.

[145] Mingyan Fan, Miloš A Popović, and Franz X Kärtner. High directivity vertical fiber-to-chip coupler with anisotropically radiating grating teeth. In *Conference on Lasers and Electro-Optics*, page CTuDD3. Optica Publishing Group, 2007.

[146] Ralph W Gerchberg. A practical algorithm for the determination of plane from image and diffraction pictures. *Optik*, 35(2):237–246, 1972.

[147] Manan Raval, Ami Yaacobi, and Michael R Watts. Integrated visible light phased array system for autostereoscopic image projection. *Optics Letters*, 43(15):3678–3681, 2018.

[148] James R Fienup. Reconstruction of an object from the modulus of its fourier transform. *Optics Letters*, 3(1):27–29, 1978.

[149] WH Zachariasen. Untersuchungen über die kristallstruktur von sesquioxyden und verbindungen abo3. *Skrifter utgitt av det Norske Videnskaps-Akademi i Oslo*, 1:1–165, 1928.

[150] BT Matthias and JP Remeika. Ferroelectricity in the ilmenite structure. *Physical Review*, 76(12):1886, 1949.

[151] RS Weis and TK Gaylord. Lithium niobate: Summary of physical properties and crystal structure. *Applied Physics A*, 37:191–203, 1985.

[152] Prem Kumar. Quantum frequency conversion. *Optics Letters*, 15(24):1476–1478, 1990.

[153] MH Chou, KR Parameswaran, Martin M Fejer, and I Brener. Multiple-channel wavelength conversion by use of engineered quasi-phase-matching structures in $LiNbO_3$ waveguides. *Optics Letters*, 24(16):1157–1159, 1999.

[154] Giulio Cerullo and Sandro De Silvestri. Ultrafast optical parametric amplifiers. *Review of Scientific Instruments*, 74(1):1–18, 2003.

[155] Matthew Pysher, Russell Bloomer, Christopher M Kaleva, Tony D Roberts, Philip Battle, and Olivier Pfister. Broadband amplitude squeezing in a periodically poled $KTiOPO_4$ waveguide. *Optics Letters*, 34(3):256–258, 2009.

[156] Krishna Thyagarajan, J Lugani, S Ghosh, K Sinha, Anthony Martin, Daniel Barry Ostrowsky, Olivier Alibart, and Sébastien Tanzilli. Generation of polarization-entangled photons using type-II doubly periodically poled lithium niobate waveguides. *Physical Review A*, 80(5):052321, 2009.

[157] Adeline Orieux and Eleni Diamanti. Recent advances on integrated quantum communications. *Journal of Optics*, 18(8):083002, 2016.

[158] Christophe Couteau. Spontaneous parametric down-conversion. *Contemporary Physics*, 59(3):291–304, 2018.

[159] Jiefu Zhu, Xuerui Sun, Tingting Ding, Yongzhi Tang, Shijie Liu, Yuanlin Zheng, and Xianfeng Chen. Sum-frequency generation in a high-quality thin film lithium niobate microdisk via cyclic quasi-phase matching. *JOSA B*, 40(5):D44–D49, 2023.

[160] Luis Arizmendi. Photonic applications of lithium niobate crystals. *Physica Status Solidi (a)*, 201(2):253–283, 2004.

[161] Di Zhu, Linbo Shao, Mengjie Yu, Rebecca Cheng, Boris Desiatov, CJ Xin, Yaowen Hu, Jeffrey Holzgrafe, Soumya Ghosh, Amirhassan Shams-Ansari, et al. Integrated photonics on thin-film lithium niobate. *Advances in Optics and Photonics*, 13(2):242–352, 2021.

[162] Cheng Wang, Mian Zhang, Brian Stern, Michal Lipson, and Marko Lončar. Nanophotonic lithium niobate electro-optic modulators. *Optics Express*, 26(2):1547–1555, 2018.

[163] Viphretuo Mere, Forrest Valdez, and Shayan Mookherjea. Improved fabrication of scalable hybrid silicon nitride-thin-film lithium niobate electro-optic modulators. *JOSA B*, 40(5):D5–D14, 2023.

[164] Andreas Boes, Lin Chang, Carsten Langrock, Mengjie Yu, Mian Zhang, Qiang Lin, Marko Lončar, Martin Fejer, John Bowers, and Arnan Mitchell. Lithium niobate photonics: Unlocking the electromagnetic spectrum. *Science*, 379(6627):eabj4396, 2023.

[165] Toshiaki Suhara and Masatoshi Fujimura. *Waveguide nonlinear-optic devices*, volume 11. Springer Science & Business Media, 2003.

[166] Hiroshi Fukuda, Koji Yamada, Tai Tsuchizawa, Toshifumi Watanabe, Hiroyuki Shinojima, and Sei-ichi Itabashi. Ultrasmall polarization splitter based on silicon wire waveguides. *Optics Express*, 14(25):12401–12408, 2006.

[167] Folkert Horst, William MJ Green, Solomon Assefa, Steven M Shank, Yurii A Vlasov, and Bert Jan Offrein. Cascaded mach-zehnder wavelength filters in silicon photonics for low loss and flat pass-band WDM (de-) multiplexing. *Optics Express*, 21(10):11652–11658, 2013.

[168] Pengxin Chen, Sitao Chen, Xiaowei Guan, Yaocheng Shi, and Daoxin Dai. High-order microring resonators with bent couplers for a box-like filter response. *Optics Letters*, 39(21):6304–6307, 2014.

[169] Sitao Chen, Yaocheng Shi, Sailing He, and Daoxin Dai. Low-loss and broadband 2×2 silicon thermo-optic mach-zehnder switch with bent directional couplers. *Optics Letters*, 41(4):836–839, 2016.

[170] Enrique AJ Marcatili. Dielectric rectangular waveguide and directional coupler for integrated optics. *Bell System Technical Journal*, 48(7):2071–2102, 1969.

[171] Amnon Yariv. Coupled-mode theory for guided-wave optics. *IEEE Journal of Quantum Electronics*, 9(9):919–933, 1973.

[172] Emanuel Marom, O Ramer, and S Ruschin. Relation between normal-mode and coupled-mode analyses of parallel waveguides. *IEEE Journal of Quantum Electronics*, 20(12):1311–1319, 1984.

[173] Charles Vassallo. Optical waveguide concepts. *Optical Wave Sciences and Technology*, 1:Sec–5, 1991.

[174] Lucas B Soldano and Erik CM Pennings. Optical multi-mode interference devices based on self-imaging: Principles and applications. *Journal of Lightwave Technology*, 13(4):615–627, 1995.

[175] Hamed Nikbakht, Mohammad Talebi Khoshmehr, Bob Van Someren, Dieter Teichrib, Manfred Hammer, Jens Förstner, and B Imran Akca. Asymmetric, non-uniform 3-db directional coupler with 300-nm bandwidth and a small footprint. *Optics Letters*, 48(2):207–210, 2023.

[176] Dan-Xia Xu, Adam Densmore, Philip Waldron, Jean Lapointe, Edith Post, André Delâge, Siegfried Janz, Pavel Cheben, Jens H Schmid, and Boris Lamontagne. High bandwidth SOI photonic wire ring resonators using MMI couplers. *Optics Express*, 15(6):3149–3155, 2007.

[177] A Maese-Novo, Robert Halir, S Romero-García, D Pérez-Galacho, L Zavargo-Peche, A Ortega-Moñux, I Molina-Fernández, JG Wangüemert-Pérez, and P Cheben. Wavelength independent multimode interference coupler. *Optics Express*, 21(6):7033–7040, 2013.

[178] Erika Andersson, Tommaso Calarco, Ron Folman, Mauritz Andersson, Björn Hessmo, and Jörg Schmiedmayer. Multimode interferometer for guided matter waves. *Physical Review Letters*, 88(10):100401, 2002.